Development and characterisation of a Total Ion Beam Analysis system based on Heavy Ion PIXE spectroscopy

Carington Masekane, Masedi

Doctoral thesis / Doktorski rad

2024

Degree Grantor / Ustanova koja je dodijelila akademski / stručni stupanj: **University of Zagreb, Faculty of Science / Sveučilište u Zagrebu, Prirodoslovno-matematički fakultet**

Permanent link / Trajna poveznica: https://urn.nsk.hr/urn:nbn:hr:217:916795

Rights / Prava: In copyright/Zaštićeno autorskim pravom.

Download date / Datum preuzimanja: **2025-01-17**

Masedi Carington Masekane

Development and characterisation of a Total Ion Beam Analysis system based on Heavy Ion PIXE spectroscopy

INTERNATIONAL DUAL DOCTORATE

Zagreb, 2024

Masedi Carington Masekane

Razvoj i karakterizacija sustava za cjelovitu analizu ionskim snopovima pomoću teškoionske PIXE spektroskopije

MEĐUNARODNI DVOSTRUKI DOKTORAT

Zagreb, 2024

Thesis presented in the:

I. College of Science, Engineering and Technology (CSET), Department of Physics, University of South Africa, South Africa

II. Faculty of Science, Department of Physics, University of Zagreb, Croatia.

Supervisory panel:

1. Prof. Sabata Jonas Moloi, Department of Physics, College of Science Engineering and Technology (CSET), University of South Africa, South Africa

2. Dr.sc. Ivančica Bogdanović-Radović, Division of Experimental Physics, Laboratory for Ion Beam Interactions, Ruđer Bošković Institute, Croatia

3. Prof. Mandla Msimanga, Department of Physics, Faculty of Science, Tshwane University of Technology, South Africa; iThemba Laboratory for Accelerator Based Sciences, Tandem AMS, South Africa

Declaration

University of South Africa student number: 62700022

University of Zagreb scientist ID: 0119058728-1

I declare that the Thesis presented is my own work and that all sources used or quoted have been indicated and acknowledged by means of complete references.

I also declare that the Thesis has been submitted to originality checking software and falls within the accepted requirements for originality.

I further declare that I have not previously submitted this work, or part of it, for examination at the University of South Africa or at the University of Zagreb for another qualification, or at any other higher education institution other than the ones stated herein.

_____   _October 2024_

Signature   Date

Supervisors

Dr.sc. Ivančica Bogdanović-Radović graduated from the Faculty of Natural Sciences at the University of Zagreb in 1991 with a degree in physics, specialising in experimental physics. In the same year, she began working as a research assistant in the Laboratory for Ion Beam Interactions, Department of Experimental Physics, at the Ruđer Bošković Institute, where she still works today. She graduated with a master's degree in 1994 and obtained her doctorate in 1997, also at the Faculty of Natural Sciences in Zagreb. After her doctorate, she completed a 13-month Lise Meitner Postdoctoral Fellowship at the Institute of Experimental Physics at the Johannes Kepler University in Linz, Austria. Since the beginning of her scientific career, she has been involved in the development and application of nuclear analysis techniques with ion beams for the analysis and modification of materials. In the last 10 years, her research has focused on the development and application of secondary ion mass spectrometry with MeV ions (MeV-SIMS) technique. Since 2019, she has been working as a senior scientist with a permanent position. To date, she has published more than 200 scientific papers, which have been cited over 2100 times according to WoSCC. She has participated in over 40 international scientific conferences and has given 18 invited talks. She has so far supervised 3 PhD theses, 2 diploma theses and 2 ERASMUS students. She has been an opponent in the defence of several foreign dissertations and a reviewer for several foreign scientific foundations. She currently leads the Horizon Europe project RIANA and also led the Horizon 2020 project RADIATE, the Unity Through Knowledge project, the Croatian Science Foundation project and several IAEA CRP projects. Since 2017 she is a member of the User Selection Panel for the Ion Beam Centre Helmholz Zentrum Dresden Rosendorf, Germany and was a member of the Nuclear Physics Division Board of the European Physical Society from 2017-2023. Since 2019, she is President of the Scientific Council of the Ruđer Bošković Institute and Chair of the Ion Beam Analysis (IBA) Conference International Advisory Board. In 2023, she became editor of the journal Nuclear Instruments and Methods B.

Prof. Sabata Jonas Moloi is an experimental Solid-State Physics professor at the University of South Africa, in the Department of Physics. He is rated as a C2 researcher by the South African National Research Foundation (NRF), focusing on improving properties of materials for various applications. His expertise in materials preparation, device fabrication, and characterization has resulted in several collaborations with a number of scientists from wide ranging institutions, including the iThemba Laboratory for Accelerator Based Sciences

(LABS). Prof. Moloi has been invited speaker at various international and national conferences. Prof. Moloi has received several grants in his career, including the NRF Collaborative Postgraduate Training Programme and the Joint Institute for Nuclear Research Programme grants. He has also collaborated with various international research institutes, including the Joint Institute Nuclear Research in Russia and the Institute of Geological and Nuclear Science in New Zealand. He is a referee to various international scientific journals and was an editorial committee member of the first ever South African Institute of Physics (SAIP) conference proceedings. He continues to serve as an invited external examiner for various universities in South Africa.

Prof. Mandla Msimanga's expertise is in ion beam based nuclear analytical techniques. He joined the Tshwane University of Technology (TUT) in 2014 after spending 10 years of combined work and study at the University of Cape Town (UCT) and the South African National Research Foundation's (NRF) iThemba LABS in Cape Town and Johannesburg. He has been involved in radiation-matter interaction research since 2003, looking at both fundamental and applied aspects of the field. He has led research groups at iThemba LABS in IAEA Coordinated Research Projects (CRPs) from 2007-2011; 2014-2018 and more recently from 2021-2024, all focusing on ion beam techniques and applications thereof. He currently serves as the Chair of the Photovoltaic Nanocomposites Research & Development Platform at the Tshwane University of Technology, working on machine learning driven research on 3rd generation photovoltaic materials and performance monitoring of photovoltaic systems. Prof Msimanga's student training portfolio includes 10 MSc and 2 PhD students between 2014 and 2024, with several students in the pipeline. He is rated as a C2 researcher by the National Research Foundation of South Africa (*i.e., someone that is recognised as an established researcher in their area of study with some international recognition*) and currently has over fifty peer reviewed articles in WoS journals.

Acknowledgements

Indeed, I can only rise as tall as the shoulders of giants upon which I stand. For this reason, I begin my note of thanks by acknowledging my mentors, for the body of work presented in this Thesis, and in overall for their invaluable contribution to my growth as both a scientist and good human:

- ♦ To my long-time mentor, Prof. Mandla Msimanga, who took me under his wing some years ago during my early undergrad training. For the guidance you have provided in navigating this journey, the many doors you have opened without hesitancy; and for patiently seeing through my ambition in science and towards a doctorate, I am eternally grateful. Thank you for your dedication to this 'project', *Inkosi ikubusise*.
- ♦ To Dr. Iva, who warmly embraced me as her student and welcomed me to the RBI family. Thank you for your kindness, consistent support and for the wealth of knowledge you have poured into my cup. Your mentorship has been uplifting.
- ♦ And finally, to Prof Moloi, for your immeasurable support and consideration, and for all the opportunities you have presented. Your presence has in many ways strengthened my pursuit, for which I am humbly grateful.

I further extend my thanks to colleagues from the RBI, namely: Drs. Zdravko Siketić, Iva Božičevic Mihalić, Stjepko Fazinić, Milko Jakšić, Matea Krmpotić and fellow peer Anja Mioković, for all your valuable and insightful inputs. Likewise, a great thank you to colleagues at iThemba LABS, Drs. Morgan Madhuku, Phillip Sechogela and Mamogo Masenya, for all your contributions. I also thank Mr. Marko Hum from the University of Zagreb, for being consistent and accommodating throughout the joint PhD. A great thank you to Ms. Lerato Makgae, the South African National liaison Officer to the International Atomic Energy Agency (IAEA), for going far and beyond in our application for my fellowship at the RBI. I finally acknowledge the IAEA, the National Research Foundation of South Africa (NRF), University of South Africa, iThemba LABS and the Ruđer Bošković Institute for financial, resource and infrastructural support.

To my broader family and the Masekane clan at large; my siblings Kgadi and Malebo; and to my dear friend Okgonne for your kind and uplifting friendship, thank you all for your support.

I finally close my note of thanks acknowledging my parents, *Nakampe Masekane* and *Dikeledi Malatji*. I sincerely thank you for all your teachings, and the efforts you made towards my growth, I see you. Above all, in what this work represents, thank you for inspiring an educated generation.

I now present this in God, Ramasedi, for my curiosity, and to whom I serve in my contribution to human thought.

Dedicated to my dear wife, Shirley, for your unwavering love and support; and to my son, Khosi, whose arrival has given life greater meaning.

Abstract

The simultaneous use of two or more Ion Beam Analysis (IBA) techniques, or 'Total IBA', is well adapted in many ion beam laboratories around the world, however using proton and/or helium ion beams. Amongst the most commonly found Total IBA synergies is the use of Particle Induced X-ray Emission (PIXE) spectroscopy for the extraction of elemental compositions and concentrations, used with other complimentary techniques providing information on depth. The implementation of PIXE in a Total IBA system using heavy ion probes, mainly aimed at countering inherent limitations in techniques such as Elastic Recoil Detection Analysis (ERDA) or Secondary Ion Mass Spectrometry using MeV heavy ions (MeV SIMS) is yet to be explored. Practical realisation of such an analytical feat is however not trivial and remains largely hindered by the sparse database of experimental heavy ion induced X-ray production cross sections (XPCS), needed for atomic quantitation. The lacking database thus further underscores the fact that many laboratories do not use heavy ion based IBA techniques (and so do not necessarily need these heavy ion induced XPCS), leaving the field of heavy ion TIBA largely unexplored.

This thesis reports on the implementation of Total Ion Beam Analysis built around Heavy Ion PIXE. The work is presented in two parts, with the first being the measurement of K-, L- and M- shell heavy ion induced X-ray production cross sections (XPCS) due to C, Cl, Si, Cu, Ag and I ions in Cr, Ni, Ge, Mo, Sn, W, Au and Bi targets within the 0.08 MeV/u – 2 MeV/u ion energy range. The generated experimental datasets were compared to predictions by the ECPSSR theory and discussed in terms of dominant atomic ionisation modes. Selected X-ray production cross section data were also used to develop a semi-empirical model for interpolating XPCS data. Calculated semi-empirical datasets from the model were compared and validated by experiment as well as Machine Learning predictions. Discrepancies between experiment, semi-empirical and ECPSSR cross section data are discussed in terms of Multiple Ionisation effects, evaluated using broad energy shifts and high resolution PIXE spectrometry. In the second part, results obtained from PIXE measurements carried out in coincidence with Time of Flight-ERDA (TOF-ERDA) are presented. A novel approach was devised to use PIXE spectra to deconvolute mass overlaps of mid-Z elements that could not be in TOF-ERDA scatter plots due to the intrinsic mass resolution limitation of the ToF-ERDA spectrometer. Furthermore, a feasibility study of the use of Heavy Ion PIXE synergistically with MeV SIMS

was carried out to determine elemental and molecular compositions on a single analytical region for ink and paint samples.

Prošireni sažetak

Osnovno načelo sustava za cjelovitu analizu ionskim snopovima bazira se na istovremenoj detekciji nekoliko reakcijskih produkata kao što su X-zrake, γ-zrake, čestice raspršene unatrag, čestice raspršene prema naprijed, itd., koji se emitiraju iz uzorka nakon interakcije s upadnim ionom a u cilju što detaljnije analize ispitivanog uzorka. U praksi se ispitivani uzorak bombardira ionima u komori koja je opremljena s odabranim brojem detektora čestica, X-zračenja i γ -zračenja koji su strateški postavljeni kako bi se uzele u obzir specifičnosti interakcija koje se mogu dogoditi, te kako bi se što bolje kvantificirali produkti reakcija. Najčešća kombinacija analitičkih metoda koju koriste mnogobrojni laboratoriji za interakcije ionskih snopova u svijetu je kombinacija metoda PIXE-a (česticama inducirana emisija X-zračenja) i RBS-a (Rutherfordovo raspršenje unatrag). Za to se najčešće koriste protoni ili alfa čestice za koje postoji prilično dobra baza podataka fundamentalnih atomskih parametara (udarnih presjeka za produkciju karakterističnog X-zračenja i raspršenja). Dok PIXE tehnika omogućuje određivanje atomskih koncentracija za elemente $Z > 11$, RBS nam daje informaciju o lakim elementima koji su vrlo često prisutni u većim količinama u uzorcima kao što su C, N, O a koji se ne mogu detektirati preko X-zračenja. Također, RBS tehnika nam daje informaciju o dubinskim profilima elemenata u uzorku. Kombinacijom dviju tehnika može se postići 3-dimenzionalna karakterizacija nepoznatog uzorka. Uz PIXE i RBS, postoje i druge tehnike koje se mogu istovremeno koristiti kod protonske pobude ili pobude alfa česticama no situacija je puno drugačija za teže ione. Razlozi za to dobrim dijelom leže u nepoznavanju fundamentalnih fizikalnih parametara kao što su udarni presjeci za dobivanje X-zračenja, dostupnosti snopova teških iona iz akceleratora, kao i zbog ograničenja računalnih kodova koji se koriste za analizu podataka. Nedavna pojavat nove generacije kodova za analizu podataka i napori u provođenju sustavnih mjerenja fundamentalnih parametara te razvoj novih analitičkih metoda potaknuli su interes za kombiniranje više metoda analiza za koje je potrebna pobuda teškim ionima..

Jedna od tehnika koja koristi za pobudu teške ione te se primjenjuje za dubinsko profiliranje elemenata u uzorku je TOF ERDA (mjerenje unaprijed izbijenih čestica mjerenjem vremena proleta). TOF ERDA ima vrlo dobru dubinsku rezoluciju (~1 nm pri površini) za analizu tankih filmova ali je ograničena u razdvajanju masa. Uzimajući u obzir da je masena razlučivost TOF ERDA metode u najboljem slučaju bolja od 1 za mase ispod 40 amu, analize uzoraka koji sadrže nekoliko težih elemenata sa sličnim masama predstavljat će problem za TOF ERDA. S druge strane, komplementarna upotreba PIXE metode s MeV SIMS (Sekundarna Ionska Masena Spektrometrija s MeV ionima) metodom već je napravljena kako bi povezala

informacija o elementnom sastavu s informacijom o molekularnom sastavu uzorka. Upotreba PIXE metode s MeV SIMS metodom do sada se, međutim, provodila korištenjem protona kao pobude, zahtijevajući prebacivanje s teških iona koji su potrebni za pobudu u MeV SIMS metodi na protone kojima se standardno radi PIXE. Prebacivanjem s jednog snopa na drugi mora se micati uzorak radi fokusiranja i optimizacije snopa te se na taj način gubi točna korelacija između elementnog i masenog mapiranja na istom mjestu uzorku. Korištenjem istog teškog iona za MeV SIMS i za PIXE mjerenje nije potrebno micati uzorak te se može napraviti korelacija između elementnog i molekularnog mapiranje na istom dijelu uzorka što je važno za primjene u biologiji, forenzici i kulturnoj baštini. Ograničenja TOF ERDA i MeV SIMS analiza mogu se izbjeći provođenjem analiza istovremeno ili uzastopno na istoj analiziranoj površini uzorka. U slučaju TOF ERDA, različiti teži elementi mogli su se lako razlikovati korištenjem informacija dobivenih iz spektara karakterističnog X-zračenja. Nažalost, naširoko korišteni teorijski modeli za predviđanje udarnih presjeka za produkciju karakterističnog X-zračenja (XPCS) koji su potrebni za kvantifikaciju ne mogu se jednostavno prilagoditi za HI PIXE, zbog višestrukih ionizacija kojih nema kod pobude protonima. Nedavni napori u mjerenjima eksperimentalnih XPCS induciranih teškim ionima i dostupnost nove generacije kodova za analizu podataka sada omogućuju analizu više spektara, čineći izglede za cjelovitu analizu uzoraka temeljenu na PIXE metodi s teškim ionima mogućim. Unatoč tome, budući da je neizvedivo mjeriti XPCS za sve kombinacije ion-atom, postoji stalna potreba za pouzdanim eksperimentalnim XPCS kako bi se ostvario potpuni pristup analizama teških iona.

Ovaj rad stoga izvještava o implementaciji totalnog pristupa analizi pomoću ionskih snopova koji se temelji na PIXE metodi s teškim ionima. Rad je podijeljen u dva dijela, prvi se bazira na mjerenjima udarnih presjeka za produkciju X-zračenja u K-, L- i M-ljuskama izazvanih teškim ionima korištenjem C, Cl, Si, Cu, Ag i I iona u metama Cr, Ni, Ge, Mo, Sn, W, Au i Bi u rasponu energija 0,08 MeV/u – 2 MeV/u. Izmjereni podaci uspoređeni su s predviđanjima ECPSSR teorije i raspravljeni u kontekstu dominantnih načina ionizacije atoma. Odabrani podaci za produkcijske udarne presjeke također su korišteni za razvoj polu-empirijskog modela za interpolaciju XPCS podataka, što je demonstrirano na Bi meti. Izračunati XPCS iz polu-empirijskog modela uspoređeni su kako s eksperimentalnim podacima tako i s predviđanjima nekoliko algoritama strojnog učenja. Nepodudarnosti između eksperimentalnih, polu-empirijskih i teorijskih ECPSSR udarnih presjeka diskutirani su u kontekstu višestrukih ionizacija, koje dovode do energijskog pomaka vrhova X-zračenja i koji su mjereni PIXE

spektrometrijom visoke rezolucije. U drugom dijelu prikazani su rezultati dobiveni PIXE -TOF ERDA koincidentnim mjerenjima. Novi pristup koristio je PIXE spektre za odvajanje srednjih Z elemenata koji se ne mogu odvojiti samo pomoću TOF ERDA mjerenja zbog loše masene razlučivosti za M > 40 amu. Nadalje, HI PIXE je proveden sekvencijalno s MeV SIMS kako bi se odredio elementarni i molekularni sastav na istom analiziranom području za forenzičke i uzorke kulturne baštine (tinte i boje).

Ključne riječi: Analiza ionskim snopovima, cjelovita analiza ionskim snopovima, spektroskopije, emisija X-zračenja inducirana teškim ionima, ToF-ERDA, MeV SIMS, udarni presjeci za produkciju X-zračenja, polu-emipirijski, višestruka ionizacija, koincidencije.

Table of Contents

List of Acronyms

ADC	-	Analog to Digital Converter
EBS	-	Elastic Backscattering Spectroscopy
ERDA	-	Elastic Recoil Detection Analysis
eV	-	Electron Volt
FWHM	-	Full Width at Half Maximum
HI PIXE	-	Heavy Ion PIXE
IBA	-	Ion Beam Analysis
MCP	-	Multi Channel Plate
MI	-	Multiple Ionisation
MVA	-	Multi Variate Analysis
PIXE	-	Particle Induced X-ray Emission
SIMS	-	Secondary Ion Mass Spectrometry
SRIM	-	Stopping and Range of Ions in Matter
TDC	-	Time to Digital Converter
TIBA	-	Total Ion Beam Analysis
TOF	-	Time of Flight
XPCS	-	X-ray production cross section

Chapter 1

1.1 General overview

The application of Ion Beam Analytical (IBA) techniques for materials analysis continues to be favourable due to the fairly non-destructive and reliable nature within which atomic, molecular and structural quantitation can be achieved. Particularly within the low MeV range, the use of ion beams has enabled several significant advancements in fundamental ion-matter interaction studies, as well as in other applied fields such as archaeology, biology, forensics, and for the development of novel materials aimed at achieving a circular economy, to name a few [1], [2], [3], [4]. The viability of ion beam analytical techniques, which remain both competitive and complimentary to newer and more compact methods is due to the accessibility of physical material properties not normally possible other than through the evaluation of ion-atom interactions. Although substantial information can be obtained from one IBA technique, the efficacy of measurements is generally improved when more than one technique is used at a time. This approach is largely effective as it provides more than one set of information about a material, such as either concentrations and/or elemental depth profiles, thus mitigating inherent limitations from either one of the techniques.

This concept, so called Total Ion Beam Analysis (TIBA), can therefore be described as a system that uses a set of particle and photon detectors to capture reaction products either in the forward or backward direction, depending on the geometry of the experimental configuration [5], [6]. The detection and analysis of multiple reaction products enables a more consolidated description of a target (*i.e.,* elemental or molecular composition, as well as lateral and/or depth profiles). While this consideration still has room for exploration of combinations not yet exploited, the concept of Total Ion Beam Analysis is in itself not new, and has been achieved in varying degrees and formats by several laboratories around the world. One of the most widely adopted configurations, first implemented in the early 1980's, is the co-implementation of Particle Induced X-ray Emission (PIXE) and Rutherford Backscattering Spectrometry (RBS) to extract both atomic concentrations and depth profiles of light and heavy elements from a single measurement [7], [8]. In this case, subsurface excitation enables the extraction of atomic elemental concentrations from PIXE (for $Z>13$) and an accurate account of sample depth profiles from RBS, with often negligible alteration to the target's chemistry. The

combination of both techniques therefore enables a 3-Dimensional characterisation of a target sample analysed self consistently on a single surface [9].

Even though ion backscattering cross sections are generally lower than ionisation cross sections for PIXE, the PIXE/RBS combination has nonetheless been efficient, optimized kinematically using the incident ion energy. Other IBA combinations also include the combination of PIXE and Particle Induced Gamma ray Emission (PIGE) spectroscopy, where the quantification of PIXE data is improved by PIGE, since Gamma rays from light elements are not prone to self-absorption as are soft X-rays (≤ 2 keV) [10], [11]. Therefore, by using both techniques concurrently, concentrations of light and heavy elements in a studied target can be calculated, attaining non-ambiguous characterization due to absorbed soft X-rays in-air or by the target itself [10].

Although IBA is widely appreciated as a powerful analytical tool for the applied sciences, it also continues to facilitate fundamental studies of low energy ion-atom collisions. One example is the study of interaction cross sections, in which ion beam techniques are used to provide physical data pertaining to slow ion induced collisions, such as scattering as well as characteristic photon emission. While it is generally accepted that IBA techniques are fairly non-destructive, it is undeniable that particle scattering and sputtering events induce varying degrees of physical changes in the studied materials during the measurements. These effects become significant where sensitive materials are concerned, such as biological samples or thin films, where material surface quantitation may become somewhat distorted by consecutive measurements using high current ion beams [12]. The use of a systematic TIBA approach is therefore needed, where multiple IBA techniques are carried out either consecutively or simultaneously, in order to mitigate uncertainties due to ion beam induced damage.

1.2 Heavy Ion Particle Induced X-ray Emission (HI-PIXE) spectroscopy

While PIXE spectroscopy is conventionally carried out using protons, the use of heavier ions (Heavy Ion PIXE) may extend the applicability of the technique, especially in the TIBA framework. Heavy ion IBA techniques generally exploit high stopping powers for slow moving ions to extract elemental depth profiles from analysed materials using recoil and scattering events. In the same consideration, ionisation cross sections due to heavy ions are generally higher compared to lighter projectiles such as protons at the same ion velocity [13]. This is largely due to Multiple Ionisation (MI) effects, which not only increase ionisation probabilities

for swift heavy ions but also enhance X-ray fluorescence and radiative transition probabilities [14]. Additionally, characteristic X-ray yields have often been seen to offset bremsstrahlung levels (*i.e.,* broad range X-rays from decelerating secondary electrons), thus leading to higher sensitivity for Heavy Ion PIXE compared to proton based PIXE at the same incident velocity [14], [15].

Even so, quantitation of PIXE spectra using data analyses software such as GeoPIXE [16] and GUPIX [17] heavily rests on the availability of reliable X-ray production cross sections (XPCS). These simply describe the probability for X-ray radiative ionisation post ion-atom impact. XPCS data is generally calculated using widely available theoretical models used for predicting ionisation cross sections; such as the Plane Wave Born Approximation (PWBA) and ECPSSR theory (*i.e.,* extension of the PWBA, with several corrections; see Chapter 2) [18]. The ionisation cross sections can then be translated to XPCS by using theoretical or experimental physical atomic parameters such as radiative transition probabilities as well as fluorescence yields [19].

Other ionisation cross section theoretical models also include the Semi-Classical Approximation (SCA), and the ECUSAR model (*i.e.,* modified ECPSSR model that considers the ion-atom impact in the frame of a United Atom). Unfortunately, existing theoretical models cannot simply be used for heavy ion interactions, and consequently ionisation cross sections [20], [21]. This is because the bulk of the current models is largely validated by a rich database of proton induced cross sections, whereas heavy ion XPCS data is largely sparse. Furthermore, the models are built upon the binary collisions approach, which fundamentally describes collision systems different from heavy ion-atom impact [20]. In addition, Multiple Ionisation effects in the low velocity range where the ion is less electron deficient are yet to be accounted for by theory, requiring an extension of the current database for multiple collision symmetries[22], [23], [24], [25], [26]. To this end, the implementation of Heavy Ion PIXE continues to be limited, by both the lack of experimental cross section data as well as atomic parameters, such that current theoretical models remain unreliable for very slow ions (< 0.5 MeV/u) [25], [27].

1.3 Semi-empirical parameterisation of heavy ion/proton XPCS ratios

As it is impracticable to carry out systematic cross section measurements for all possible ion-element atom combinations, a semi-empirical approach for the calculation of reliable cross section data may be quite useful. In this work, semi-empirical XPCS were calculated through the parameterisation of the ratio of experimental heavy ion and theoretical proton induced X-ray production cross sections. Measurements were carried out at the Tandem Accelerator Mass Spectrometry (TAMS) department of the iThemba Laboratory for Accelerator Based Sciences (LABS) in South Africa, and validated by experimental data measured at the laboratory for Ion Beam interactions of the Ruđer Bošković Institute (RBI) in Croatia. The description of the methodology and the calculated data, which are compared to experimental XPCS from literature, are articulated. Presented in the current study, is therefore an extension of the current experimental heavy ion induced XPCS database, and the novel method, aimed at fully realising the implementation of Heavy Ion PIXE in the TIBA frame.

1.4 Total Ion Beam Analysis (TIBA)

Even as there are several possible TIBA synergies, heavy ion TIBA remains largely unexplored. This has been particularly due to factors such as the lack of accurate fundamental physical parameters such as interaction cross sections, accelerator limitations, as well as limitations in data analysis codes [28], [29]. The recent availability and continued development of new generation data analysis codes such as DataFurnace [30] and the measurement of heavy ion induced atomic parameters has made the pursuit of a heavy ion TIBA approach much more feasible [5], [6], [29].

The synergy of powerful heavy ion-based depth profiling techniques such as Time of Flight Elastic Recoil Detection Analysis (TOF ERDA), may lead to improved sensitivity when applied self-consistently with Heavy Ion PIXE. While TOF ERDA is sensitive to light elements in a target matrix including hydrogen and its isotopes, it is intrinsically limited by its low mass resolving power for heavier elements. Simultaneous analyses with PIXE could be used to either consolidate data by providing separate heavy element concentrations, or be used in coincidence to resolve the TOF ERDA spectra for heavier masses. Reliable XPCS data therefore becomes important not only for atomic quantitation of PIXE spectra, but also for optimizing analytical conditions [29], [31].

In another consideration, MeV Secondary Ion Mass Spectrometry (SIMS) is a powerful technique which uses electronic sputtering for the desorption of surface molecules using heavy ions. Detected molecules are often used to draw conclusions about the chemical environment of a material for a range of applications, such as in forensics, biological as well as cultural and heritage research [32], [33]. PIXE has been used sequentially with MeV SIMS, to correlate molecular with elemental data, however induced by protons [32]. This means that the analysis is not carried out on exactly the same analytical region. On the other hand, Heavy Ion PIXE can be applied consecutively with MeV SIMS without changing the ion beam or moving the sample. Similarly, XPCS data then becomes useful for determining energies at which both the ionisation and electronic sputtering probabilities are close. The exploration of the implementation of Heavy Ion PIXE with TOF ERDA and with MeV SIMS was the focus of this study. The study reports on the pertinent theoretical principles and practical implementation of the two TIBA approaches and limitations thereof.

1.5. Thesis outline

The current chapter presents an overview of the motivation on which the study is based. Conceptual physical considerations are articulated in the second chapter, in which fundamental ion-atom interaction phenomena are discussed. An overview of the experimental setup used for measurements from both iThemba LABS and at the Ruđer Bošković Institute (RBI) is provided in Chapter 3. Experimental and semi-empirical X-ray production cross sections are presented in Chapter 4. The chapter discusses discrepancies between experiment and theoretical cross sections in terms of Multiple Ionisation effects, evaluated in part using high resolution PIXE spectrometry. Proof of concept measurements on the use of TOF ERDA and MeV SIMS self-consistently with Heavy Ion PIXE are presented in the 5th Chapter, highlighting relative strengths and inherent limitations of heavy ion TIBA. Overall findings are thus presented in the closing Chapter (6), reflecting upon the overall contribution of this body of work to the field.

Chapter 2

The interaction of charged particles with atoms in matter is of great importance in the implementation of ion beam analytical techniques. Knowledge of fundamental physical phenomena, such as ion stopping, sputtering, kinematics and scattering, as well as radiative ionisation, enables the qualitative and quantitative inference of a wide range of materials' properties. In the focus of expanding current heavy ion analytical technologies (as briefly covered in the previous chapter), this chapter discusses the fundamental processes upon which either one of the applied methods are based.

2.1 Ion – atom interactions

2.1.1. Ion stopping in matter

The interaction of a beam of mono-energetic charged projectile ions, dispersed in space time, colliding with a matrix of stationary atoms can be characterised by several mechanics. Well established amongst these are elastic and inelastic scattering about the constituent target atoms' nuclear mean field potential(s), depending on the ion impact parameter [34]. The impact parameter describes the relative distance between the projectile ion and the target nucleus, dictating both the degree of projectile ion energy loss as well as the projectile angle of deflection from the target nucleus [35]. As the ion traverses a given target length, a probable number of deflections result in consecutive centers of momentum transfer, such that the interaction between the incident ions with the surrounding atoms in a target can be observed in terms of ion energy loss (or stopping) [36]. This loss of energy (*i.e.,* transferred energy) is determined as an average of the summed moments of interaction due to both the nuclear and electronic Coulomb potential (*i.e.,* mean potential of the bound target electrons) imposed on the ion by the constituent atoms. With this consideration, energy loss by means of radiative emission due to decelerating electrons (*i.e.,* Bremsstrahlung) is not applicable and is thus considered to be zero. The main contribution to ion stopping therefore, due to nuclear and electronic coulomb forces acting on an incident projectile ion, is generically described by the stopping force '*S(E)*' for a given target mass density (Equation 2.1.) [37], [38].

$$S(E) = -\frac{1}{N_\rho} \int \frac{1}{dX} dE \qquad\qquad 2.1.$$

where *dX*, *dE* and N_ρ are the target depth, differential ion energy and number of scattering centers per *target density*.

Although the stopping force is well described for light projectiles such as protons, the description of ion stopping for heavier charged particles in the same mass density is comparatively and fundamentally different. This is mainly because theoretical frameworks have been largely based on Binary collision approximations, with only recent efforts and simulations focusing on models based on molecular dynamics [39]. Even so, the theoretical description of stopping powers for protons is constricted to specific projectile energy ranges, such that no single universal theory can be used across all ion velocities. This is mainly because the contributing forces to ion stopping depend on ion velocity, where regions are defined by either dominating electronic or nuclear stopping forces.

Two widely adopted successful models are the Bethe-Bloch formalism, as well as the classical Bohr theory [39]. These frameworks are based on the Born approximation, as well as Binary collisions approximations respectively. Since ion energy loss is non-linear, the influence of either electronic or nuclear stopping force depends on both the ion energy and charge states, which can be correlated to the projectile electron(s) *Thomas-Fermi velocity (v_{TF})* [35]. This parameter is described as $v_{TF} = v_0 Z_1^{2/3}$, where v_0 is the Bohr speed given by $e^2/\hbar$ and Z_1 is the projectile atomic number.

The *1/E* dependence of the nuclear stopping contribution as the ion velocity increases implies an electronic stopping force dominance for incident point charge densities in the high energy range (which lies in the $0.1v_0 \leq v_1 \leq v_{TF}$ range), and a dominance of the nuclear stopping force in the opposite end. With these are a few considerations [39], [40]:

- The validity of the Bohr framework for ion-electron scattering is given by $\frac{2Z_1 e^2}{hv} \gtrsim 1$, based on the classical orbit description.
- The Born approximation-based Bethe's theory is therefore valid at $\frac{2Z_1 e^2}{hv} \lesssim 1$. Bohr and Bethe's foundational descriptions are given as:

$$-\frac{dE}{dx} = \frac{4\pi Z_1^2 Z_2 e^4}{mv^2} N.B \qquad 2.2.$$

where N is the number of atoms per unit volume in a target matrix, and B is the stopping number given as:

$$B_{Bethe} = \ln(\frac{2mv^2}{h w}) \ or \ B_{Bohr} = \ln(\frac{Cmv^2}{Z_1 e^2 w}) \qquad 2.3.$$

where ω is the target electron effective resonance frequency given as the quotient of the mean excitation energy and the reduced Planck constant (*i.e., I/ℏ*).

The classical Bohr description uses approximate impact parameter values, including a kinematic factor that considers ion mass, charge, and energy/velocity. Within its criteria, the Bohr model estimates empirical datasets up to ~0.5 MeV/u. On the other hand, from a practical view, the extension of Bethe's theory in the form of the Bethe-Bloch formula, lies in that momentum transfer is a measurable quantity compared to the impact parameter [41]. The oscillator strengths for the target electrons, central to the Bethe-Bloch formula, are obtained through semi-empirical calculations which include the mean excitation potential. In this case, one of the corrections adapted to Bethe's theory was charge asymmetry, approximated using Bloch's method [35], [41]. Charge asymmetry corrections are particularly important for collisions where $v_1 \lesssim (Z_1 Z_2/2)^{1/3} v_B$, a state which can be described intermediately by projectile screening and shell corrections. As widely covered in literature, the Bethe-Bloch formula is largely valid for elemental targets up to $Z_2 \leq 26$ and $0.01 \leq \beta \leq 0.05$ (i.e., $\beta = V_1/C$) [35].

The non-validity of the Bethe-Bloch and the Bohr model below this range is largely due to the binary description of the collisions, where the projectile is considered to have a velocity greater than that of its bound electrons. This means that the ion is essentially treated as a localised/point charge density, where both descriptions do not adequately account for projectile screening imposed by the Coulomb interaction between the projectile bound electrons and those of the target. This also includes shell corrections (*i.e.,* target electron orbital motion) in the stopping cross section which are valid for the target at the *Thomas-Fermi* velocity, which are only partially treated by the Bethe-Bloch formulism. Therefore, under the condition $v_1 \lesssim v_B Z_2^{2/3}$, projectile screening dominates where $Z_1 > Z_2$. Conversely, shell corrections are more valid where $Z_1 < Z_2$. Thus, for large screening corrections, where the validity (*i.e.,* $\frac{2Z_1 e^2}{hv}$) of either two

models is more than 1 (*i.e.*, $v_1 = v_{TF}$), the criteria becomes such that both the Bohr and Bethe-Bloch formula are no longer valid.

At $0.01 \geq \beta$ therefore, particularly important for slow heavy ion stopping in matter, the Lindhard-Scharff theory becomes applicable. The Lindhard-Scharff electronic stopping power is described as [42]:

$$-\frac{dE}{dx} = \xi_e a_B 8\pi N e^2 \frac{Z_1 Z_2}{Z} \frac{v}{v_B} \qquad 2.4.$$

where the term ξ_e is equivalent to a factor equal to $Z_1^{1/6}$, and $Z = Z_1 + Z_2$.

Other means for calculating stopping power data include an *ab initio* approach, in which the time-dependent density functional theory is used to predict electronic stopping power data without any empirical input [43]. Also using the *ab initio* framework, the use of Green's function with extensions to finite momentum transfer have been explored and seen to approximate experimental data fairly well. *Ab-Initio* calculations are also useful for approximating stopping power data in compounds, where even empirical data is still lacking for heavy ion transport [44]. This is expansive to wide efforts at parameterising experimental stopping power data due to heavy ion impact in pure elements as well as in compounds. Programs based on current theoretical models, include the PASS code [45] based on the binary stopping theory, as well as the Convolution Approximations for Swift Particles (CasP) code based on *Ab-initio* calculations [46], [47].

One prominent database is called the Stopping and Range of Ions in Matter [48] (SRIM), which also includes Monte Carlo calculations and simulations using the binary collision approximation. The SRIM framework uses randomly selected impact parameters as the ion traverses past a series of collision centers to predict ion energy loss/stopping in a medium. Electronic stopping powers are then determined through an empirical fit using an extensive experimental database [41], [48].

Since non-relativistic heavy ions possess a non-zero mean electronic Coulomb potential, the dominant electronic stopping force results in larger degrees of screening as the collisions become more symmetric. This means that although electronic screening is not as dominant with adiabatic non-relativistic collisions (*i.e.*, energy loss in the eV/Å range), it does feature in what is mainly dominated by nuclear stopping for slow heavy ion impact due to significant

perturbations of the target electron wavefunction [49]. As previously pointed out, theoretical frameworks which treat the projectile as a point charge do not suffice for non-binary heavy ions as electronic Coulomb perturbation is rather strong. Furthermore, momentum transfer also occurs through charge-exchange or charge asymmetry, such that both shell and screening corrections become significant in ion stopping. Currently, SRIM approximations of stopping power data agrees more with experiment compared to *ab initio* calculations from CasP [39], however remains only accurate where such experimental data exists (as it is periodically corrected). This means that the model cannot be simply adapted for heavier ions, where stopping power data is still lacking [50]. While the use of SRIM continues to be a mainstay for approximating stopping powers required for IBA applications using heavy ions, such as for the determination of depth profiles using ERDA, additional stopping power data is still needed for the improvement of its predictions as well as that of other models such as the *ab initio* framework [51].

2.1.2. Sputtering

Cascade theory

Another important aspect of ion stopping is sputtering, caused by energy dissipation during ion impact in matter [52]. As an ion undergoes stopping due to multiple collisions within the stationary atomic matrix, the energy transferred by the projectile to the target atom(s) may overcome static force such that the constituent atoms (initially at rest) within the ion path are set in motion. When the kinetic energy of the displaced atoms is sufficient, the recoiled/displaced atoms may cause secondary displacements in the matrix, resulting in a cascade of recoiled atoms proportional to the initial impact ion energy [53]. These 'linear' cascades extend beyond the initial localised ion impact area, as more recoils in proximity are produced. Amongst these, recoiled atoms moving in a direction perpendicular to the surface plane are likely to escape the target matrix, on the condition that their kinetic energy is larger than the surface binding energy [53], [54]. This process in part describes the cascade theory, a model for sputtering. Since recoils are produced beyond a local impact area, they can be thought of as dispersing laterally, simply meaning that the area from which poly-atomic ions are sputtered is slightly larger than the beam impact area [55]. Thus, consecutive collisions for MeV ion current densities may result in the production of several cascades, resulting in a shallow (<10 nm) crater [56].

In-ward recoils on the other hand cause matrix damage effects, such as the development of vacancy and interstitial pairs in crystal structures [54]. This means that the production of either outward- or in-ward recoils makes cascade production somewhat deterministic, which can therefore be used to make inferences on an atomic matrix (*i.e.,* physical structure or chemical environment) [57]. The study of cascades has been widely undertaken using Monte Carlo and Binary Collisions Approximations' simulations, such as Transport and Range of Ions in Matter (TRIM), which is also a part of the SRIM package [58]. As already mentioned in the discussion on ion stopping, the scheme is reliable for elemental matrices, but is limited for compound and molecules, prompting the wider use of simulations based on molecular dynamics.

Indeed, cascade production is promoted by high energy transfer due to electronic stopping of heavy ions in matter, which is the basis of Secondary Ion Mass Spectrometry using projectiles in the MeV energy range (MeV SIMS). The sputtering yield of the poly atomic recoils ejected from a depth Δx can thus be calculated using Sigmund's formula [53], encompassing the surface binding energy U, the stopping cross section S_m, as well as the interaction potential (*i.e.,* correlating ion energy and electronic screening in a mass density) of the recoils m [56], [57]:

$$Y = \frac{1}{8} \frac{\Gamma_m F_D(E_0, z = 0)\Delta x}{U} \qquad \qquad 2.5.$$

The energy deposited by the projectile to enable sputtering is described by $\Gamma_m F_D(E_0, z = 0)$, and is directly proportional to the stopping power. The proportion of ion stopping depends on the symmetry of the initial projectile-target collision. This of course means that when the mass of the projectile is higher than that of the target, higher energy transfer is likely to promote a higher degree of recoil production compared to when the target is instead heavier [39], [40]. The recoil energy ranges between E_o, and the energy at z, where '$z = 0$' describes recoils existing beyond the surface boundary. In this case, the surface binding energy may be considered as the sublimation energy, since surface atoms are less bound than those within a bulk matrix. The 1/8 fraction describes an estimate of the number of atomic recoils likely to be oriented at a direction perpendicular to the surface. The depth Δx is described as [52]:

$$\Delta x = \frac{1}{1 - 2m} \frac{1}{N_\rho S_m} U^{2m} \qquad \qquad 2.6.$$

where N_ρ is the atomic density number.

Surface topographical effects may cause a fluctuation of the sputtering yield. This is due to the fact that ion stopping in matter is stochastic, and therefore variations in the surface structure result in variations in ion energy transfer, thus affecting cascade production in different regions [53]. Nonetheless, since the average recoil flux is measured in experiment, these fluctuations can therefore be viewed through the changing sputtering rate.

The cascade theory is a widely accepted theory for describing the extraction of high energy recoils from a target. In the latter, polyatomic or molecular desorption can be described using Hit theory or thermal desorption models [59]. In the case of Hit theory, desorption occurs as a result of energy transferred to the target through delta rays emitted by the projectile ion traversing the target matrix. The molecular ion is then desorbed when the accumulated energy is higher than the target surface binding energy.

On the other hand, when an incident ion undergoes stopping in a target, energy may be dissipated in thermal mode [60]. The increase in temperature in the impact area may thus result in either the sequential evaporation of the constituent molecules in the target (activated desorption), or the sudden evaporation of all atomic constituents (bulk desorption) [53], [60]. For activated desorption, the thermal energy gained by the molecule should be such that it enables molecular dissociation. In both cases, processes can be modelled using molecular dynamics simulations [61].

Another view is that incident ion stopping in a localised region results in a shock wave or pressure pulse, causing the propagation of molecules around the region of initial impact. These models are useful for describing the momentum obtained for molecular desorption even with low direct internal energy transfer from the projectile [54], [60], [61].

The different modes of molecular ion desorption result in varying degrees of molecular fragmentation, which can enable the qualitative evaluation of a target's chemical environment. These are useful for MeV SIMS, however detrimental for other scattering based Ion Beam Analysis (IBA) techniques such as RBS and ERDA.

2.1.3. Kinematics, atomic scattering, and recoil
Scattering

The evaluation of energy and momentum transfer (*i.e.,* kinematics) is also important for scattering occurring post an ion-atom collision. Since projectile or target atomic scattering depends on both the ion and target masses, the scattering/recoil energy describes the final state

energy of a scattered atom in either the forward or backward direction. The scattering direction depends on the orientation of the target plane relative to the projectile, dictating the scattering angle. The probability for the ion to scatter from the target is higher when the mass of the target is much larger than that of the projectile [37]. Ion scattering from the target, particularly where the target plane is perpendicular to the projectile incidence angle, is the basis for Elastic Backscattering Spectroscopy (EBS). Data curation entails the evaluation of the distribution of projectiles with varying kinematic energies as they scatter from different depths (*i.e.,* energy loss) from a target. For an initial ion energy E_0, a kinematic factor K_S can be described by the ratio of the ion backscattering energy E_1 at a scattering angle θ to E_0 [38].

$$K_S = \frac{E_1}{E_0} = 1 - \frac{4m_1 m_2 . \cos^2 \theta}{(m_1 + m_2)^2} \qquad 2.7.$$

The probability of ion scattering may be described using the Rutherford cross section, given in the Equation below. As the randomness of the impact parameter dictates varying degrees of either forward- or back- scattering, the scattering cross section can thus be increased through optimising the scattering angle by geometrically aligning the target plane relative to that of the projectile [37].

$$\left(\frac{d\sigma}{d\Omega}\right)_{Rutherford} = \left(\frac{Z_1 Z_2 e^2}{2E_0}\right) \frac{\left(\sqrt{m_2^2 - m_1^2 \sin^2 \theta} + m_2 \cos \theta\right)^2}{m_2 \sin^2 \theta \sqrt{m_2^2 - m_1^2 \sin^2 \theta}} \qquad 2.8.$$

The validity of the Rutherford cross section depends on the ion energy, and assumes screening effects are minimal. Where the Rutherford cross section is valid, the term EBS is commonly re-phrased as the Rutherford Backscattering Spectroscopy (RBS), as colloquially labelled in Ion Beam Analysis literature. However, for low energy projectiles, higher electronic screening results in increased contribution to the interaction potential, which is not factored in the Rutherford calculation [62]. In this case, screening corrections to the Rutherford cross section have been approximated before [63]. Additionally, a database of experimental cross sections for several ion-atom combinations are present in the IBANDL repository [64].

Atomic recoil

Conversely, the likelihood for a target atom to recoil from its atomic matrix increases when the projectile mass is larger than the target mass. The kinematic relation between the projectile and

target may be given by the kinematic factor K_R, which can be determined using the recoil energy E_2 and initial ion energy E_0 as [65]:

$$K_R = \frac{E_2}{E_0} = \frac{4m_1 m_2 . \cos^2 \theta}{(m_1 + m_2)^2} \qquad \text{2.9.}$$

Since atomic recoil is largely due to electronic stopping of the heavy projectile mass in the target matrix, the recoil cross section can thus be described in the frame of the interaction potential [65]:

$$\left(\frac{d\sigma}{d\Omega}\right)_{Recoil} = \left(\frac{Z_1 Z_2 e^2}{2E_0}\right)\left(1 + \frac{m_1}{m_2}\right)^2 \frac{1}{\cos^3 \theta} \qquad \text{2.10.}$$

In the laboratory frame, the recoil cross section can be deduced from the number of incident ions N_i and the recoil yield Y, as shown in Equation 2.11 below. The number of incident ions can be determined experimentally using the measured accumulated charge. As described by Equation 2.10, the recoil cross section increases with the projectile mass. Such is the basis for Elastic Recoil Detection Analysis (ERDA), where atomic recoils from a target matrix are produced by significantly heavier incident projectiles [66];

$$\left(\frac{d\sigma}{d\Omega}\right)_{Rec} = \frac{Y}{N_i (\rho t)\Delta\Omega} \qquad \text{2.11.}$$

where ρ, t and $\Delta\Omega$ are the atomic density, target thickness and detector solid angle.

For a given reaction geometry in the laboratory frame, the scattering and recoil cross sections can together with the collected reaction yields be used to calculate relative atomic concentrations in a target using RBS or ERDA. A visual aid of ion scattering, recoil and also X-ray emission (discussed later in the text) is shown in Figure 2.1 as the major interactions pertinent to Total Ion Beam Analysis.
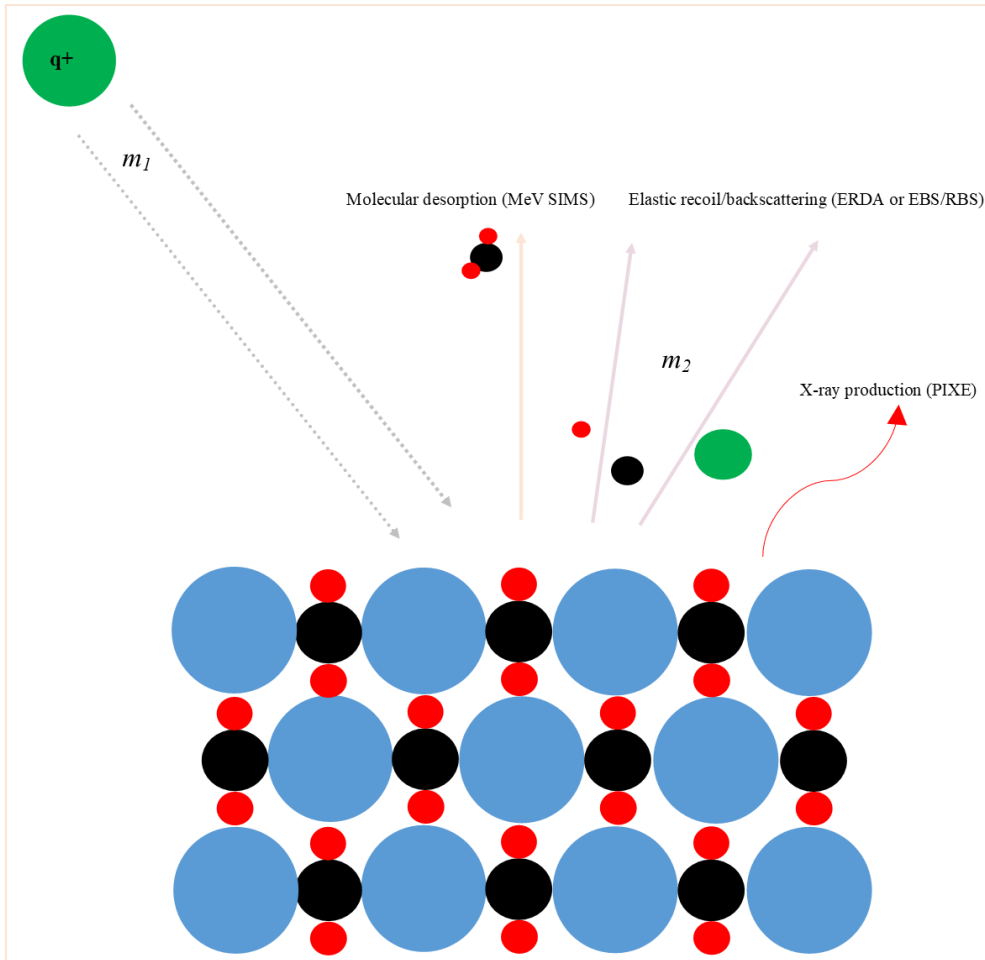
Figure 2.1. *Ion Beam Analysis schematic depicting EBS, ERDA, SIMS and PIXE spectroscopy*

2.2. Atomic ionisation

2.2.1 Direct Ionisation and the Binary Encounter Approximation

Momentum transfer in an atomic matrix through either elastic or inelastic scattering with the target atom nuclear mean field is not only important for understanding and quantifying ion stopping and range in matter, but also for radiative and non-radiative ionisation due to perturbations of the target atom's electronic field. For light ion-atom collisions, where electronic perturbation is largely weak at velocities below the Thomas-Fermi level, the primary mode of ionisation (*i.e.,* removal of an electron from orbit due to large ion-atom momentum transfer) becomes direct [67]. This means that dominant inelastic scatterings which result in close collisions that sees the removal of an electron from its subshell can be described using the Rutherford cross section. Indeed, as the velocity of the projectile nears the Thomas-Fermi

velocity (v_{TF}), the target electron densities are characterised by a cloud within which an increased number of ionisations may occur through distant collisions within the cloud density, notwithstanding the impact parameter [67]. Conversely, higher ion velocities result in atomic ionisations through the photoelectric effect where energy transfer is by virtual photons. Where slow (*i.e.*, $v_1 < v_{TF}$) light ions are concerned, ionisation probabilities may be described using the Binary collisions approach (*i.e.*, where the target atom is seen by the projectile as a large nuclear field), described by [34]:

$$-U = \frac{1}{2}m_e v_e^2 - \frac{Z_1 Z_2 e^2}{r}$$

2.12.

The denotations m_e, v_e, r, Z_1 and Z_2 are the electron mass, electron velocity at a relative distance r, the projectile as well as the target atomic number. The term $\frac{Z_1 Z_2 e^2}{r}$ describes the interaction potential *V(r)* between the projectile ion and the target atom, which in this case only factors in the mass of the target for point charges, as Z_1=1. The potential describes the exponential relation between the ion velocity and electronic screening in a target field of varying distance from the nuclear field. As already mentioned before, the screening effect largely exists for point charges at higher velocities where nuclear stopping is low. Therefore, for light ions such as protons at non-relativistic energies, the screening function *X(r)* in the interaction potential is not included in the Binary collisions equation 2.12, as *X(r)* =1.

The energy transfer by the point charge projectile v_1 to the inner shell electron is therefore described by:

$$E_T = 2m_e v_e v_1 + 2m_e v_1^2$$

2.13.

Essentially, the condition for any ionisation to occur in a given inner shell should satisfy the condition $E_T > U$, which depends on the projectile velocity. Thus, for low velocity ions, inner shell electron ionisations where binding energies are high only occur when the impact parameter is low and the projectile is fairly close to the nucleus. The ion velocity and energy can be related by the kinetic energy given as:

$$E = \frac{m_1 v_1^2}{2}$$

2.14.

Since the nuclear stopping force is largely dominant where the projectile velocity v_1 is much smaller than the Thomas-Fermi velocity v_{TF}, especially for point charges, the large nuclear

mean field thus prohibits the projectile from residing within its vicinity, causing ion deflection at distances proportional to the field strength [62], [68]. The large scattering cross sections at low energies thus result in a lower probability for the projectile to ionise strongly bound electrons in the innermost shell closest to the nuclear mean field. Of course, the ionisation probability (cross section) depends on the number of bound electrons in the ground state target atom, as larger atomic systems have a greater nuclear potential, and subsequently larger electron binding energies in the innermost electron shell.

While larger projectile velocities imply higher ionisation cross sections, the increasing cross section is however finite, even with an infinitely increasing ion velocity. Therefore, similar to ion stopping where regions of maximal stopping are given by the Bragg peak, ionisation cross sections peak at given ion energies described by $E = \frac{m_1 U}{m_e}$. The relationship between the inner shell binding energy, the mean kinetic $\bar{K}$ and potential energy $\bar{V}$ can be observed using the Virial theorem, where $\bar{K} = \bar{V}/2$, and is described as [68], [69]:

$$\bar{K} \equiv \langle \frac{m_e v_e^2}{2} \rangle \qquad ; \qquad \bar{V} \equiv \langle \frac{Z_1 Z_2 e^2}{r} \rangle \qquad\qquad 2.15$$

Here the probability of ionising an electron bound at a given radial distribution from the nuclear Coulomb potential is assumed to be at its maximum at the mean of such a distribution, where the electron is most probable to be found. Using Heisenberg's uncertainty principle, $\Delta x . \Delta p \geq \hbar/2$, the electron position term can be assumed as the orbital radius, given as $\frac{n a_B}{Z_2}$ [69].

The momentum term is given as:

$$\Delta p = \sqrt{2 m_1 E} - \sqrt{2 m_1 (E - U)} \approx \frac{\sqrt{m_1 U^2}}{2E} \qquad\qquad 2.16.$$

Thus the relation:

$$\left(\frac{n a_B}{Z_2} \right) . \left(\frac{\sqrt{m_1 U^2}}{2E} \right) \approx \hbar/2 \qquad\qquad 2.17.$$

The condition $E = \frac{m_1 U}{m_e}$ is therefore obtained, where the binding energy is equal to $U^2 R_c / n^2$. The denotations are namely: R_c – Ryberg constant, a_B – Bohr radius and the principal quantum number n. It is clear then, that the highest ionisation cross section can be based on the relation $E . m_e = m_1 . U$, where the ion velocity is equal to that of the bound electron. Therefore, the

ionisation cross section σ_i can be expressed as a function of this relation. This is the basis of the Binary Encounter Approximation (BEA), given as [70], [71]:

$$f\left(\frac{E.m_e}{U.m_1}\right) = \frac{U^2\sigma_i(E,U)}{q^2} \qquad \text{2.18.}$$

2.2.2 Plane Wave Born Approximation

The BEA, which is based on classical Rutherford scattering, is however not complete in its description. Although the theory gives somewhat of a satisfactory description of the main collision mechanics, it however does not appreciate the probabilistic nature of both the projectile and electron quanta. Since electrons in a spherically symmetric atom reside in defined regions of probability, ionisation by an incident projectile such as a proton therefore describes highly perturbed states of the electron wavefunction as the proton is scattered by a fixed nuclear mean field potential. Such an interaction can be described by the Born approximation, where the ejected electron motion is described using the hydrogenic wavefunction, thus describing the collision/impact by a plane wave function (*i.e.,* with a constant amplitude at all points of measurement) [72]. The BEA is therefore underpinned by the single state of the projectile wavefunction, where electronic perturbation is only by point charges with minimal electron screening and that partially interacts with the nucleus before deflection. Therefore, by considering the electron form factor of the target, the ionisation cross section in the *s* shell can be determined using what is referred to as the Plane Wave Born Approximation (PWBA), given as [72]:

$$\sigma_{i_s}^{PWBA} = (2j_2 + 1)4\pi a_B^2 \frac{Z_1^2}{(Z_{2s})^4\theta_s} \cdot \int_{w_{min}}^{w_{max}} dW \cdot \int_{Q_{min}}^{Q_{max}} \frac{dQ}{Q^2}\left|F_{\omega_s}(Q)\right|^2 \qquad \text{2.19.}$$

where $Z_{2_s} = Z_2 - S$, and S – screening parameter equal to 0.3 for the K-shell and 4.15 for the L-shell. The terms in equation 2.19 are as follows:

j_2 – Total angular momentum, θ_s – reduced binding energy, 'w$_{min}$, w$_{max}$' and 'Q$_{min}$ and Q$_{max}$' are the minimum and maximum energy and momentum transferred to the target atom, respectively.

The energy and momentum transferred are thus calculated using the following relation [73]:

$$W = \frac{2\delta E}{Z_2^2} \; ; Q = \frac{q_m^2}{Z_2^2}$$

2.20.

Here the term δE is denoted as the energy transfer, equal to the difference in the electron binding energy and the final electron energy. The q_m^2 is the magnetic momentum transferred to the electron by the projectile ion.

2.2.3. ECPSSR and ECUSAR theory

By including corrections for projectile energy loss (E) as it is deflected by the nuclear Coulomb potential (C) in the target, for which the ionisation cross section is dependent; the changes in the binding energies of the perturbed electron shell (P) for an atom in its stationary state (SS) , and the relativistic (R) nature of the inner shell electron velocities, the PWBA is modified to [74], [75]:

$$\sigma_{i_s}^{ECPSSR} = C_s \left(\frac{2\pi d q_{o_s} \zeta_s}{Z_s (1 + Z_s)} \right) f_s(Z_s). \sigma_{i_s}^{PWBA} \left(\frac{\xi_s^R}{\zeta_s; \; \zeta_s \theta_s} \right)$$

2.21.

The terms are represented by: the PWBA cross section $\sigma_{i_s}^{PWBA}$ as a function of the reduced velocity corrected for relativistic effects ξ_s^R, the coulomb deflection factor C_s describing the extent to which the ion may be deflected by the target nuclear field, the reduced binding energy θ_s, the correction for changes in the binding energy and polarisation effects ζ_s, the energy loss correction factor $f_s(Z_s)$, half distance of closest approach $(d \equiv \frac{Z_1 Z_2}{M v_1^2})$ and the minimum momentum transfer by the projectile to the target atom q_{o_s} [76]. Momentum transfer can be described as the quotient of the binding energy U_{2s} of the s shell and the projectile velocity v_1.

For projectiles heavier than protons, the binary collisions approach in the impact induced ionisations is not valid. When a projectile has a group of electrons bound to its nuclear potential, electron field perturbation no longer occurs mainly because of classical Rutherford scattering, but also occurs as a result of enhanced screening effects. As mentioned in the section on ion stopping, the screening effect becomes proportional to the mass and charge state of the projectile, as related using Bohr's effective charge estimate for ions traversing a target matrix depth [76]:

$$\frac{Z_e^+}{Z_e} = \frac{v_1}{v_B Z_1^{2/3}} \qquad\qquad 2.22.$$

The ratio of the ion positive charge state and the number of bound electrons in the projectile ground state describes the degree of screening in the target, where larger charge states (*i.e.,* high Z_e^+/Z_e ratios) results in substantially lower screening. The screening correction in the ECPSSR provides a partial treatment of electronic screening where the charge states are very high, such that stopping is largely due to the interacting nuclear potentials of the projectile and target for inelastic scatterings [77]. Since larger projectiles result in larger electron wavefunction perturbations compared to binary collisions, they resemble quasi-molecular interactions, where the projectile and target combine in the collision moment to form a United Atom (UA) (*i.e.,* $Z_1 + Z_2$) [78]. Since a Z_1 dependence on the deflection factor exists, unlike in the case of point charges where only the Z_2 nuclear potential is considered, polarisation effects and binding corrections extend beyond single hole ionisation. Altered target electron binding energies in the subshells of a target are due to a state at which ion and atomic unification resembles a quasi-molecule with altered target electron binding energies. These require compensatory corrections, introduced in the form of the ECUSAR theory [79]. Here the PSS terms are replaced by the USA terms, in essence correcting both the deflection factor and reduced binding energies as in Equation 2.23. The deflection factor in the UA limit is mainly valid for low Z_e^+/Z_e ratios ($= \frac{v_1}{v_B Z_1^{2/3}}$), where the projectile is slow [79].

$$\sigma_{i_s}^{ECUSAR} = C_s \left(\frac{2\pi dq_{o_s}\zeta_s^{USA}}{Z_s(1 + Z_s)}\right) f_s(Z_s) . \sigma_{i_s}^{PWBA}\left(\frac{\xi_s^R}{\zeta_s^{USA}} ; \zeta_s^{USA}\theta_s\right) \qquad\qquad 2.23.$$

The modified binding correction ζ_s^{USA} is however conditional to the ion velocity, where $\zeta_s^{USA} \leq \zeta_s$ for slow ion impact, and conversely $\zeta_s^{USA} \geq \zeta_s$ for fast and intermediate ions.

2.2.4. Semi-Classical Approximation

One other approach is the Semi-Classical Approximation (SCA), which undertakes the quantum mechanical treatment of the transition of a bound state electron ejected from a subshell *s* to its free state *f* [80]. In this observation, ionisation is viewed from two states; one in which electron charge densities are discrete and 'unified', and the other where ionised electrons exist as separate charges in the continuum. The time evolution of the transition from the initial state

where the atom is whole/unified, to the separate state then becomes the basis of the SCA. In this treatment, atomic ionisation is viewed as being caused by a projectile whose motion is described by a classical trajectory (*i.e.,* the so-called straight-line approach with an impact parameter p); such that the transitioning electron (from bound to free state) and the subsequent ionisation probability can be described using the time-dependent perturbation theory. Thus, the description of the ionisation cross section [81]:

$$\sigma_i^{SCA} = 2\pi \int_0^\infty p\,dp \sum_f |a_f(p, t = \infty)|^2 \qquad \text{2.24.}$$

Here $a_f(p, t)$ describes the transition amplitude, within a time t by which the initial state moves to the final state. Several modulations of the SCA approach exist, including the United Atom and the coupled shell states approach initially discussed by Sarkadi and Mukoyama [82], [83]. In both these approaches, correction factors are added to the standard SCA model which assumes a straight-line trajectory of the projectile. Binding energy p and trajectory corrections (*i.e.,* from straight line *sl* to the more realistic hyperbolic *hyp*) are given by [83]:

$$\sigma_i^{SCA}(p, hyp) = \left(\frac{\sigma_i^{(1)}(p, hyp)}{\sigma_i^{(1)}(sl)} \right) \cdot \sigma_i^{SCA}(sl) \qquad \text{2.25.}$$

The terms $\sigma_i^{(1)}(p, hyp)$ and $\sigma_i^{(1)}(sl)$ are the first order ionisation cross section(s) with binding and hyperbolic trajectory corrections determined using the effective binding energy, and the simple first order ionisation cross section using a straight-line trajectory. Similarly, the coupled shell model correction can be deduced from the ratio of the cross section corrected for the projectile's hyperbolic trajectory, and that corrected for both the binding energy and hyperbolic trajectory, as seen in Equation 2.26 below [84].

$$\sigma_i^C = \frac{\sigma_i^{(1)}(hyp)}{\sigma_i^{(1)}(p, hyp)} \qquad \text{2.26.}$$

This correction can be adopted to either the SCA or ECPSSR as in [85]:

$$\sigma_i^{ECPSSR}(CSM) = \frac{\sigma_i^{(1)}(hyp)}{\sigma_i^{(1)}(p, hyp)} \qquad \text{2.27.}$$

In addition, where Direct Ionisation is enhanced by Electron Capture (EC) in the context of Multiple Ionisation, the appreciation of electron capture in the ionisation cross section is underpinned by its dependence on the equilibrium ion charge state. In one case, the EC contribution can be deduced from measured ionisation cross sections using different charge states at high ion energies where the EC contribution is rather large. On the other hand, EC can be viewed from a total subshell vacancy production perspective, whose cross section is given as [83]:

$$\sigma_{Eq} = \sigma_i^{DI} + \sum_q F(q)\sigma_i^{EC}(q) \qquad \text{2.28.}$$

where F(q) is the ion charge fraction.

An example of the ionisation cross section dependence on ion energy is shown in Figure 2.2 below.
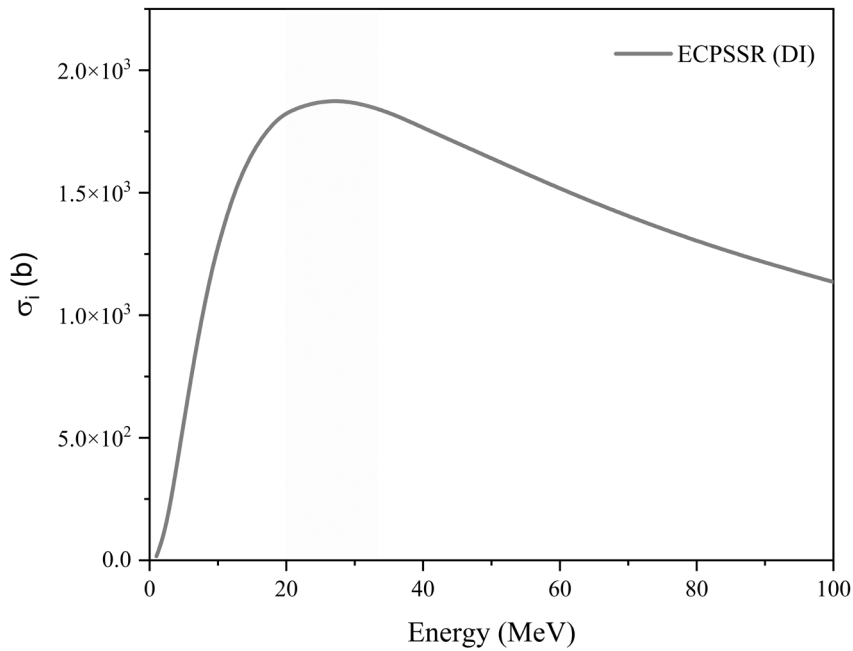
Figure 2.2. *Proton induced Au total L-shell ionisation cross sections calculated using the ECPSSR model. Calculations carried out using the ERCS08 code* [86]

The ionisation cross section can be seen to peak between ~20 MeV – 30 MeV as the Bohr velocity is approached, and thereafter reduces with the reducing electronic stopping power as the cross section for nuclear excitation increases. In cases where both electronic stopping and ionisation are exploited, such as with the complementary use of more than one IBA method, the lower energy range below the ionisation peak is generally favourable.

2.3. X-ray production

2.3.1. Atomic de-excitation

The theoretical background of radiative ionisation is widely covered in literature [18], [73], [87], and has over the decades enabled the implementation of X-ray spectrometry based on either charged particles from an accelerator or highly energetic electrons from synchrotrons. With this consideration, in order to maintain the focus of this discussion, radiative ionisation is only covered as far as energetic charged particles are concerned [88]. The fundamental principle is such that when intra-shell ionisation of an atom occurs, the ejected electron from the subshell results in an excited state of the ionised atom, lest the ejected electron is from the outermost subshell (Auger emission). In the initial case, where some electron densities exist at higher subshell levels from the electron vacancy, atomic relaxation/de-excitation (*i.e.,* transition from excited to stable state) may occur when the vacancy is filled by a loosely bound electron from a higher subshell level [87]. The transfer/transition of the initial subshell vacancy from the strongly bound subshell state to the more loosely bound subshells is described by 'Coster-Kronig' electron transitions, which become important more so when more than one intra-shell vacancies exist.

Photon emission therefore occurs during such a transition, where the energy of the photon is equal to that of the difference in the binding energies of the ejected electron (prior to ionisation) and of the higher state electron transitioning into the subshell vacancy [18]. An illustration of these transitions and their respective designations is given in Figure 2.3.
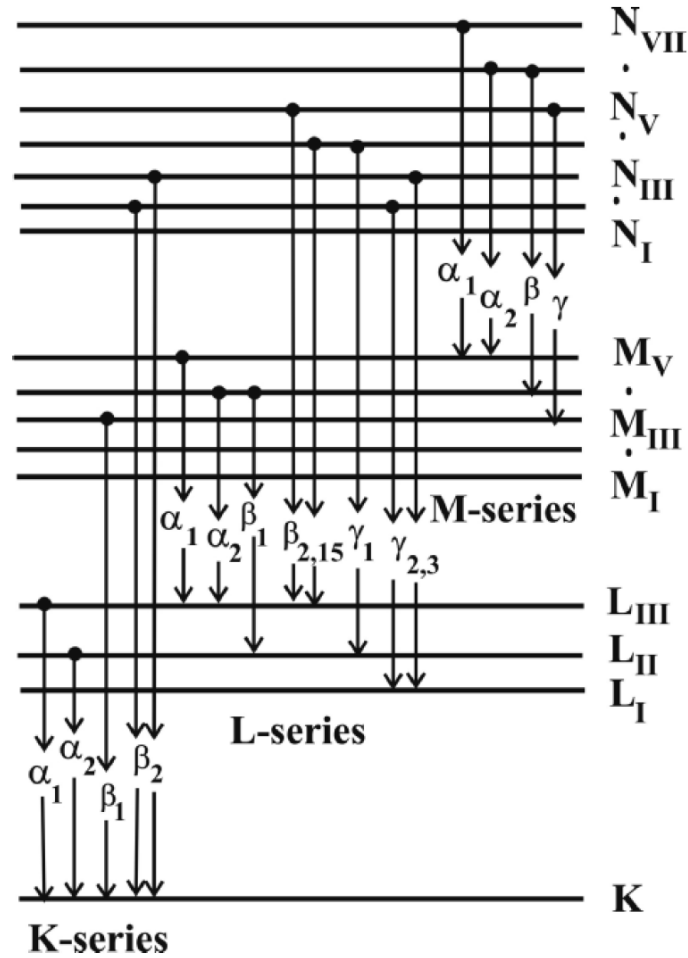
Figure 2.3. *Electron decay modes for X-ray emission post subshell ionisation. Figure reprinted from* [18]

The characteristic photon energy, assuming the formation of a single vacancy, is given by [88]:

$$E = -\frac{m_e e^4 (Z-1)^2}{2(4\pi\varepsilon)^2 h^2 n^2} \qquad 2.29.$$

where ε is the electron shell potential energy.

Since electron subshell binding energies depend on the mass of the nucleus, due to differences in nuclear mean field potentials, photon energies for specific transitions can be defined as characteristic to specific atomic masses. The spectroscopic evaluation of multiple characteristic photon energy distributions can then be used to determine both elemental composition and concentrations. This, the electron subshell ionisation by an incident ion, is the foundation for

Particle Induced X-ray Emission (PIXE) spectroscopy. In the laboratory frame, for thin targets, atomic concentrations C_X in matter can be calculated from the following Equation [17], [18]:

$$Y_X = C_X . \varepsilon_X . \Omega_X . \frac{Q}{e} . \sigma_X \qquad 2.30.$$

The parameters are namely the X-ray yield Y_X, detector efficiency ε_X and solid angle Ω_X, the accumulated charge Q and elementary charge e, as well as the X-ray production cross section σ_X. The quantitation of atomic concentrations in intermediate and thick targets includes corrections to energy loss effects, namely the variation of the ionisation cross section due to reducing impact ion energies E_x, as well as X-ray attenuation μ_x in the target layer [89], [90].

$$Y_X = \frac{Q}{e} \int_0^X C_X . \sigma_X . E_x e^{\mu_x / \sin \theta} dx \qquad 2.31.$$

The X-ray production cross section (*i.e.,* probability of X-ray emission post atomic ionisation), can be translated from the ionisation cross section. This translation considers the relative emission rates describing the fraction of X-rays emitted for a given electron transition, Coster-Kronig transition probabilities (describing the probability for electron decay once a vacancy is created), and the X-ray fluorescence yield ω for given electron decays/transitions (describing the ratio between the X-ray and Auger electron emission rates) [91]. The fluorescence yield essentially describes the probability that a vacancy is filled by a radiative transition. In the case of K-shell ionisations where only a single subshell is ionised, only a few electron decays are possible, to the extent that a single fluorescence yield can be used. The separate K-transitions are instead distinguished using relative emission rates, as described [92]:

$$\sigma_X^{K_\alpha} = \sigma_i . \omega_k . \left(\frac{\Gamma_{K_\alpha}}{\Gamma_K} \right) \qquad 2.32$$

$$\sigma_X^{K_\beta} = \sigma_i . \omega_k . \left(\frac{\Gamma_{K_\beta}}{\Gamma_K} \right)$$

The transition specific or relative emission rates are described by Γ_{K_α} and Γ_{K_β}, where the total emission rates for the K-shell is given as Γ_K. The much more complex L- and M- shell transitions are translated from ionisation cross sections using Equations 2.33 below [92].

$$\sigma_X^{L_l} = (\sigma_{L1}(f_{13} + f_{12}f_{23}) + \sigma_{L2}f_{23} + \sigma_{L3}) . \omega_3 \frac{\Gamma_{L_l}}{\Gamma_{L_3}} \qquad 2.33.$$

$$\sigma_X^{L\alpha} = (\sigma_{L1}(f_{13} + f_{12}f_{23}) + \sigma_{L2}f_{23} + \sigma_{L3}).\omega_3 \frac{\Gamma_{L\alpha}}{\Gamma_{L_3}}$$

$$\sigma_X^{L\beta} = \sigma_{L1}\omega_1 \frac{\Gamma_{L\beta}}{\Gamma_{L_1}} + (\sigma_{L1}f_{12} + \sigma_{L2}).\omega_2 \frac{\Gamma_{L\beta}}{\Gamma_{L_2}}$$

$$+ [\sigma_{L1}(f_{13} + f_{12}f_{23}) + \sigma_{L2}f_{23} + \sigma_{L3}].\omega_3 \frac{\Gamma_{L\beta}}{\Gamma_{L_3}}$$

$$\sigma_X^{L\gamma} = \sigma_{L1}\omega_1 \frac{\Gamma_{L\gamma}}{\Gamma_{L_1}} + (\sigma_{L1}f_{12} + \sigma_{L2}).\omega_2 \frac{\Gamma_{L\gamma}}{\Gamma_{L_2}}$$

$$\sigma_X^{Mp}(1) = \sigma_{M1}\omega_{M_1} \frac{\Gamma_{Mp}}{\Gamma_{M_1}}; p = M_1 - N_{23}, M_1 - O_{23}$$

$$\sigma_X^{Mp}(2) = \left(\sigma_{M1}f_{M_{1,2}} + \sigma_{M2}\right)\omega_{M_2}\left(\frac{\Gamma_{Mp}}{\Gamma_{M_2}}\right);$$

$$p = M_2 - N_1, M_2 - O_1, M_2 - O_4, M_2 - N_4$$

$$\sigma_X^{Mp}(3) = \left(\sigma_{M1}\left(f_{M_{1,2}}f_{M_{2,3}} + f_{M_{1,3}}\right) + \sigma_{M2}f_{M_{2,3}} + \sigma_{M3}\right)\omega_{M_3}\left(\frac{\Gamma_{Mp}}{\Gamma_{M_3}}\right);$$

$$p = M_3 - N_1, M_3 - O_1, M_3 - O_{4,5}, M_3 - N_5, M_3 - N_4, M_3 - N_{6,7}$$

$$\sigma_X^{Mp}(4) = \left(\sigma_{M1}\left(f_{M_{1,4}} + f_{M_{1,2}}f_{M_{2,4}} + f_{M_{1,3}}f_{M_{3,4}} + f_{M_{1,2}}f_{M_{2,3}}f_{M_{3,4}}\right) +\right.$$

$$\left.\sigma_{M2}\left(f_{M_{2,4}} + f_{M_{2,3}}f_{M_{3,4}}\right) + \sigma_{M3}f_{M_{3,4}} + \sigma_{M4}\right).\omega_{M_4}\left(\frac{\Gamma_{Mp}}{\Gamma_{M_4}}\right);$$

$$p = M_4 - N_2, M_4 - N_3, M_4 - N_6, M_4 - O_3, M_4 - O_2$$

$$\sigma_X^{Mp}(5) = \left(\sigma_{M1}\left(f_{M_{1,5}} + f_{M_{1,2}}f_{M_{2,5}} + f_{M_{1,3}}f_{M_{3,5}} + f_{M_{1,4}}f_{M_{4,5}} +\right.\right.$$

$$f_{M_{1,2}}f_{M_{2,3}}f_{M_{3,5}} + f_{M_{1,2}}f_{M_{2,4}}f_{M_{4,5}} + f_{M_{1,3}}f_{M_{3,4}}f_{M_{4,5}} +$$

$$\left.f_{M_{1,2}}f_{M_{2,3}}f_{M_{3,4}}f_{M_{4,5}}\right) + \sigma_{M2}\left(f_{M_{2,5}} + f_{M_{2,4}}f_{M_{4,5}} + f_{M_{2,3}}f_{M_{3,5}} +\right.$$

$$\left.f_{M_{2,3}}f_{M_{3,4}}f_{M_{4,5}}\right) + \sigma_{M3}\left(f_{M_{3,5}} + f_{M_{3,4}}f_{M_{4,5}}\right) + \sigma_{M4}f_{M_{4,5}} +$$

$$\left.\sigma_{M5}\right).\omega_{M_4}\left(\frac{\Gamma_{Mp}}{\Gamma_{M5}}\right);$$

$$p = M_5 - N_3, M_5 - N_7, M_5 - N_6, M_5 - O_3$$

The total relative emission rates $\Gamma_{L_i}(i = 1, 2, 3)$ and $\Gamma_{M_i}(i = 1, 2, 3, 4, 5)$ are comprised of fractional radiative widths (*i.e.*, based on the respective decay channels) within a given subshell.

2.3.2. Multiple Ionisation

Available fluorescence yields are generally either from experimental measurements or calculated using Dirac-Hartree-Slater (DHS) wavefunctions, where the perturbation theory under the Frozen orbitals approximation is used to calculate Auger rates, with j-j coupled states as the basis [93]. Although these calculations are valid for protonic collisions, they deviate for heavier ions where ionisation extends beyond just single-vacancy production [94]. This is because a larger number of vacancies not only changes the ratio between the number of Auger electrons and X-ray photons emitted in a single collision, but also results in changing binding energies [95]. Emergent 'satellite' energies are thus essentially altered X-ray energies for the same transition, due to changes in the binding energies. The result of satellite decay channels affects the evaluation of the DHS wavefunctions, due to the shift from ground state electron configuration. Thus, the use of new final state (or characteristic) X-ray energies in self-consistent mean field calculations yields augmented fluorescence yields [91], [93]. In a multiply ionised subshell therefore, where multiple satellite decay channels exist, characteristic X-ray production no longer retains the dominance of the so-called diagram lines (*e.g.,* $K_{\alpha 1}$ in the overall $K_{\alpha 1,2}$ distribution), but instead represents a cumulative distribution of several satellite transitions [96], [97]. These satellites, pronounced for '*beyond protonic*' impact, can be seen experimentally using high resolution spectrometers, as in Figure 2.4 [98].
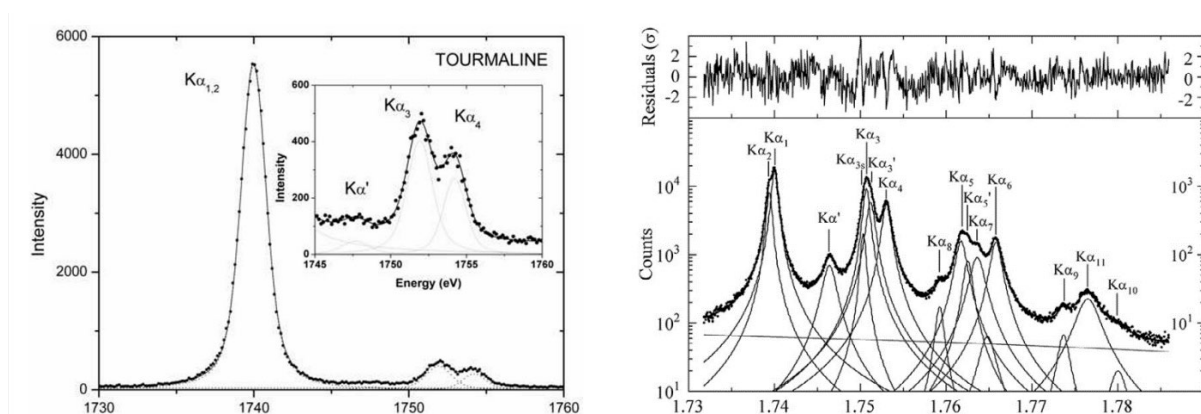

Figure 2.4. *High resolution Si Kα line due to protons (left) and 3 MeV alpha particles (right). Energy axis of spectra (left) in eV, and of (right) in keV. Figures reprinted from* [98]

One methodology for appreciating the extent to which MI vacancies affect the fluorescence yield is through observing the difference between the intensities of the overall K_α and K_β transitions. Comprehensively covered by Tanis and co-workers, it was shown that the ratio of K_β/K_α correlates the degree of 3p to 2p ionisations depending on the energy of the projectile

[94]. Since MI vacancies in the L-shell are reflected in cumulative characteristic peak energy shifts for K-shell ionisations, MI can essentially be quantified by using the number of 2p vacancies calculated using the Hartree-Fock-Slater (HFS) model. Larkins scaling can then be employed to approximate 3p subshell vacancies using the HFS calculated 2p vacancies and corresponding characteristic energy shifts, as in the relation below [99]:

$$\frac{I_{K_\beta}}{I_{K_\alpha}} = \frac{I_{K_\beta}^0}{I_{K_\alpha}^0} \cdot \left[\frac{1 - \frac{V_{3p}}{6}}{1 - \frac{V_{2p}}{6}} \right] \tag{2.34.}$$

Here $\frac{I_{K_\beta}^0}{I_{K_\alpha}^0}$ represents the K-shell intensity ratio for single-hole ionisation, due to protonic impact. The terms $1 - \frac{V_{3p}}{6}$ and $1 - \frac{V_{2p}}{6}$ are essentially the number of 3p (n_{3p}) and 2p (n_{2p}) electrons in a subshell during ionisation, respectively. The K-shell relative emission rates, which factor in the number of electrons in the 3p shell, are described as:

$$\Gamma_{K_\alpha} = \Gamma_{K_\alpha}^0 \cdot \left(\frac{n_{2p}}{6} \right) \tag{2.35.}$$

$$\Gamma_{K_\beta} = \Gamma_{K_\beta}^0 \cdot \left(\frac{n_{3p}}{6} \right)$$

The modified K-shell X-ray fluorescence yield is thus given as [94]:

$$\omega_K = \omega_K^0 \cdot \left[\omega_K^0 + (1 - \omega_K^0) \cdot \frac{\left[1 + \frac{\Gamma_{K_\beta}^0}{\Gamma_{K_\alpha}^0} \right] B}{\left[1 + \frac{\Gamma_{K_\beta}^0}{\Gamma_{K_\alpha}^0} \right] A} \right]^{-1} \tag{2.36.}$$

The number of subshell electrons are represented by the terms $A = \frac{n_{3p}}{n_{2p}}$ and $B = \frac{6}{n_{2p}} \cdot \left[\frac{\Gamma_{K_{LL}}^0}{\Gamma_A^0} \cdot \left(\frac{n_{2p}+2}{8} \right) \cdot \left(\frac{n_{2p}+1}{7} \right) + \frac{\Gamma_{K_{LM}}^0}{\Gamma_A^0} \cdot \left(\frac{n_{2p}+2}{8} \right) \cdot \left(\frac{n_{3p}+2}{8} \right) \right]$, where the term Γ_A^0 corresponds to single-hole ionisation Auger transitions for either one of the shells (*e.g.,* KMM or KMN transitions). The use of energy shifts for the estimation of vacancies for the more complex L- and M- shell transitions, is reserved for the fourth Chapter.

3.1. Introduction

The implementation of Total IBA at iThemba LABS and likewise at the RBI was built upon the expansion of already commissioned IBA techniques, namely ToF-ERDA and ToF-MeV SIMS. To this end, the focus of this chapter is not so much the full description of the technical development of either method, as this has already been comprehensively covered in other literature [100], [101], [102], but rather to give an overview describing the experimental setup, electronic configurations and adaptations where applicable as it pertains to the different PIXE synergies for each laboratory.

3.2. Experimental setup at iThemba LABS

PIXE spectroscopy and ToF ERDA were carried out simultaneously on the zero-degree beam line from the 6 MV Van de Graaff Tandem Accelerator at iThemba LABS TAMS. Ion beams were accelerated from an 860C Source of Negative Ions by Cesium Sputtering (SNICS) for the generation of several heavy ion beams. Preliminary target characterisation measurements were carried out on the microprobe chamber, positioned at the 15° angle of the switching magnet. A schematic of the accelerator complex layout is shown in Figure 3.1.
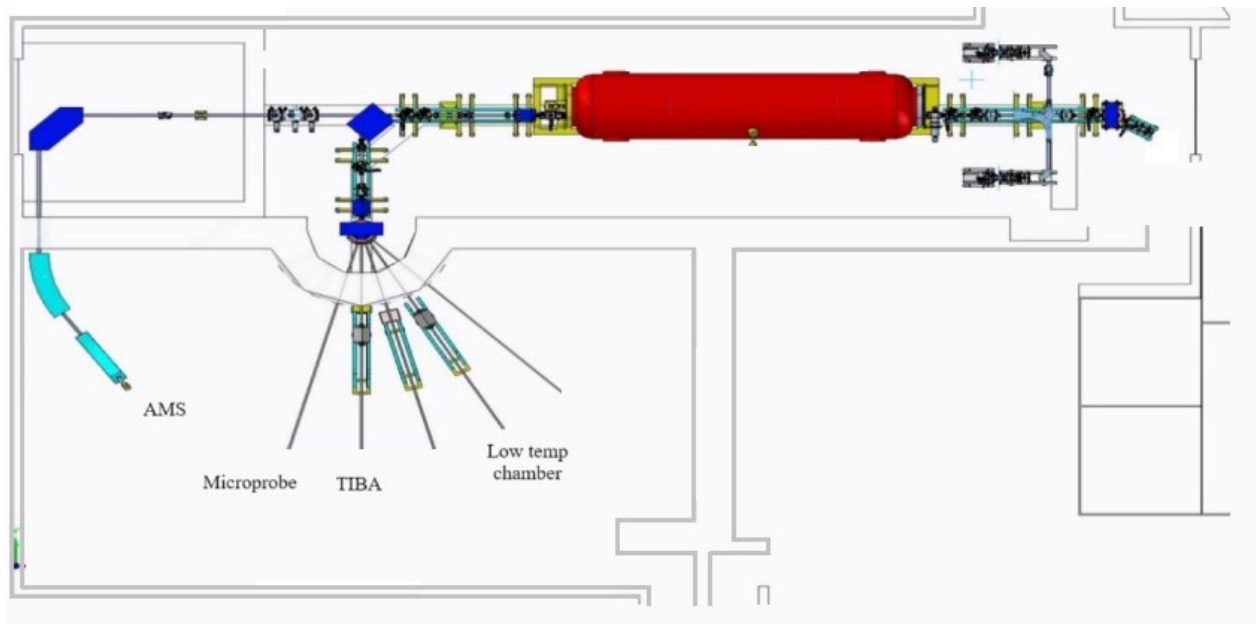

Figure 3.1. *iThemba LABS TAMS accelerator layout*

The microprobe is a standard Oxford microbeam configuration fitted with a Germanium X-ray detector and a Canberra Passivated Implanted Planar Silicon (PIPS) detector for the detection of backscattered ions. Data acquisition on the microprobe was carried out using OMDAQ [103]. Both the Germanium and PIPS detectors were connected using a simple counting (pre-amplifier – amplifier – ADC) configuration, where maximum event count rates were set by, among other factors, the 1 nA current limit of the charge integrator unit.

3.2.1. Total IBA chamber setup

The placement of the Heavy Ion TIBA chamber on the 0° beam line was to obtain the heaviest ion masses as well as the highest beam energies possible, to overcome the rigidity of the switching magnet. The TIBA chamber was fitted with a Canberra Surface barrier detector (SBD), subtended on a stage with a rotational axis about the target stage ranging between 0° – 90° relative to the zero-degree beam incidence angle. The SBD, biased at +80 V, was used for broad beam Elastic Backscattering spectroscopy (EBS) and was positioned at an angle of 150°. The target ladder stage was fixed to a motorised manipulator operating in the X, Y and Z directions and up to 90° along its rotational axis. X-rays were detected using a Si(Li) detector biased at -500 V and positioned at 90° to the beam incidence angle, 30 cm from the target stage. The distance of the Si(Li) detector from the target stage was constricted by the short detector nozzle and large target chamber radius, resulting in a small detector solid angle (~0.035 mSr). The X-ray count rate was therefore optimised using the beam current to obtain working rates around ~1 – 2 kHz for standard PIXE measurements.

The ToF-ERDA telescope fitted to the chamber had only been moved from the previous 30° east beam line as it has been previously developed and commissioned [101]. A side view image of the telescope and Si(Li) detector are seen below:

Figure 3.2. Side view of the *Total IBA chamber at iThemba LABS TAMS*

ToF – ERDA detector telescope

The telescope is comprised of two timing detectors separated by a distance of 60 cm, and a Canberra Surface Barrier Detector (SBD) (~0.15 mSr) positioned at ~3 cm from the second timing detector and ~98 cm from the target. The timing detectors are made of ~9 μg/cm^2 thin carbon foils on steel frames (96 mm^2 apertures) and are fixed at ~5 cm from a Microchannel plate (MCP) chevron configuration for electron signal amplification. As the recoil or scattered incident ion(s) pass through and ionise the thin carbon foil, the ejected electrons are accelerated towards the MCPs by the electric field between the foil and the MCP assembly. The carbon foils are tilted relative to the scattering/recoil angle to reduce the kinematic broadening of the recoiled ions or beam from the foil (straggling). Straggling would deteriorate both the timing and energy resolution, thereby reducing the accuracy of the technique. This is because increased recoil scattering or beam straggling would lead to different and potentially unresolvable flight times for the same energetic ion, provided the detection solid angle is sufficiently large. Tilted foils facilitate an intrinsic kinematic correction and minimise straggling [104].

The ejected and accelerated electrons traverse into the micro-channels coated with an electron rich glass layer, forming a secondary electron flux due to excitation as they collide with the constituent glass atoms. The acceleration of the electrons and subsequent ionisation of the electron rich layers in the micropores results in an avalanche of secondary electrons, which can be read out as the output timing signal. This process is similar to electron flux amplification using a photomultiplier tube, where electron drift occurs due to a potential divided across a series of dynodes. Similarly, the migration/drift of the electron avalanche in the MCP is promoted by a divided potential bias. The potential divider uses a series of resistors, gradually increasing the potential along the MCP up to the signal electrode. The bias voltage across the MCP(s) chevron configuration(s) for both timing detectors ranged up to 1.2 kV, powered by a supply voltage of up to a 5 kV maximum. This provided an electron amplification factor of up to 10^7.

The third/reference timing signal was drawn from the pre-amplifier timing output of the SBD. Although the third timing signal is detected at the end of the telescope, the electronic configurations were such that the TDC gate signal was in fact the third timing signal. The electronic configuration is discussed later in the text.

The ToF – ERDA telescope was positioned at a scattering angle of 30° relative to the zero-degree beam incidence angle, where the target stage could be positioned at 70° relatively. The telescope can be moved into (*i.e.,* closer to the target sample) and out of the target chamber as needed, using a rail and bellows system. A bird's view schematic of the target chamber internal geometry where the sample stage is positioned at 70° is shown in Figure 3.4.
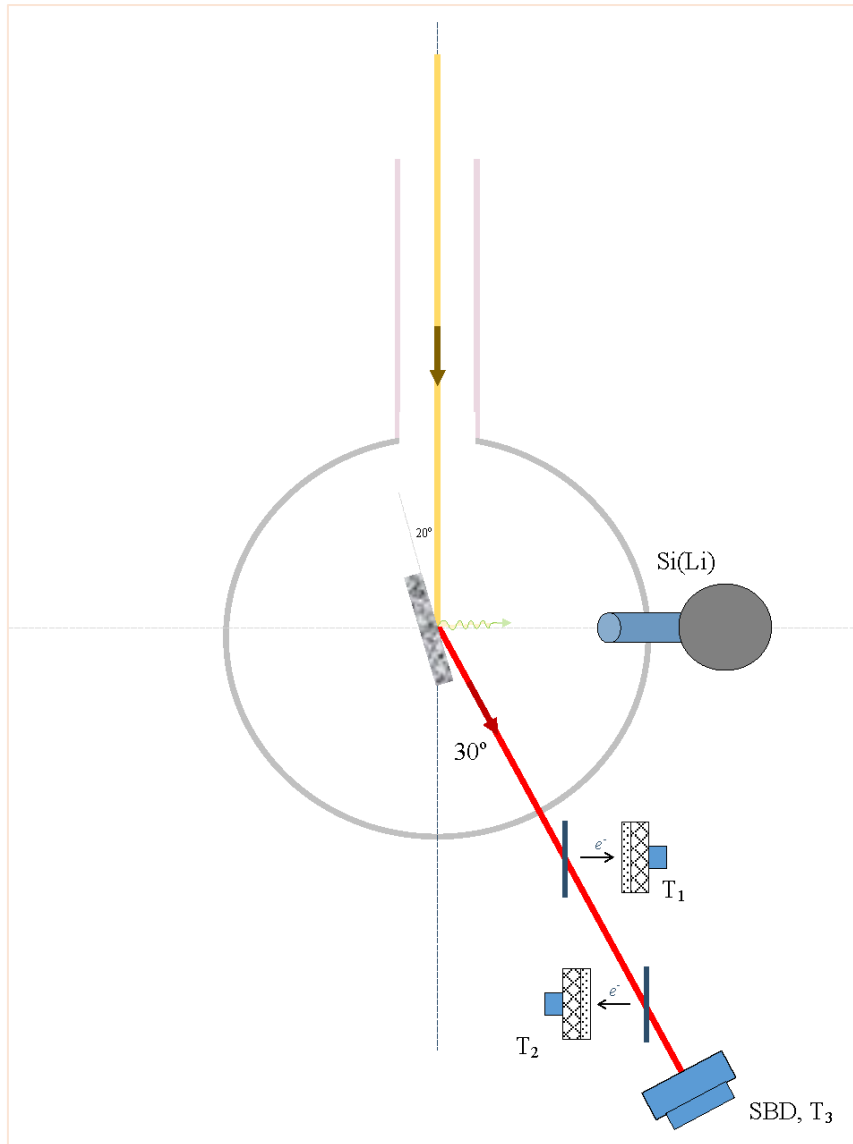
Figure 3.4. *Schematic: TIBA chamber internal geometry*

The targets were loaded into the chamber using a load-lock system in order to avoid breaking vacuum in the main chamber and subsequently compromising the sensitive timing detector foils. The position of the target stage along its rotational axis was manually calibrated during the installation of the manipulator, where input values were correlated to physically measured angles relative to the 0° beam angle. The broad ion beam spot could be observed in real time using scintillating quartz placed on the target ladder stage and would thereafter be marked on a separate monitor connected to the viewing optical camera (live feed) positioned at ~45° from the beam normal. The beam spot was marked in the zero-degree stage position, even on the occasion where the stage would be rotated for ToF-ERDA. This was done to compensate for

beam grazing along the quartz once rotated at 70°. A visual aid of the beam spot, taken from the accelerator control room, is provided in Figure 3.5.
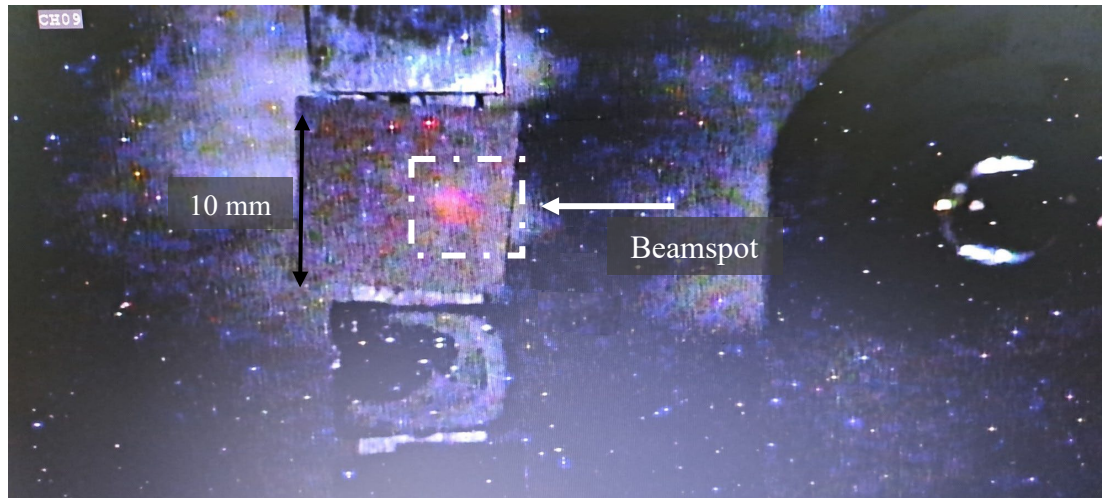
Figure 3.5. *2 MeV proton beam spot on scintillating quartz*

Electronics configuration

On the working principle of the ToF – ERDA system, since the distance between both timing detectors is known, the time of flight of recoils or scattered ions can be determined. The kinetic energy of the ions is measured by the SBD at the end of the telescope, meaning that the mass of either scattered ion or recoils could be determined. A classical physical description of such an event is given by the kinetic energy equation, where the measured kinematic energy E_k is related to the known distance between the timing detectors δX and the measured flight time δT.

$$E_k = \frac{m}{2} \cdot \left(\frac{\delta X}{\delta T}\right)^2 \qquad\qquad 3.1$$

The principle of this technique is thus premised on the basis that recoiled atomic species of different masses emerging from a given target depth (*i.e.,* up to typically about 500 nm) will possess different velocities/flight times and kinetic energies due to the electronic stopping of the inward probing beam and the outward recoils. Thus, measurement of kinetic energies and flight times may be used to infer the depth from which constituent atomic species were recoiled (*i.e.,* from known stopping force data). This follows the stopping power equation described in Chapter 2, which reads:

$$S(E) = \frac{1}{N_\rho} \int_{Ef}^{Ei} \frac{dE}{dX}$$

<div align="right">3.2</div>

The accuracy of this technique for given atomic masses depends on the ToF detector timing resolution as well as the rise time, which therefore requires the use of fast ns signal processing electronics. Both signals from the two-timing detectors were fed to a constant fraction discriminator (CFD) to provide fast logic output signals T_1, and T_2 respectively. The third timing signal T_3 served as the trigger (reference start) and gate signal for the TDC and ADC respectively. Both T_1 and T_2 were delayed in order to only be read after the T_3 trigger/gate signal. The stop signal, T_2, was connected to the fast-timing amplifier with a rise time of <1 ns and registered only after T_1. Signal delays for both T_1 and T_2 were adjusted using a set of delay boxes, which enabled an interval adjustment of between 50 - 200 nanoseconds. The width of the ADC gate from T_3 was on the other hand adjusted using the gate and delay generator unit, ranging between 5 ns - 1μs. Since timing signal reflections could range up to ~100 ns, the gate width was carefully adjusted to avoid more than one single trigger for the same coincident event. The ADC gate width was adjusted to accommodate the X-ray signal as well. Signal attenuation in the cables was minimised using a fan in fan out unit. Oscillations from T_1 and T_2 were on the other hand minimised using a 50 Ω terminator. The reference signal T_3 from the SBD and E_2 from the Si(Li) detector were split using a tee connector, and visualized using an oscilloscope to ensure that the X-ray signals were detected within the same window as the energy signal from the SBD.

A snapshot taken from an oscilloscope showing both signals is given in Figure 3.6.
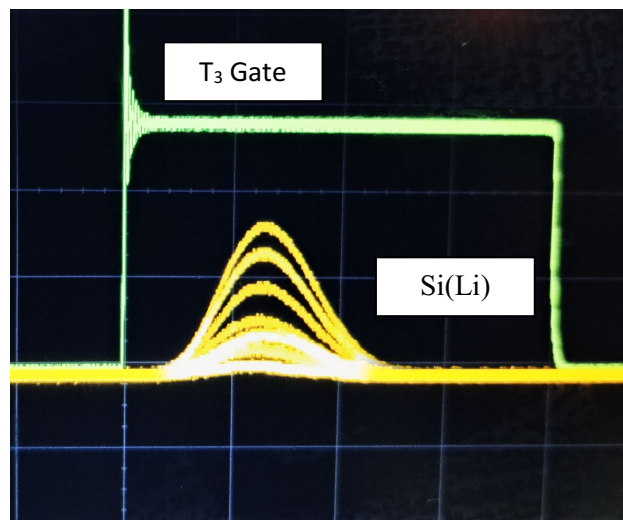

Figure 3.6. *T_3 gate signal (green) and unipolar energy signal (yellow) from Si(Li) detector*

The TDC and ADC were connected to a 2 GHz Intel Core VME crate controller which assumes the role of a front-end computer. It should be noted that the Si(Li) energy output was not used as part of the gate signal due to the large delay (*i.e.,* in the order of μs) inherent to the spectroscopic energy amplifier chain. Although using the timing signal from the Si(Li) detector along with that from the SBD would be ideal for coincidence measurements, this was unfortunately not explored. The main limitation was due to the in-built and fixed Si(Li) pre-amplifier which had no timing output nor could be replaced by one that does. This meant that the use of a coincidence unit for the inclusion of both the SBD and Si(Li) X-ray signal outputs could not be undertaken. For this reason, all gate signals (ADC and TDC) were derived only from the SBD. The practice adopted here to use the SBD events as the trigger events was to avoid excessive count rates (>10 kHz) since the SBD solid angle is the smallest. The PIXE – ERDA electronic configuration is shown in Figure 3.7.
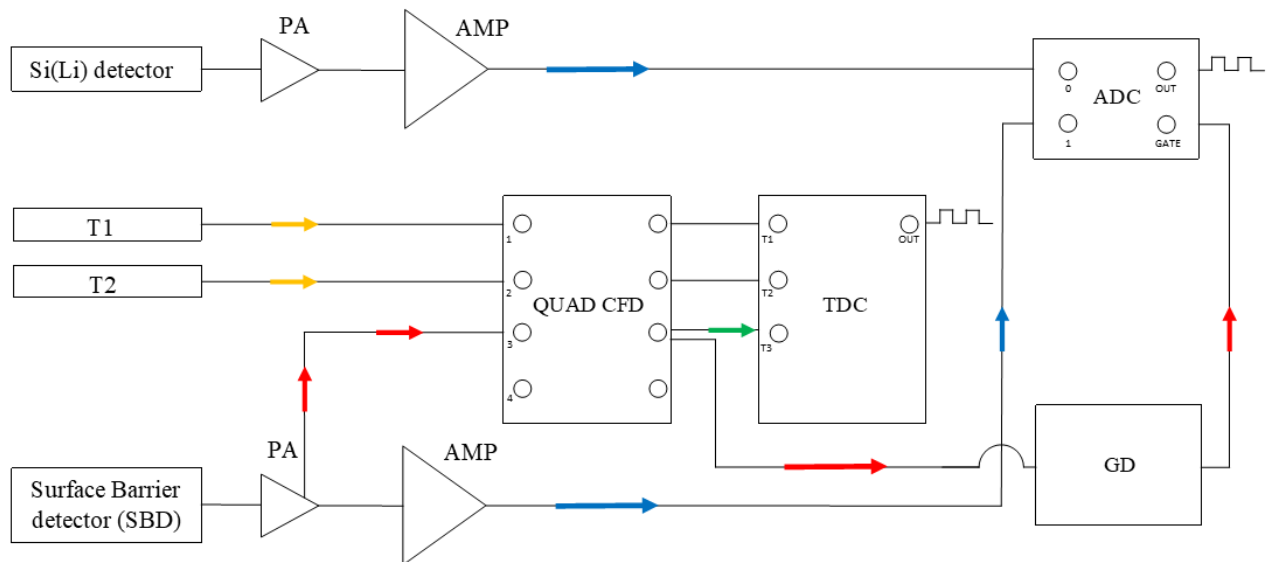

Figure 3.7. *PIXE – ERDA electronic setup*

The TIBA system was initially tested using a 30 MeV ^{63}Cu^{7+} beam on a quartz viewer (SiO$_2$). The timing signals T$_1$ and T$_2$, along with the energy signal from the SBD are shown in Figure 3.8. below.
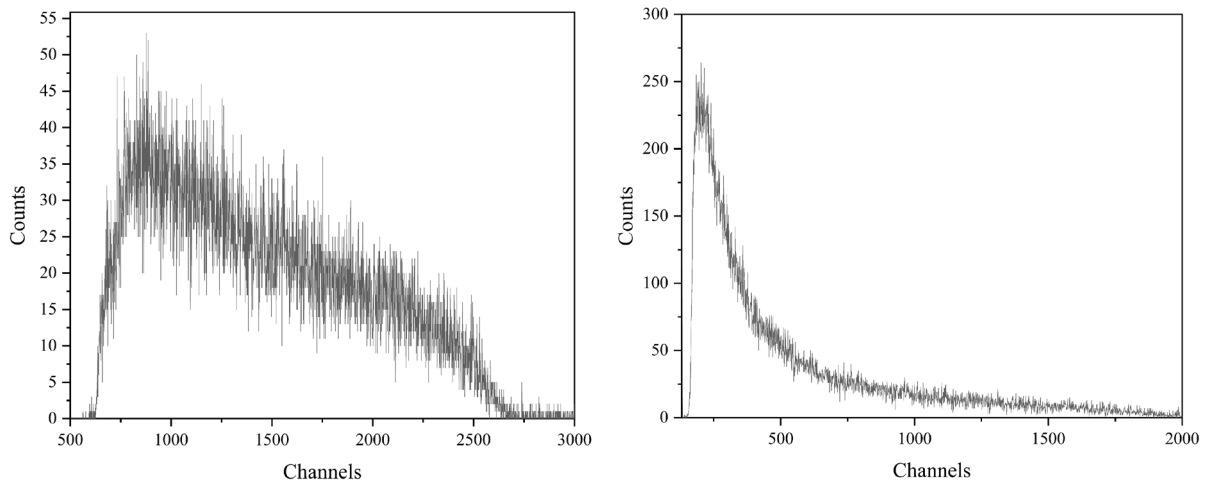
Figure 3.8. *Time of flight (left) and energy (right) events*

Since the sample was homogenous, no information aside from elemental composition along the entire target depth was sought. The X-ray detector was also tested using the silicon and copper beam X-ray lines in order to carry out signal processing adjustments where needed. These largely included a reconfiguration of the Si(Li) spectroscopic amplifier settings, such as the shaping time, amplification gain, pole-zero and threshold adjustments. As the ToF-ERDA system is typically configured according to experimental needs, the maximum bias on the MCPs was not used as high detection efficiencies for the timing resolutions usually required for hydrogen recoils was not needed. In the interim, the time of flight – energy is shown in Figure 3.9.
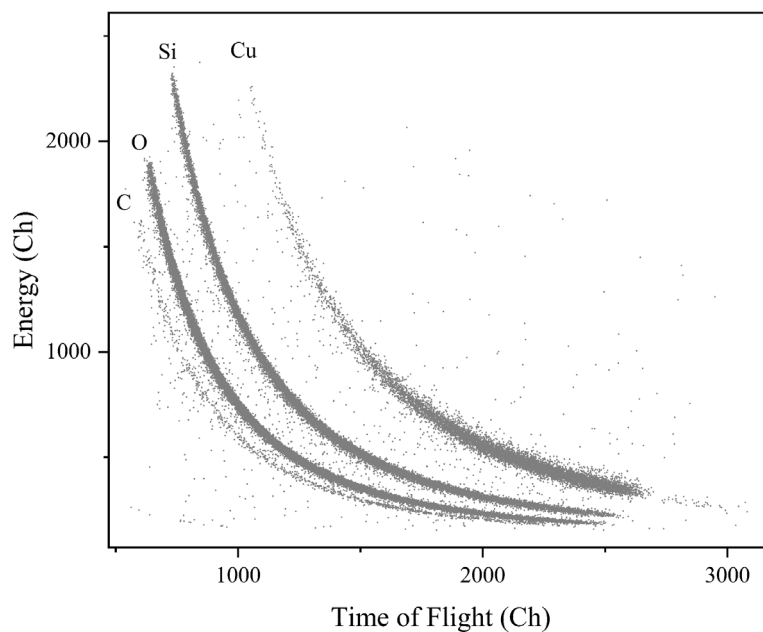

Figure 3.9. *2D ToF-E scatter plot for quartz due to 30 MeV $^{63}Cu^{7+}$*

Data acquisition and analysis

Data acquisition was carried out using the Maximum Integrated Data Acquisition system (MIDAS) framework, which houses a central database and back-end computer over an ethernet network that connects several front-end computers and workstations [105]. Drivers for the Virtual Machine Environment (VME) front-end computer enable readout of steady data rates of around 1MB/second from the ADC and TDC. The MIDAS framework was modified in-house to enable control of the VME as well as the storage (in '***'.mid format) and analysis of the collected data in real time. The analysis of data was carried out using the CERN based ROOT [106], interfaced with MIDAS to enable both real-time and offline data analysis. Both MIDAS and ROOT were launched using Scientific Linux, where either time of flight – energy 2D scatter plots, EBS or PIXE data could be evaluated using the ROOT data analysis framework.

For coincidence measurements, discussed in Chapter 5, offline data analysis was used. In this approach, a ROOT data tree format was established, where the data branches of the tree represented data streams from the acquired TDC and ADC inputs. Since the signals are correlated, conditional plotting of the Time of flight – energy spectra could be carried out using PIXE data. As the Si(Li) and SBD were configured in order for both signals to be recorded within the same gate window, recoil energies would be recorded within the same narrow window at which the corresponding X-ray signals for the same element would also be recorded. This then meant that recoil inputs would have the same time-stamps as those of the X-ray inputs. By selecting a range of X-ray datasets, the corresponding (same time-stamps) time of flight – energy data would also be selected. Further discussion is reserved for the 5th Chapter, as it relates to actual experimental measurements.

In the case of experimental X-ray production cross section measurements with heavy ions, RBS/EBS data was recorded using a simple counting configuration. The obtained EBS data was exported to ASCII format and analysed using SIMNRA, a widely used program for simulating and fitting EBS experimental data [38]. The simulations were carried out using calculated and available experimental scattering cross sections from the IBANDL repository [64]. Reference standards were used to calibrate the channel spectra to energy scale using kinematic energies calculated in SIMNRA. In some cases however, where multiple ion energies for the same projectile in the same target matrix were used, MultiSIMNRA [107] was instead used for fittings. The same procedure was followed for measurements also carried out

at the RBI, where applicable. MultiSIMNRA is a self-consistent computational program that enables the evaluation of multiple experimental datasets, simulated over a range of selected iterations. The program uses several parallel SIMNRA sessions for each of the evaluated experimental data. The main objective function used for the simulation of experimental data is the minimised mean reduced. This function ensures that the analysed spectra (*i.e.,* across the multiple EBS datasets) have the same statistical weights. Although comparatively larger integrated counts for one single experimental spectra ought to have larger statistical weights, the function prioritises such large spectra first in the minimisation processes. This means that the function eventually converges to the same statistical weights as it approaches its minimum [107]. SigmaCalc scattering cross sections by Gurbich [108] were then used for spectral fittings carried out at 150 – 200 iterations. The selection of the SigmaCalc cross sections was premised on their representation of an empirical mean of experimental cross sections, making them reliable.

3.3. Experimental setup at the RBI

The implementation of TIBA at the Ruđer Bošković Institute was based on two separate beam lines [109], [110]. For experimental X-ray production cross section measurements due to heavy ions, technical work was largely limited to the fitting and optimisation of a Silicon Drift Detector (SDD) on the ToF- ERDA chamber (E5) positioned on the zero-degree switching angle. PIXE – MeV SIMS experiments were carried out on the old microprobe beamline (E9), which houses multiple detectors for a number of IBA techniques, including PIXE. The selection of the MeV SIMS system on the old microprobe was premised on the fact that there was no open flange for the inclusion of the SDD detector on the Capillary/collimator based MeV SIMS system. While the Capillary system provides better mass resolution and may enable higher ion energies for the same masses (*i.e.,* not limited by the switching magnet rigidity), the exploration of MeV SIMS using the standard Time of flight configuration was deemed adequate as ions and energies optimum for both PIXE and MeV SIMS could be obtained.

Finally, for the evaluation of the influence of Multiple Ionisation effects within the study of heavy ion induced X-ray production cross sections, the High-Resolution Wavelength Dispersive X-ray Spectrometer (WDS), adapted on the old microprobe beam line (E9) was used. The description of the spectrometer is detailed in chapter 4, in the discussion on Multiple Ionisation. A schematic of the LIBI accelerator complex is thus shown in Figure 3.10 below.
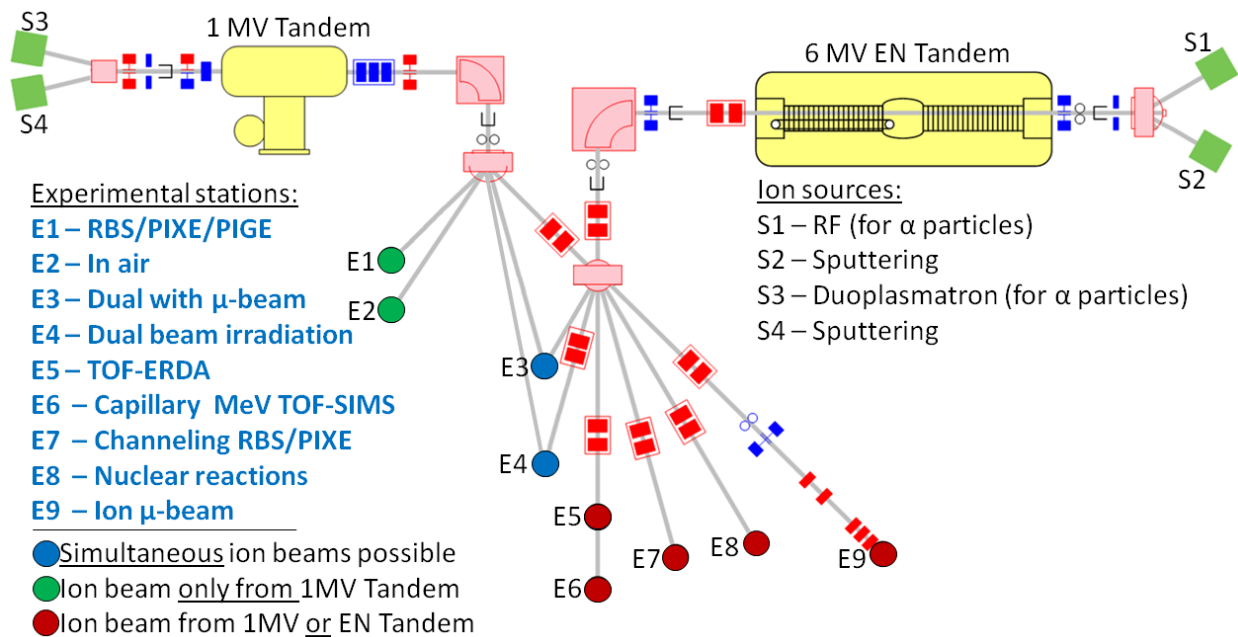
Figure 3.10. Schematic: *RBI accelerator complex*

3.3.1. PIXE – MeV SIMS

The MeV SIMS system mounted on the nuclear microprobe beamline E9 (see Fig.3.10) is essentially a linear time of flight spectrometer. Accelerated ions from either the 1 MV Tandetron or 6 MV Van de Graaff Tandem accelerator were pulsed using metal plates biased at several hundred volts switched using a MOSFET push pull. Beam pulsing not only lowers the beam current but also provides the start signal for the time of flight MeV SIMS measurements. Low beam currents ensure that the fluence is below the static limit, mitigating radiation damage effects, especially for sensitive targets. The stop signal is on the other hand obtained from the Multi-channel Analyser (MCA), where the time of flight can be deduced since the distance between the deflector and the sample stage, as well as the drift length from the extractor (~10 mm from the sample) to the MCP is known. A schematic of the experimental configuration is shown in the Figure 3.11.
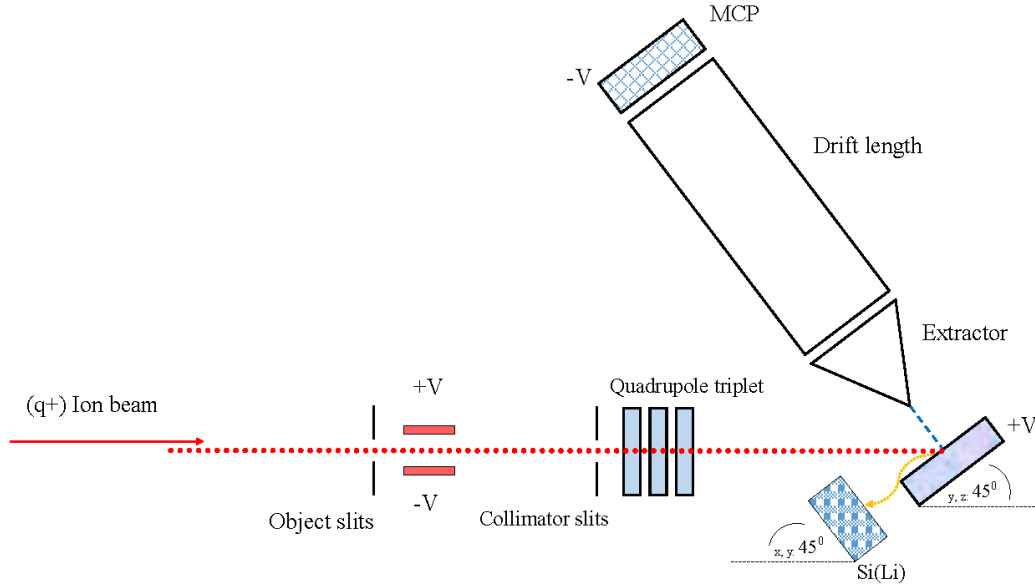
Figure 3.11. *Schematic: MeV SIMS – PIXE experimental setup on the E9 microprobe beamline*

In order for extraction to occur, a ± 5 kV potential bias is placed on the sample stage to create an extraction field that repels either positive or negative molecules into the extractor. The use of either positive or negative modes is dictated by the chemistry of the analysed target, where inferences can be made from either or both cationic and anionic molecular species. The extracted molecules from the target surface oriented perpendicular (tilted at 45^0 along the *z*-axis) to the extractor, drift along the 43.7 cm flight tube, where heavier molecular masses or fragments have longer flight times than lighter ones. This velocity dependence on mass can be viewed in terms of the kinetic energy, simply described by the relation $eV = \frac{1}{2}mv^2$. With the known drift length D_l, the time of flight can therefore be deduced as:

$$TOF = \left(\sqrt{\frac{m}{2eV}}\right).D_l \qquad 3.3$$

Since all molecules are extracted at the same energy (based on the target bias), faster and lighter molecules are recorded first, whereas heavier molecules are recorded later, all of which are recorded and dispersed across a channel axis. The number of channels is then converted to the mass unit using Equation 3.3. as the energy, drift length and time of flight are known.

PIXE spectroscopy was carried out in the same chamber, using a Si(Li) detector positioned at 45^0 relative to the beam incidence angle. A simple counting system was used for the X-ray detector (140 eV FWHM at 5.9 keV), biased at -700 V and positioned between $\sim (10 - 30)$ mm

from the target stage. The measurement procedure for synergistic PIXE and TOF MeV SIMS analyses entailed the use of MeV SIMS in low current mode (in the low fA range), where the deflector would be switched off in order to carry out PIXE spectroscopy on the same beam spot in high current mode (in the low nA). Analytical conditions were therefore only optimised as far as the X-ray detector chain was concerned. The electronic configuration and picture of the target chamber are shown in Figure 3.13.

(a)
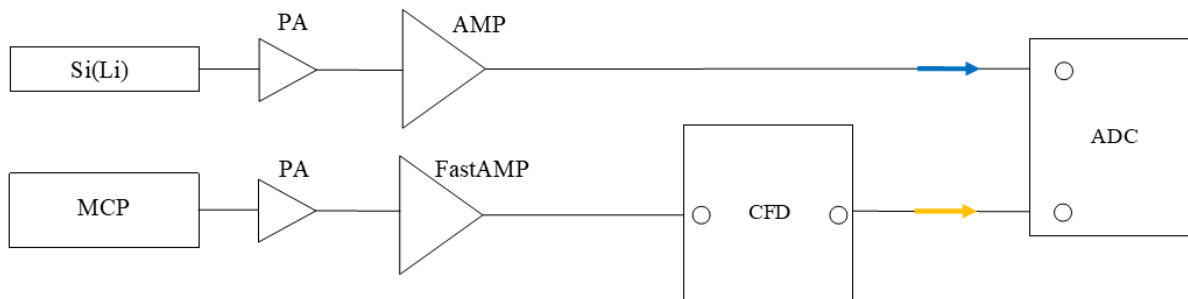
(b)

Figure 3.13. *Picture (a) and DAQ electronics schematic (b) of the ToF MeV SIMS – PIXE setup at the E9 microprobe beamline*

3.3.2. ToF ERDA chamber

Measurements of heavy ion induced X-ray production cross sections using ion beams such as Si, Cu and I were carried out on the ToF-ERDA chamber (E9) at the RBI. The reaction chamber houses a Time of flight – energy telescope positioned at 37.5° relative to the 0° incident beam angle. The chamber also houses a Surface Barrier Detector (SBD), subtended at 165° relative to the beam normal for EBS/RBS. The SBD was connected using a simple counting system (*i.e.,* pre-Amp → amplifier → ADC). A Silicon Drift Detector (SDD) (nominal resolution of 125 eV FWHM at 4.9 keV) was mounted at 45° relative to the beam normal at a distance of ~10 cm from the target stage. The target stage was in the form of a ladder with 4 sample positions, which was manipulated in the X, Y, Z and theta directions by a motor. A simple counting configuration was also used for X-ray detection, where accumulated charge in the thin targets used was collected using a Faraday cup positioned behind the target stage, measured using a charge integrator and counter.

3.3.3. Data acquisition and analysis

The acquired data was processed using the in-house built SPECTOR (DAQ), based on the Microsoft Windows framework [111]. The DAQ also enables adjustments to live time per pixel (dwell time) and grid parameters for scanning purposes. The calibration of deadtime is deduced from the live time obtained from the ADC, and the real time from the start of the acquisition. The DAQ connects to NIM ADC modules using a fast MPA/PC adapter and MPA/LBB bus-box. The MPA/PC enables the storage of data acquired in a number of modes, such as in single, multiple as well as in list mode. Particularly useful for techniques such as ToF-ERDA and MeV SIMS, list mode allows for the allocation of time stamps, triggered by the ADC at the instant a signal pulse height breaches the LLD threshold. The timestamp resolution is naturally limited to ~100 ns, as a result of the signal propagation delay in the interface between the ADCs and the PC. However, particularly for timing applications such as ToF-MeV SIMS and ToF-ERDA, the timing resolution can be adjusted to ~4 ns by using FPGA Mezzanine Card (FMC) ADCs. Delays due to signal propagation are in this way significantly reduced since signals are processed internally in the FPGA. This allows for the offline reconstruction of time dependent events, as with the processing of ToF MeV SIMS data discussed later in the text.

Considering that multiple data analyses software were used for the analyses of PIXE spectra, or ToF MeV SIMS, their descriptions have been omitted from this chapter. For purposes of coherence, data analyses tools are instead described in either the 4th or 5th Chapter, as it relates to the reported measurements.

In this chapter, the measurement and analyses of experimental X-ray production cross sections, along with the development of a semi-empirical model are discussed. Both the experimental and semi-empirical X-ray production cross sections were compared to ECPSSR predictions, as well as experimental data from literature. The use of Machine Learning is also discussed in part, only relating to the validation of calculated semi-empirical cross section datasets. Overall agreements and discrepancies between the measured and calculated datasets are discussed in terms of the dominant Multiple Ionisation effects. The implementation of heavy ion induced X-ray production cross sections for actual PIXE analyses is finally featured in the closing of the chapter.

4.1. Materials and characterisation

The measurement of X-ray production cross sections in material samples was carried out using mono - elemental thin films individually deposited on Polyethylene Terephthalate (Mylar) and thin carbon foil substrates from Micromatter®. The selection of the substrate considered the constituent matrix elements, such that no coinciding characteristic X-ray peaks would emerge within the X-ray energy range of interest. Ideally, transparent targets, namely films with a thickness that would ensure large ion beam transmission (while retaining structural integrity under vacuum), were desired. This was in addition to the selection of substrates with an invisible matrix (*i.e.,* comprised of elements undetectable using PIXE).

To this end, in the first case, Mylar ($C_{10}H_8O_4$) substrates were chosen in two sets of thicknesses based on the experimental setup. For measurements carried out using the scanning nuclear microprobe at the iThemba LABS TAMS department, 0.5 mm thick substrates were used. The targets in the microprobe setup were fixed on a non-hollow hexagonal steel sample stage, meaning that the steel target stage would become visible for thin targets and thus result in large detector deadtime from the high event rate due to the bulk frame. The deposited material layer thicknesses were also selected to prevent excessive energy loss (*i.e.,* keep it below 10%) the incident projectile ions. For this reason, 100 nm – 150 nm mono - elemental layers of Sn and Bi were individually deposited on 0.5 mm thick Mylar® substrates at room temperature in high vacuum, using resistive heating and electron beam Physical Vapor Deposition (PVD). The evaporator internal geometry was varied between (10 – 15) cm to prevent thermal damage on

the polymer backings, while retaining a good deposition rate for homogeneous film layer development.

All measured X-ray production cross sections, using both thin and thick targets, were corrected for ion energy loss in the target layers (discussed later in the text). Even though energy loss corrections are mainly aimed at integrating some energy variations along the cross section limits, in some cases, when ion stopping is large enough, these variations become significantly large. Furthermore, heavy ion stopping induces film erosion/radiation damage, which was in this case non-negligible at lower ion energies in targets backed by Mylar. Therefore, in the selection of the target thicknesses as well as ion energies, stopping power calculations and simulations using SRIM were carried out.

Although a larger number of vacancies/atomic displacements are created in the target matrix by higher ion energies, damage was seen (through TRIM simulations) due to significant ion beam straggling and stopping forces for slower ions approaching the film/substrate interface and substrate edge. The variations in ion energy, causing large ion deflections in the target field, were due to a higher electron screening potential. This, as it shall become even more apparent in the discussion, implied larger energy limits in the integration of X-ray production cross sections. For this reason, target thickness and ion energy directly contributed to the calculated uncertainty of the measured cross section data. Thus, considerations of target thicknesses included the structural retention of the films in vacuum, the non-generation of signal artifacts in the analytical spectra, as well as the minimisation of statistical uncertainties in the XPCS measurements for low velocity ions.

In the case where charge was measured using a Faraday cup positioned behind the target stage, thin Mylar substrates were used. This was particularly for proton measurements, in which the target stage was hollow and therefore no X-ray generation from the target chamber walls would occur. Indeed, the projectile ions would traverse the insulating polymer (Mylar) backing, with minimal energy loss in both the film and the foil. To achieve this, target films with a mass density of 20 $\mu g/cm^2$ were deposited on thin 20 $\mu g/cm^2$ Mylar substrates. The Mylar substrates were mounted on aluminium frames, with an open area window of 0.38 cm^2. The target films withstood experimental conditions for proton irradiations with currents ranging around ~1 nA at varying ion energies, maintaining minimal to no visible damage. However, significant

generation of thermal energy in the stopping of heavy ions was noted, primarily with the use of low energy silicon and chlorine beams. The generated non-linear cascades in the impact area as well as the large energy transfer in the target resulted in a concentrated increase in temperature that surpassed the low melting point of the insulating Mylar substrate, causing total film erosion within the irradiated area. The material failure indicated a need for a conducting substrate with a low lateral heat capacity (*i.e.,* to transfer dissipated heat to the frame/sample stage) for heavy ion irradiation where charge collection was required. While these effects were offset by large film thicknesses for experiments carried out at iThemba LABS, a complete revision of the target film and substrate layer and thicknesses was carried out for measurements at the RBI.

Cross section measurements at the RBI were carried out using thin carbon substrates, allowing high ion beam transmission/passage into a Faraday cup positioned behind the target stage. The selection of carbon was due to its electrical and thermal conductivity. Therefore, 20 µg/cm^2 mono-elemental thin films were deposited onto 20 µg/cm^2 carbon foil substrates fixed onto aluminium frames using ultra-purified (milli Q) water. The deposition was undertaken in room temperature using a CMS-18 magnetron sputtering system at the Laboratory for Thin Films of the RBI. The depositions produced 5 mm diameter active target windows to enable passage of a broad 1 mm x 3 mm beam spot size in the ToF-ERDA chamber. No assessment of film homogeneity was carried out, since the targets were positioned from the source at a distance that allowed uniform deposition over the small analytical area. The uncertainty for film homogeneity, considering the low thickness values of the film layers, was therefore estimated to be ≈ 1% [52, 55, 57]. Mass densities of the element and substrate layers were not only selected with the prerequisite that the foil be transparent to the ion beam at all energies, but to also ensure that the sensitive foils retained their physical structure under high vacuum conditions.

Nominal target thicknesses were measured using Rutherford Backscattering Spectroscopy (RBS) with 2 MeV H$^+$ ion beams. The obtained spectra were then analysed using SIMNRA. An example of an obtained RBS spectrum for Bi deposited on a carbon substrate is shown in Figure 4.1.
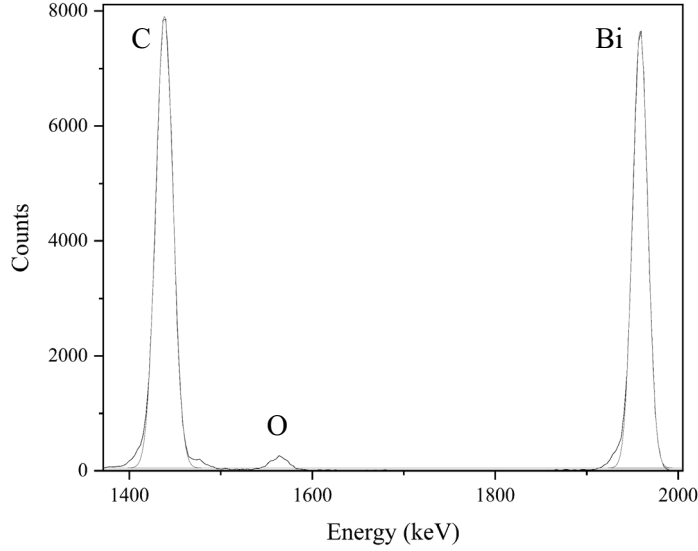
Figure 4.1. *2 MeV proton RBS spectrum for 20μg/cm² Bi (peak on the right) on 20 μg/cm² carbon (peak on the left) substrate. A shallow oxide peak is seen at ~1560 keV*

A linear calibration of the RBS spectrum was carried out, correlating the channel numbers to which known peaks where registered, and their corresponding kinematic energies. Kinematic calculations were carried out using a calculator function in SIMNRA. Given the nature of the experiments, in that several measurements were carried out in different target chambers and under different experimental conditions; calibration was carried out for each experimental run.

A graphical illustration is shown in Figure 4.2, where the gradient from the linear regression was used to provide the calibration factor (keV/channels), and the calibration offset (represented by the function intercept).

The detector solid angle $(\Delta\Omega_R)$ was verified through the correlation of the number of incident ions in terms of collected charge and ion backscattering. In such a relation, the $Q.\Delta\Omega_R$ term (*i.e.,* from the number of incident ions: $N_i = {Q}/{n.e}$) using the measured accumulated charge Q was normalised to the backscattering yield assessed using SIMNRA, such that the solid angle could be determined. However, since the RBS detector position is fixed and therefore retains the same known detector solid angle under all experimental conditions, the known detector solid angles were instead used for charge normalisations in X-ray production cross section measurements. This assumption is of course valid only where the target stage is not significantly displaced along the Z-axis. A graphical illustration of the ratio of the RBS and X-ray detector solid angles is shown in Figure 4.2.
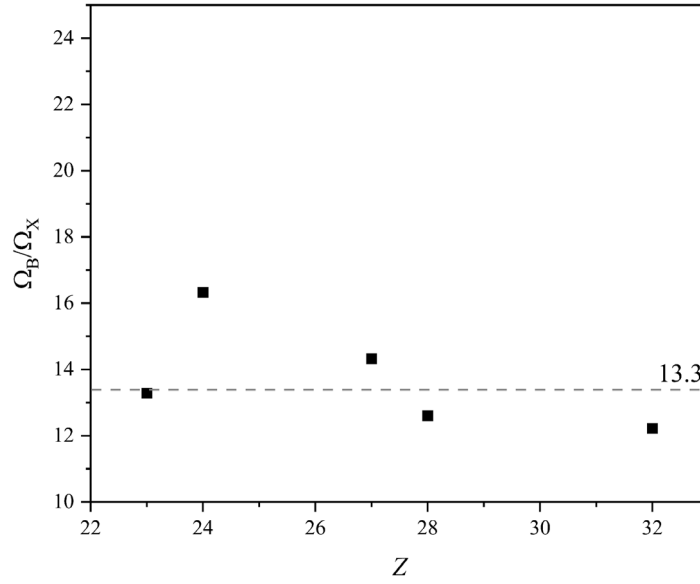
Figure 4.2. *Ratios of RBS and SDD X-ray detector solid angles measured using 2 MeV proton beams*

The uncertainty pertaining to the measurement of target thicknesses considered the estimated target inhomogeneity (ΔT) $\approx$ 1%, the SIMNRA code accuracy (ΔC) $\approx$ 1% [38], detector resolution (ΔE) $\approx$ 1% and stopping power data of the incident ions in the target layer (ΔS) $\approx$ 3% (see Equation 4.1.).

$$U_{dX} = \sqrt[2]{(\Delta C)^2 + (\Delta T)^2 + (\Delta E)^2 + (\Delta S)^2} \qquad 4.1$$

Nominal thickness uncertainty was thus estimated at $\pm$ 4%, for the deposited targets, namely with thickness values (in units of $\mu g/cm^2$): Cr (20), Ni (20), Ge (20), Mo (25), Sn (22.3), W (21.4), Au (22.6) and Bi (13.9). Standard reference target materials, with certified mass density values and an overall nominal uncertainty of $\pm$ 5%, were also used for energy calibration as well as the calibration of the X-ray detector. The reference materials were composed of Na (18.5), Mg (21.7), Al (22.1), Si (20), K (21.3), Ca (20.1), V (23), Co (19.5), Cr (20), Ni (19.5), Ge (20) and Mo (20) thin foils, deposited on 20 $\mu g/cm^2$ polyethylene terephthalate (Mylar) substrates. The standard reference materials were from MicroMatter® and are routinely used for calibration.

4.2. X-ray production cross sections

4.2.1. X-ray data extraction

Characteristic X-ray yields from K –, L – and M – shell ionisations were collated and corrected for deadtime using three separate data acquisition software, namely OMDAQ, ROOT and SPECTOR, as previously mentioned in chapter 3. X-ray detector solid angles were determined from 2 MeV proton induced X-ray spectra, analysed using GUPIX. Since the certified mass densities of the reference standards were known, the average H-value (*i.e.,* X-ray detector solid angle) for each detector was determined by adjusting its input in GUPIX to compute the known atomic concentrations.

As GUPIX [112] uses known relative intensity ratios to determine corresponding line intensities from the principal X-ray peak, such as using the K_α line intensity to determine the intensity of K_β; its reliability for spectral fittings was limited to proton ionisations. Considering that intensity ratios change with increasing ion energy and mass in the same target element due to Multiple Ionisation (MI) effects, Origin® [113] was instead used for extracting peak fractions for different heavy ion-atom interactions. The peak intensities were extracted using a least square fitting routine of the Gaussian distributions. Although peak broadening, due to the inclusion of X-ray satellites in the cumulative distribution was observed in some cases, particularly in cases where the ion-atom collision approached symmetry (*i.e.,* $Z_1/Z_2=1$), multiple Gaussian functions were used to deconvolute the compounded peak areas. Lorentzian functions were also used, however for the deconvolution of X-ray lines evaluated in high resolution, discussed later in the Chapter. An illustration of a deconvoluted X-ray spectra obtained using an SDD detector for the assessment of Au L- subshell lines due to 2 MeV proton excitation is shown in Figure 4.3.
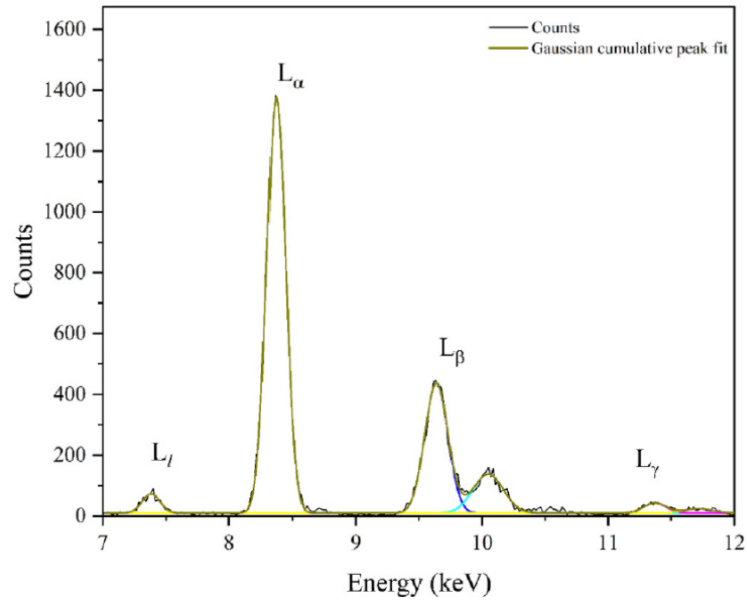
Figure 4.3. *Multi-gaussian fittings of L- subshell X-ray lines of Au obtained with 2 MeV protons*

Similarly, cumulative peak fittings for the extraction of total M-shell X-ray line intensities for heavy elements were treated using multiple Gaussians. In some cases, instead of deconvoluting the overlapping intensities, as this would lead to high uncertainties in the calculation, multiple Gaussian fittings were instead used to model the total distribution. This was particularly important where heavy ions are involved, as the asymmetric distortion of the total intensities meant that separate lines could in some cases not be modelled. This was exacerbated by the small differences between the M_α and M_β X-ray lines (see Fig 4.4) in the M- intensities, which can be overcome by peak broadening due to MI.
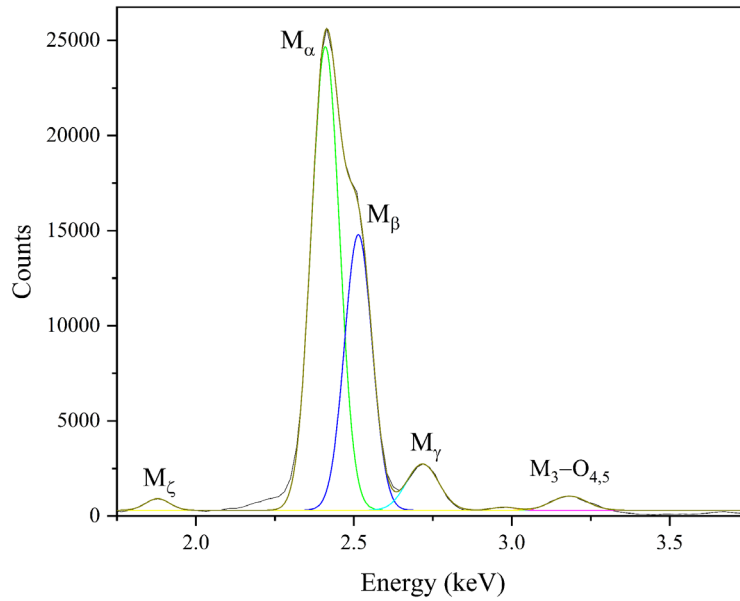
Figure 4.4. *Bi M-shell X-ray spectrum induced by 2 MeV protons*

Satellite formation which extends the Mα line (*i.e.,* peak broadening, see Fig.4.5) can be seen for heavy ion impact, because of Multiple Ionisation in the N- and O- subshells.
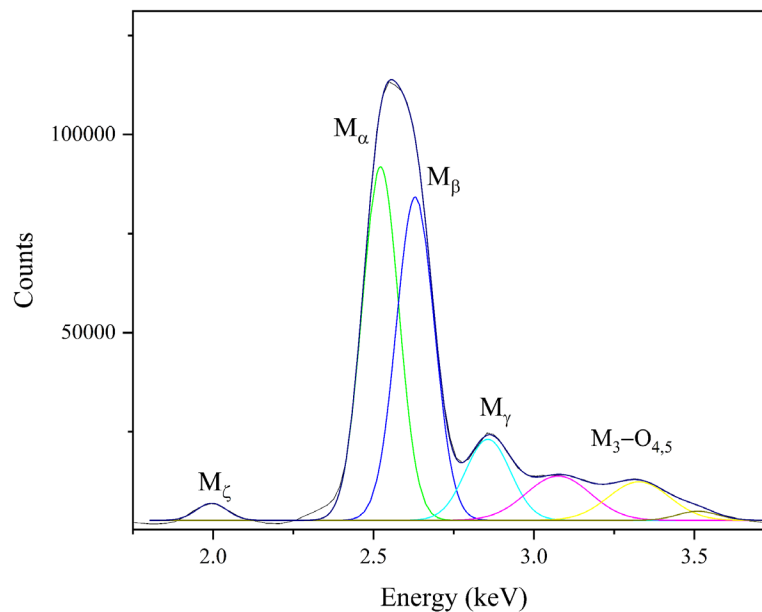

Figure 4.5. *Bi M-shell X-ray spectrum induced by 21 MeV $^{63}Cu^{7+}$*

The statistical peak uncertainty of the X-ray lines was kept at a maximum of 3% for low energy collisions, as the event count rates were very low due to the low ionisation cross sections. Thus, for long data acquisitions, the implication of the 3% limit resulted in significant film erosion

in cases where high currents of very heavy and slow ion beams were involved. This was the case with low intensity Lγ lines above ~7 keV excited with heavy ions.

Despite the low emission rates for slow ions, the target thicknesses for the transparent films were retained, even for measurements of L-shell XPCS due to slow heavy ion collisions with heavy target atoms like Bi. Although this was done to minimise significant projectile energy loss due to straggling and screening effects, comparative measurements with thicker targets nonetheless yielded low intensities for L_γ lines. The very low intensities, although amounting to undesirably large statistical uncertainties, could be used to draw some conclusions pertaining to ionisation probabilities, as discussed later in the subsection on XPCS.

The low ionisation cross sections meant that target thicknesses, although partly influential for major intensities, was largely immaterial in improving X-ray yields of the minor L_γ intensities of heavy target atoms. Therefore, along with mitigating large degrees of ion energy loss, X-ray attenuation and self-absorption in the target matrix; thin targets were maintained as a means of minimising significant charge state variations (*i.e.,* which influence X-ray production cross sections). Furthermore, thin targets were used to obtain more accurate accumulated charge measurements, which were useful for normalising the ion backscattering yield.

Estimates of ion energy loss for corrections of XPCS measurements were made using an in-built function in SIMNRA, using an integral of total stopping powers within the initial and exit ion energy. The reliability of these SIMNRA calculations was tested through comparisons with manually calculated exit energies (*i.e.,* energy after ion transmission through the target) from the stopping power equation. The requirement for the low target mass densities used, was that no more than 5% of the beam energy would be lost after transmission and/or backscattering. A function ($f(E)$) of the inverse total stopping powers ($1/S(E)$) obtained from the SRIM database [58] was computed within an estimated energy range that was ± 10% the incident ion energy. From the stopping power equation $f(E)dE = dx$;

$$\Delta x = \int_{E_e}^{E_i} f(E)dE = g(E_i) - g(E_e) \qquad 4.2$$

where E_i and E_e are the incident and exit ion energy respectively.

From Equation 4.2, the difference between the stopping power as a function of the incident ion energy and the target thickness is equal to the function of the ion exit energy $g(E_i) - \Delta x = C$, which is a constant C for the same incident ion energy (*i.e., of the same ion-atom interaction*). Therefore, the difference between this constant C, and the stopping power function of the exit energy is equal to zero (Equation 4.3). This describes the inverse stopping power as being equal to zero where the ion energy is equal to the exit energy.

$$C - g(E_e) = 0 \qquad\qquad 4.3$$

For a fixed E_i, a graph of $C - g(E)$ vs E, where E represents possible exit energy values, will have an intercept on the energy axis when $E = E_e$. An example of this approach is shown in the Figure 4.6 for 21 MeV ^{48}Ti in Au, where the theoretical dataset is evaluated using a third order polynomial function.
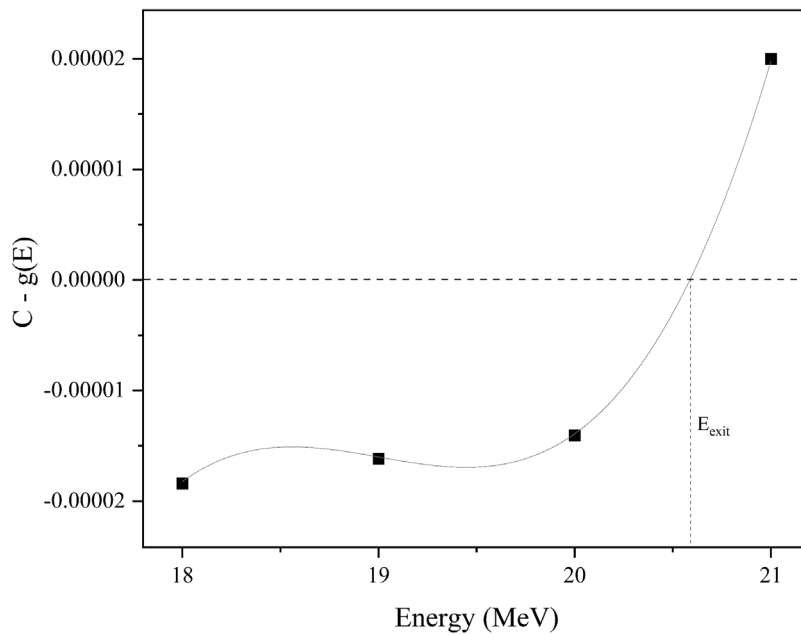

Figure 4.6. *21 MeV ^{48}Ti ion exit energy in 20 nm Au*

The calculated exit energy was compared to that calculated using SIMNRA and found to be within an error below 1%, validating the use of SIMNRA calculations.

The calculated ion exit energy was also important for estimating the target layer thickness prior to film deposition, to establish a reasonable degree of beam transmission through the foils. Furthermore, as already mentioned, significant variations between the incident and exit ion energy would result in even higher uncertainties on the measured cross sections. One such

approach is detailed later in the text, correlating variations of the X-ray production cross section due to a variance in ion stopping and X-ray attenuation.

4.2.2 Experimental measurements

The experimental XPCS were evaluated through the correlation of the number of incident ions in terms of X-ray production and ion backscattering, as shown in Equation 4.4 [27], [114], [115], [116]:

$$\sigma_X^{k,L,M} = \frac{4\pi . Y_x . \sigma_B(E_i) . \Omega_B . F_{(a,E)}(E, \Delta E)}{Y_B . \varepsilon_p(E_i) . \Omega_X} \qquad 4.4$$

where the terms are: Y_x – X-ray yield, Y_B – backscattering yield, σ_B – backscattering cross section, $\varepsilon_p(E_i)$ – X-ray detection efficiency (determined from proton spectra), Ω_X – X-ray detector solid angle, Ω_B – ion backscattering detector solid angle and $F_{(a,E)}(E, \Delta E)$ – ion energy loss and X-ray attenuation correction factor.

The X-ray detector efficiency was determined using Equation 4.5, where the accumulated charge for an ion beam impinging on the target during the measurement was normalised to the backscattering yield, as this directly relates to the number of incident ions prompting X-ray emission [117]. In some cases, where it was experimentally permissible, accumulated charge was collected and compared to the ion backscattering yield.

$$\varepsilon_x = \frac{4\pi . N_x^p}{N_B^p} . \frac{\sigma_B^p}{\sigma_x^p} . \frac{\Omega_B}{\Omega_X} \frac{1}{e^{-\mu_f . \rho_f . \Delta x_f}} . \left[\frac{\mu_t . \Delta x_t}{1 - e^{-\mu_t . \Delta x_t}}\right] \qquad 4.5$$

The relative X-ray detection efficiency could be deduced from the ratio constant of the backscattering and X-ray (*i.e.,* $\Omega_B/\Omega_X\varepsilon_X$) detector solid angles, moreover in cases where either one of the solid angles is not known (Equation 4.4). In all measurements reported here however, the method detailed in Equation 4.5 was applicable as the solid angles have been determined. In cases where no X-ray filter of thickness Δx_f was placed in front of the X-ray detector, X-ray attenuation only considered photon self-absorption through the target layer of thickness Δx_t. The reader is referred to the section on energy loss correction below for elaboration. Theoretical X-ray production cross sections σ_x^p were calculated using the ECPSSR(DI) model. Although it may be ideal to use experimental proton cross section data, as widely available in

literature, experimental datasets are however prone to large uncertainties and do not always converge when compared to each other. The ECPSSR model, particularly within the $(1 - 3)$ MeV range has been widely validated, comparing to an empirical fit of multiple experimental cross section datasets.

The experimental relative efficiency was compared to the theoretical efficiency (Equation 4.6) which considered X-ray attenuation and transmission through the detector thick beryllium window μ_{Be}, gold electrode μ_{Au}, the silicon crystal μ_{Si} and silicon dead layer μ_{Si}^d. The layer thicknesses are represented by ΔX_{Be} (25μm), ΔX_{Au} (10nm), ΔX_{Si} (5mm), ΔX_{Si}^d (250nm) [118].

$$\varepsilon_X(E) = \left(1 - e^{-\mu_{Si}(E)\Delta X_{Si}}\right)\left(e^{\left(-\mu_{Be}(E)\Delta X_{Be} - \mu_{Au}(E)\Delta X_{Au} - \mu_{Si}^d(E)\Delta X_{Si}^d\right)}\right) \qquad 4.6$$

Since only X-rays within a limited energy range were evaluated, a few relative efficiencies were therefore measured and compared to theoretical efficiencies for the X-ray detector. The theoretical efficiency was used for energies not covered by experiment, substantiated by the agreement between experimental values and theory as shown here in Figure 4.7. This agreement was therefore assumed across all other energies not covered by experiment. As it is seen, the efficiency above ~2 keV is close to 100%.
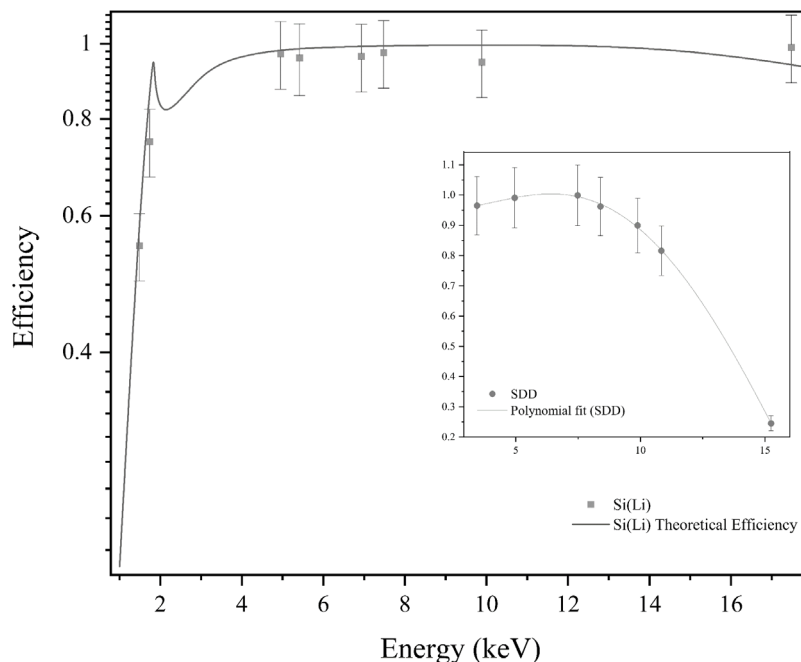

Figure 4.7. *Theoretical and experimental X-ray detector efficiency. Silicon absorption edge observable in the theoretical curve from ~1.7 keV*

Due to the particularly low backscattering yield for heavy ions such as Cu and I, charge measurements were used instead. This was done to have an accurate account of the number of incident ions. The accumulated charge Q can be viewed in terms of Equation 4.1, by substituting the ion backscattering parameters using the following relations:

$$N_i = \frac{Q}{ne} = \frac{Y_B}{\sigma_B . dx . \Omega_B} \qquad 4.7$$

where dx is the target thickness, e the elementary charge and n the ion charge state.

The differential X-ray production cross section in terms of charge is then written as:

$$\sigma_X^{k,L,M} = \frac{Y_x . F_{(a,E)}(E, \Delta E)}{N_i . N_T . \varepsilon_{Abs} . 4\pi} \qquad 4.8$$

$$N_T = \frac{N_A . \rho . dx}{A}$$

where N_T is the number of target atoms, in terms of the target mass density $\rho . dx$, Avogadro's constant N_A and the atomic mass number A.

Energy loss, target thickness and X-ray absorption corrections

As it is well established that interaction cross sections, as with the XPCS, are (ion) energy dependant, variations in the ion energy significantly contributes to uncertainty. Thus, when an incident ion losses energy along the target depth, the X-ray production cross section also varies and is integrated along the same energy range. This means that the ion stopping in the target and X-ray production are directly correlated. One method, detailed by Zuchiatti and co-workers [119], is to evaluate the X-ray production cross section within the limits of the incident and exit ion energy. The correction factor, ' $F(\Delta E)$ ', reads:

$$F(\Delta E) = \left(\int_{E_f}^{E_i} \frac{\sigma(E)}{S(E)} d(E) \right) . \left(\frac{1}{dx . \sigma(E_0)} \right) \qquad 4.9$$

where $\sigma(E), S(E), dx$ and E_0 represent the X-ray production cross section due to the ion energy E, the stopping power, target thickness and the incident ion energy.

The integral is solved using Simpson's rule, giving the expansion:

$$\int_{E_f}^{E_i} \frac{\sigma(E)}{S(E)} d(E) = \frac{E_0 - E_f}{6} \left[f(E_0) + f(E_f) + 4f(\frac{E_0 + E_f}{2}) \right]$$

4.10

The final energy loss correction factor is thus:

$$F(\Delta E) = \left(\frac{1}{dx. \sigma(E_0)} \right) \cdot \left[\frac{E_0 - E_f}{6} \left[\frac{\sigma(E_0)}{S(E_0)} + \frac{\sigma(E_f)}{S(E_f)} + 4 \left(\frac{\sigma(\frac{E_0 + E_f}{2})}{S\left(\frac{E_0 + E_f}{2}\right)} \right) \right] \right]$$

4.11

The stopping power data used in this correction was extracted from the SRIM database. The SRIM stopping power data was assumed valid as the performance of the code is well established to be reliable for pure target elements, as was the case here. Particularly for the thin targets used in this work, the degree of ion energy loss was low, as shown by the energy loss fractions (*i.e.,* percentage of the ion energy lost in the target depth (E_f/E_0))) in Figure 4.8.
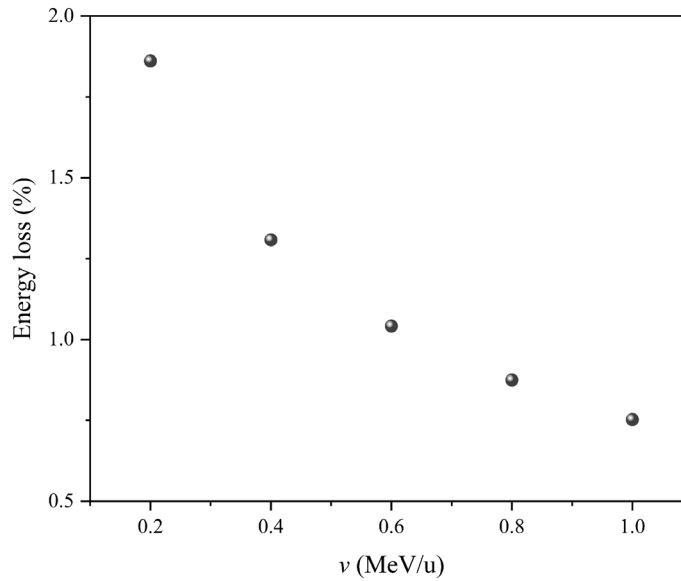

Figure 4.8. *Energy loss percentage of $^{48}Ti^{q+}$ in Au in the 0.2 MeV/u – 1.0 MeV/u energy range*

Although the variance of the ion beam energy about a given target thickness influences the statistical uncertainty in the measurement of XPCS, another source of uncertainty is also an important factor in the laboratory frame. This is the attenuation and self-absorption of the X-rays emitted within the target layer, which may influence the number of detected X-rays. In addition, while the same mass densities could be maintained for different measurements, the

use of detector filters for the intentional absorption of soft X-rays (*i.e.,* (0 – 2) keV) to control event count rates and subsequently minimise detector deadtime, X-ray attenuation then becomes exacerbated by the mass density of both the filter and target layers. This means that for a larger target thickness, the true number of X-rays emitted from below the surface of the atomic matrix will not be reflected in the measured cross section as some of them will have been completely attenuated, thus reflecting lower than true cross section values. Therefore, since the thickness of the target layer not only results in a variation of incident ion energy but also significant X-ray attenuation, an additional correction was made. The correction here factors in the thickness *X*, density *ρ* and mass absorption coefficients *μ* of both the target layer *t* and detector filter *f*. The mass absorption coefficients by Hubbell and Seltzer [120], [121] were used. This correction factor is also reflected in the measurement of the X-ray detection efficiency, as included in Equation 4.6.

$$F_{(a)}(E) = \left(\frac{\mu_t . X_t}{1 - e^{-\mu_t . X_t}} \right) . (1/e^{-\mu_f . \rho_f . X_f}) \qquad \text{4.12}$$

The energy loss correction was up to a maximum of ~5% uncertainty for all thin targets, and up to ~15% for the thicker targets, where thin targets could not be used. Furthermore, ion beam currents were optimised to limit detector deadtime, contributing an uncertainty of ~2% across all measurements. Thus, the overall fractional uncertainty was evaluated using the expression below:

$$\frac{\delta U_X}{U_X} = \sqrt{\left(\frac{\delta Y_X}{Y_X} \right)^2 + \left(\frac{\delta \sigma_X}{\sigma_X} \right)^2 + \left(\frac{\delta \varepsilon_X}{\varepsilon_X} \right)^2 + \left(\frac{\delta Y_B}{Y_B} \right)^2 + \left(\frac{\delta \sigma_B}{\sigma_B} \right)^2 + \left(\frac{\delta \Omega_B}{\Omega_B} \right)^2} \qquad \text{4.13}$$

Contributions to uncertainty include the X-ray Y_x and backscattering yield Y_B, X-ray detection efficiency ε_X, theoretical proton induced backscattering σ_B and X-ray production cross sections σ_x, as well as the backscattering detector solid angle Ω_B.

Experimental K-shell XPCS measurements were carried out using protons and silicon ions in the (0.3 – 1.0) MeV/u ion velocity range in 20 μg/cm² mono-elemental Cr, Ni and Ge foils backed by 20 μg/cm² carbon substrates. These low velocity proton experiments were carried out on the air pollution beam line at the Ruđer Bošković Institute at beam currents ranging between (9 – 10) nA, to compensate for the low ionisation cross sections below 1 MeV/u. The measured cross sections are presented in the data tables in *Appendix* A.

Experimental datasets were compared to theoretical XPCS to validate the use of ECPSSR cross sections within the investigated ion velocity range for protonic ionisations. The use of theoretical proton cross sections was important for the calculation of semi-empirical XPCS, where available experimental heavy ion and theoretical proton XPCS were used to predict new cross section datasets. The methodology is discussed in detail, later in the text.

The theoretical ECPSSR ionisation cross sections were calculated using the ISICSoo [122] and ERCS08 codes [86], and thereafter translated to X-ray production cross sections using experimental and Dirac Hartree-Fock (DHS) calculated fluorescence yields, relative emission rates as well as Coster Kronig transition probabilities [91], [123].

The influence of atomic parameters, on the translation of theoretical ionisation cross sections to XPCS was evaluated using cross section ratios. Compared K- proton XPCS in Ni were translated using recommended values from the ANSTO compilation [92], comparing Walters and Bhalla's datasets [124] with those from Bambynek [91] and Krause [125]. Scofield's DHS calculations [126]were later used in the translation of ionisation CS to XPCS datasets for L-shell ionisation.
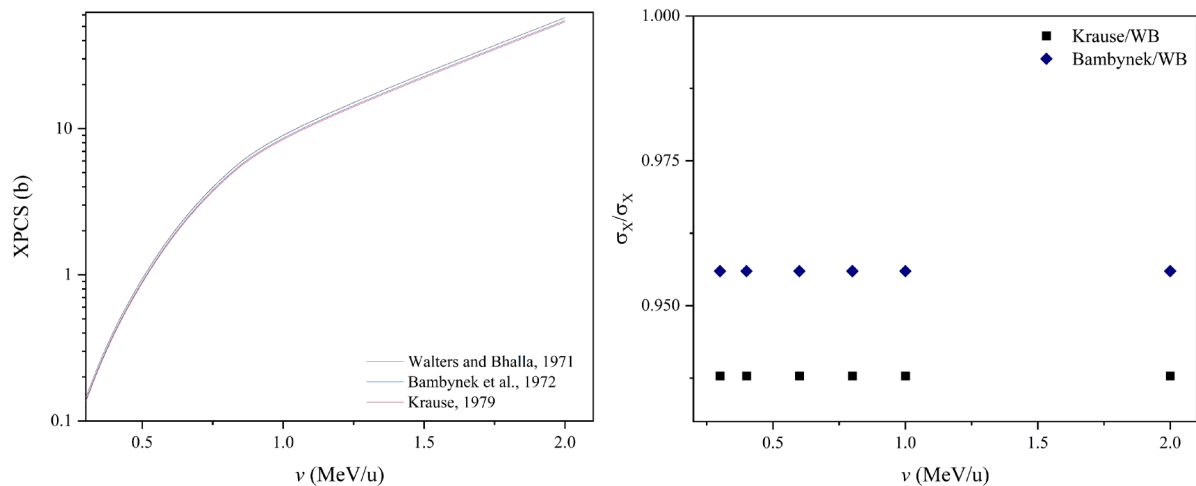

Figure 4.9. *Theoretical $K_{\alpha 1,2}$ XPCS (left) and XPCS ratios (right) translated using fluorescence yields from Krause, Bambynek, and Walters and Bhalla (WB)*

The atomic parameters were seen to influence the XPCS at only up to 10% for K-shell ionisation, and similarly for L-shell cross sections. A comparison of the measured experimental proton induced K-shell XPCS in Ge are shown in Figure 4.10 below.
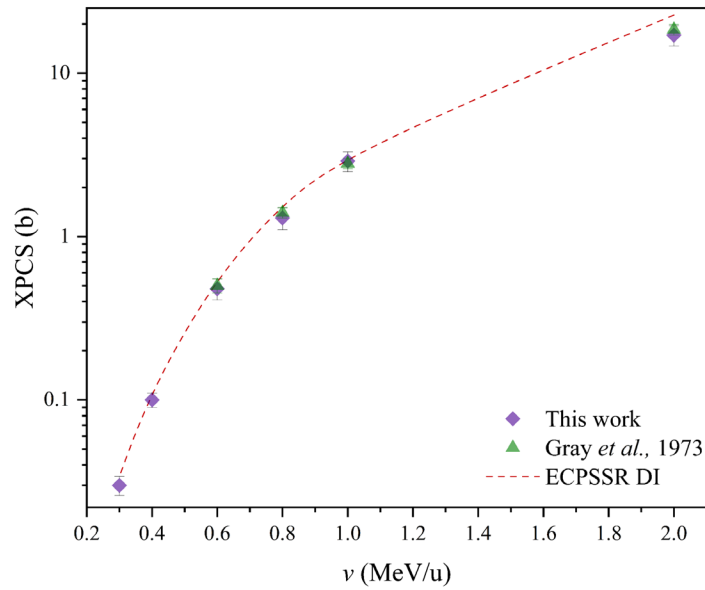
Figure 4.10. *K-shell proton induced X-ray production cross sections in Ge at 300 keV – 2 MeV*

Ratios of experimental and theoretical cross sections were used to evaluate agreement and discrepancies using percentage scores. The agreement between the measured dataset and ECPSSR predictions ranged between 75% and 88%, while comparisons with the dataset from Gray *et al* [127] agreed within a 92% – 96% range.

On the other hand, for L- subshell ionisations, the validity of the ECPSSR was seen to deteriorate in the lower energy range where Multiple Ionisation effects are not fully accounted for, particularly for heavy ions. These effects include high electron capture cross sections as well as coupled shell states for electrons in the M- and N- subshells. Such a discrepancy can be seen in the Figure 4.11, for silicon L-shell ionisation in Sn.
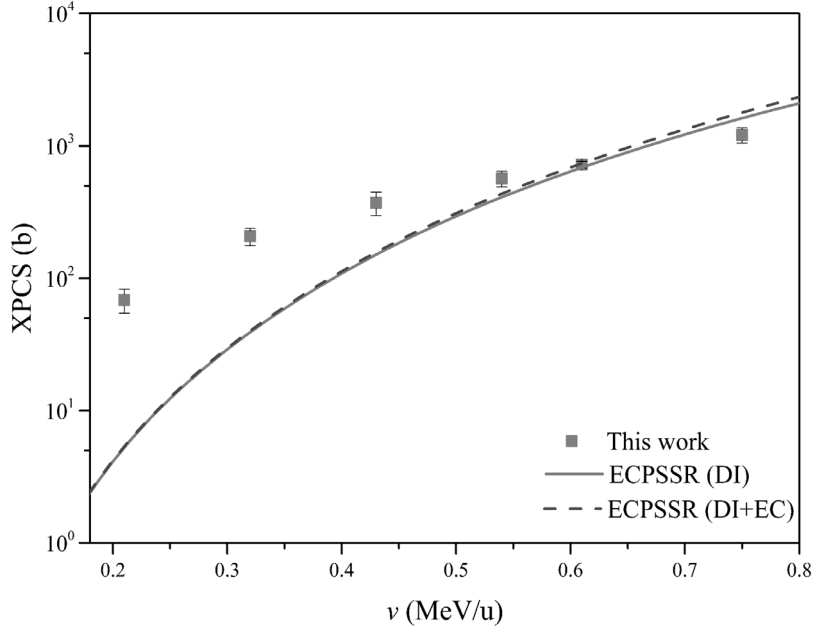
Figure 4.11. $^{28}Si^{q+}$ *in Sn experimental vs ECPSSR XPCS*

These large discrepancies are a result of the collision symmetry (*i.e., $Z_1/Z_2 = 0.3$*), as the Si and Sn masses are of the same order of magnitude. The deviation from the binary collisions approach, fundamental to the ECPSSR, implies a quasi-molecular state during ion-atom impact. Since the incident silicon ion has some electronic screening potential, collision with the Sn atom(s) results in a state in which both the ion and target electron densities overlap. The overlapping electron orbitals underpins the Molecular Orbital Theory (MOT) [128]. The theory approximates the formation of a molecular orbital Ψ_i, which can be considered as the linear combination of the constituent atomic orbitals Φ_r given in the first approximation by: $\Psi_i = \sum_r a_{ri} \Phi_r$ [128]. The term a_{ri} is a coefficient describing the contribution of each constituent atomic orbital to the molecular orbital.

The limitations of single-hole ionisation theories based on Rutherford scattering is in that high electronic screening at low energies is unaccounted for. The high electronic stopping, compounded by the low incident velocity thus results in higher than protonic Direct Ionisation (DI) due to the long ion dwell times within the target electron density prior to projectile scattering from the mean nuclear field. Even with the inclusion of electron capture (EC) corrections in the ECPSSR calculations, modifications for single-hole ionisation see only a slight increase from the DI model. This is because fundamentally, the ECPSSR assumes the perturbation of the electronic field as being caused only by increasing ion energy, since protonic ionisation is due to hyperbolic scattering from the nucleus. In this case, the interaction

potential is calculated with a screening function equal to 1, which is not valid for heavy ion impact where two electron fields 'collide'. While it may be asserted the discrepancies observed between experiment and DI theories is purely due to ion mass, it should be appreciated that the same heavy ion mass may resemble asymmetric collisions with very large target systems. The concept of collision symmetry is therefore a more suitable term for classifying different ion-atom collision systems, and the degree to which screening subsequently affects the XPCS.

Such is shown for several collisions using Si ions in different target groups, where reducing Z_1/Z_2 ratios signify reducing collision symmetry. The large discrepancy between experiment and theory in Sn compared to those in W, Au and Bi demonstrates large screening at low energies, as can be seen in Figure 4.12.
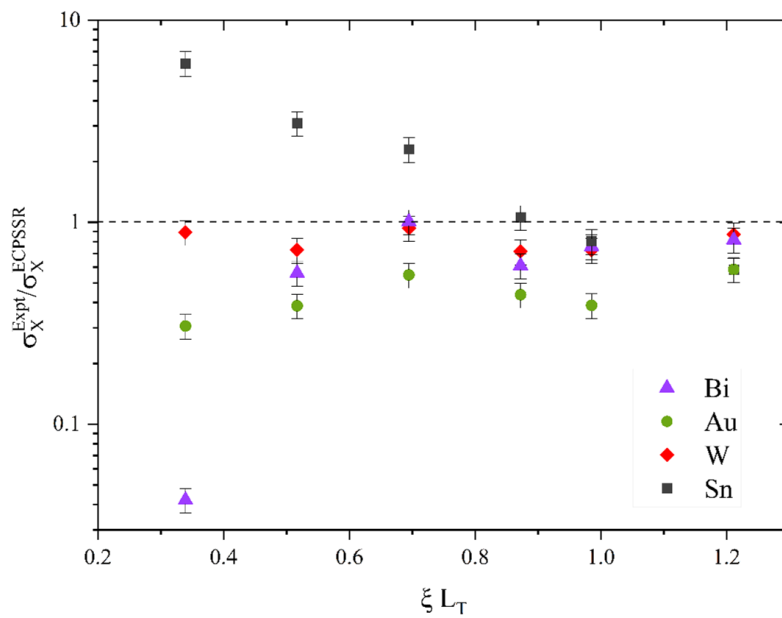

Figure 4.12. *Experiment vs theory for Si ionisations in Sn, W, Au and Bi*

The cross section ratios, which can also be considered as data agreement scores were correlated to the reduced velocity, an adiabaticity parameter relating ion velocity v_1 with the velocity of the ith subshell electron v_{L_i} ($i = 1, 2, 3$).

$$\xi_{L_i} = \frac{2v_1}{\theta_{L_i} v_{L_i}} \qquad\qquad 4.14$$

The reduced electron binding energy is described as $\theta_{L_i} = n^2 U_{2L}/Z_{2L_i}^2 \mathcal{R}$, comprising the principal quantum number n, experimental target electron binding energy U_{2L} and the screened nuclear charge $Z_{2L_i}^2 = Z_2 - 4{,}15$, determined from Slater's rule. For the evaluation of total

subshell cross sections, a weighted mean of the reduced velocities for the ith subshells (i = 1, 2, 3) was used.

Discrepancies with experimental data were expected for very symmetric collision systems, as seen for $L_{\alpha 1,2}$ XPCS induced by $^{127}I^{q+}$ in the $0.08 - 0.2$ (MeV/u) slow velocity range (Figure 4.13).
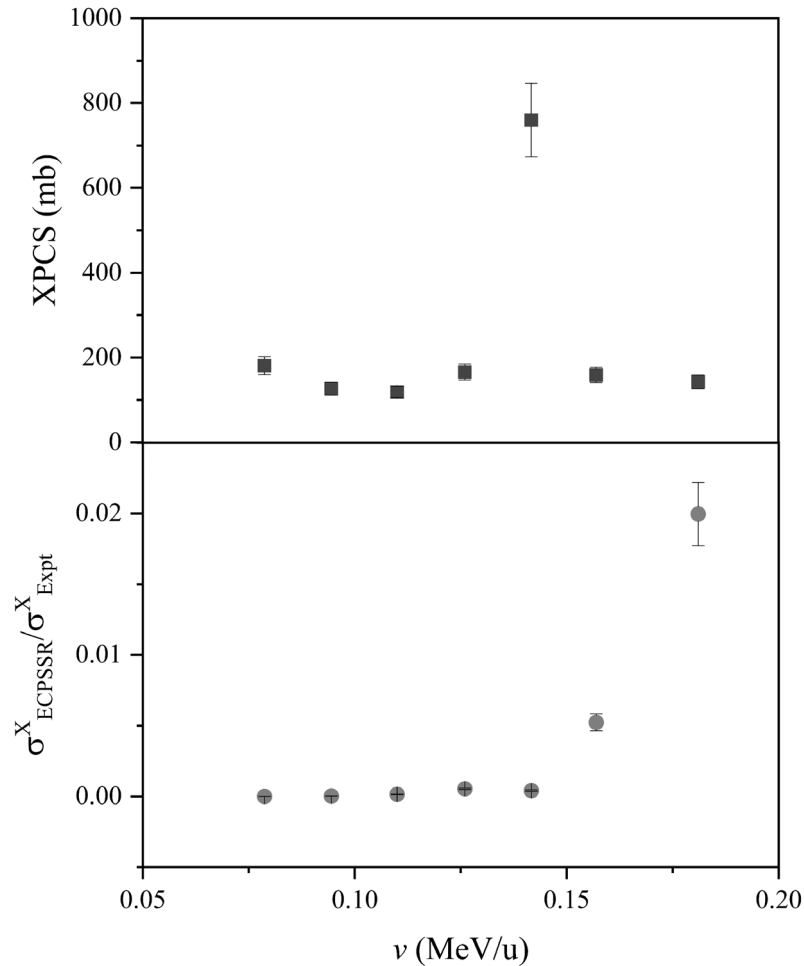

Figure 4.13. 0.08 MeV/u $- 0.2$ MeV/u $^{127}I^{q+}$ *induced XPCS in Sn*

The sudden increase in the X-ray production cross section at 0.14 MeV/u seen in Figure 4.13 may be due to pronounced multiple ionisations in the united (or molecular) atom. Similar behaviour was seen with other near symmetric collision systems, although seen at less intensity as reported later in the text. Multiple ionisation (MI) effects due to near-symmetric heavy ion-atom collisions (where $Z_1 \approx Z_2$) are not yet fully explored, as shown in the works of Mokler and Folkmann [129] which indicated resonance in near symmetric ion-atom collisions as being a feature of Molecular Orbital (MO) formation. Furthermore, works by Saha and co-workers

[130] as well as Ren and co-workers [131] observed an L- subshell correlation between the target atom and the projectile ion, which could lead to increasing X-ray yields at given ion energies. A similar correlation can be seen in Figure 4.14, where the projectile Lα intensity, which is also convoluted with the target (Sn) Lβ lines, is lower than the corresponding projectile Lβ lines. This is in addition to the incident projectile electron deficiency/charge state (*i.e.,* q = +6), which reduces the screening potential. The mechanism by which MI effects enhance XPCS, along with projectile ion energy dependence for heavy ion-target collisions is yet to be fully explored, and thus requires further extensive investigation beyond this reporting. The uniform distribution of theory *vs* experimental cross section ratios seen in Figure 4.13 is due to the very low theoretical cross sections, which in overall have agreement scores with experimental data of less than 3% within the measured ion energy range. The measured cross sections were limited to the $L_{\alpha 1,2}$ line due to overlapping projectile L- and target L- lines in the X-ray spectra (see Fig.4.14).
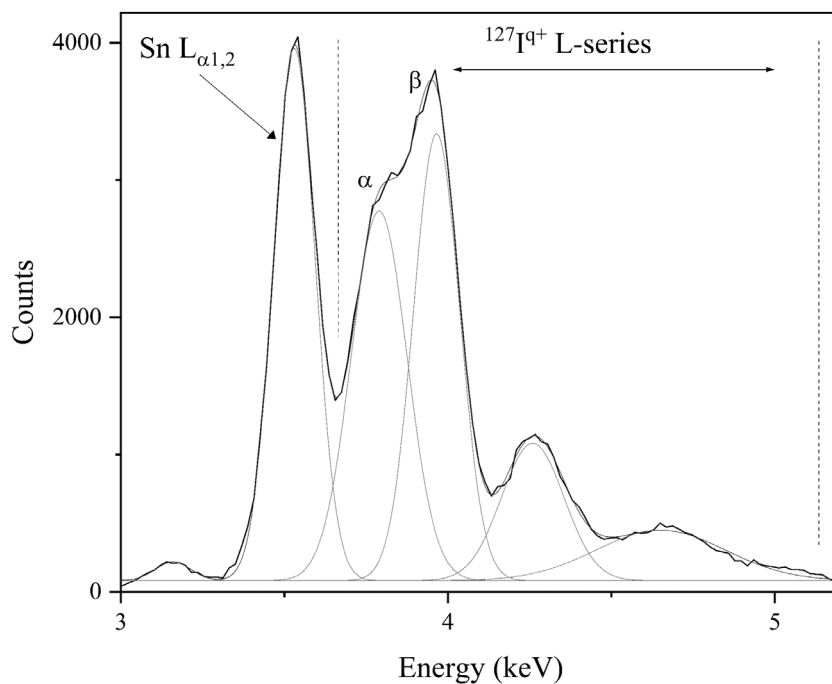

Figure 4.14. *18 MeV $^{127}I^{6+}$ in 20 μg/cm^2 Sn/C X-ray spectra collected with SDD detector*

Overlapping projectile and target X-ray energies were seen in greater effect for W L-shell ionisation due to Cu, resulting in the omission of the Cu – W L-shell XPCS. As a result, only the W M-shell cross sections due to Cu were measured. It was however expected, as previously noted for L-shell ionisation with Si below 0.4 MeV/u, that DI models such as the ECPSSR would be invalid as only the low projectile nucleon energy range was investigated. The non-validity of the ECPSSR would further be exacerbated by even larger screening effects by Cu

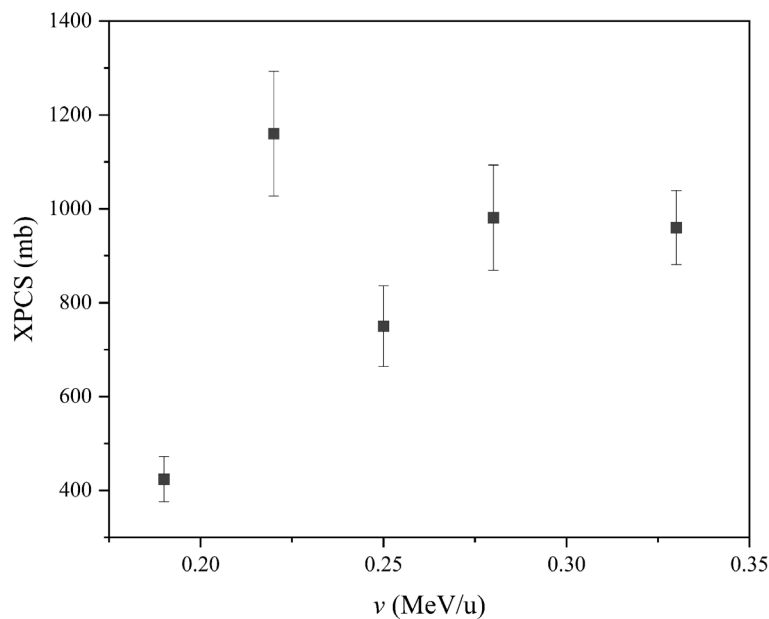compared to Si. An illustration of the measured Cu induced M-shell XPCS in Au are shown in Figure 4.15.

Figure 4.15. *Cu induced M-shell XPCS in Au*

It was determined, drawing from Figure 4.12, that ECPSSR calculations within the Cu ion energy range were outside the model's range of validity. This can also be seen in Figure 4.13, where ECPSSR predictions are less than 5% of the experimental values. The emphasis of symmetry of course not only affects ionisation cross sections predicted by theory, but also extends to modifications of radiative transition probabilities and fluorescence yields during atomic relaxation for a multiply ionised atom.

Therefore, while XPCS measurements are undertaken to strengthen the current database as well as validate theory, the provision of line intensity ratios for the estimation of the average number of subshell vacancies is equally important for estimating modifications of other atomic data (see section on Multiple Ionisation). In the main, while a significant set of cross section data has been generated (*Appendix A*), it remains an impracticable undertaking to measure all possible ion-target combinations. Also considering the extent of scatter in published experimental datasets, the generated database ought to provide additional data from which empirical mean values can be drawn. One effort towards enriching the current database was to use a semi-empirical approach encompassing both measured experimental XPCS and theoretical proton XPCS. The interpolation of XPCS data using cross section ratios is demonstrated in the following subsection.

4.3. Semi-empirical parameterisation of heavy ion/proton XPCS ratios

4.3.1. Methodology

The measured (experimental) heavy ion induced XPCS data was scaled with theoretical ECPSSR proton cross section data calculated using the ERCS08 code. The experimental *vs* theoretical proton XPCS ratios for the same nucleon energy, labelled *R*, is defined as:

$$R = \frac{\sigma_{X(HI)}}{\sigma_{X(p)}} \qquad\qquad 4.15$$

As opposed to simply carrying out a universal fit of experimental proton XPCS data to obtain empirical values, ECPSSR approximations were instead used as they have been widely validated for protonic ionisation. Additionally, the preference of ECPSSR cross sections is based on their proximity to empirical mean values of a wide experimental dataset. The use of ECPSSR proton cross section data also enabled an offset of uncertainties from experiment, as it pertains to the discrepancies between multiple datasets from literature. The designation of the term 'discrepancy' for evaluating differences between experimental datasets with those from literature as a metrological concept was retained. This is because reference to 'error' would assert the existence of absolute or validated empirical cross section values, which are currently unavailable. An example of compared experimental vs ECPSSR theoretical proton cross section data is shown in Figure 4.16:
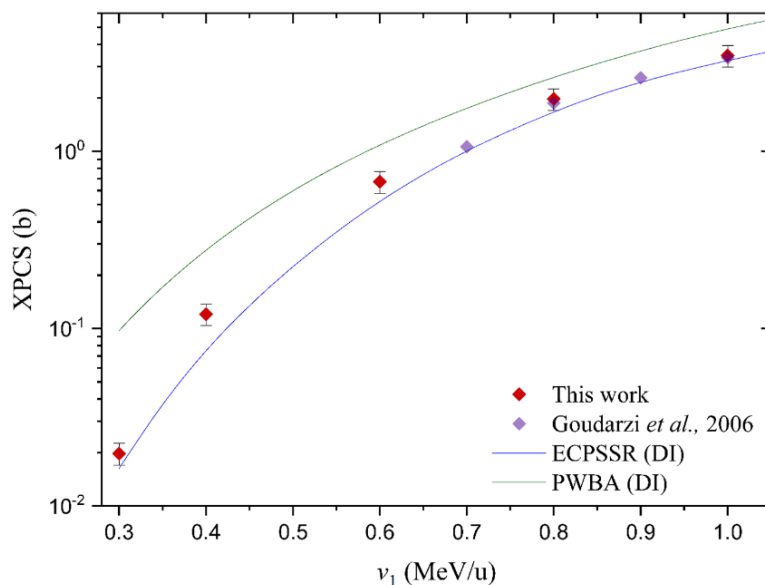

Figure 4.16. *0.3 MeV – 1.0 MeV proton induced total L-shell XPCS in Bi*

Experimental uncertainties were higher particularly in the low energy range due to significantly low L_γ cross sections. Furthermore, comparisons were limited by the sparse availability of experimental data, moreover in the low energy range. Nonetheless, predictions by the ECPSSR corresponded well with the measured experimental dataset. Validations of the measured cross section data were carried out through comparisons with data from literature, namely by *Goudarzi and co-workers* [132], which was evaluated to be within 95% – 97% in agreement all round.

While it may in principle be ideal to carry out parameterisations purely on heavy ion induced experimental XPCS datasets, statistical variations/discrepancies commonly seen between measured XPCS create unideal conditions for reliable estimations. Such is the case with the measured $^{12}C^{q+}$ induced XPCS in Bi compared to data found in literature. The agreement scores determined using ratios of literature vs experimental datasets were calculated at: 57% – 62% (Gorlachev et al. [27]), 47% – 56% (Bhattacharya et al. [133]), and 79% – 94% (Ejeh et al. [134]). A graphical representation of these scores is shown in Figure 4.17 below.
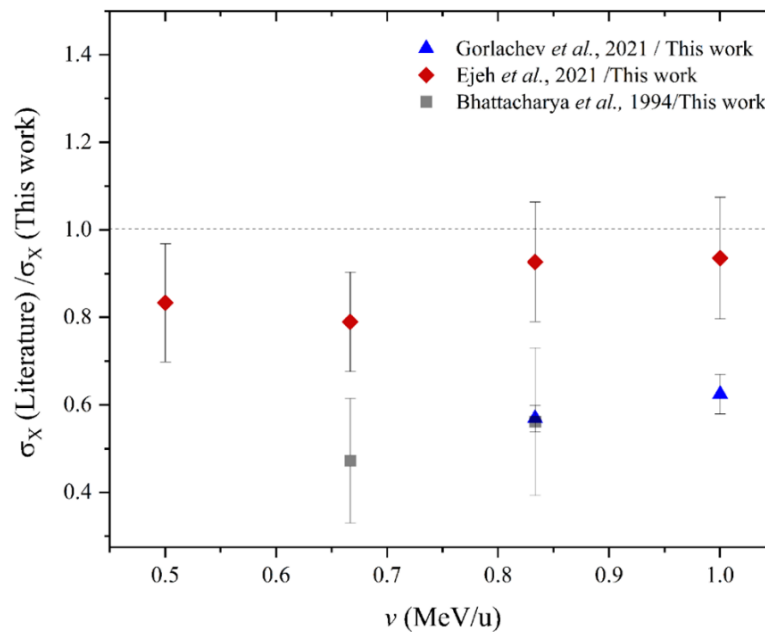

Figure 4.17. *0.5 MeV/u – 1.0 MeV/u $^{12}C^{q+}$ induced XPCS ratios in Bi*

The calculation of *R*-ratios using measured experimental data with ECPSSR proton cross section data is shown in Figure 4.18 as follows.
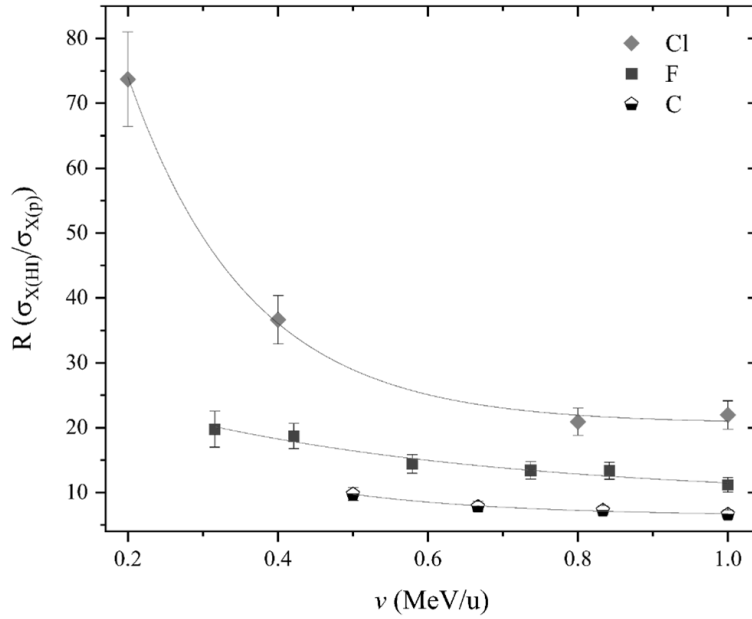
Figure 4.18. *R-ratios due to $^{12}C^{q+}$, $^{19}F^{q+}$ and $^{35}Cl^{q+}$ in ^{209}Bi*

Heavy ion/proton cross section ratios *R* were seen to saturate with increasing ion energy, by a magnitude characteristic to the projectile ion mass. The exponential decay shows the degree to which screening effects are enhanced in the low energy range, sharply saturating at a lower degree with increasing ion energy. This difference is due to the increasing projectile charge state at incidence required to obtain higher ion energies from the accelerator. Thus, the deficiency of the projectile electron density at higher energies results in lower screening, increasing the dominance of Direct Ionisation (*i.e.,* ionisation through ion scattering from the nuclear potential). This has been the basis of agreement between ECPSSR predictions with experiment at higher energies for some collisions, as already shown. The effect of projectile screening was previously shown in Figure 4.14, observed by the reducing $M_{\alpha1,2}$ intensity in the X-ray spectra for Sn L-subshell ionisations due to $^{127}I^{6+}$. Of course, since the degree of Multiple Ionisations depends on collision symmetry, the function gradient becomes larger for heavier ion masses, as can be seen for Cl. The C and F trends thus resembled linear-like trends in comparison to the Cl trend, which is only a representation of the extent to which screening occurs for different heavy ion masses. The *R* ratios for C and F are in Figure 4.19, where the function amplitudes are very close, to an extent that the differences are negligible.
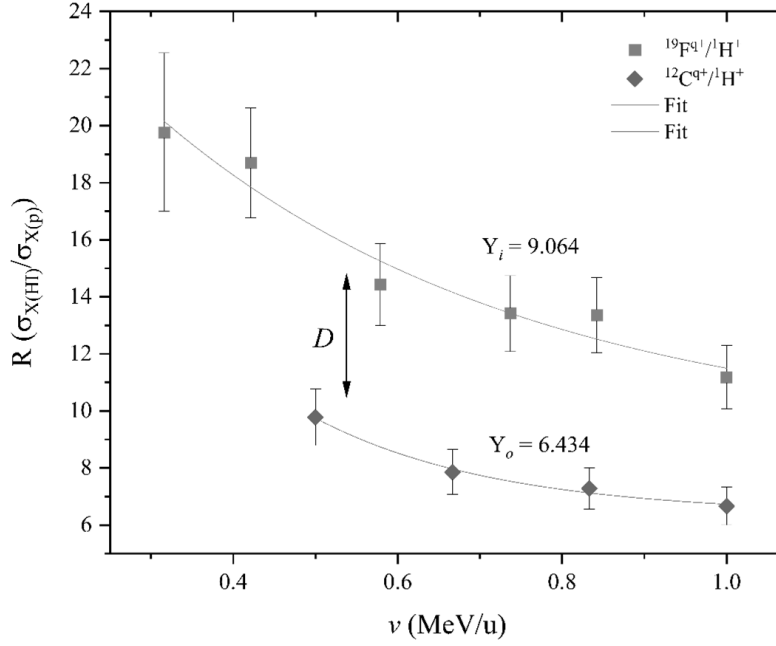
Figure 4.19. *R ratios of C and F in Bi*

The datasets were analysed using a multi-parameter exponential decay function, where the difference between the two functions (*i.e.,* of the same amplitude) was the function offset Y_j (*j = 0, i)*. The function trends' displacement by a magnitude D was calculated as the difference between the two function offsets. The displacement size D can be segmented into several steps deduced from the mass difference Δm $(m_i - m_0)$, and the step sizes K (*i.e.,* distance per atomic mass unit within the reference *j* ion mass range). The relation is given as:

$$K = \frac{D}{\Delta m}$$ 4.16

Therefore, the *R* ratio function for a given *Z* ion (*or in another case target*) based function is given as the sum of the initial function offset and the displacement size for the initial and desired ion/target mass, written as:

$$f(v)_z = f(v)_{z_0} + K(m_i - m_0)$$ 4.17

The exponential decay function, referred to as the *reference* function, can therefore be written as:

$$f(v) = Ae^{\left(\frac{-v}{t}\right)} + \left[f(v)_{z_0} + K(m_i - m_o)\right]$$ 4.18

69

The parameters here are namely the function amplitude *A*, ion energy per nucleon *v* and the proportionality constant *t*.

4.3.2. R-calculated XPCS: Bi target

An illustration of the methodology is given in the case of carbon and fluorine, with the function offset given by $f(v)_z = 6.434 + 0.376(m_2 - 12)$, for an investigated mass m_2. The reference function is therefore described by:

$$f(v) = 27.84e^{\left(\frac{-v}{0.348}\right)} + [6.434 + 0.376(m_2 - 12)] \qquad 4.19$$

The C – F reference function was then used to calculate/simulate *R*-ratio functions for oxygen and silicon ions in the same target.
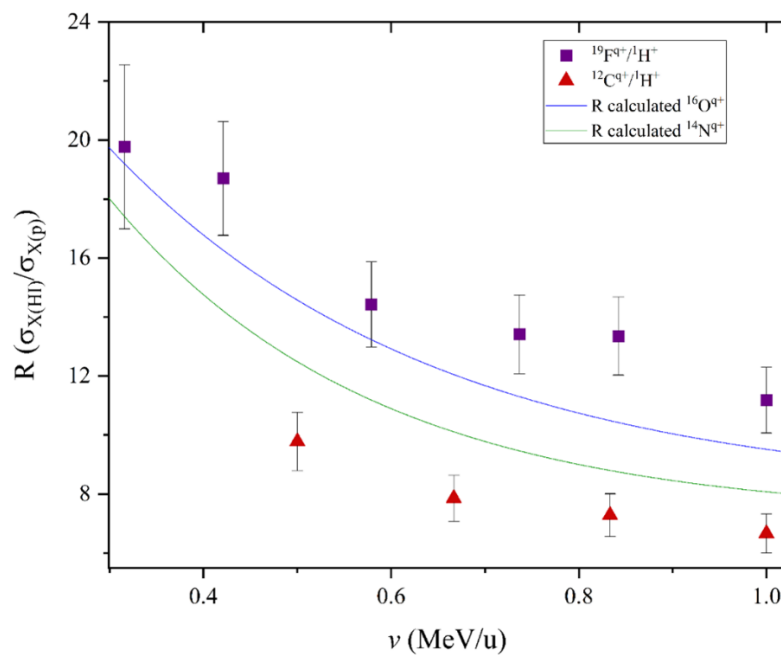

Figure 4.20. *N and O R-ratios in Bi*

The R-ratios were then converted to experimental XPCS using ECPSSR proton cross sections. Since ECPSSR proton ionisation cross sections are converted to XPCS using experimental atomic parameters (*i.e.,* fluorescence yields), the uncertainties for *R* calculated cross sections was given as:

$$\Delta U = \sqrt{\left(U_{experiment}\right)^2 + \left(U_{theory}\right)^2} \hspace{3cm} 4.20$$

The uncertainties for measured heavy ion induced XPCS are denoted by the term $U_{experiment}$, and due to ECPSSR calculations as U_{theory}. The calculated R cross sections are given in the table below.

Table 4.1. *O and N induced XPCS in Bi*

Ion	*v* (MeV/nucleon)	Semi-empirical (*R*)	ECPSSR (DI)
O	0.32	1.2 (1)	0.97
	0.4	4.1 (5)	2.9
	0.5	11 (1)	7.53
	0.7	35 (4)	27.5
	0.9	73 (9)	65.1
	1.0	98 (12)	91.4
N	0.32	1.1 (1)	0.93
	0.4	3.6 (4)	2.7
	0.5	10 (1)	7.03
	0.7	30 (4)	25.2
	0.9	61 (7)	59
	1.0	83 (10)	82.3

The data was thereafter compared with experimental cross sections measured by Pajek et al [83] and Gorlachev [135], as well as ECPSSR approximations as shown in Figure 4.21.
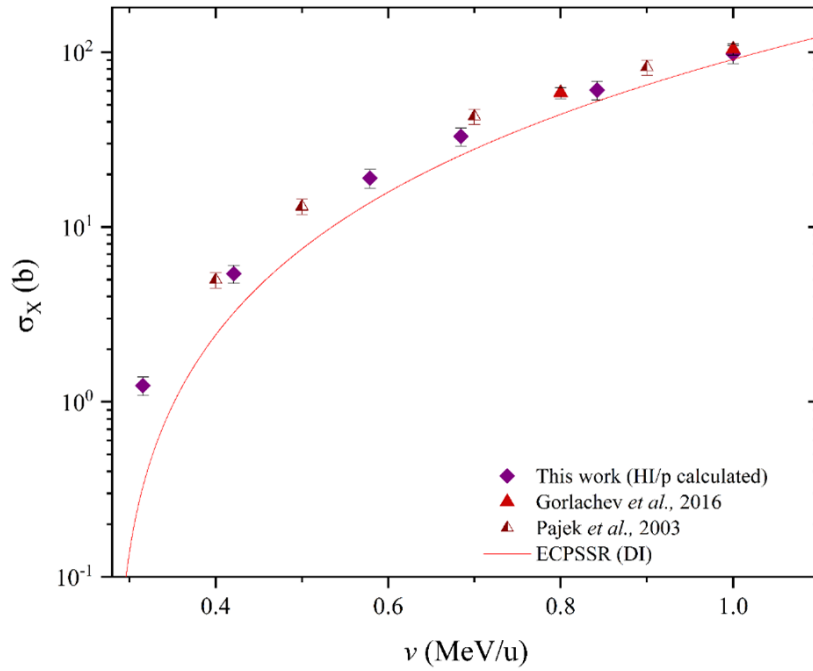
Figure 4.21. *O induced XPCS in Bi compared to the ECPSSR (DI)*

Similarly, as pointed out before, the ECPSSR model underestimates experimental (and in this case semi-empirical) cross sections in the low energy end, drawing closer as the ion energy is increased. Ratios of *R* cross sections with literature as well as ECPSSR calculations were used to determine the degree of agreement between the datasets. The agreement scores were calculated at ~80% – 90 % compared to the dataset of Pajek et al. [83], and at ~90% – 95% with that of Gorlachev et al [135]. Comparisons with the ECPSSR were calculated at ~50% – 70% in the low energy range (*i.e.,* $0.2 \leq v_I \leq 0.5$ (MeV/u)) and at ~95% at 1 MeV/u. These agreements and discrepancies are shown in Figure 4.22.
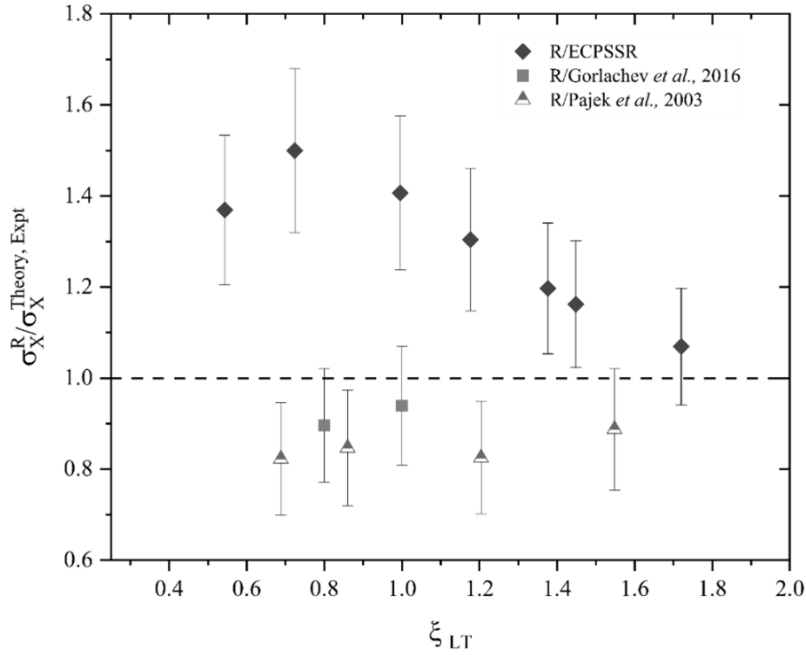
Figure 4.22. *Semi-empirical XPCS ratios vs ECPSSR and data from the literature*

Although the initial reference function was calculated for ion masses in the carbon – fluorine range, the limits of the function were nonetheless tested for heavier projectiles, namely Na and Si in the same target. The calculated X-ray production cross sections are tabulated below as:

Table 4.2. *Semi-empirical XPCS (in barns) due to Si and Na in Bi*

Ion	*v* (MeV/nucleon)	*R* (calculated)	ECPSSR (DI)	ECPSSR (DI + EC)
Si	0.4	2.6 (4)	2.6	3.6
	0.6	12 (2)	15.8	24.2
	0.8	30 (5)	48.1	80.2
	1.0	49 (7)	106	192
Na	0.4	2.3 (4)	3.0	3.4
	0.6	11 (2)	17.1	20.6
	0.8	26 (4)	50.1	62.2
	1.0	42 (6)	107	138

The largest discrepancies between semi-empirical and theoretical data were in the high energy range, where the degree of disagreement seemly increased with ion energy. Figures 4.23 give a visual aid of these discrepancies, which show the degree to which the validity of this approach may be constricted in as far as available data for parameterisations is concerned.
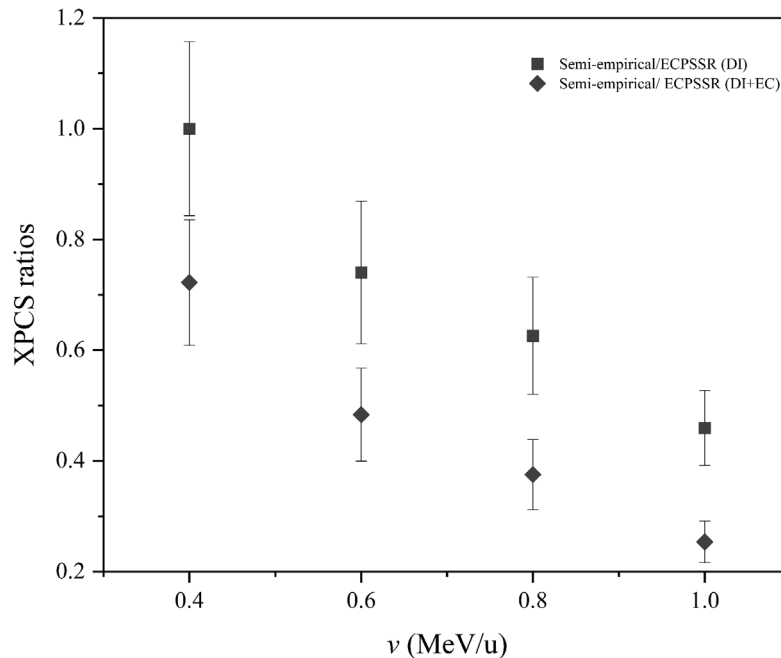

Figure 4.23. *Semi-empirical vs ECPSSR Si in Bi XPCS ratios*

Semi-empirical XPCS due to Cu, Ag and I were not evaluated due to the low ion energy range (< (0.2 - 0.3) MeV/u) within which the validity of proton ECPSSR cross sections is yet to be widely tested. Add to this, the non-uniformity of the XPCS trends for very slow and highly symmetric collisions would thus distort the R ratios due to the uniform exponential rise for proton cross section data. The discussion on Multiple Ionisation, which features the non-uniform increase in XPCS for slow near symmetric collisions, is reserved for section 4.4.

Nonetheless, the calculated semi-empirical XPCS were particularly important as a framework for enabling Total IBA applications using Heavy Ion PIXE, such as with the use of Si for MeV SIMS. The calculated R-XPCS were however unfortunately not compared to experimental values from literature, as not enough data was present at the time of this reporting.

4.3.3. Machine Learning (ML) predictions

Another statistical approach was taken, where measured experimental cross sections were used as training input data into a few supervised Machine Learning (ML) algorithms. The input variables/features used for the ML classifications were the ion energy and atomic numbers (*i.e.,* Z_1 and Z_2), with the Z_1/Z_2 ratio used as the meta data and the XPCS as the target. The ML classifications used were namely, a decision tree, Linear Regression (LR), Random Forest (RF) and Neural Network (NN) [136], [137]. The predictions were run using the Orange data mining software [138], using a 80/20 training *vs* test data ratio, where 20% of the training data was used for validation of the trained model. A schematic of the workflow in Orange is shown in Figure 4.24 below.
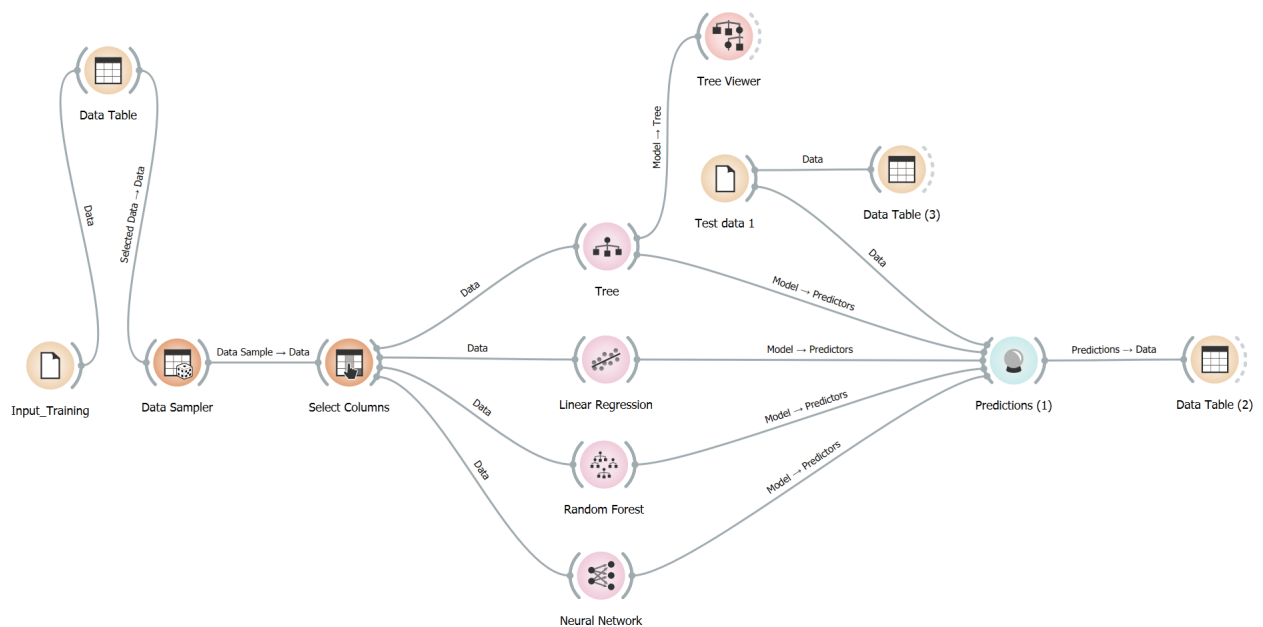

Figure 4.24. *Machine Learning workflow in Orange*

The calculated semi-empirical datasets were then compared to predictions by the ML algorithms, as well as ECPSSR datasets. Of course, to test the validity of this approach, predictions using Si ions, where data is available, were used. The input dataset was in this case the Si induced XPCS in W and Au, which were then used to predict XPCS datasets of Bi. The predictor variables were the ion energy and target mass, represented through changing Z_1/Z_2 ratios. The limited data however resulted in some challenges, particularly with the Tree and RF model. The Random Forest (RF) algorithm trains random decision trees to generate subsamples by splitting the datasets based on the predictor variable(s). This splitting would be used to discriminate the dataset to develop several 'possible cases'. The cases would then be used to

generate independent response variables (or outputs) when probed for specific/different predictor variables. The true or predicted output would then correspond to either the mean value or most predicted value from the probability distribution (*i.e.,* output values from the random decision trees). With only few datasets, the statistical limitation would result in only a few case groups being formed, and therefore a very limited number of decision trees [137]. This would mean that the generated 'possible cases' by the trees may in fact be the same, therefore resulting in the same output (see Table 4.4 below). Furthermore, as related to the single decision tree, lacking experimental datasets result in limited tree nodes, potentially resulting in the same output even for different predictor variables. A statistically richer input database would therefore be needed to improve predictive accuracy.

Of course, one consideration would be to include both light and heavy element targets in the training dataset – for instance, silicon L-shell XPCS in elements ranging between Sn and Au. However, inconsistent cross section trend gradients due to changing collision symmetries would distort the input dataset, thus producing incorrect output data. This approach was different from other ML algorithms used, such as the linear regression model, which is based on statistical linear regression that assumes a linearity in the correlation between datasets. These are namely the input variables/features, the Metas and the target; in this case, ion energy, Z_1/Z_2 ratios and the XPCS. Certainly, it is expected that this model may not generally be ideal for XPCS measurements, as the XPCS trends change with varying Z_1/Z_2 ratios (collision symmetry). Linearity was however assumed in this case since the collision symmetry of the training dataset (*i.e.,* Si in W and Au) was close to that of the predicted dataset (*i.e.,* Si in Bi).

The Neural Network (NN) algorithm used was carried out using logistic regression. Essentially, the logistic regression classification is in its nature dichotomous (*i.e.,* provides a binary output for every input(s)), and was used only to connect input to output values. These are namely the connection between ion energy and collision symmetry inputs to specific XPCS output values. Neural Network (NN) was then used to learn the non-linear correlations between the input and output dataset that could not otherwise be captured using logistic regression. Stochastic Gradient Descent (SGD) was used to optimise the NN learning, by reducing the gradient of the loss function (*i.e.,* difference between predicted and actual/test values) [136]. The SGD carried out this optimisation by selecting random data points in the training datasets and calculating weights/gradients, and iteratively making small changes (*i.e.,* learning rate) to its function parameters until the lowest gradient (also the minimum of the loss function) was obtained. For

these calculations, a 2000 neuron NN algorithm was used, and optimised using SGD configured at 500 iterations.

The predicted Si induced XPCS in Bi are thus presented in Table 4.3 below:

Table 4.3. *Machine Learning predicted Si induced XPCS (in barns) in Bi*

| v (MeV/u)	Tree	Random Forest	Linear regression	Neural network	Semi-empirical
1.00	24.6	23.3	37.1	36.6	48.7
0.8	24.6	23.3	24.9	24.8	30.1
0.6	24.6	23.3	12.7	12.6	11.7
0.4	3.04	4.71	0.5	0.4	2.6

As mentioned before, the same output values for the RF and decision tree algorithms are seen for all ion energies, except for at 0.4 MeV/u. This was due to the lack of experimental data, where only few tree branches/nodes from the single decision tree as well as from the forest of independent decision trees could be formed, yielding the same output. Nonetheless, the data was in this case compared to predictions by the Linear Regression (LR) as well as Neural Network (NN). The largest agreement between the ML and semi-empirical datasets was evaluated at 92% – 93% at 0.6 MeV/u, with the largest discrepancy at 15% – 19% for 0.4 MeV/u ions. The 55% – 85% correlation between the RF and decision tree with the semi-empirical datasets at 0.4 MeV/u respectively, indicates that the use of an ensemble due to a larger training dataset may yield more reliable XPCS outputs.

The measured experimental, Semi-empirical, and ML predicted Si induced XPCS in Bi were compared to the ECPSSR and available literature as shown in Figure 4.25 below. Although there are discrepancies between the measured experimental data with the dataset from literature, bias in the measurement was eroded by the fact that the semi-empirical Si XPCS were calculated from the carbon – fluorine dataset from iThemba LABS. The experimental silicon XPCS was on the other hand measured at the Ruđer Bošković Institute, using a different set of targets. This therefore eliminated any systematic errors in the measurements that would have pivoted the data to the same result. Furthermore, discrepancies between experimental datasets are well reported in the literature, which has been the basis for the need of a stronger

experimental pool from which universal empirical fits can be carried out. Thus, while a larger experimental dataset is needed for validation, the agreement between the experimental and ML predicted values with the semi-empirical cross sections further validates the *R*-ratio approach.
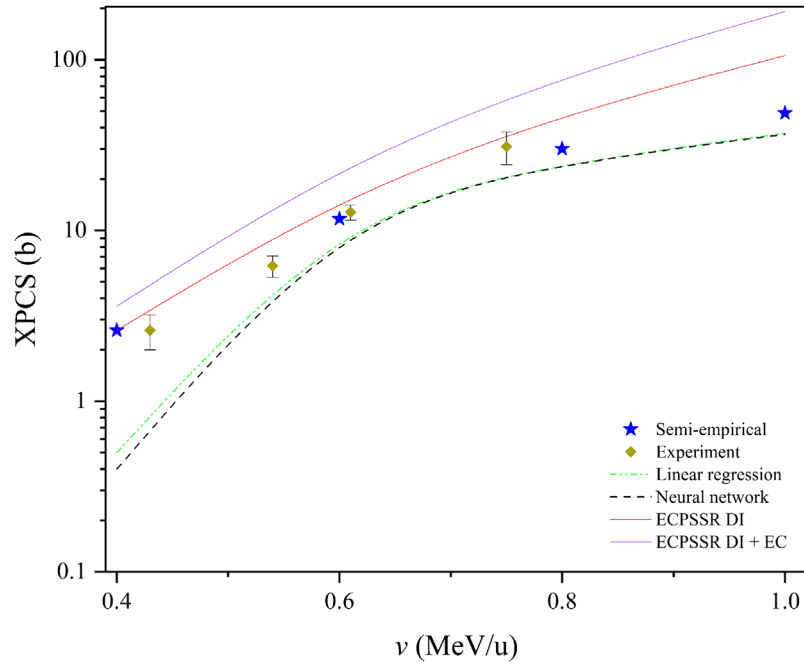
(a)
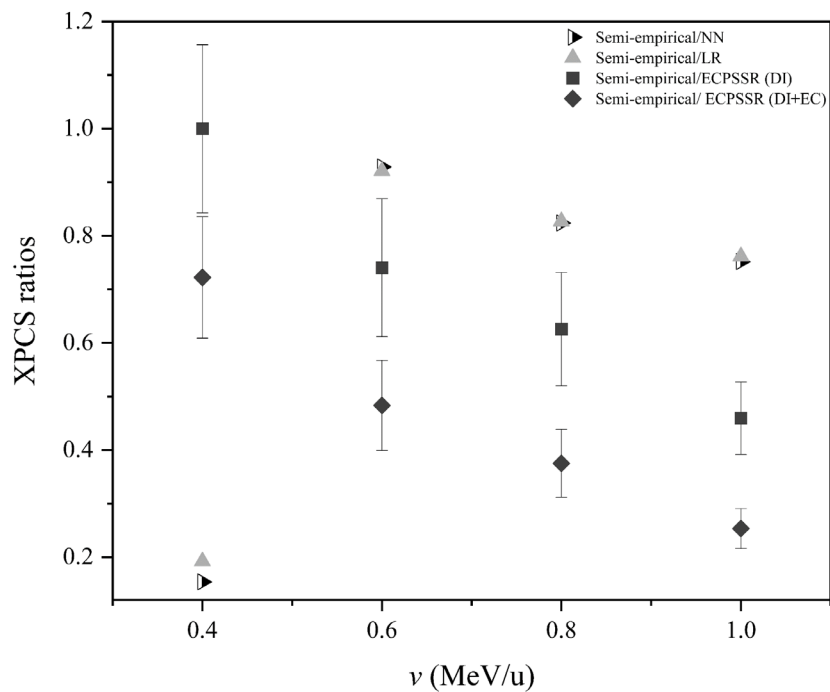
(b)

Figure 4.25. *Experimental, Semi-empirical, ML, and ECPSSR Si induced XPCS (a) and XPCS ratios (b) due to (0.4 – 1.0) MeV/u Si in Bi*

4.4. Multiple Ionisation

As already emphasised, the observed discrepancies between experiment and theory especially in the low energy range are attributed to Multiple Ionisation (MI) effects, based on collision symmetry. Work on the evaluation of MI effects has been substantial for K-shell excitation, allowing considerable estimations of the modification of K-shell atomic parameters. One example is the work of Tanis and co-workers [94], as partially covered in the second chapter. The more complex MI effects for L-subshell ionisation, due to introduced vacancies in the M- and N- subshells, can be seen through characteristic energy shifts and the asymmetric peak distortions/broadening, as with the K-shells. However, since more subshells are involved, X-ray peak energy shifts and broadening for L- and M-shells is much larger than that of the K-shells, causing greater degradation of spectral resolution, seen even with high resolution X-ray spectrometers.

4.4.1. High resolution X-ray spectrometry

An example of these distortions can be seen for proton, carbon and silicon L_α ionisation in Sn comparatively, evaluated using a downsized Wavelength Dispersive X-ray Spectrometer (WDS) from the Ruđer Bošković Institute [139]. The WDS is based on the principle of X-ray diffraction from a crystal, where the diffraction pattern is recorded by a Charge-Coupled Device (CCD) camera. The spectrometer is housed on a modular chamber consisting of a flat diffraction crystal and a thermoelectrically cooled 1024x1024 pixel array CCD camera from Greateyes. The CCD chip and backside was cooled at -70° to reduce dark current (*i.e.,* charge accumulation in the pixels due to thermal excitation, which may 'overlap' with actual signal electrons). A Ge(220) X-ray diffraction crystal (4.0 Å diffraction constant '2d') peeking at 3 mm from the crystal holder was used and translated along its linear axis relative to the CCD camera to select the Bragg angle (see Fig.4.27). The evaluation of the Sn $L_{\alpha 1}$ line (~3.4 keV) and L_β (~3.6 keV) X-ray lines were carried out by shifting the crystal position along its axis. Initial position estimations and the selection of the diffraction crystal were simulated using an in-house built Matlab based program, where both X-ray energy range and resolution were considered. The chamber also houses a Silicon Drift Detector (SDD) with a nominal resolution of 124 eV FWHM at 4.9 keV. Proton, carbon and silicon beams with different ion energies and currents up to 1 nA from the 6 MV Van de Graaff Tandem accelerator were transported downstream of the microbeam line, where the chamber was externally mounted. The ion beam spot sizes were ~ 10 x10 μm^2 focused using a set of quadruple triplet lenses, since broad beams

would potentially result in shifts in the X-ray diffraction patterns depending on the sample plane.

The target used was in the form of a ~10x10 mm² bulk ~100 μm thick Sn foil, selected to obtain a reasonable X-ray rate to compensate for the low current densities as well as low event collection efficiency intrinsic to the CCD [140]. The low collection efficiency is mainly due to a gradual signal readout (*i.e.,* charge shift register) and processing protocol typical for CCDs [140]. The ion beam was pulsed to avoid the pile up of new events over the CCD array during the serial charge readout protocol (*i.e.,* 2 s readout time). Thus, an electrostatic deflector was biased at at least 500 V and switched using the CCD camera high state Transistor-Transistor Logic (TTL) signals at 5 V to enable ion beam exposition times ranging between (5 – 10) s. A schematic of the spectrometer is shown in the Figure 4.26:
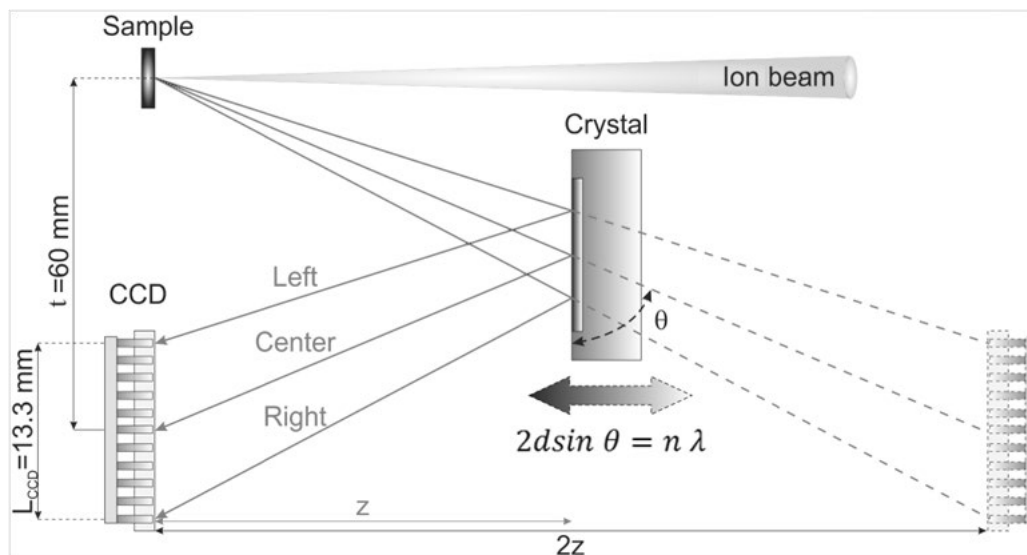
Figure 4.26. *Wavelength Dispersive high resolution X-ray spectrometer schematic. Figure reprinted from [139]*

The non-linear calibration of the obtained X-ray spectra from the diffraction pattern is based on a few parameters. These are namely the distance between the beam spot and the center of the CCD t, as well as the distance z between the diffraction crystal (grating constant d) and the CCD. The evaluated X-ray (of wavelength λ) energy window can be adjusted using the position of the diffraction crystal by using Bragg's law with the dimensions of the system:

$$\sin\theta = \frac{z/2}{\sqrt{z/2^2 + t/2^2}} = \frac{n.\lambda}{2d} \; ; \; \lambda = \frac{h.c}{E} \qquad 4.21$$

which simplifies to:

$$t^2 = (A^2 E^2 - 1).z^2; A = \frac{2d}{n.\lambda} \; ; \qquad 4.22$$

$$t = t_0 + (13.5 \times Ch)$$

where the channel width is 13.5 μm, corresponding to one pixel width.

Due to the small solid angle coverage of the CCD, only a part of the diffracted X-rays were detected, as shown below for the Sn L$\alpha_{1,2}$ line induced by 2 MeV protons.
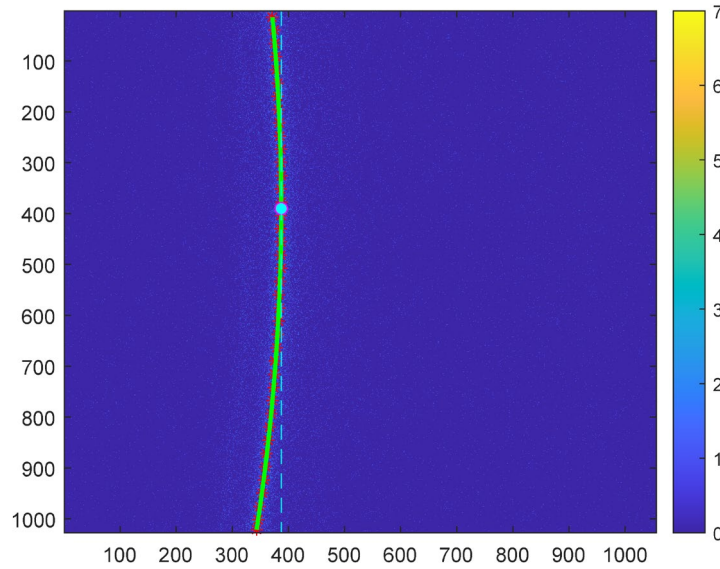

Figure 4.27. *Diffraction pattern of the Sn L$\alpha_{1,2}$ line*

The observed curvature is due to the finite crystal plane from which only some of the X-ray waves were diffracted, in addition to the solid angle of the CCD. To evaluate the distribution of the X-ray intensities scattered at different angles (*i.e.,* depending on their characteristic energies), a curvature correction was performed. This correction was done by carrying out several image slices, and thereafter fitting each slice distribution using a Gaussian function. The peaks of each of the Gauss fits was then used to center the distributions, where the difference between the peak positions of the minority was subtracted from the majority. These

were performed using the data analysis software XSPECTRA [139]. A visual aid of this correction is shown in Figure 4.28.
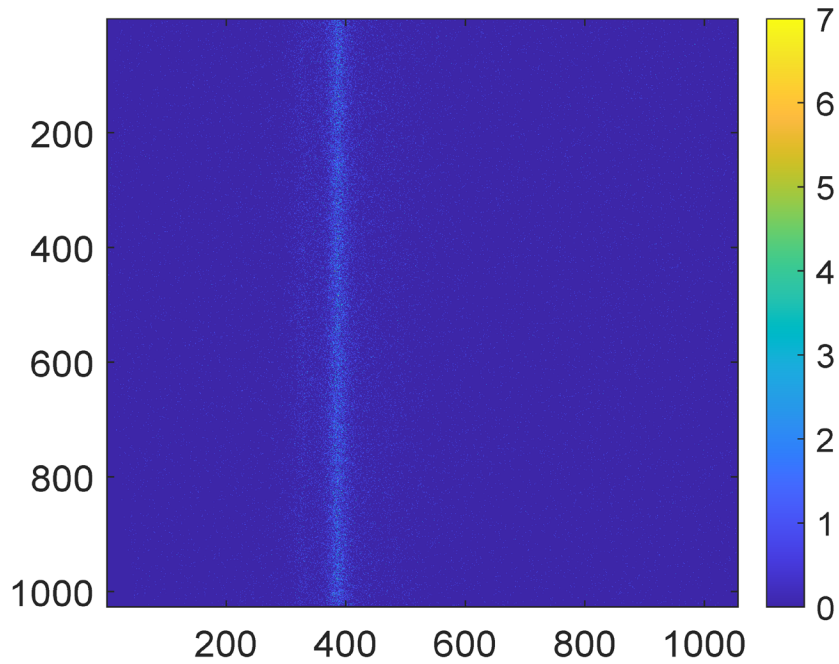

Figure 4.28. *Diffraction pattern curvature correction*

The intensities in the diffraction pattern were thereafter projected onto a channel axis, which was later energy calibrated as seen in the Sn $L_{\alpha1,2}$ X-ray spectra in Figure 4.29 below.
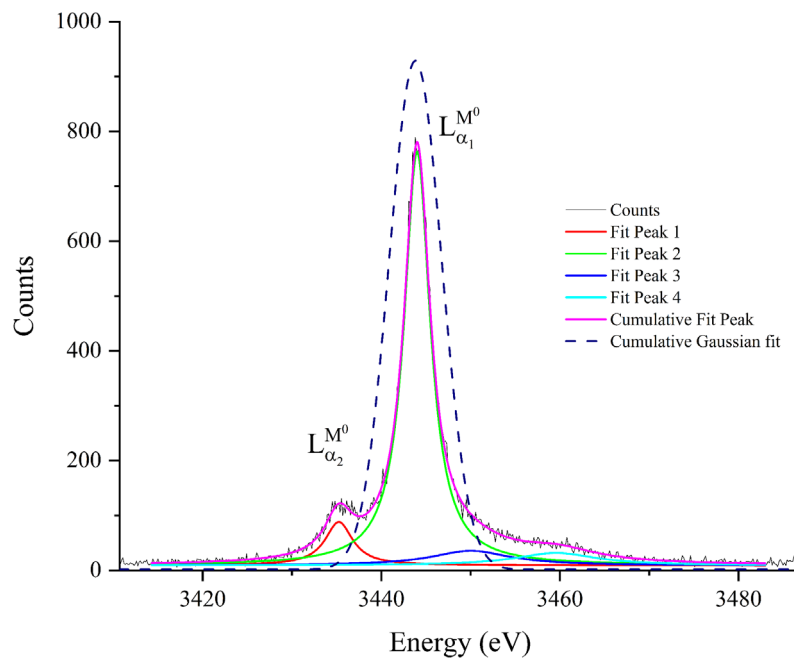

Figure 4.29. *2 MeV proton induced Sn $L_{\alpha1,2}$ X-ray spectra*

The cumulative Gaussian peak modelled the two diagram $L_{\alpha1,2}$ peak Lorentzian fits, where the peak centroid can be seen to correspond to that of the $L_{\alpha1}$ line. This shows that $L_{\alpha1,2}$ intensities detected with spectrometers with resolution above 100 eV correspond to the centroid of the largest intensity in the overall. The shallow high energy tail extending from the diagram $L_{\alpha1}$ line is due to very low Multiple Ionisation satellite intensities, seen in larger effect for heavy ions. These satellites are L3 – M5 transition X-rays formed in the presence of one or more vacancies in either the M- or N- shell. Energy calibration was carried out using $L_{\alpha1}$ and $L_{\alpha2}$ channel numbers and known characteristic X-ray energies. The calibration curve was fitted using a 5th order polynomial function, where calculated values slightly deviate from the linear regression, as shown in Figure 4.30.
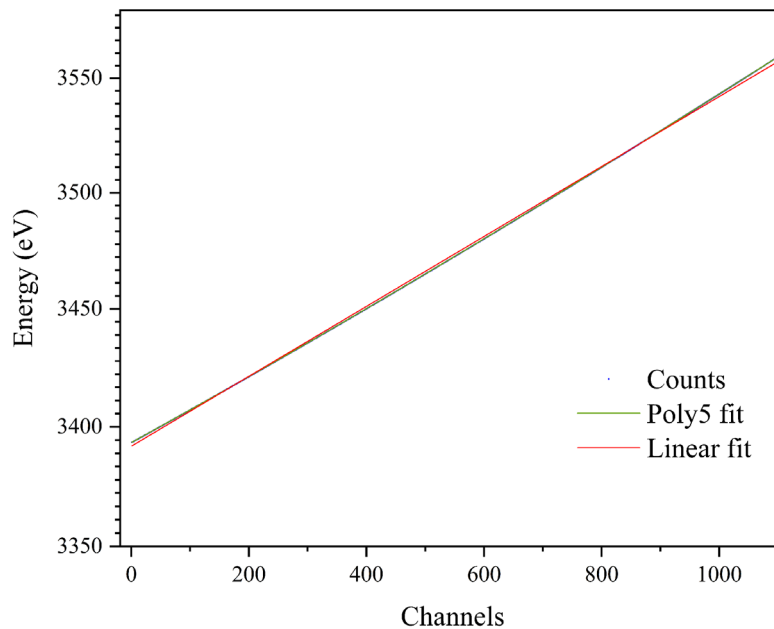
Figure 4.30. *Calibration curve calculated using the Sn $L_{\alpha1,2}$ line*

The WDS resolution was measured using the $L_{\alpha1}$ line at 3.74 eV FWHM at 3443 eV. L_{β} spectra due to proton impact were also collected, as shown in Figure 4.31.
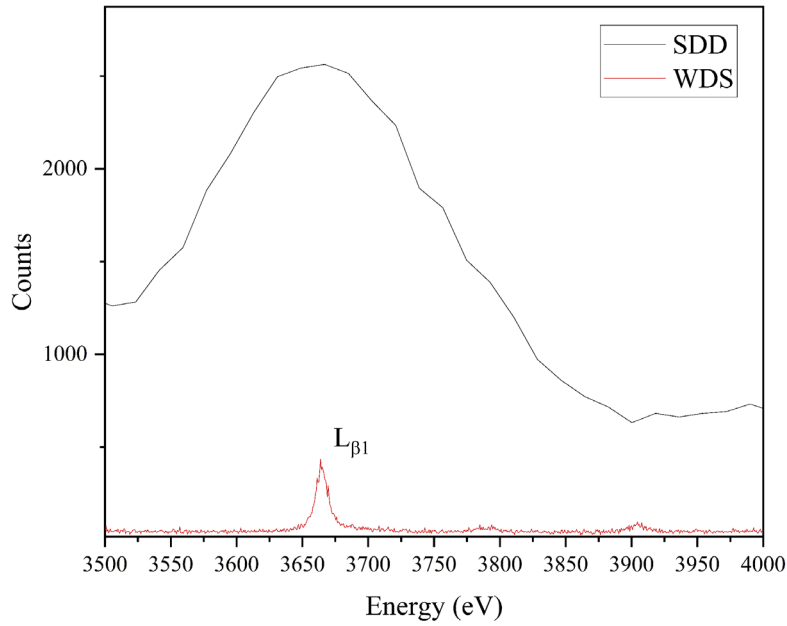
Figure 4.31. *Proton induced Sn Lβ₁ high resolution X-ray spectra, superimposed with peak from SDD detector*

In order to evaluate the effects of MI using the intensity distributions in the L-transition lines, which cannot be seen with low resolution Si(Li) or SDD detectors, carbon and silicon spectra were obtained using the same target. 8 MeV $^{28}Si^{4+}$ induced Sn Lα X-ray spectrum is shown in Figure 4.32 below.
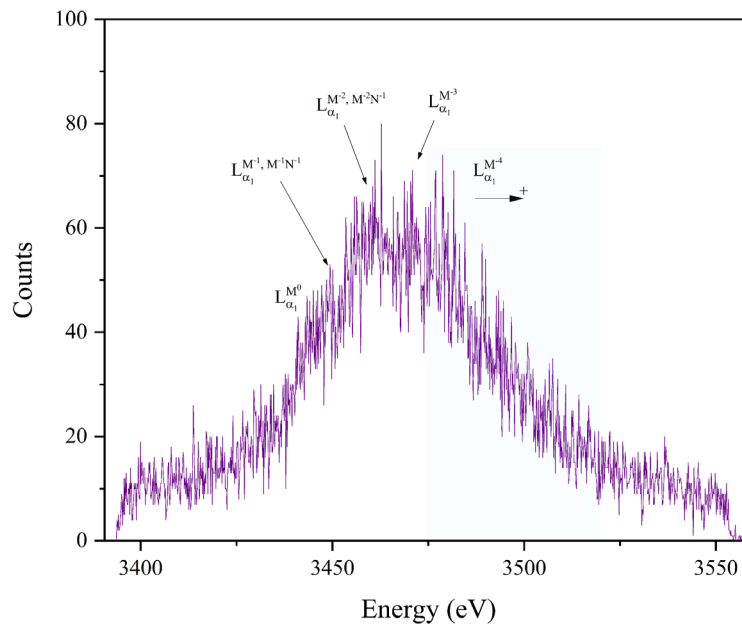
Figure 4.32. *Sn Lα line due to 8 MeV Si⁴⁺ impact*

Due to the low X-ray production cross section and CCD collection efficiency, only a few counts were collected, even with a long acquisition time. Furthermore, the limitation of the selection

magnet rigidity (*i.e.,* $ME/q^2 < 14$) on the beam line limited the silicon ion energy to 8 MeV. Nonetheless, even at these low energies, the satellite distribution can be seen far extending beyond the diagram line compared to the previously shown proton spectra. As it will later be shown, satellites in the Lβ line significantly overcame the detection resolution, prompting no further investigation. Therefore, to investigate changing satellite distributions in their effect on characteristic peak energy shifts due to heavy ion impact, only the Lα line was further investigated. Lα X-ray spectra from the same Sn target were acquired using $(8 - 15)$ MeV $^{12}C^{q+}$ (q = 3, 4, 5) ions, for higher XPCS compared to silicon. Ion beam currents were monitored throughout the measurements to mitigate the formation of clusters in the CCD array due to increased X-ray flux (due to higher currents). These variations would cause a rejection of the spectra by the data analysis algorithm, thus resulting in the loss of an image and thus yielding lower X-ray events. The carbon induced spectra and the best fit to all lines are therefore shown in the Figures 4.33 (a) – (d).
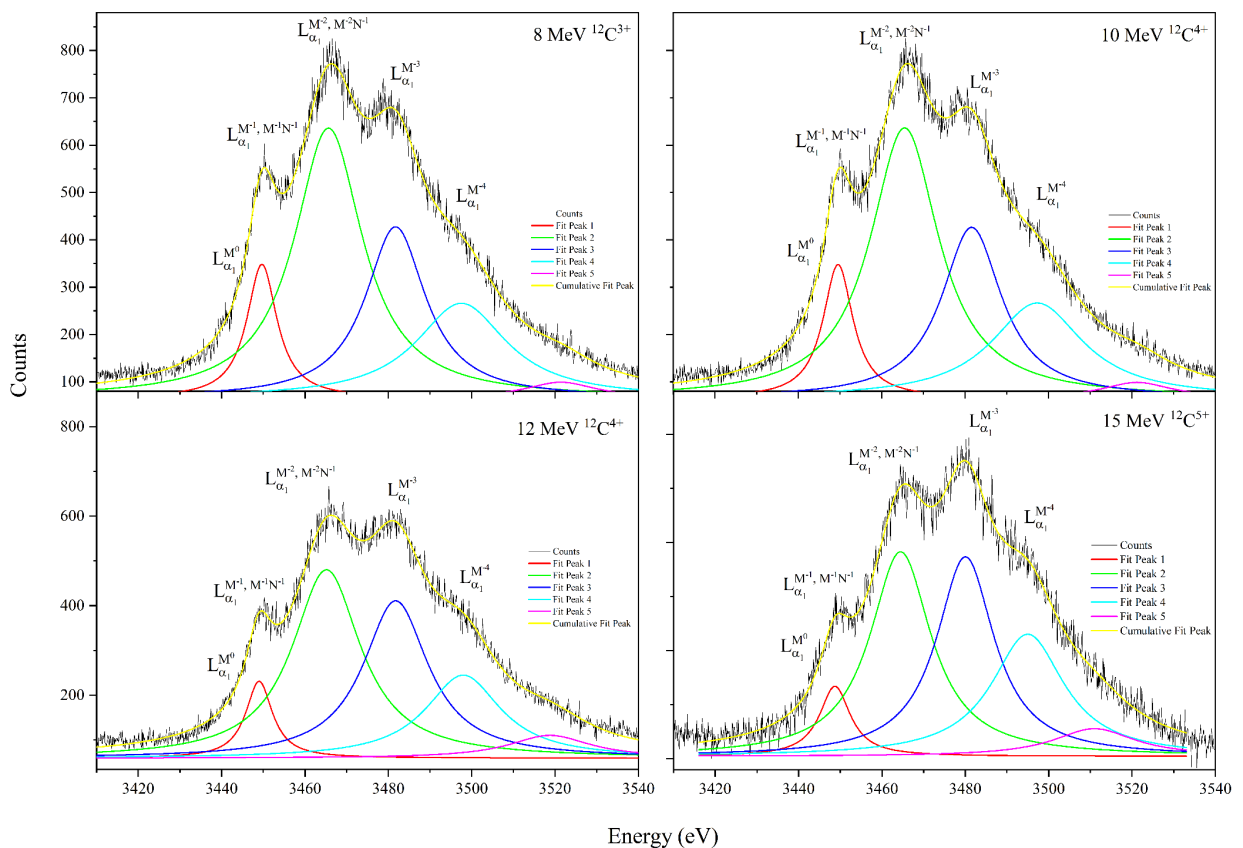

Figure 4.33. *Sn Lα line induced by (a) 8 MeV C^{3+}, (b) 10 MeV C^{4+}, (c) 12 MeV C^{4+} and (d) 15 MeV C^{5+}*

The diagram line is represented by the term $L_{\alpha_1}^{M^0}$, where the superscript in this case signifies the non-existence of vacancies in the M-subshell. The MI satellites are a result of several M- and N- subshell vacancies in the L_α transition, shown in the corresponding superscript. Due to the very close proximity of some satellite radiative widths, not all satellite lines could be separated from the total distribution. This was the case with the diagram line and the first satellite peak, seen across all carbon ion energies in Figure 4.34. Additionally, the $L_{\alpha_1}^{M^{-1}}$, $L_{\alpha_1}^{M^{-1}N^{-1}}$, $L_{\alpha_1}^{M^{-2}}$ and $L_{\alpha_1}^{M^{-2}N^{-1}}$ MI satellites [141] were respectively inseparable, as seen in Figure 4.34. Even with the convoluted distributions, satellite intensities peaking from the total yield were seen to increase with energy, proportional to the number of MI vacancies in the M- and N- shells. This was due to changing binding energies of the electron deficient higher subshells, thus resulting in shifting characteristic X-ray energies. The average characteristic X-ray energies correspond to the centroid of the cumulative peak, as previously shown with the proton spectra (Fig.4.29). The satellite intensity distribution can be seen to shift to higher energies with increasing ion beam energy. This is because for non-relativistic energies, as is the case with the studied incident ion energy range, increasing ion energy also increases the ionisation cross section for the M- and N- shells, since the subshell electron binding energies are well below that of the incident ion. This is in addition to higher electron capture cross sections, due to larger perturbation of the target electron density by both the projectile nuclear and especially electronic field. The influence of significant projectile screening has already been partially shown by the highly perturbed projectile characteristic M-shell X-ray intensity ratios of iodine colliding in Sn (Fig.4.14). As seen in the high resolution spectra, radiative Coster-Kronig and super Coster-Kronig transitions due to collisions resulting in more than four vacancies beyond the L-shell are represented by the high energy tail extending the partially resolved $L_{\alpha_1}^{M^{-4}}$ peak.

The diagram $L_{\alpha_1}^{M^0}$ contribution, convoluted with the first satellite peak, demonstrates the shifting peak cumulative centroid even at lower ion energies, due to changes in the L3 – M5 electron decay channels. The presence of subshell vacancies in either the M- or N- subshells for the L-shell ionisation not only change the binding energy due to reducing electron densities, but essentially results in the electron decay for the diagram line becoming energetically forbidden. Thus, for the diagram transition, the reduced M5 binding energy results in the formation of new radiative decay channels, further shifting the $L\alpha_1$ line proportional to the overall ionisation of the M-shell.

Diagram and satellite line intensities were deconvoluted and evaluated using Lorentzian functions, where the combined peaks can be seen to resemble a Voigtian function. The energy corresponding to the overall peak centroid was compared to the peak energy obtained from the SDD. This was done to verify the calibration of the spectra, since changing beam energies may shift the beam spot region (*i.e.,* sample surface topographical effects) and therefore slightly alter the intensity position on the image from the CCD. Additionally, the proton $L_{\alpha 1}$ line was compared to that of the different carbon energies in the WDS, showing the overall energy shifts of the peak due to carbon (Fig.4.34).
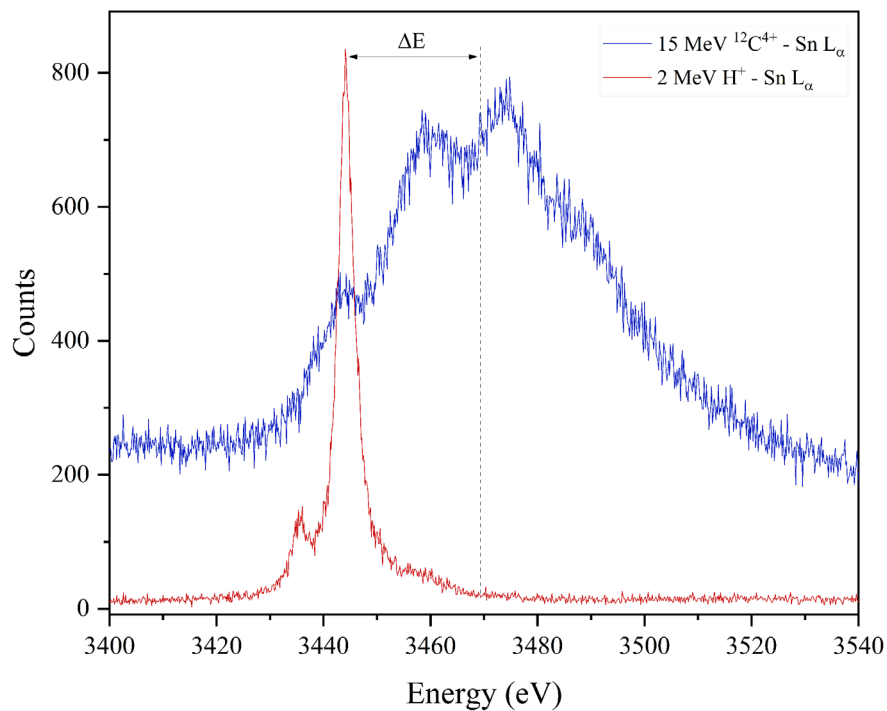
Figure 4.34. *High resolution spectra of the Sn La X-ray line obtained with 2 MeV protons (red) and 15 MeV carbon ions (blue)*

Multiple Ionisation effects were therefore observed by evaluating the changing intensities of the satellite distribution, particularly since the diagram line becomes convoluted in the first satellite peak. Hyper-satellite formation, resulting from more than one ionisation in the L-subshell per collision, was not evaluated as these satellite peaks formed outside the analytical energy window. Furthermore, the intensity of the hyper-satellite peaks was expected to be very low, since the ionisation probability was highest for the loosely bound M-subshell electrons instead.

Relative distributions for carbon induced L_α X-rays were thus used to determine the average number of vacancies for each carbon energy, and thereafter correlated to the observed peak centroid energy shift.
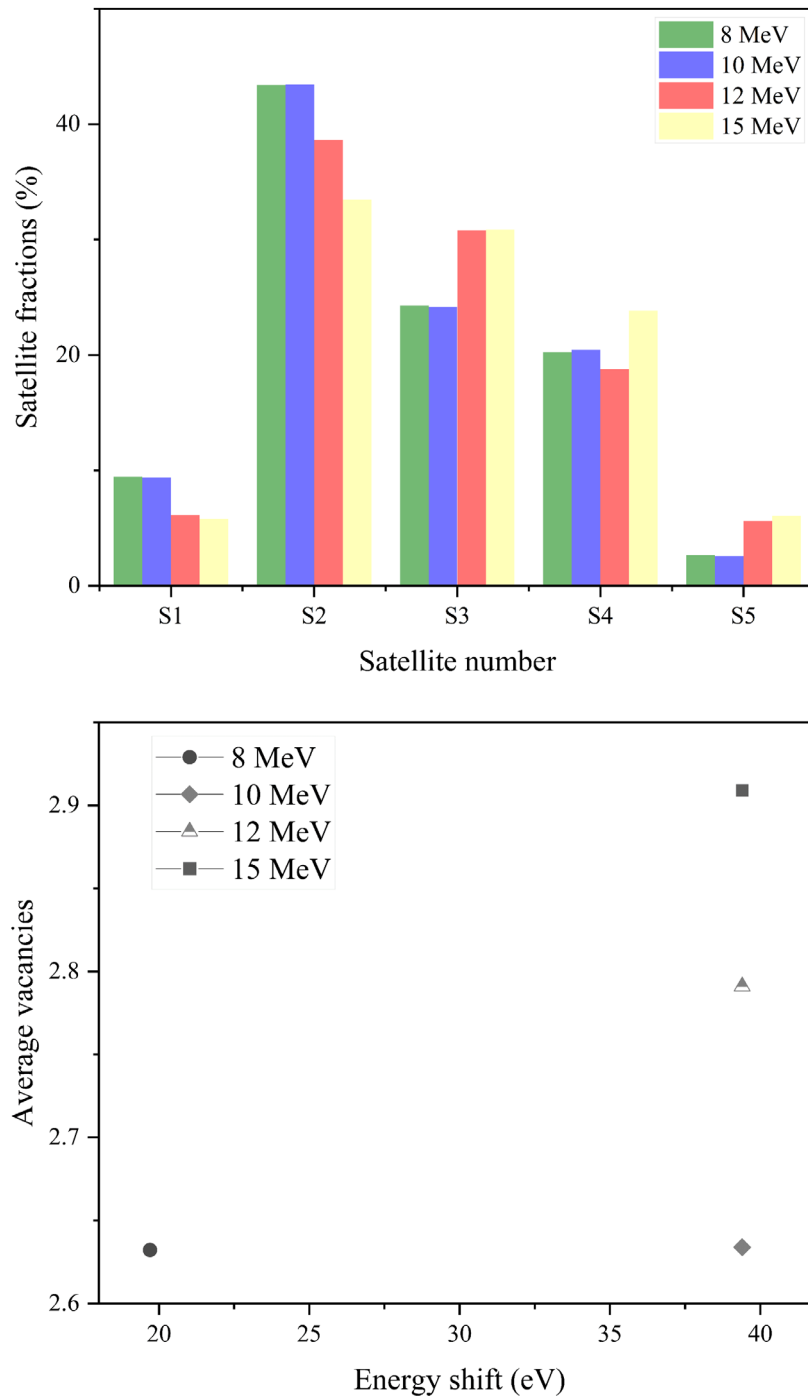
Figure 4.35. *$L\alpha$ total peak transition(s) and distributions (top) and number of vacancies vs ion energy shift (bottom)*

The measured energy shift by 10 MeV carbon ions measured with an SDD detector corresponded to the same average energy shift for 12 MeV and 15 MeV carbon. This was because of the minimal shift in the average number of vacancies, as seen in Figure 4.35, thus resulting in no centroid shift.

Although it would be ideal to evaluate MI effects due to varying ion masses using relative satellite intensity distributions, for either the L- or M- lines, energy shifts from SDD detectors were instead used since the WDS energy range was limited. An ideal apparatus would be a high efficiency broadband high-resolution spectrometer, moreover for the evaluation of L-subshell ionisations in heavy elements such as Au or Bi, where ionisation cross sections are low. Nonetheless, due to experimental limitations, only the C ionisations in Sn were observed, mainly as a means to elaborate on the shifting and broadening of X-ray peaks. Additionally, for heavier ions, the large number of MI satellites would result in the deterioration of the resolution, similar to that seen when comparing the proton and carbon spectra. The satellite distribution for heavier incident ions which result in a higher average number of vacancies would extent beyond the analytical window, a major limitation for Wavelength Dispersive Spectrometers. Even with a broadband high resolution PIXE spectrometer, such as Transition Edge Sensor (TES) with 1 eV FWHM resolution at 2 keV, the large satellite volume across the transition energy band would be difficult to resolve with certainty. An example of the broad energy line spread where multiple satellites are present is shown for the Sn L_β line due to proton and carbon ionisations in Figure 4.36.
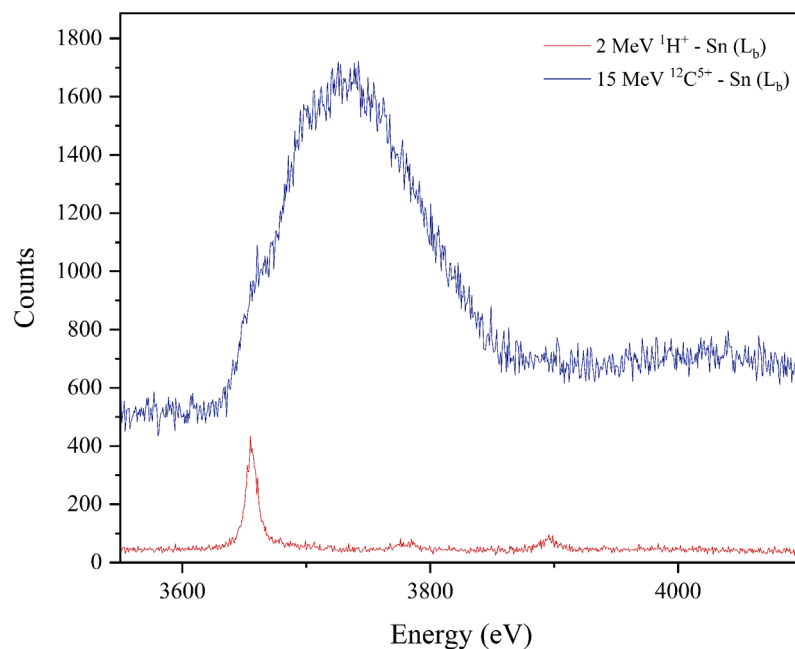
Figure 4.36. *Sn L_β line due to 2 MeV proton and 15 MeV $^{12}C^{5+}$ impact*

4.4.2. Broad X-ray energy shifts

Cumulative Gaussian peak centroid shifts were therefore used for other ion-atom combinations, as illustrated for Cu and I ions compared to protons in Figure 4.37. The peak centroids are designated the label L$_\alpha$, as it cannot be asserted that the centroid represents a 'shifted' diagram line (*i.e.,* L$_{\alpha 1,2}$).
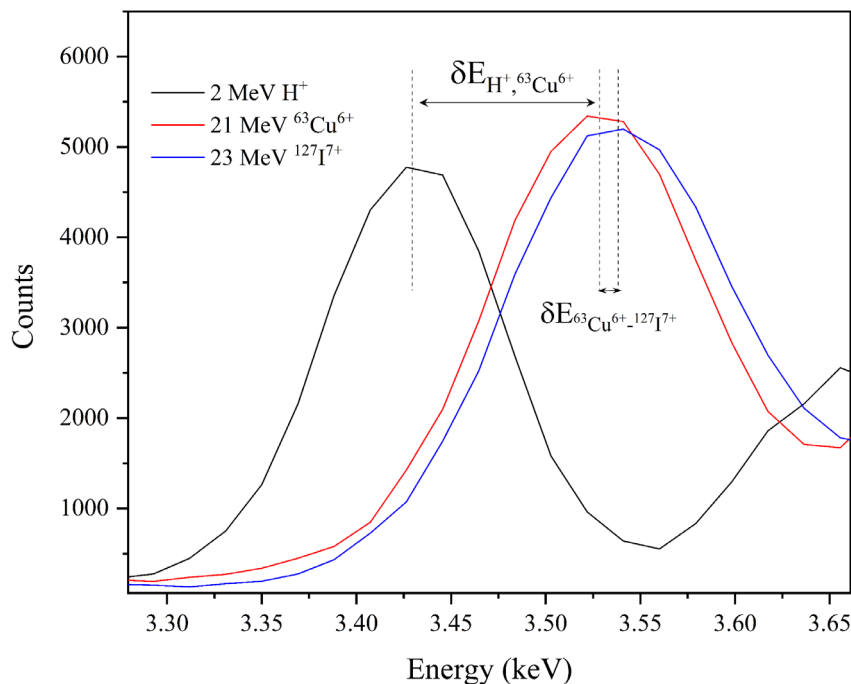
Figure 4.37. *X-ray energy shifts from protonic ionisations, due to Multiple Ionisation of Sn induced by Cu and I*

As shown with the high-resolution spectra, the shifted X-ray energies can be used to deduce the average number of vacancies in the M- and N- subshells. Since the subshell binding energies are known, energy shifts per vacancy produced could be established. The satellite energy for a Coster-Kronig transition from an electron deficient S- shell (S = M or N) can be calculated by incorporating the screening effect in the frame of the electron binding energy $B_s(Z)$, by using the so-called 'Z + 1' method [83], [142]. As mentioned in Chapter 2, the Z+1 represents the modification of the screening potential for non-binary collisions. The satellite energy is thus represented by:

$$\epsilon_{satellite}^{i-jk}(s) = B_i(Z) - B_j(Z) - B_k(Z+1) + B_s(Z+1)$$

$$- B_s(Z+2)$$

4.23

Where the change/shift of the Coster-Kronig electron energy per vacancy in the M- or N- shell is:

$$\Delta B_s = B_s(Z+1) - B_s(Z+2) \qquad\qquad 4.24$$

Giving the expressions:

$$\epsilon_{satellite}^{i-jk}(m,n) = \epsilon_{diagram}^{i-jk} + m\Delta B_m + n\Delta B_n; \qquad\qquad 4.25$$

$$\epsilon_{diagram}^{i-jk} = B_i(Z) - B_j(Z) - B_k(Z+1)$$

Using arbitrary m and n vacancy numbers, X-ray energy shifts per vacancy for each analysed element were determined.

The energy shift per vacancy for Sn was calculated at ~21 eV, which is slightly higher than the energy shift (~15 eV) measured using the high-resolution spectrometer. The difference between the measured and calculated energy shifts where due to changes in the atomic physical states, which were not estimated in the calculation. The calculated energy shifts per vacancy where nonetheless used to estimate the average number of MI vacancies from the energy at the shifted cumulative peak centroid. A distribution of the average number of vacancies for different ion energies is shown for Cu and I in Au in the Figure below.
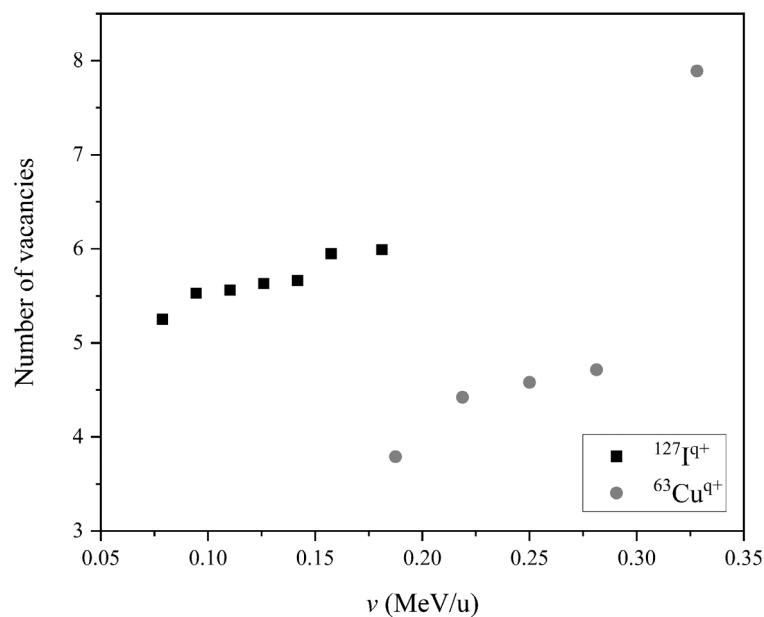
Figure 4.38. *Estimated Cu and I induced average number of vacancies for the M-subshell ionisation in Au*

As shown by the carbon high resolution data, satellite formation manifests even at low energies for heavy ions. Indeed, the average number of vacancies increase with increasing ion mass, and more so for near symmetric collisions, as seen with the I – Sn collision.
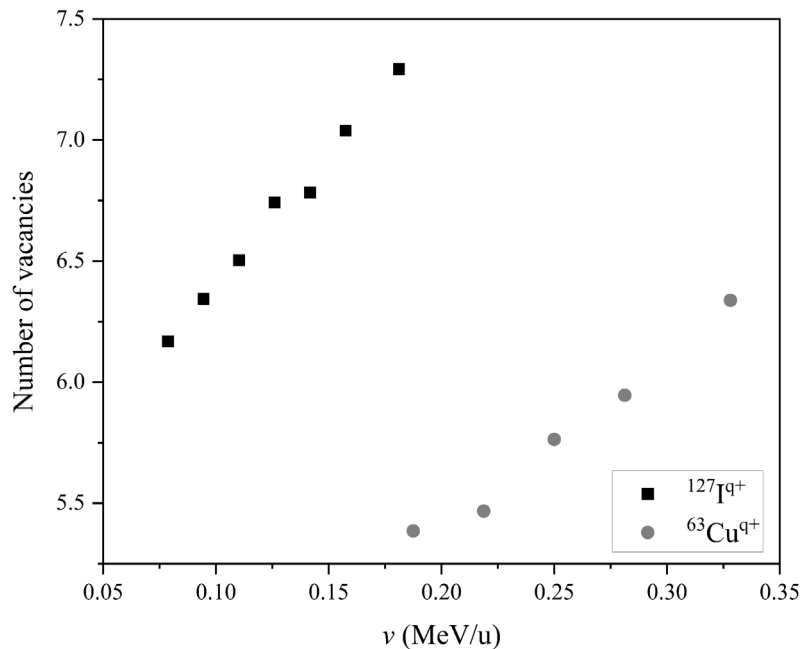
Figure 4.39. *Estimated Cu and I induced average number of vacancies for the Sn $L_{\alpha1,2}$ transition*

Although the increasing number of vacancies is proportional to increasing peak widths, the evaluation of the widths was limited by the low energy resolution of the detector. While small peak width differences compared to the proton peak could be detected in some cases, the small deviations in large satellite distributions would lead to large uncertainties in the estimation of the average number of vacancies. The use of energy shifts was therefore seen as a reliable approach, retained for all ion-atom combinations.

Vacancy estimations are especially important at lower ion energies, where the slow heavy ion can be characterised as having a long dwell time within the target nuclear field (depending on its impact parameter). Along with lower ion charge states, a longer dwell time significantly extends ionisation beyond single-hole DI, and cannot simply be estimated using perturbation theory. On the other hand, depending on the mass of the ion, collisions may be viewed as constituting a united 'quasi-molecule' where the electron wavefunctions of both the projectile and target overlap. Although, the United Atom (UA) approach has been adopted for a number of theoretical models, most prominently being the ECPSSR, ECUSAR and SCA. The limitation of hydrogenic wavefunctions in these theories however results in inaccurate binding energy

corrections, making the UA limit ineffective for slow and especially highly symmetric heavy ion-atom collisions. The limitations of theory also extend to intrashell coupling effects which promote the formation of new radiative decay channels as a prominent feature of MI [83], [84]. While the incorporation of coupling effects has shown improvement in the theoretical predictions of some L-subshell transitions, as demonstrated by Pajek and co-workers who used a Coupled Shell Model (CSM), its improved performance compared to UA corrections still needs to demonstrate universality [83]. Even so, as these limitations remain pertinent, experimental data, moreover the determination of the average number of MI vacancies remains important in the improvement of theoretical approximations. These also include approximations of other atomic parameters, such as X-ray fluorescence yields, Auger and emission rates, as well as transition probabilities, extending beyond the scope of this reporting.

Therefore, characteristic M- and L- subshell X-ray energy shifts were evaluated for Sn, W, Au and Bi where applicable. 2 MeV proton spectra were collected preceding each measurement, as reference to the heavy ion induced spectra. The measured energy shifts are tabulated in *Appendix A*, and are visually illustrated in the Figure 4.40.
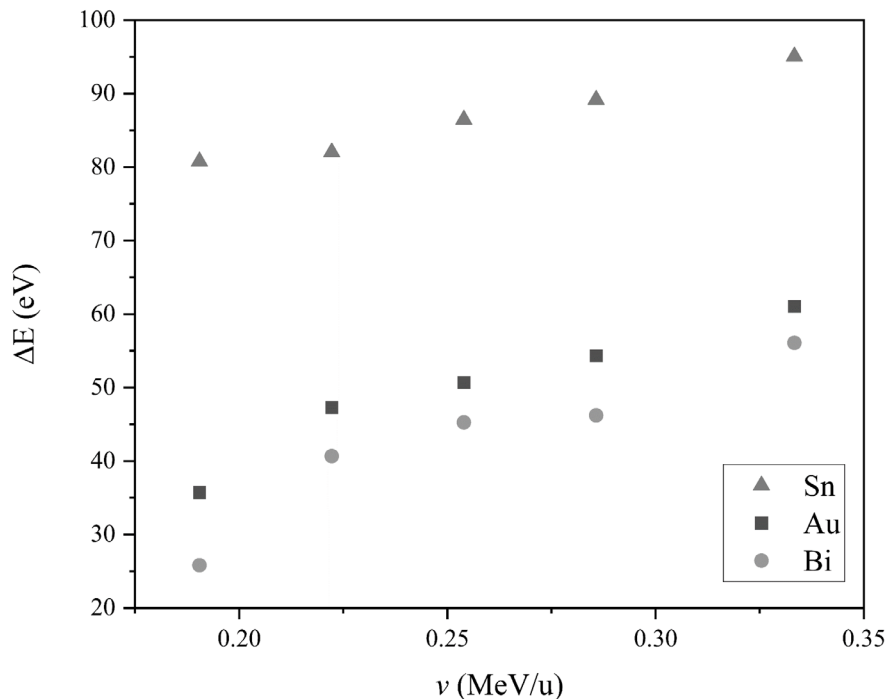

Figure 4.40. *Cu induced Lα energy shifts in Sn, Au and Bi*

The energy shifts can be seen to uniformly increase with ion energy, with varying magnitudes based on the ion and target masses (as this pertains to collision symmetry).

M$_\alpha$ X-ray energy shifts were also evaluated, however with a view to qualitatively observe the influence of MI effects in the N- subshells. The quantitative evaluation of multiple ionisation effects for satellite M-lines was limited by the large number of vacancies in the L-, M- and N- series, the complex nature of which would result in significant uncertainties. This is moreover the case, as the presence of M- and N- shell MI vacancies had already been established in the analysis of L-shell ionisation, pointing to both satellite and hyper-satellite formation. These are characterised by complex Coster-Kronig electron transitions, vacancy production, transfer and sharing between the target and projectile, which result in physical changes in both projectile and target electronic systems. As a result, the evaluation of MI effects in the M-shell would far extend the approach taken with the evaluation of L-shell satellites.

Since X-ray yields were obtained from both the L- and M- subshell, all of which exhibited energy-shifted characteristic peaks, it cannot be assumed that energy shifts for the M-shell are only due to ionisations in the N- and/or O- shells (where applicable). This is drawn from the shifted L-shell peak, which signifies the existence of vacancies in the M-shell. The characteristic energy shift of the M-shell is therefore a result of altered binding energies in the M-shell itself, as well as the higher even more loosely bound N- and O- subshells. Such is premised on high ionisation cross sections, where M-shell peaks are significantly more intense than those of the L-subshell. While the average number of subshell vacancies in the M-shells can be estimated for L-shell ionisation, the estimation of N- and O- vacancies for the M-shell itself becomes unreliable. This is again due to the existence of vacancies in the M-shell itself, where observed energy shifts are due to electron deficiencies in the M-, N- as well as the O- subshell. The evaluation of MI effects in the M-shell was for this reason constricted to energy shifts, seen in varying degrees based on the collision symmetry. An illustration of X-ray energy shifts due to ^{127}I^{q+} in ^{209}Bi is shown in Figure 4.41.
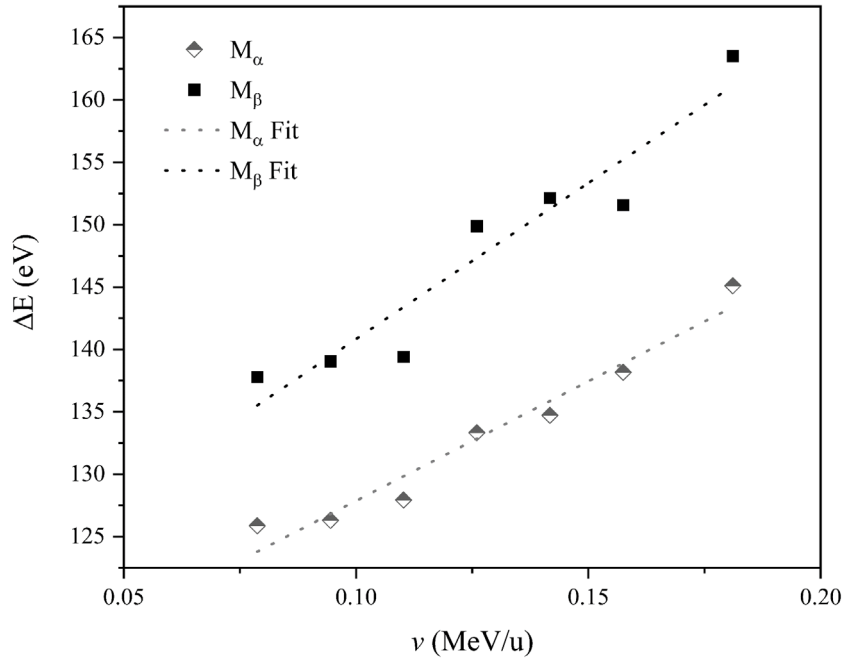
Figure 4.41. *M-shell energy shifts in Bi due to I*

Figure 4.41 shows larger M_β energy shifts compared to the M_α shifts. This is because the presence of vacancies in the N- shell result in more augmented binding energies for the N_6 and conversely the M_4 subshell, where M-shell vacancies are present. On the other hand, the high ionisation probability for the loosely bound N_7 and M_5 subshells result in shallower decay channels, thus a smaller average number of vacancies. Similarly, small variations in the energy shifts were observed, where a sharper increase in the M_β shifts can be seen compared to those of the M_α transition. The comparative energy shifts can be better viewed using energy shift ratios, as in Figure 4.42, where increasing ratios are due to the M_β shifts.
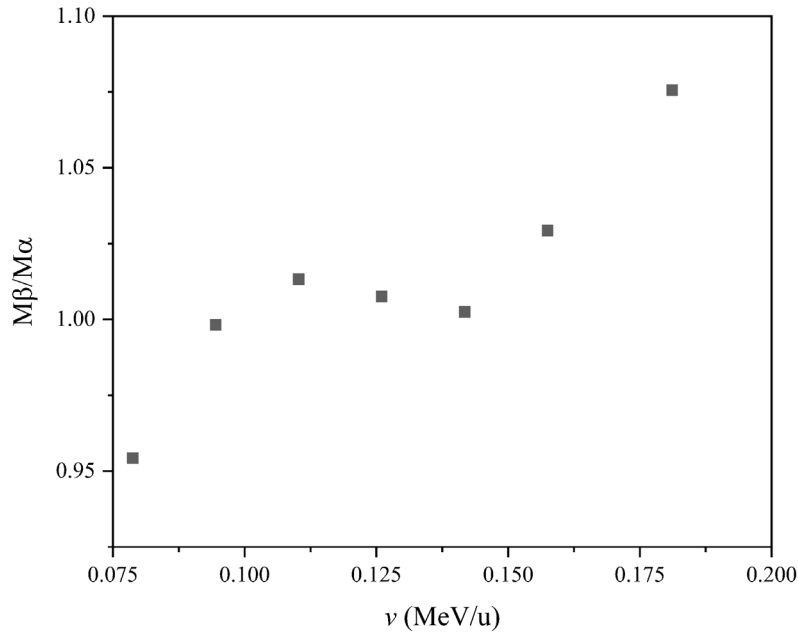
Figure 4.42. *M_β/M_α energy shift ratios in Au due to $^{127}I^{q+}$*

The ratios of the X-ray energy shifts gradually increase towards unity, and thereafter increase even further. It is assumed that this is due to intrashell coupling effects in the N-shell, where the N7 and N6 subshells are spatially and energetically close to each other. The non-uniform distribution of the shift ratios with increasing subshell vacancies shows a variation of the creation and transfer processes resulting in variating radiative widths. Changing vacancy transfer processes are further enhanced by changing projectile electron densities, shifting the symmetry of the molecular orbital. It therefore seems that in some cases the satellite decay channels are almost equal, owing to modified vacancy distributions due to the strongly coupled N6 – N7 subshells post ionisation. This is seen by the approach of the energy shift ratios towards unity, as shown in Figure 4.42.

In a similar way, reducing L_α/L_β intensity ratios signify an increasing number of vacancies in the M-subshell, as these show increasingly closing decay channels for either the $L_{\alpha1,2}$ or $L_{\beta1,4,5}$ transition. Indeed, while even single M-shell vacancies for L-shell ionisations would imply the formation of some satellite decay channels; sufficient ionisations in the M-shell can modify the shake-off process in favour of the $M_{4,3,2} - L_{2,1}$ and $N_5 - L_3$ Coster-Kronig transitions for the L_β intensities. An illustration of this is shown in Figure 4.43 for L_α/L_β intensity ratios for $^{28}Si^{q+}$ in Au.
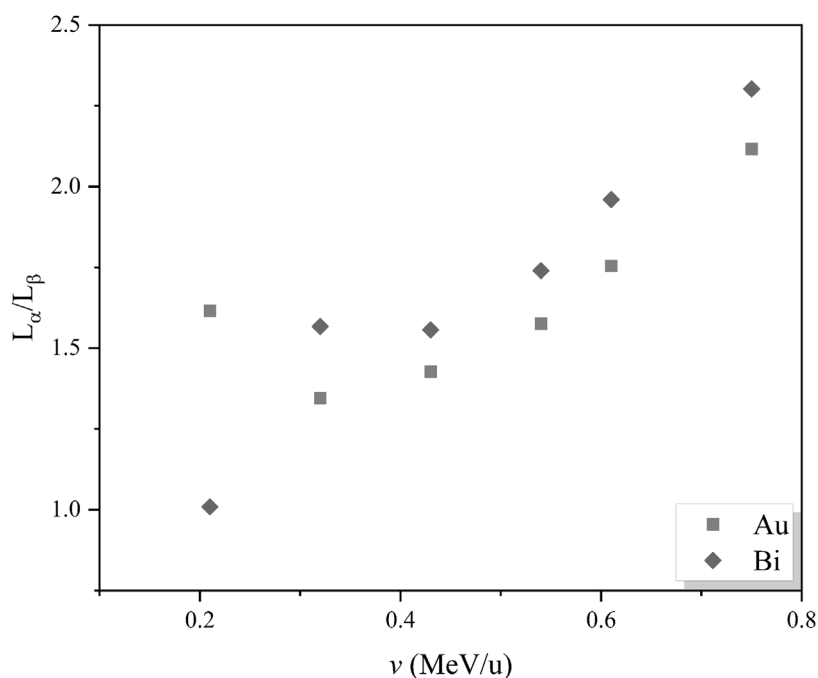
Figure 4.43. *$^{28}Si^{q+}$ induced L_α/L_β X-ray intensity ratios in Au and Bi*

The intensity ratios can be seen to increase with ion energy, proportional to the energy shifts. Increasing ratios signify a reduction in the transition probability for the M5 – L3 channel, owing to an increasing number of average vacancies in the M- subshells. The difference between the intensity ratios for Si in Au compared to Si in Bi is low, due to the changing but similar collision symmetries. The intensity ratios are seen to reach unity for Bi in the low energy range, indicating a high effect of the M-shell coupled shell states. On the other hand, it was assumed that the Au metastable state, in which the M4 and M5 coupled channels are equal, would appear at lower energies, as seen for M-shell ionisations shown later in Figure 4.46.

Larger differences in the intensity ratios were otherwise seen where the collision is much more symmetric. Such a difference was evaluated for $^{63}Cu^{q+}$ impact in Au (Figure 4.44), with a low nucleon energy range (0.18 – 0.33) MeV/u.
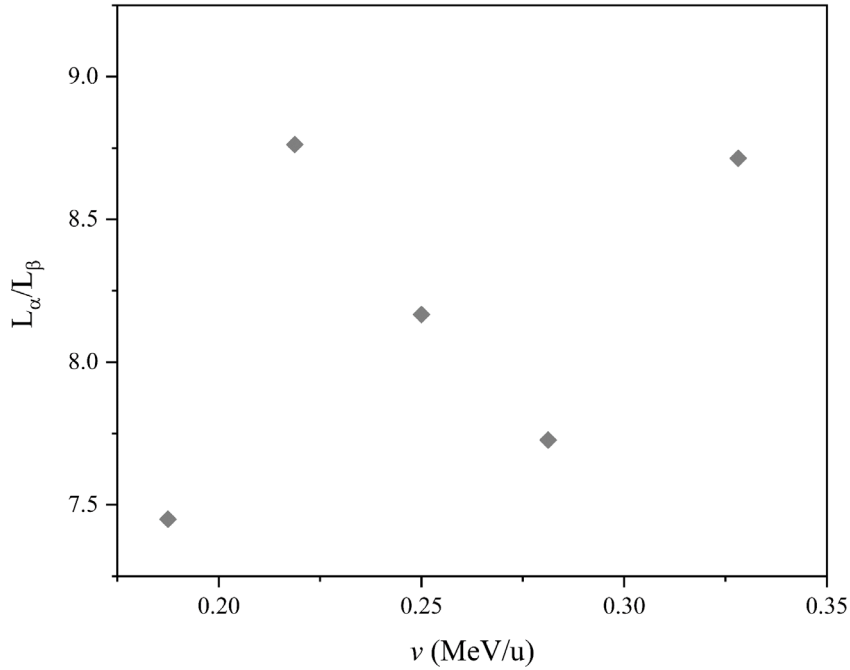
Figure 4.44. 0.18 MeV/u – 0.33 MeV/u $^{63}Cu^{q+}$ *in Au L_α/L_β intensity ratios*

Similar to the uneven distribution of energy shifts already discussed, the fluctuating intensity ratios can be seen as a result of changing vacancy distributions and splits within the M- and N-subshells. This is in addition to the influence of the projectile electron field. As seen in the high-resolution spectra, the concentration of the average number of vacancies in either the M- and/or N- shell is dependent on ion energy. Since this anomalous trend is not observed for smaller degrees of symmetry, especially when the projectiles are all moving slowly, it could be assumed that different screening potentials lead to multiple ionisations on more than just the two target shells. As the projectile and target masses are close, changing vacancy transfer and sharing probabilities may be highly influenced by intrashell coupling, as well as that of the coinciding projectile and target subshell electron densities. This ought to be prevalent especially where the subshell binding energies and electron velocities of the projectile and target are close. Subsequent changes in the Coster-Kronig transition probabilities between both the projectile and target may therefore create varying states within which some radiative transitions become forbidden, seen as reducing L_α intensities in favour of the L_β lines. This effect may also be aided by varying electron capture probabilities by the projectile, depending on its screening. The changing ratios can therefore be seen as a consequence of shifting decay channels due to changing quasi-molecular states (or symmetry). Unfortunately, due to experimental limitations, the benefit of observing the ratios up to 1 MeV/u in order to evaluate

uniformity could not be realised. Nonetheless, the current dataset clearly points to the significance of MI effects in the slow velocity range, particularly as it pertains to the review of ionisation theories in the heavy ion impact frame. A similar trend was seen for Bi due to Cu impact, where shifting decay states are seen to alter the L_α/L_β ratios with increasing ion energies (Figure 4.45).
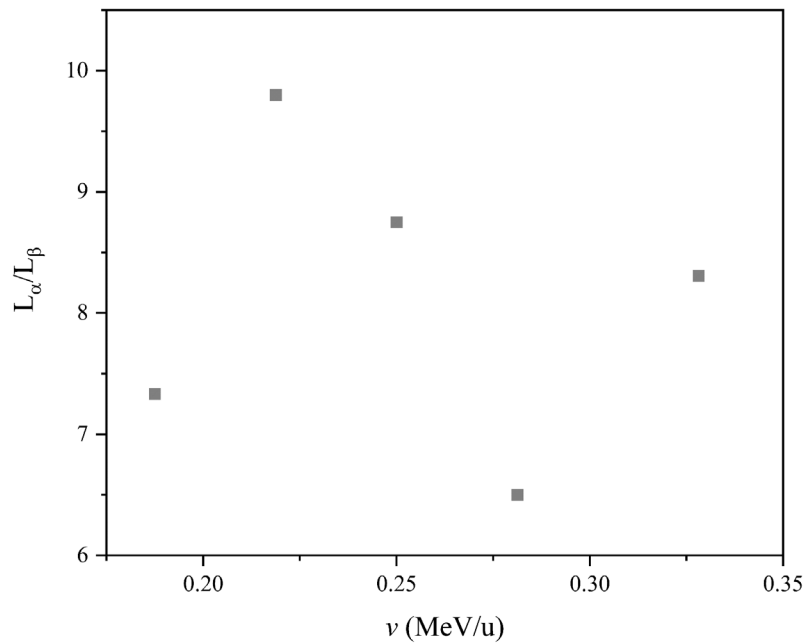
Figure 4.45. *Bi L_α/L_β intensity ratios induced by Cu ions*

The L_α/L_β ratios can also be correlated to M_α and M_β X-ray production cross sections in Au and Bi within the same energy range induced by Cu and I ions as shown in Figure 4.46 below.
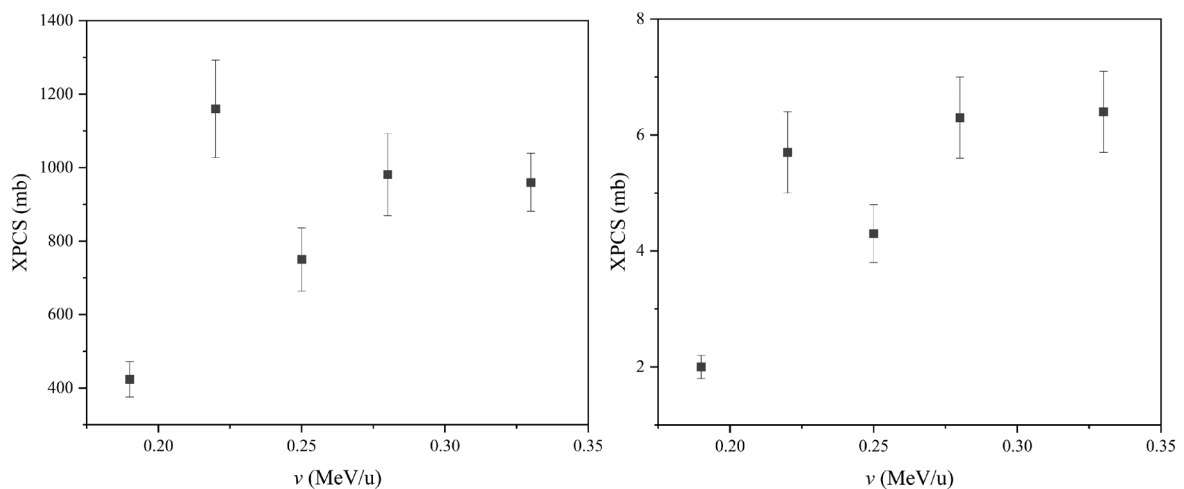
Figure 4.46. *M_{Total} (left) and $L_{\alpha1,2}$ (right) XPCS in Au due to $^{63}Cu^{q+}$*

99

Changes in the transition probabilities can be seen in the non-uniformity of the exponential rise of the cross section trends due to Cu. In the case of I, for which the collision is much more symmetric, sharp cross section peaks can be seen within the narrow velocity range. These shifting MI effects are also observed in the ionisation of W and Au induced by Ag ions, where a slight increase in the XPCS is seen at 0.22 MeV/u for the more symmetric Ag – W compared to the Ag – Au combination.
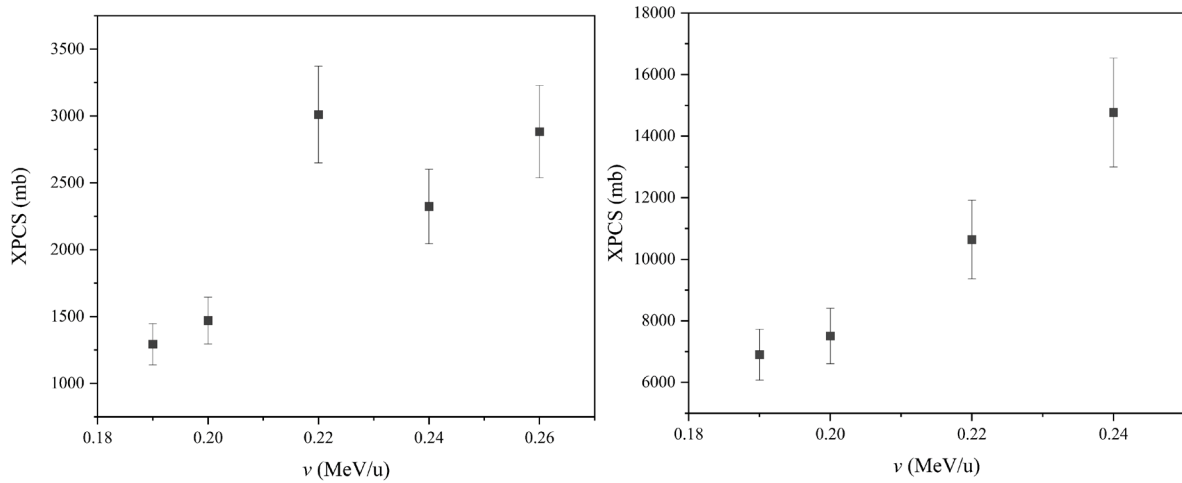
Figure 4.47. *Ag induced L_α + L_β XPCS in W (left) and Au (right)*

Gross underestimations by the ECPSSR theory in its comparison to experiment for slow and near symmetric collisions were as expected, but are nonetheless shown using cross section ratios in Figure 4.48.
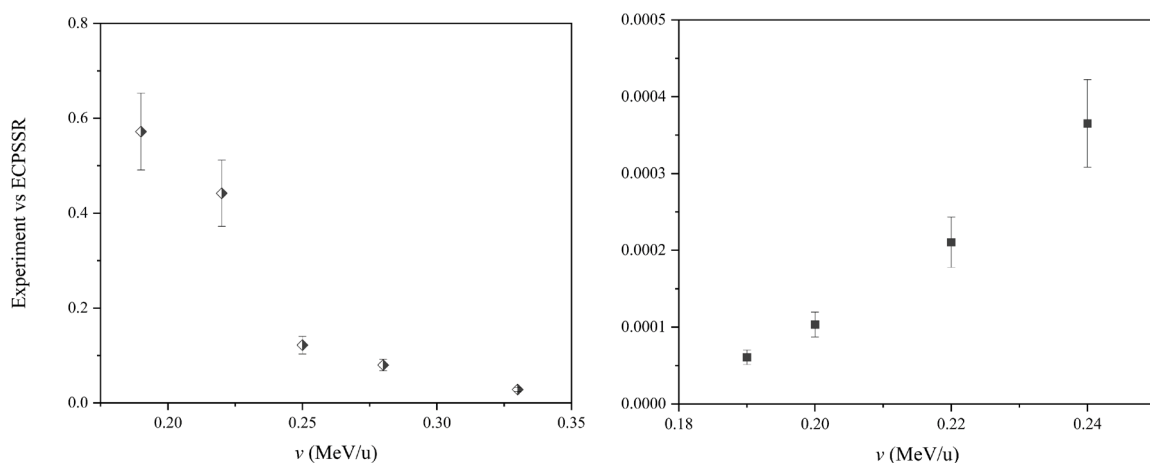
Figure 4.48. *Cu $L_{\alpha1,2}$ (left) and Ag L-Total (right) ECPSSR/Experiment XPCS ratios in Au*

The unsuitable nature of theoretical models based on protonic ionisations therefore warrants the need for more experimental efforts, especially for near symmetric collisions due to heavy ions in the low velocity range. This is more so the case for projectiles generally used for other heavy Ion Beam Analysis techniques, such as MeV SIMS or ToF-ERDA. In the case where HI PIXE is combined with another heavy ion technique, measured intensity ratios and XPCS may become useful for enabling quantification using PIXE. An example is shown using 12 MeV $^{12}C^{4+}$ ion beams incident on a sample prepared at the RBI.

4.5. Application of heavy ion XPCS

4.5.1. Ag and Cd in soil matrix

A certified reference soil matrix (*i.e.,* 1 grams XRF08, with known Al, Si, Ca, Ti and Fe composition) was mixed with 0.13 grams of $AgNO_3$ and 0.21 grams of $CdCl_2.H_2O$. The sample mixture was combined using a pestle and mortar, and thereafter pelleted (~1 mm pellet thickness) using a 5 t press. The target was prepared to resemble a soil pollution sample, where Ag and Cd contaminants are of interest for environmental monitoring. Ag and Cd contamination/pollution have adverse effects on microbial reproduction in soil, which negatively affects nutrient cycles and overall physical and chemical properties [143], [144]. Elevated concentrations of either one of these heavy elements can also cause an uptake in agricultural products such as crops and rice grains, exceeding limits for food safety [145], [146]. This makes the quantification of these contaminants in agricultural soil important for monitoring. The use of PIXE for the analysis of Ag and Cd is however limited by low detector resolution (>120 eV), as a majority of the Ag and Cd L-shell X-ray lines overlap.

In the first case, PIXE spectroscopy was carried out using 2 MeV broad/unfocussed proton beams on the old microprobe at the RBI. Accumulated charge could not be collected since the Faraday cup was positioned directly behind the target stage. The PIXE spectra induced by 2 MeV protons compared to the spectra induced by 12 MeV $^{12}C^{4+}$ ions is shown in Figure 4.49.
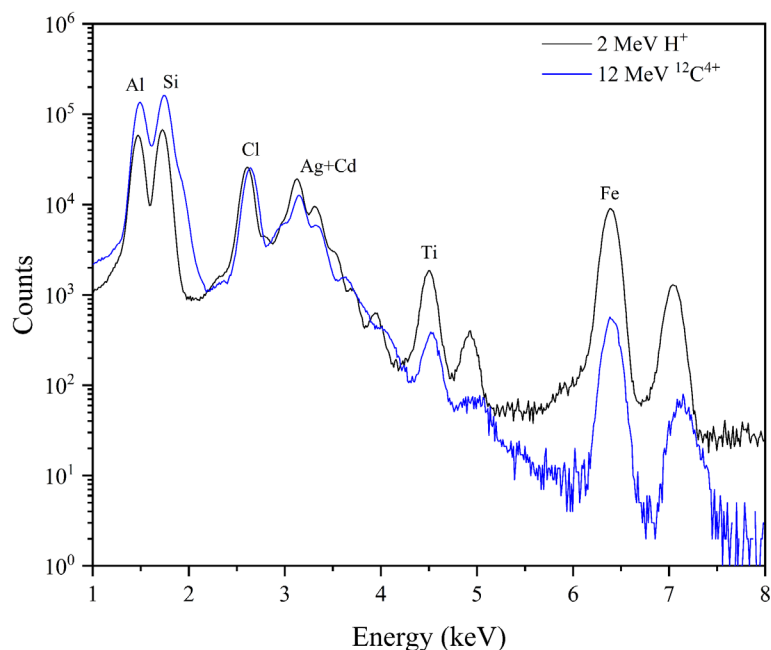
Figure 4.49. *Ag and Cd contaminated soil matrix spectra using 2 MeV H⁺ and 12 MeV ¹²C⁴⁺*

Peak broadening and changing intensity ratios can be seen for both the Ag and Cd contaminants and matrix elements comparing the carbon and proton PIXE spectra. To demonstrate the use of experimental XPCS measurements, relative intensity ratios were used for the extraction of the Lβ and Lγ intensities using the Lα intensity. These intensity ratios were obtained using the High Resolution PIXE spectrometer as well as an SDD detector. Initial calibration measurements were carried out using a focussed 10 μm x10 μm 2 MeV proton beam, later scanned over a 1 mm x 1 mm area to verify sample homogeneity, measured using an SDD (Fig. 4.51).
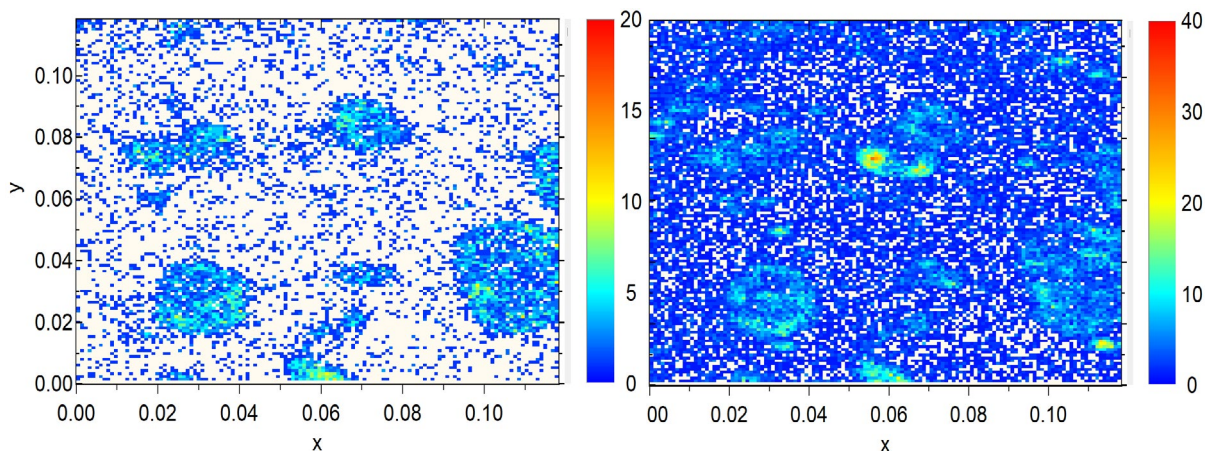
Figure 4.51. *Ag (left) + Cd (right) PIXE 2D intensity maps. x- and y- axis scale in cm*

Even though the sample was mixed, it was found to be heterogeneous, with localised structures correlating both Ag and Cd. It was posited that these clusters were formed due to the chemical reaction, $AgNO_3 + CdCl_2 \rightarrow AgCl + Cd(NO_3)_2$, resulting in varying Ag and Cd concentrations. As mostly larger concentrations of Cd were recorded, the PIXE scan was used to evaluate different regions of interests (*i.e.,* clusters) to find areas where Ag was either equal to or larger than Cd. Once these regions were identified using the SDD, the high-resolution spectrometer was then used to evaluate the intensity ratios of the overlapped lines in the SDD. A Si(111) diffraction crystal was used, positioned at 12.5 cm from the CCD. The collected spectra, for 200 beam exposures over a 10 s exposure time, is shown in Figure 4.52.
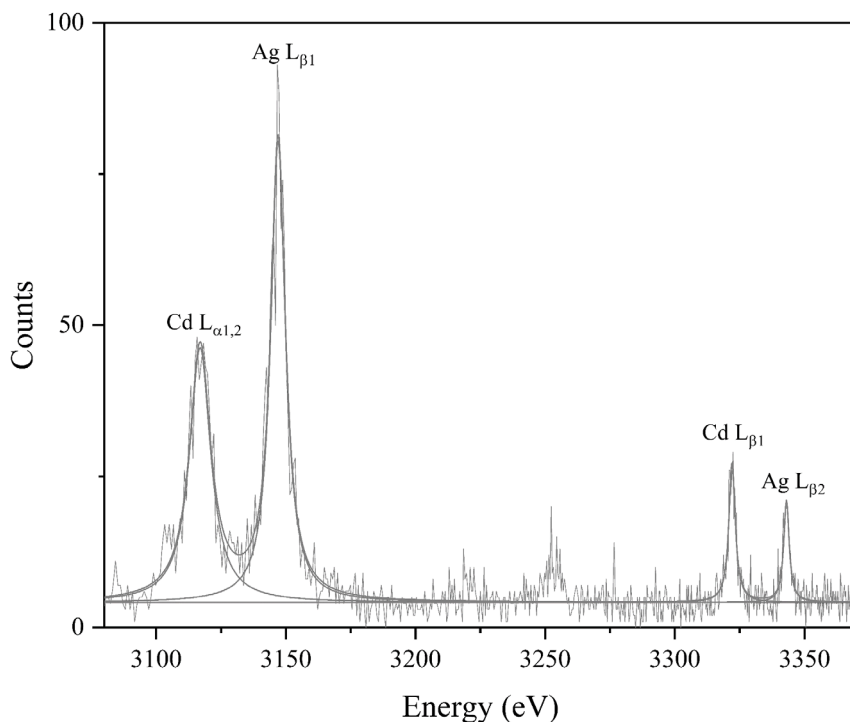
Figure 4.52. *High resolution spectrum of Ag and Cd X-ray lines induced by 2 MeV protons. Peak fitting carried out in Origin using Lorentzian functions*

The L-shell lines for single-hole ionisation are clearly separated, easily enabling the identification of the Ag and Cd diagram lines. The benefit of using high resolution spectrometry for evaluating overlapping element lines in a matrix can be deduced from the spectra, showing a low detection limit. Indeed, the use of proton based PIXE is incomparable to PIXE using heavy ions, due to lacking cross section data and more importantly multiple ionisation effects. These effects were seen using 12 MeV $^{12}C^{4+}$ ions in the same reaction chamber configuration. The overlapping intensities were exacerbated by peak broadening due to MI effects, as shown in Figure 4.54. The Cd $L_{\alpha 1}$ diagram line was convoluted with both its satellite distributions as

well as the Ag $L_{\beta 1}$ diagram and satellite lines. This meant that the deconvolution of the spectra using high-resolution PIXE was not possible as previously shown for protons. Although the crystal position as well as detector geometry were not changed for both the proton and carbon experiments, the spectra was energy shifted due to the pellet peeking out on one side by ~1 mm from the sample holder. This voided the calibration from the proton spectra, as seen in Figure 4.53. The Ag and Cd L-line centroids could however be estimated using the known difference between the Cd $L_{\alpha 1}$ diagram line and Ag $L_{\beta 1}$, as well as what appears to be an artifact with a centroid corresponding to twice the Cd $L_{\alpha 1}$ channel number at ~700 channels (~3.2 keV).
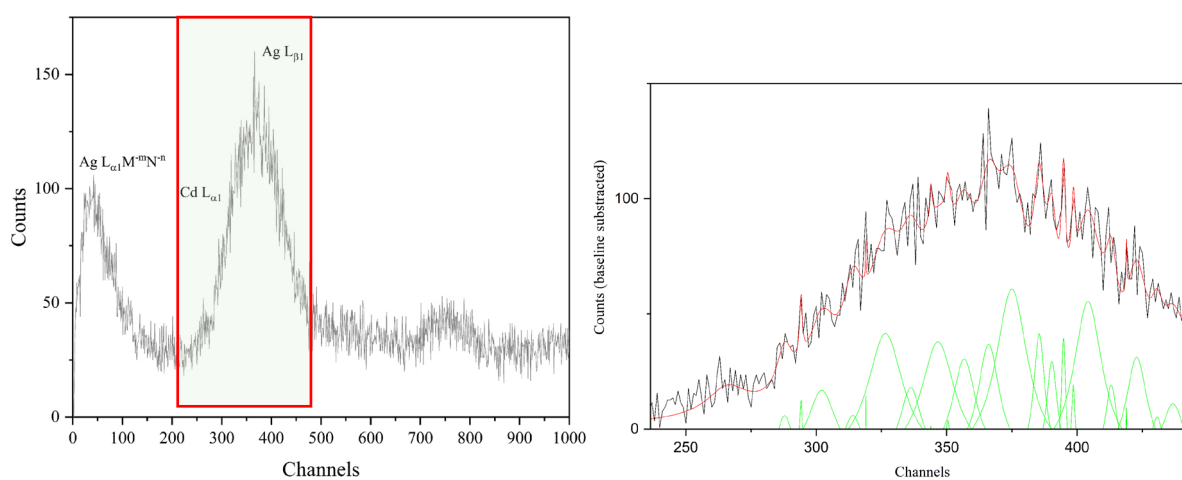
Figure 4.53. *Ag and Cd lines in high resolution (left), for ionisation with carbon ions. Peak fitting for ROI (red highlight on left figure) is shown in the spectra on the right. Peak fitting was carried out using Origin®*

However, since the Ag $L_{\alpha 1,2}$ peak could be extracted from the SDD spectra (see Fig.4.54), previously measured intensity ratios could thus be used to estimate the relative Ag L_{β} and L_{γ} intensities, and subsequently the Cd $L_{\alpha 1,2}$ and its relative intensities. While another consideration was to use the Cl K- and Cd $L_{\alpha 1,2}$ ratios to estimate the Cd L_{β} peak fraction and subsequently the Ag $L_{\beta 1,2}$; the chemical reaction between both $AgNO_3$ and $CdCl_2$ meant that the Cl K- peak not only correlated to the Cd intensities alone. Such an approach would therefore provide misleading relative line intensity estimates for both the Ag and Cd peaks.
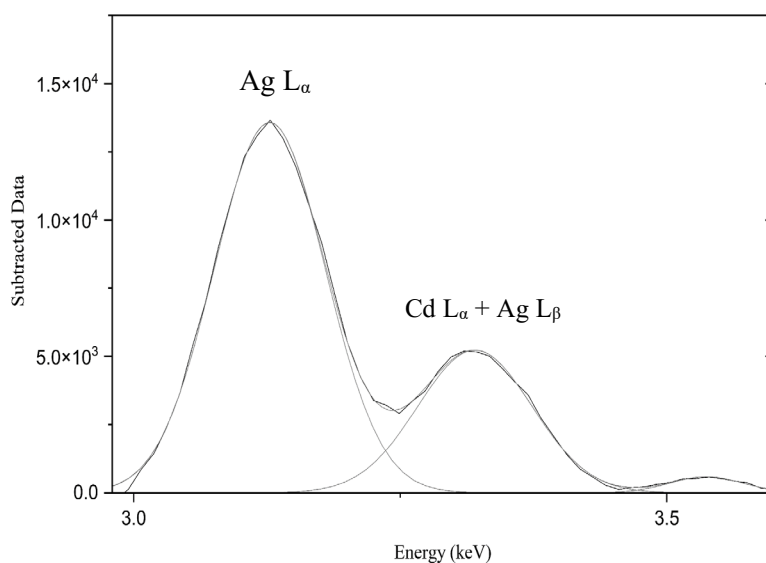
Figure 4.54. *Ag L_α, Cd L_α and Ag L_β X-ray lines due to 12 MeV $^{12}C^{4+}$ ions measured using an SDD detector*

Table 4.5. *Ag and Cd L-line intensity ratios*

Element	$\dfrac{L_\alpha}{L_\beta}$	$\dfrac{L_\alpha}{L_\gamma}$	Ion beam
Ag	2.8	17.5	2 MeV/u H^+
Cd	2.19	13.3	
Ag	1.88	15.1	1.0 MeV/u $^{12}C^{4+}$
Cd	2.18	12.9	

Experimental total L-shell XPCS data by Gorlachev and co-workers [27] for both Ag and Cd induced by 12 MeV $^{12}C^{4+}$ ions were used (*i.e.,* 4440 ± 590 barns for Ag and 3890 ± 590 barns for Cd). Relative intensities for the Ag L_β and L_γ and also the Cd L-lines were thus obtained using the measured Ag L_α line intensity (see Table 4.5). A quotient of the relative X-ray intensities and X-ray production cross sections was thereafter used to obtain relative atomic concentrations.

Accurate quantitation could not be carried out in GUPIX due to the inaccuracy of the estimated charge and also due to the fact that the software is limited to only protons and helium ions. Measurement uncertainties were largely due to ion energy loss in the thick target layer. The ion energy loss correction factor was thus calculated using Equation 4.26, derived from the

energy loss correction factor previously detailed in Equation 4.11, with a contribution of 3% from the SRIM stopping power data (expressed in units of keV/μm).

$$F(\Delta E) = (10) \cdot \frac{1}{S(E_i)}$$
4.26

Energy loss due to X-ray attenuation and self-absorption in the target layer was also calculated using the relation: $F_\gamma(E) = \left(\frac{\mu_t \cdot X_t}{1 - e^{-\mu_t \cdot X_t}}\right)$.

The overall uncertainty in the calculation of the atomic concentrations was ~12%. The calculated Ag and Cd concentrations were initially normalised to 100%, in order to treat the Ag + Cd convoluted peak as one fraction in the entire spectral intensity distribution. Thus, the Ag and Cd fractions for one of the clusters were evaluated, yielding concentration values of $81.2 \pm 12\%$ for Ag and $18.8 \pm 3\%$ for Cd. A multi-Gaussian fit of the element peak intensities was then carried out, in order to correlate the measured concentrations of the matrix elements along with that of the investigated Ag + Cd cluster. The evaluated concentration values are given in Table 4.6 below.

Table 4.6. *Estimated concentrations of one Ag+Cd cluster using $^{12}C^{4+}$ ion beam*

Element	Concentrations (%)
Al	21 (3)
Si	33 (4)
Cl	9 (1)
Ag	22 (1)
Cd	5 (1)
Ti	0.97 (3)
Fe	10 (6)

Fe and Ti semi-empirical XPCS were calculated from experimental data by Gorlachev et al [27]. ECPSSR cross sections for other matrix elements were also used, owing to the lack of experimental data in that range.

The major shortfall of this approach was thus the inability to validate concentration values using protons in the same analytical region, as such a position estimate would be unreliable.

Although the sample position was initially assumed to be the same as that of the proton spectra already shown, it was unfortunately refuted by the spectral channel shift. As mentioned before, the channel shift indicated that the analysed region for carbon ions was at a position slightly peeking out from the holder, thus resulting in a small change in geometry. This underpins the basis of Total IBA, as this would be the case if the sample was investigated using another heavy ion IBA technique and thereafter proton PIXE. Even though the measured data remains unvalidated, it however demonstrates the feasibility of quantitative Heavy Ion PIXE in cases of dual application with another IBA technique using heavy ions. Therefore, additional, and more targeted XPCS data is needed to cover a wider ion-target range for the improvement of theory, semi-empirical parameterisations as well as machine learning models.

4.5.2. X-ray – atomic recoil correlations

Aside from atomic quantitation, another useful application for either measured or calculated heavy ion induced XPCS is the determination of optimum ion energies for Total IBA. In the case of Heavy Ion PIXE – ToF ERDA or Heavy Ion PIXE – ToF MeV SIMS combinations, the optimum incident ion energy is one at which both scattering and X-ray emission probabilities are equal or close. Such can be viewed by correlating the recoil cross section with the XPCS within the working ion energy range. An example is shown in the Figure 4.55, for $^{48}Ti^{q+}$ ionisations in a Bi/Mylar target. In this case, the calculated X-ray production cross sections are for the Bi L-lines, where the recoil cross sections are for the hydrogen, carbon, and oxygen atoms from Mylar.
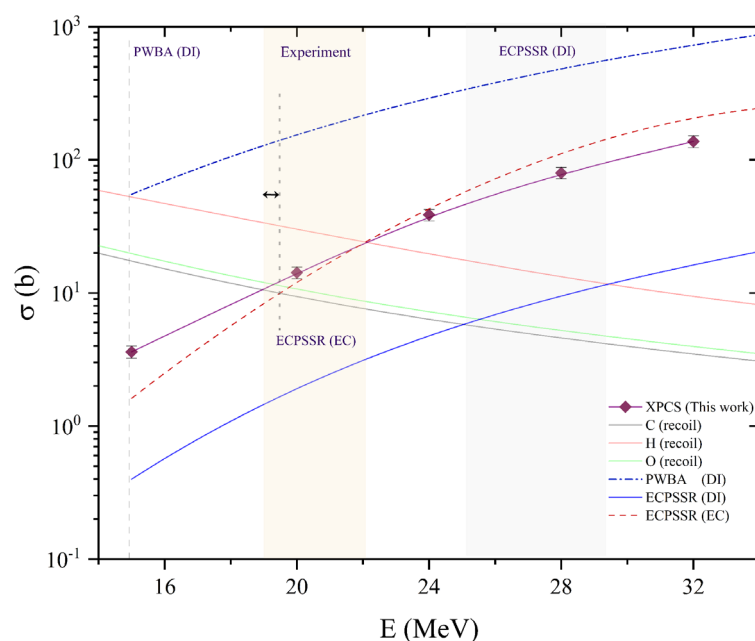
Figure 4.55. *0.2 MeV/u – 0.8 MeV/u $^{48}Ti^{q+}$ in Bi/Mylar*

While the recoil cross section (*i.e.,* Rutherford + screening) is well known, the discrepancy between experimental and theoretical XPCS results in different energy regions. As shown in Figure 4.55, the overestimated XPCS data by the PWBA intercepts the recoil cross sections at lower ion energies, implying a significantly lower optimum ion energy (<16 MeV) compared to that seen from experiment (~19 MeV – 22 MeV). On the other hand, underestimated values by the ECPSSR model intercepted recoil cross sections at higher ion energies, predicting an optimum ion energy in the ~25 MeV – 29 MeV range. As can be seen, the correction for electron capture (EC) in the ECPSSR calculation predicted an optimum ion energy range within the experimental range, with only a slight increase in the minimum ion energy (~19.5 MeV). The agreement between experiment and the ECPSSR with corrections to electron capture (EC) however depends on collision symmetry, as already discussed in the text. The discrepancies observed between the models, especially for slow and near-symmetric collisions where the EC correction may be inadequate, may be detrimental for optimising analytical conditions. This is the case for coincidence measurements, where experimental XPCS are unavailable and available theoretical models remain unvalidated for some heavy ion-atom collision systems. The discussion is continued in the 5th Chapter, detailing the implementation of TIBA using Heavy Ion PIXE.

This Chapter reports on the implementation of Total Ion Beam Analysis (TIBA) using Heavy Ion PIXE. As already introduced, this was approached in two cases, the first being the simultaneous implementation of HI PIXE spectroscopy with ToF-ERDA to overcome inherent poor mass resolution (*i.e.,* better than 1 for masses up to 40 Da) for heavier ions/recoils in ToF-ERDA. The second case explores the implementation of HI PIXE with ToF MeV SIMS, to correlate molecular with elemental imaging. The advantages and drawbacks of varying analytical conditions are discussed with a view to establish the feasibility of either one of the mentioned IBA synergies. This includes the evaluation of the generated HI PIXE and MeV SIMS spectra using different incident heavy ions.

5.1. Heavy Ion PIXE – ToF-ERDA

Exploratory HI PIXE and ToF-ERDA measurements were carried out on a 10 mm x 10 mm stainless steel sample (~1 mm thick), using a 30 MeV $^{63}Cu^{7+}$ ion beam at iThemba LABS TAMS. The use of recoil and X-ray production cross sections for the optimisation of the incident beam energy, as partly mentioned in the 4th Chapter, is shown in Figure 5.1.
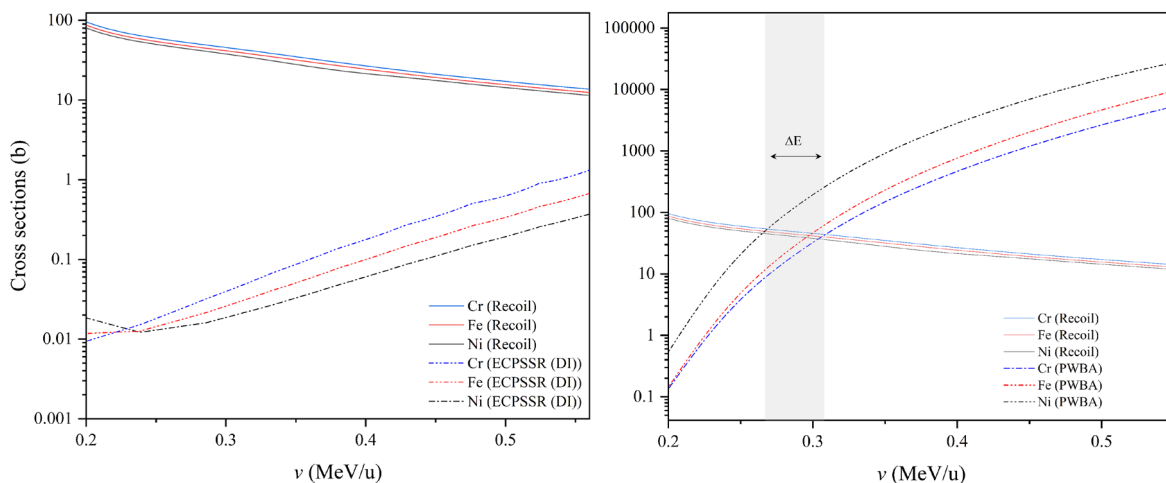
Figure 5.1. *Recoil cross sections vs ECPSSR (DI)(left) and PWBA XPCS (right) in Cr, Fe and Ni due to incident Cu ions for different ion velocities*

As already mentioned in the previous Chapter, discrepancies between experimental and ECPSSR XPCS for heavy ion-atom collisions extend beyond the low energy range for near symmetric collisions. It may thus be assumed, given the symmetry of the Cu – Cr, Fe and Ni

collisions, that ECPSSR predictions are outside the model's range of validity. Especially with the absence of experimental data, ECPSSR predictions which have already been shown to underestimate empirical data, may be assumed to overestimate optimum ion energy ranges in the DI mode. This can be seen in Figure 5.1, where lower ECPSSR DI predictions indicate a recoil – X-ray cross section intersection at higher ion energies compared to the intersection with the more pronounced PWBA cross sections. Although the addition of the EC correction as previously shown for the Ti in Bi/Mylar (Chapter 4) predicted values close to experiment, it unfortunately could not be assumed here due to differences in collision symmetry. This was particularly the case, where the electron capture (EC) correction to ECPSSR predictions enhanced the cross section data by ~2%. The optimum ion energy for simultaneous PIXE and ToF-ERDA could still be estimated from Fig 5.1, even with the scant experimental data available in the literature. This is because PWBA predictions, which generally overestimate experimental data, could describe a trend similar to that of experiment in the case where MI effects are high, such as with the Cu-ionisations. Of course, the difference between the PWBA and the experimental trend gradients cannot be compared to that of Ti in Bi shown in Chapter 4, since it has already been shown that MI effects are much larger in near-symmetric collisions.

Nevertheless, the estimation of the energy range based on theoretical predictions should guide experimental exploration, which would in any case be confirmed by measured event rates as a function of beam current and reaction geometry. In this work, the use of low ion energies (< 0.4 MeV/u) as suggested by Figure 5.1 was not favourable, due to the small X-ray detector solid angle that would lead to a low X-ray rate. A higher Cu ion energy than that suggested in Figure 5.1 was therefore used, where the nucleon energy (0.5 MeV/u) was high enough to compensate for the small X-ray detector solid angle but still low enough to ensure high recoil yields within the target layer of interest. This was particularly important for obtaining comparable event rates for both the recoil ions and X-ray photons.

Overall ion beam currents were in the ~(10 – 25) nA range, corresponding to ~ (1.4 – 3.6) particle nA. X-ray detector calibration was carried out using a set of samples of known composition, namely TiN, VO_2, NbN, In_2O_5Sn, Y/Mylar and Bi/Mylar using a 2.0 MeV H^+ beam. The X-ray detector resolution calculated at 368 eV FWHM at 8.64 KeV using the Zn K_α peak, as shown in the Figure 5.2.
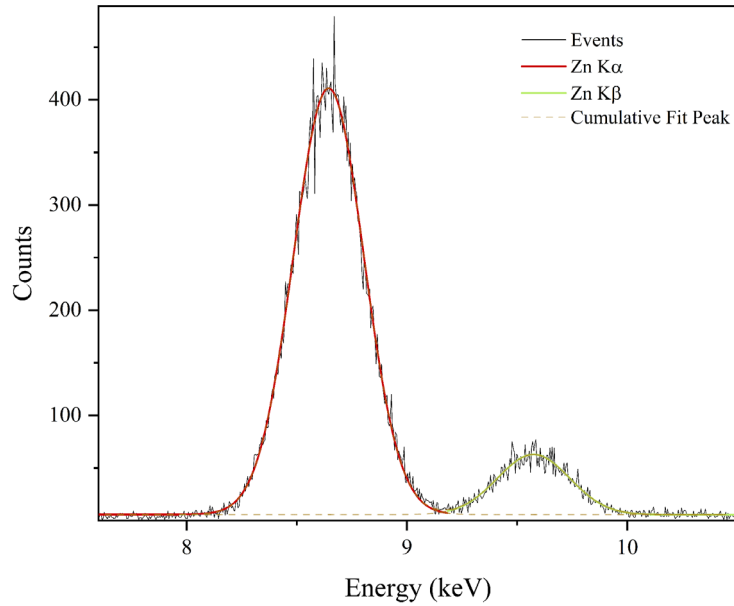
Figure 5.2. *Si(Li) detector energy resolution calculated using Zn K_α (red) and K_β (green) X-ray lines induced by 2 MeV protons. Peak fitting carried out using Origin®*

5.1.1. Deconvolution of mass overlapped ToF-E scatter plots: demonstration of principle

Experimental conditions configured the ADC to poll input signals only when there was an event recorded by the recoil energy detector. The condition for simultaneous ERDA and PIXE was set up using a Logic Unit NIM module, with the window set at ~50 µs. This was deemed sufficient for both detectors to accommodate differences in the internal delays in the two detectors' amplifier chain, and also because the individual (direct) count rates were well below 10 kHz. For the ToF-ERDA detectors, the coincidence window was set a 400 ns.

Due to the statistical nature of recoil yielding ion-atom collisions, and similarly the random emission (and detection) of X-rays as well as the small solid angles of the detectors, the probability of detecting an X-ray photon in coincidence with the emitting recoil or scattered ion is quite small. This coincidence rate can be described using Poisson statistics [147]. The observed count rate is comprised of largely false coincidences, since most photon-ion events are not correlated. The false coincidence rate describes the number of simultaneous events between recoil (or scattered) ions and X-ray photons emitted by a different ion altogether – for example, coincidence between a ^{56}Fe ion and an X-ray photon emitted by a ^{58}Ni atom. Considering the Poisson distribution of correlated recoil and X-ray detection, the true coincidence rate between a given recoil species R_i and its characteristic X-ray photons X_i may be obtained from an expression of probabilities given in this form:

$$P(true)_i = P(X_i \cap R_i) = P(X_i) \cdot P(R_i) \qquad\qquad 5.1.$$

where $P(X_i \cap R_i)$ is the intersection between X_i and R_i, and $P(X_i)$ is the probability of detecting a photon X_i and $P(R_i)$ is the probability of detecting a 'parent' recoil R_i.

The separate probabilities $P(X_i)$ and $P(R_i)$ are, in principle, obtainable experimentally, by selecting the mass overlapped region as the region of interest (ROI) in the ToF -ERDA scatter plot and likewise in the PIXE spectra:

$$P(X_i) = {Y_{X_i}}\big/{Y_{X_T}} = Q \cdot \varepsilon_i \cdot \Delta\Omega_x \cdot \frac{d\sigma_{x_i}}{d\Omega} \cdot A_i \cdot \frac{1}{Y_{X_T}} \qquad\qquad 5.2.$$

and similarly,

$$P(R_i) = {Y_{R_i}}\big/{Y_{R_T}} = Q \cdot \Delta\Omega_R \cdot \frac{d\sigma_{R_i}}{d\Omega} \cdot A_i \cdot \frac{1}{Y_{R_T}} \qquad\qquad 5.3.$$

where terms are namely the accumulated charge Q, the detector solid angle $\Delta\Omega$, the element i and the total X-ray Y_{X_T} and recoil Y_{R_T} yields, as well as the target atomic density A_i.

For any two recoil species (*1, 2*) the ratio of their true coincidences can be taken as being equal to their atomic ratios in the target sample:

$$\frac{A_1}{A_2} = \frac{P(X_1) \cdot P(R_1)}{P(X_2) \cdot P(R_2)} \qquad\qquad 5.4.$$

Combining 5.2 and 5.3, equation 5.4 simplifies to:

$$\frac{A_1}{A_2} = \frac{Y_{X_1}}{Y_{X_2}} \cdot \frac{\varepsilon_2}{\varepsilon_1} \cdot \frac{\sigma_{x_2}}{\sigma_{x_1}} \qquad\qquad 5.5.$$

The correlation of both the X-ray and recoil rates was then used for the deconvolution of the time of flight - energy spectra where heavy masses, cannot be resolved. The convolution of the ToF-E spectra was due to the limited intrinsic energy detector resolution, where heavy ion recoils produced with very close energies (spread) could not be separated. This is exacerbated by particle scattering in the timing foils, which further leads to small fractions of energy loss. The same is true for the timing resolution, where two recoils or scattered ions with very close kinematic energies drift at very close flight times. This leads to a considerable deterioration in the mass resolution, which is usually the limit for ToF-E spectrometers. By detecting X-ray photons simultaneously with recoils, the convoluted distribution could be 'separated'. The

deconvolution of the spectra was in this case carried out offline, by replotting the ToF-E plot for a given element by using the corresponding X-ray peak intensity. It should be emphasised here that the individual mass lines (shown later in Fig. 5.7) are not completely true events for each element, but rather presentations of the relative amount of each element in the mass overlapped region, as dictated by the X-ray yield.

As pointed out before (Chapter 3), the input data streams were stored using a tree structure, where the nodes were from the Si(Li), PIPS and timing detector ADC and TDC inputs. An 'event' in this data scheme is characterised by the time of flight, recoil energy and X-ray photon energy – but bearing in mind that, for most of the time, there may be no direct connection between the X-ray energy and the other two variables. On building a 3-D histogram of ToF vs E_{recoil} vs $E_{X\text{-}ray}$, for the mass-overlapped region a pattern emerges however, showing the relative concentrations of the target elements in this mass region. These elemental fractions are according to the characteristic X-ray yields (see Fig 5.6). Recoil events 'tagged' to X-ray events could nonetheless be extracted regarding of any correlation between them. The filtered spectra can then be saved into ASCII format and further processed using Potku. Potku is an open source C based software from the Pelletron laboratory at the University of Jyväskylä, which calculates depth profiles from time of flight – energy data. The software also carries out Monte-Carlo (MC) simulations of scattered and recoiled ions (Elastic Recoil Detection (ERD)), using the long used MCERD framework [148].

5.1.2. Analysis of stainless steel

To demonstrate this approach, a stainless steel target was analysed, where the constituent Cr, Fe and Ni recoil events, along with the scattered events from the Cu beam are overlapped in the Time of Flight – Energy spectra (see Fig.5.3).
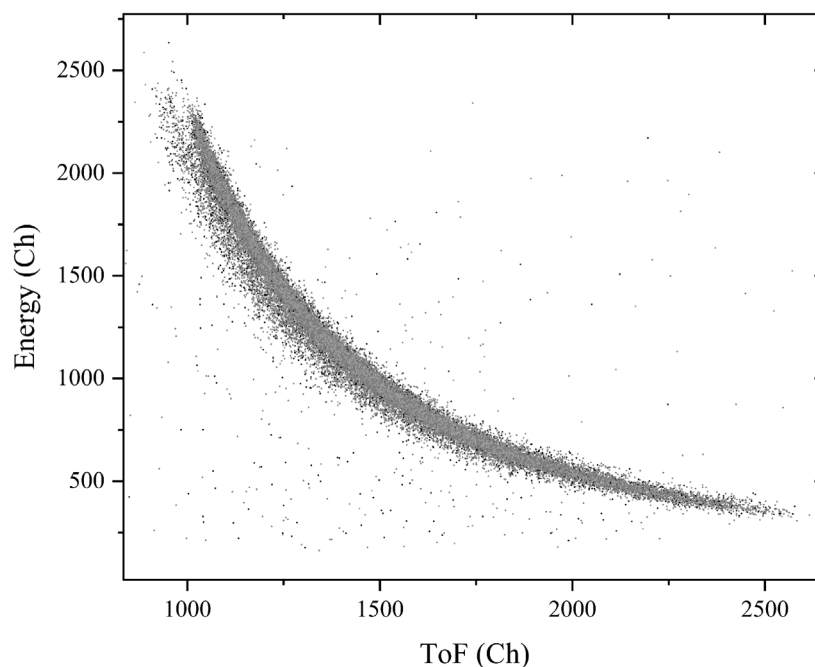
Figure 5.3. *Time of Flight – Energy spectra of mid-Z elements in stainless steel*

Simultaneous HI PIXE – ToF ERDA measurements carried out were aimed at separating Cr, Fe and Ni recoil signals. Data filtering was carried out by re-plotting the spectra in Fig. 5.3 for each element using the corresponding X-ray peak as a condition. It was then possible to visualise the ToF-E spectra make up according to its constituent elements. In another view, the extraction of elemental fractions from the overlapped/total recoil yield could be carried out by multiplying the recoil yield by a 'deconvolution' factor equal to the X-ray yield atomic ratios for each neighbouring element (Equation 5.5). Of course, this becomes valid assuming that the total yield is due to an even distribution of the Cr, Fe, Ni atoms in the target matrix since no information on depth is obtained from PIXE data. Given the unavailability of reliable heavy ion induced XPCS and the inadequacy of widely available theoretical frameworks, the method is for now heuristic in nature. Even with lacking theoretical XPCS data, the assumption made was that the *ratio* of the X-ray production cross sections as shown in Equation 5.5 could be estimated using ECPSSR predictions. It is expected that the uncertainty for the cross section ratios would be much smaller than that of the absolute ECPSSR cross section values.
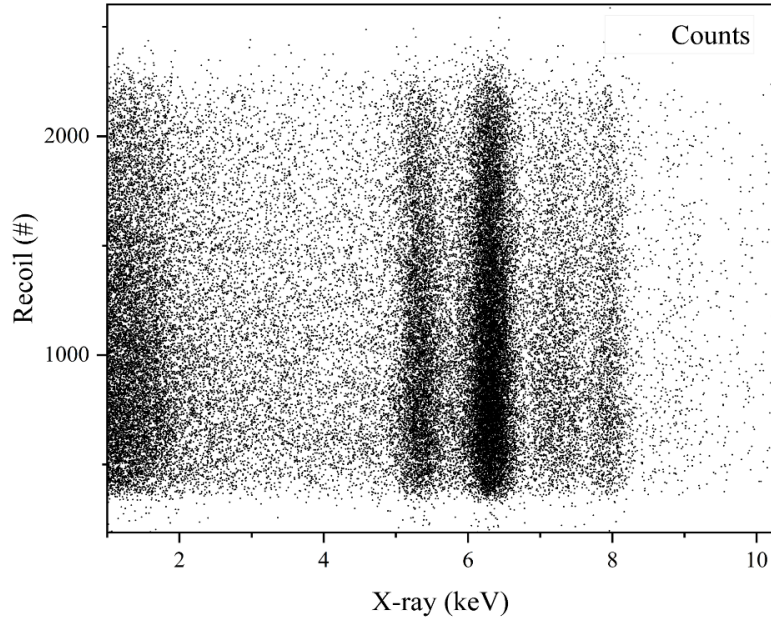
Figure 5.4. *X-ray – recoil energy correlation*

Another replay of events collected simultaneously can be in the form of recoil energy vs X-ray energy. The varying intensities in the X-ray spectra (see Fig 5.5.) can be directly linked to the recoil intensities, as seen in Fig 5.4.
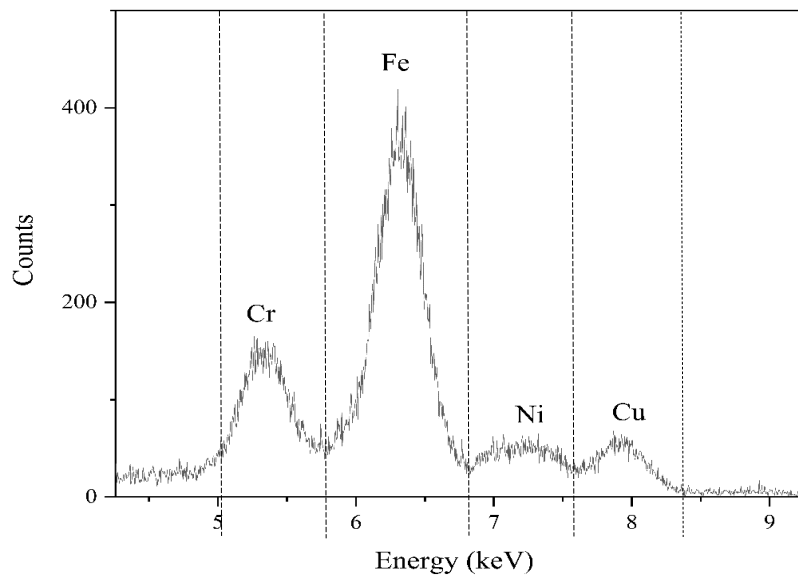
Figure 5.5. *Stainless steel X-ray spectra*

Poor energy resolution of the Si(Li) detector used for these measurements unfortunately prohibited the separation of the constituent K_α and K_β line intensities for the investigated elements, where some K_β intensities overlapped with neighbouring K_α intensities. Nonetheless,

since the Cu projectile used was significantly heavier than protons, the K_β intensities were assumed to be low due to MI effects, such that the K_α could be said to constitute more than 90% of the peak fraction. Since the Cu induced collisions are near symmetric for all Cr, Fe and Ni combinations, the likelihood that K_β X-rays are relatively lower compared to protonic ionisation is high.

On building a 3-D scatter plot of ToF vs E_{recoil} vs $E_{X\text{-}ray}$ event data from the mass overlapped region, a pattern emerges showing the splitting of the ToF vs E_{recoil} scatter plot according to the X-ray energy and yield. This again gives a visual display of the relative content of each element (in the mass overlapped region) from the target sample analysed as shown in Figure 5.6. Noise events in the X-ray detector manifest in 'false coincidences' with recoils over a fairly wide X-ray energy range.
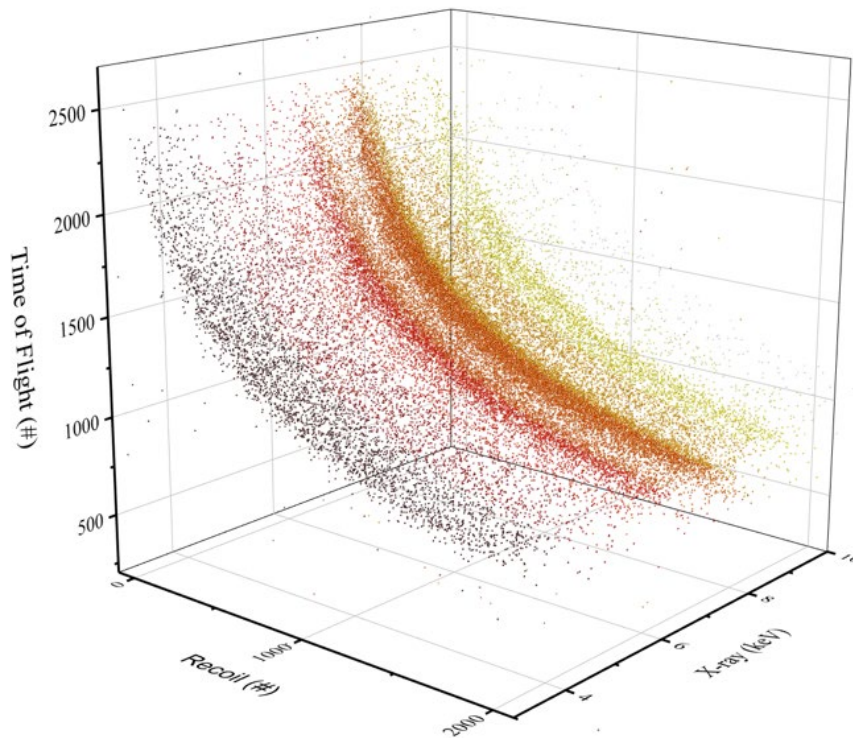
Figure 5.6. *Stainless steel ToF – E – X-ray correlation*

Data filtering was carried out in ROOT, where X-ray energy gates shown in Figure 5.6 were used, corresponding to each element total K_α X-ray peak. The separated 2D element ToF-E distributions are shown in Figure 5.7 below. As pointed out earlier, these were used to provide relative recoil yields for each element in the mass overlapped region. In other words, the events in the 'Fe' mass line for instance are not strictly from Fe recoils alone, there are counts from

Cr, Ni and Cu as well. However, the four sub-plots must be looked at collectively; it is the relative elemental yields that matter.
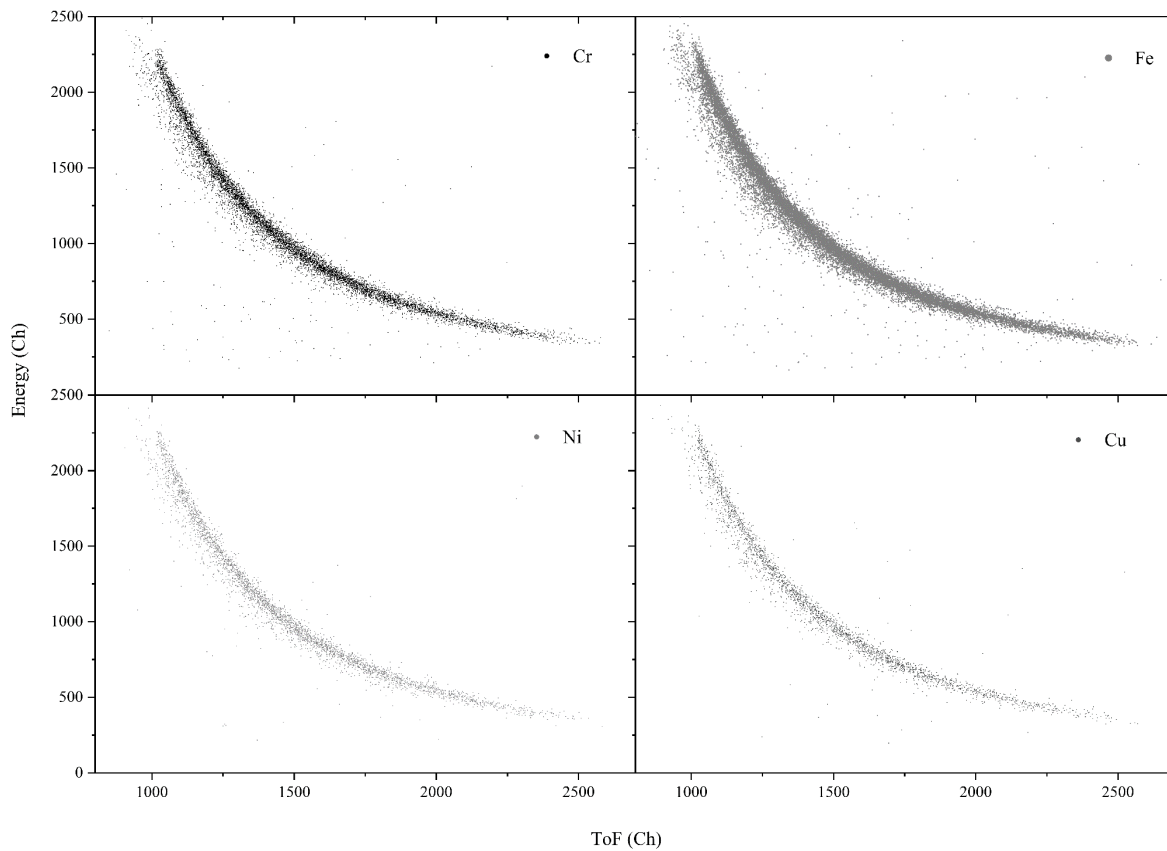
Figure 5.7. *Cr, Fe, Ni and Cu ToF – E cuts obtained using the PIXE spectra*

The separate element distributions were thereafter imported into Potku, to determine the analytical depth of the measurement. In a typical ToF – E spectra, where multiple time resolved energy distributions are present, cuts refer to data selected (or ROI) to identify a specific element mass. Since this could not be achieved from the convoluted spectra, the cuts obtained from the separate PIXE resolved data were instead imported into the 'cuts' folder in the Potku data files, enabling the selection of the individual elemental cuts into the Potku workspace for analyses. The Potku calculation converts elemental energy spectra into depth profiles. In this instance though, the calculation only provides the analytical depth since the atomic fractions are already pre-determined and are constant over the depth scale. This would become useful for including some information about the heavy elements present in a given matrix, alongside the light element depth profiles. The calculated relative element concentrations from the filtered data are thus represented in Figure 5.8 below, indicating an analytical depth of about 300 nm.
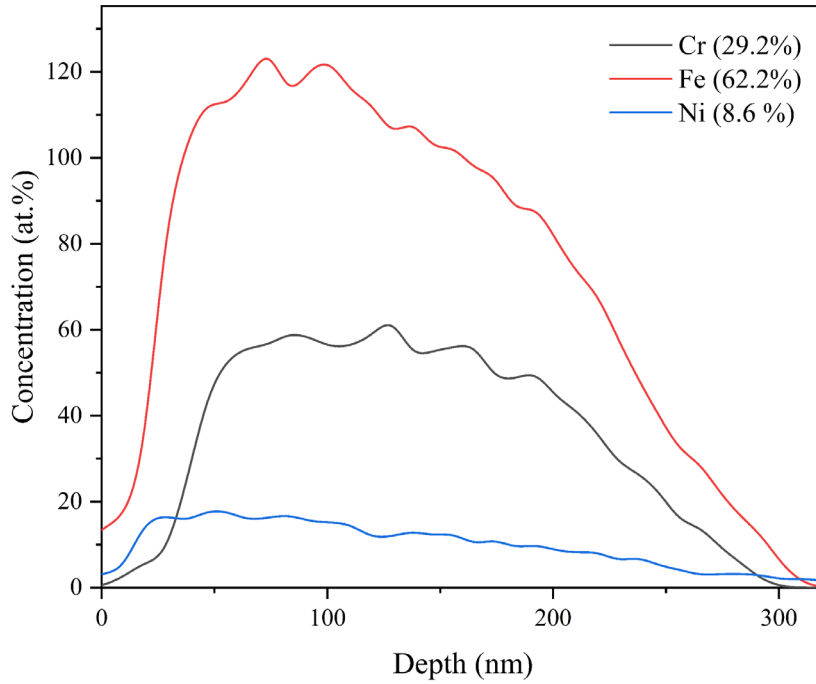
Figure 5.8. *Stainless steel relative concentrations*

The calculation did not factor in the Cu intensity, as it did not form part of the target matrix. The filtered ToF – E calculated concentrations were compared to concentrations determined using 2 MeV proton induced X-ray spectra. The proton spectra is shown in Figure 5.9, obtained from the microprobe beamline (E9) at the RBI.
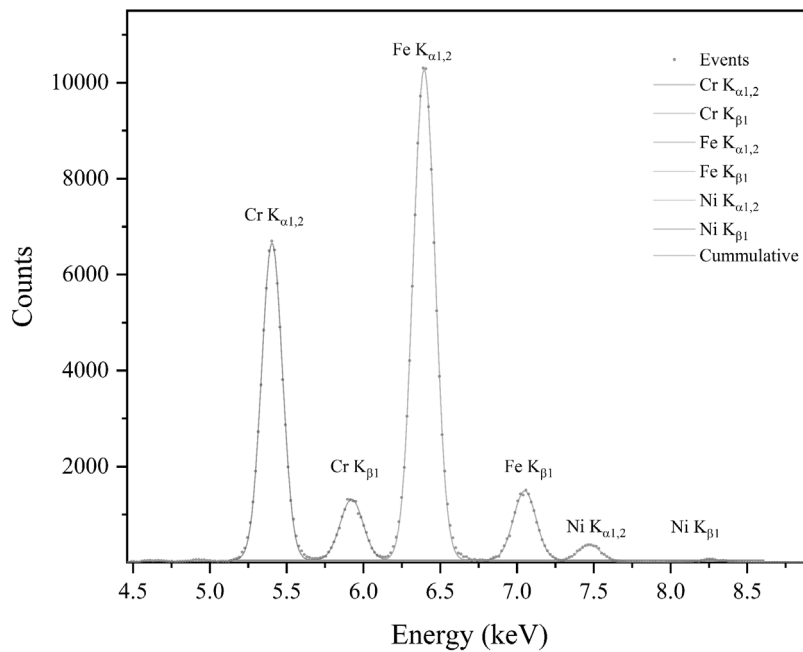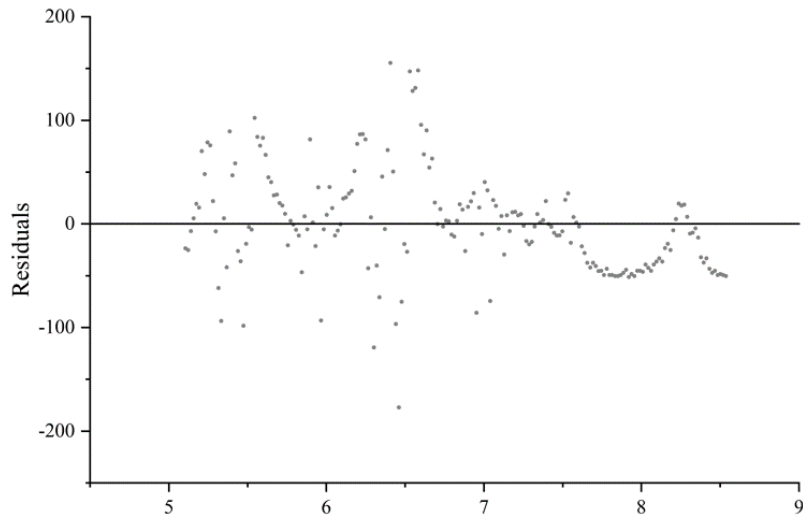
Figure 5.9. *Stainless steel proton induced spectra (top) (resolution at 140 eV at 5.9 KeV). Residuals (bottom) for all element peak fits were less than 10%*

The individual line intensities were extracted using Origin® and thereafter weighted against the combined/total X-ray intensity. Although the accumulated charge could not be accurately measured; since the detector solid angle and accumulated charge were the same for all target elements, a ratio of the X-ray intensity and a product of the ECPSSR XPCS and detector efficiency was instead used (Equation 5.6.). As the intensities were normalised to 100%, charge and solid angle were considered as a constant *K*, retained at unity for all calculations.

$$\frac{Y_X.K}{\varepsilon.\sigma_X} = C_X \; ;$$

$$K = \frac{e}{Q.\Omega}$$

5.6.

The combined intensities were viewed as the sum of the combined element ratios C_X, since a sum of the X-ray yields alone would misrepresent each element fraction. The calculated relative concentration values (21% estimated uncertainty) from the proton PIXE spectrum, are thus:
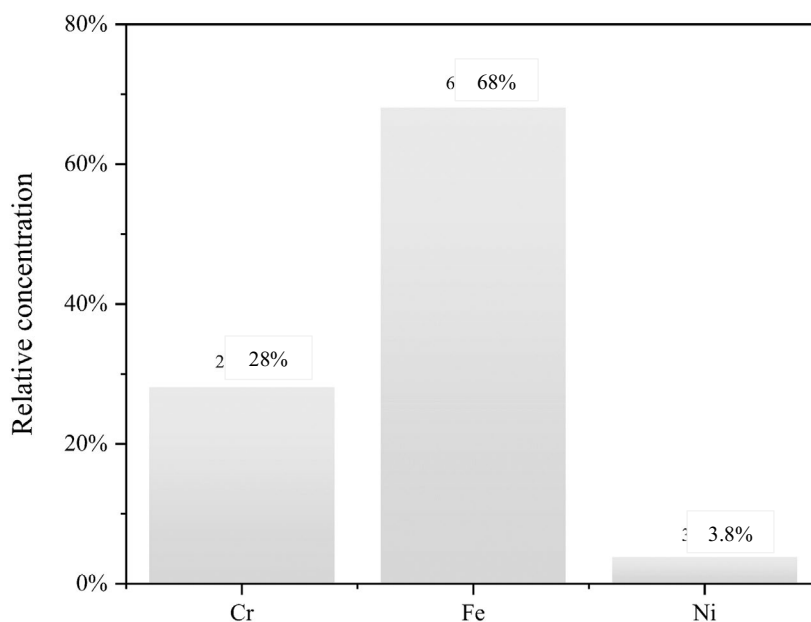
Figure 5.10. *Steel relative concentrations from 2 MeV proton PIXE spectra*

The discrepancy between the proton and simultaneous HI PIXE – ToF-ERDA measurements may be attributed to the unknown Cu-induced X-ray production cross sections, which particularly for Ni, resulted in poor statistics in the X-ray spectrum. The agreement scores comparing the simultaneous HI PIXE – ToF – ERDA and proton PIXE data was 96% for Cr, 91% for Fe and 44% for Ni. The feasibility of the technique therefore indicates the need for additional experimental work for different ion and target types, as well as heavy ion induced X-ray production cross section data.

5.2. Heavy Ion PIXE – ToF MeV SIMS

The second TIBA approach entailed the use of HI PIXE with ToF MeV SIMS. ToF MeV SIMS was carried out in positive ion mode, that is, to extract positively charged molecules from the target surface. An extraction field was obtained using a +5 kV bias on the target stage. Although the use of both positive and negative ion modes may be beneficial for investigating an unknown chemical environment in a given target, negative ion extraction was in this case not explored. The present work reports on the identification of several paint pigments, as well as the discrimination of ink pigments for forensic studies. The complementary use of PIXE with MeV SIMS has been undertaken before, to obtain subsurface elemental maps which were linked to molecular signals seen with MeV SIMS. The use of PIXE has however so far been carried out

using proton beams, requiring a change in the target position and beam type (*i.e.,* switching from a heavy ion to protons) and subsequent beam optimisation prior to each measurement. Although the analytical region investigated with MeV SIMS may be approximated for protons, the potential for inaccuracies in determining exact analytical regions may result in the area under investigation not completely overlapping between the two techniques. This is moreover the case with non-homogeneous materials, where the overall sample material has significant lateral molecular and depth elemental distributions. One such case is that of biological samples, were precise correlations between molecular and elemental distributions is extremely important for understanding disease pathogenesis [149].

Heavy Ion PIXE on the other hand, using the same ion beam for MeV SIMS may be carried out sequentially. Elemental spectra from PIXE may thus be directly linked to molecular data, as the same ion beam and experimental geometry would be used for both techniques. In the present work, since the Time of Flight configuration (see Chapter 3) resulted in the use of low current beams (<10 fA) for MeV SIMS, sequential HI PIXE was adopted. This method was approached by switching off the ion beam deflector after MeV SIMS analysis in order to obtain higher beam currents (*i.e.,* in the ~1nA range) for PIXE. The study thus entailed the exploratory use of different heavy ion beams for PIXE and MeV SIMS for different targets of known composition(s).

5.2.1. Inks and toners

In the first case, the isolation of inks from writing tools using their respective chemical compositions using ToF MeV SIMS and HI PIXE was carried out. The investigation of ink or toner deposition order on paper is important for forensic studies and may be carried out to determine either forgeries or text alterations for cases such as will disputes or fraud cases. The detection of desorbed secondary molecular ions from ink pigments, as well as the extraction of elemental data for inks deposited subsurface using PIXE was important in overcoming limitations from commonly used optical techniques. An example of an optical image taken with a microscope is shown below, where the deposition order of two different toners of the same colour cannot be distinguished.
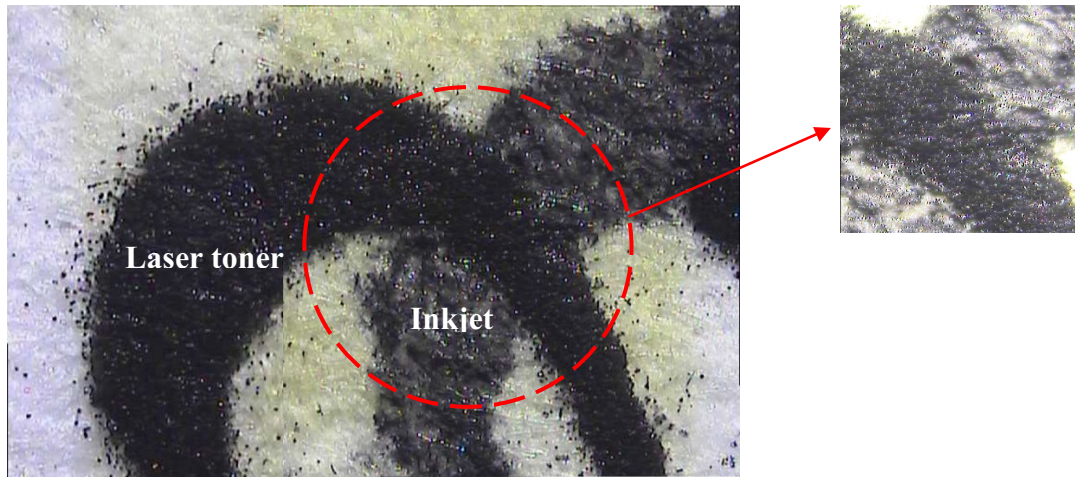
Figure 5.11. *Optical image of two toners on paper, image taken with microscope at 4X magnification. Intersection region shown in dashed line. Coloration on the paper substrate is due to heavy ion beam irradiation*

As shown in Figure 5.11, there is some ambiguity in the interpretation of the optical image as far as the chronological sequence of deposition is concerned. Moreover, since there is no information on the chemical composition of the toners, optically establishing whether an ink was deposited before or after another becomes highly subjective. The same remains true with the use of other contemporary characterisation techniques such as Atomic force Microscopy (AFM), Scanning Electron Microscopy (SEM), Raman spectroscopy and Fourier Transform Infrared Imaging (FTIR), to mention a few. The issue of analytical ambiguity is thus significant for forensic cases, as there are serious implications to the outcomes from analyses. This is moreover the case where toners are concerned, compared to inks from pens, on which a bulk of research has been largely focused [32], [150], [151]. Although some work has already been carried out to determine deposition orders in the case of printer toners, the reported data instead investigates the improvement of the efficacy of measurement by using the same ion species, as already mentioned.

Using MeV SIMS, the deposition orders could be established by observing the ink line continuity in the molecular maps, where the breakage in either ink deposition may indicate whether deposition occurred before or after. The ability of these inks to be identified and separated using MeV SIMS is premised on the surface deposition of the inks, which is valid for most inks (*e.g.,* ballpoint pen, laser toner)[152], [153]. Laser toners are deposited through heating a polymer-based binder, which then deposits the ink pigments on the surface of the

paper substrate. Liquid inks, used by inkjet printers, are made up of either dye or pigments with a largely water-based binder [154]. These inks thus penetrate the surface of the paper and thereafter disperse laterally and in depth, before evaporating from the surface [154]. The adhering properties of the inkjet and laser toners are shown in Figure 5.12.
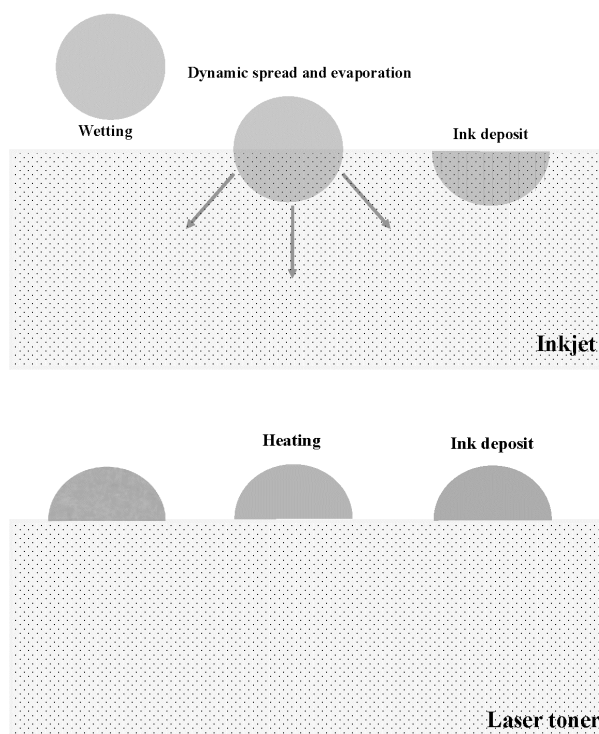
Figure 5.12. *Schematic of ink deposition on paper substrate*

Several letters were printed using two different inks on the same paper, to produce different letter combinations. The deposition order was varied using the printing sequence, to produce two sets of samples, one inkjet over laser (inkjet/laser) and the other with the opposite deposition order (laser/inkjet). Secondary molecular ion mass and X-ray spectra as well as 2D molecular/elemental maps were obtained using 15 MeV $^{12}C^{5+}$, 12 MeV $^{16}O^{4+}$ and 8 MeV $^{28}Si^{4+}$ ion beams.

The SIMS channel spectra was mass calibrated using positive ions of hydrogen, Na, K, Polydimethylsiloxane (PDMS) and Leucine whole and fragment molecular peaks. The samples were scanned over a $1000\ \mu m \times 1000\ \mu m$ area, using a $10\ \mu m \times 10\ \mu m$ focused beam spot size. The images were scanned using a 128×128 pixel array, with a $1800\ \mu s$ pixel dwell time, acquired using SPECTOR.

Both the HI PIXE and MeV SIMS maps were saved in list mode, and thereafter accessed using external image processing software. One method for evaluating different elements in the PIXE map could be carried out using PyMCA [155] to view the inkjet and laser toners, or even directly in SPECTOR by replaying the spectra. The advantage of using PyMCA is the establishment of elemental variations in the image, which can be made much clearer compared to SPECTOR 2D maps by implementing image processing tools. MeV SIMS spectra may on the other hand be analysed using software such as mMass [156] for the determination of molecular compositions. The software is however limited in that only MeV SIMS spectra could be evaluated, which would require the evaluation of molecular maps to be carried out by replaying the data for selected ROI in SPECTOR. However, unlike PIXE, the 'forest' of peaks makes it difficult to evaluate molecular variations in the MeV SIMS image.

5.2.1.1 Multi-Variate Analysis (MVA)

Multi-Variate Analysis (MVA), the use of unsupervised machine learning algorithms for carrying out statistical dimensionality reduction are crucial for the analysis of variations in PIXE and especially MeV SIMS maps [2], [32]. One of the most widely used algorithms is Principal Component Analysis (PCA), which reduces hyperdimensional datasets such as multiple spectra stored in a data cube. The reduced dataset, essentially correlations of the initial variables (*i.e.,* mass or X-ray peak), is then presented on isolated orthogonal axes, each of which represents separate principal components (PC) [157]. Principal components are linear combinations of the initial variables (mass or X-ray peaks), organised at varying levels of importance. The different levels of importance are ordered in descending degrees of statistical variance between the principal components, compared to the maximum variance of the original dataset. The first principal component would thus have the largest statistical variance, where the last PC would have the least variance, where the sum of all PCs is equal to the maximum variance. The ith principal component can be calculated using statistical weights a_{ij}, where N is the number of variables and $j = 1 \dots N$ [157].

$$Y_j = a_{ij}.X_j \qquad\qquad 5.7.$$

The magnitude of the variances is described by the eigenvalues in the orthogonal axes, where the different PC directions ($Y_1 \dots Y_N$) are the eigen vectors, as described by Equation 5.7 and shown in Figure 5.13.
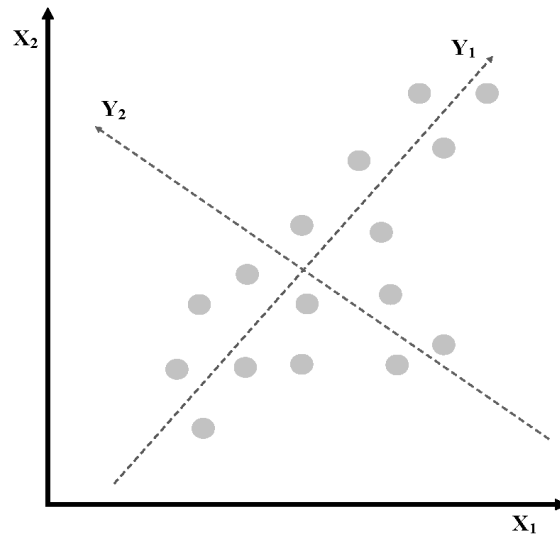
Figure 5.13. *Schematic of Principal components' orthogonal axes for X_1, X_2 variables*

A *K-means* clustering algorithm was used to group principal components with comparatively close statistical variances [158]. The PCs were assigned to specific cluster groups in which the Euclidean distances between the datasets and the cluster centroids are closest. This was carried out to enable a correlation of the datasets, to determine similarities between different PCs.

The largest variations in the analysis of inks were mainly between the two inks and paper substrate. This simplified and eliminated ambiguities in the analysis of MeV-SIMS images, where the evaluation of small variations of multiple main molecular and fragment peaks in the spectra can make the analyses complex. On the other hand, only a few variables existed for the PIXE spectra, meaning only few principal components. This was because the main variations were due to the large sodium peak from the laser toner, as well as the sulphur from the inkjet, along with the large Ca peak from the paper substrate. Smaller variations were seen from some minor anomalies along the scan area. PCA analyses were carried out using Orange, where image pre-processing was carried out using a program developed in-house, called LIBImaging. The program enabled image normalisation (*e.g.,* pixel binning) and scaling to compensate for differences in molecular extraction efficiencies.
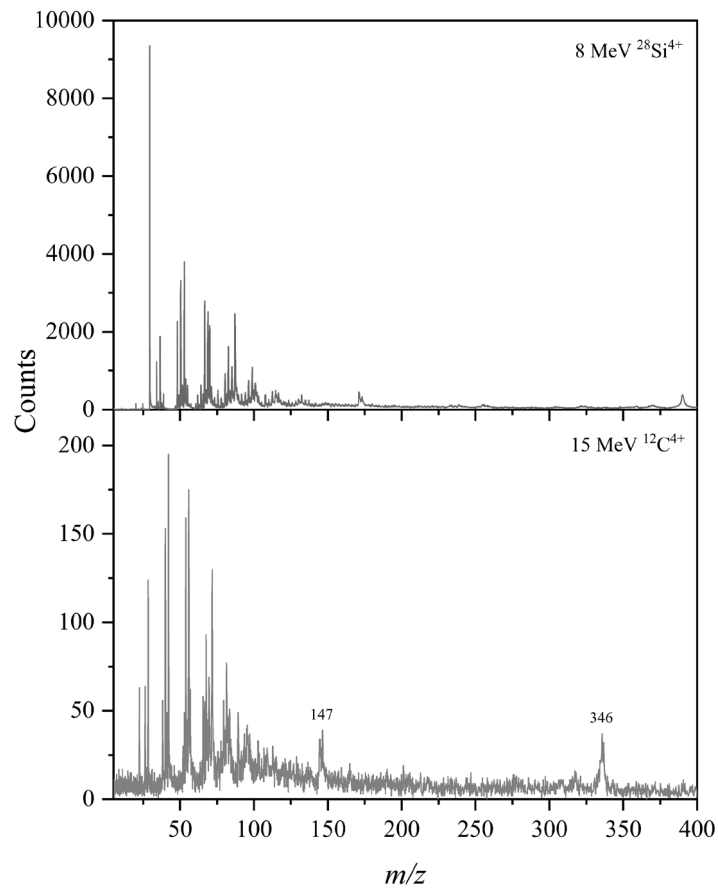
Figure 5.14. 15 MeV $^{12}C^{4+}$ and *8 MeV $^{28}Si^{4+}$ induced inkjet + laser toner MeV SIMS spectra*
up to 400 dalton

The inkjet pigment can be identified from the high intensity Na peak (23 *m/z*) in the low mass range, where an unknown peak at 385 *m/z* from the laser toner was detected in the silicon spectra. The laser toner could also be identified at 346 *m/z* in the spectra due to carbon, however, was not seen in the silicon spectra. It is noteworthy that the overall intensity of the carbon spectra was significantly lower than that of silicon. The low extraction efficiency for carbon was mainly due to lower stopping powers compared to the heavier and slower silicon ions. Lower stopping powers also limited the desorption of heavier masses for carbon, as seen in Figure 5.15.
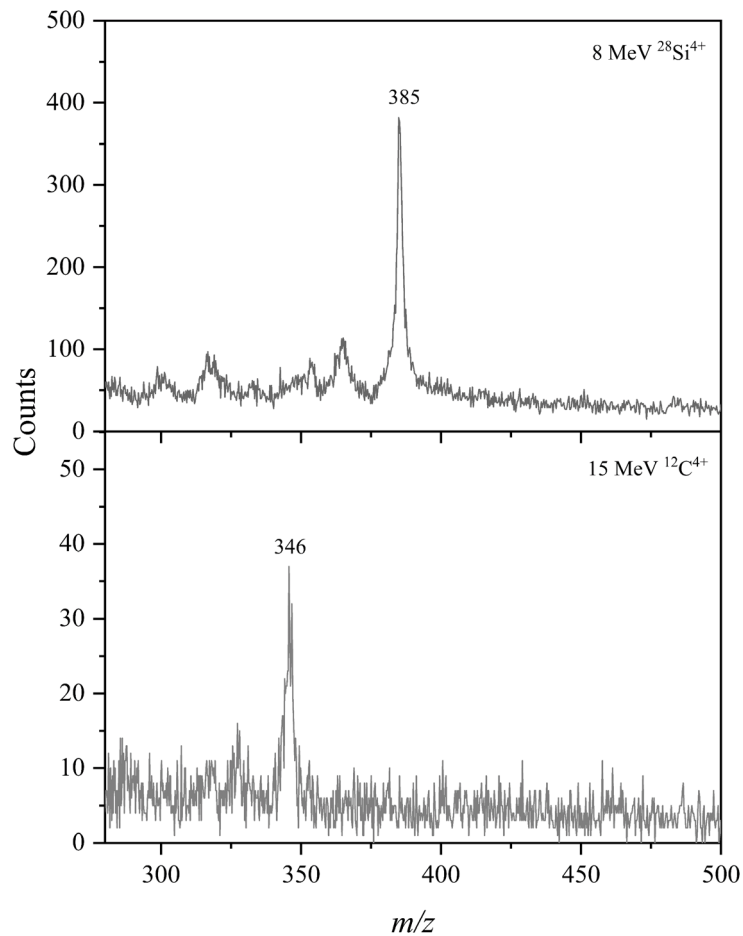
Figure 5.15. 15 MeV ^{12}C^{4+} and *8 MeV ^{28}Si^{4+} induced MeV SIMS spectra (heavy mass region)*

Other peaks in the spectra (Fig. 5.14) represent molecular fragments mostly due to the laser toner, as well as traces of PDMS at 147 *m/z*. The deposition order between inkjet and laser becomes ambiguous at line intersections in the MeV SIMS spectra since the molecules are desorbed from the uppermost layers. In cases where the laser toner ink was deposited above inkjet, only the surface molecules from the toner were detected. The same would be true if the toner was deposited first, since the water-based inkjet would not permeate the laser toner polymer surface, due to the composition of its binder. In both cases, only the laser toner would be visible in the intersection. The PCA analysed image is shown in Figure 5.16.
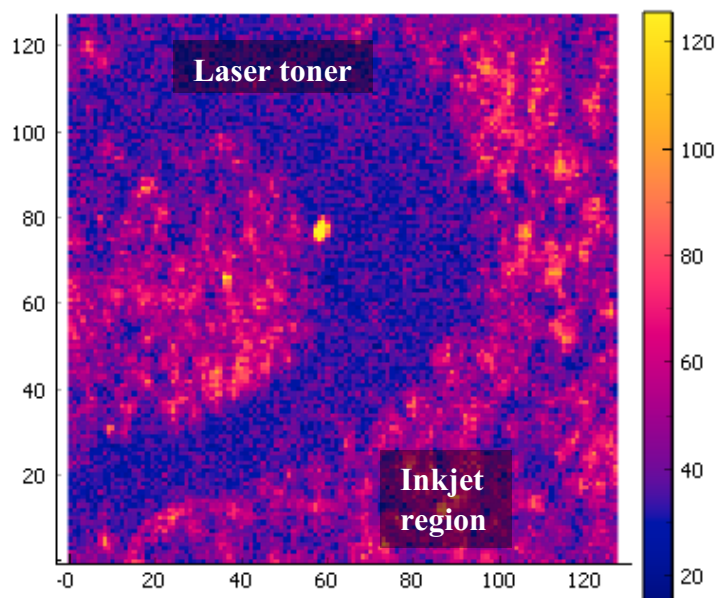
Figure 5.16. *8 MeV $^{28}Si^{4+}$ induced MeV SIMS PCA 1 image, inkjet over toner. 125x125 pixel array*

The largest variation between the paper substrate and the laser toner line was seen using PCA analysis, where the inkjet line was not visible. The same was seen for both carbon and silicon, with the difference only being the intensity of the map. The use of PIXE however, due to the fact that X-rays are produced and detected from deeper layers, enabled the evaluation of the inkjet layer. The continuity or breakage of the inkjet line determined using PIXE complemented MeV SIMS data in deducing the deposition order. The Heavy Ion PIXE spectra is thus shown in Figure 5.17, comparing the same incident ions evaluated with MeV SIMS.
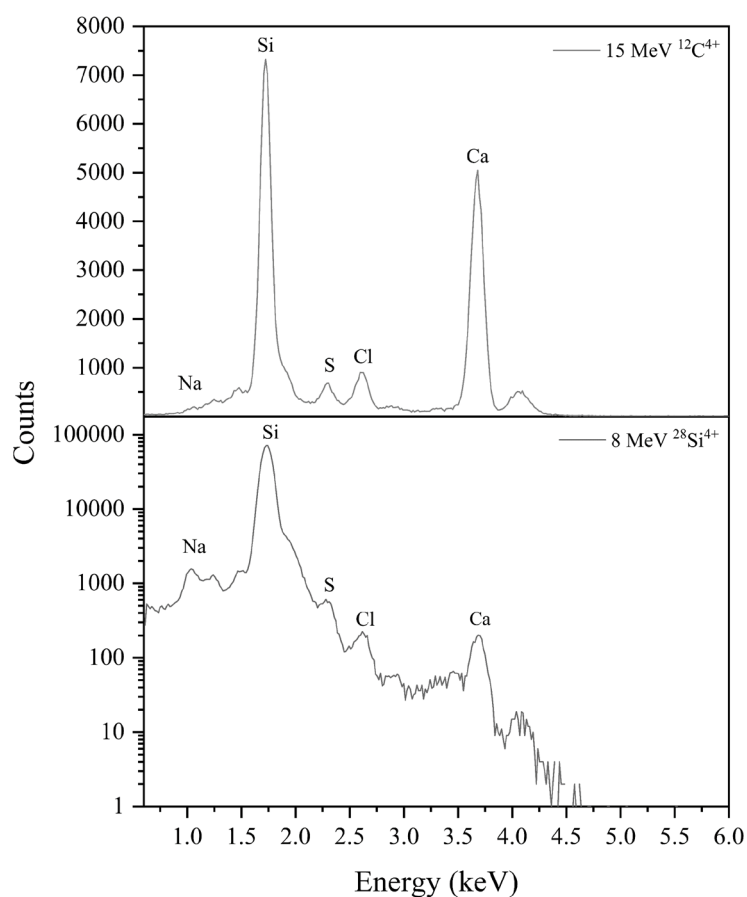
Figure 5.17. *15 MeV $^{12}C^{4+}$ and 8 MeV $^{28}Si^{4+}$ inkjet + toner PIXE spectra*

A 12.5 *μm* Mylar detector filter was used for all measurements to attenuate the high intensity silicon peak from the laser toner or from the beam itself in the case of 8 MeV $^{28}Si^{4+}$ ions. The samples were mounted on a silicon wafer to generate an extraction field (*i.e.,* bias on the target) for MeV SIMS. Since the laser toner contains silicon in the spectra, variations of the silicon intensities in pixels where the toner was deposited and the rest of the sample area could be carried out using PCA, for the case where the silicon ion beam was used. The same extends for X-rays emitted by the silicon projectile in the target. It becomes clear that carbon is much more suited for PIXE compared to silicon – of course, due to fewer MI effects. The comparison of the spectra shows an opposing effect, where not only are the lines better resolved for carbon (almost comparable to protons as shown before), but have a significantly higher X-ray yield. This is owing to higher X-ray production cross sections, the benefit of which shall be seen later on in the analysis of paint samples. Although the shallow sodium line was barely distinguishable due to low detector efficiency and attenuation by the detector filter, the sulphur line from inkjet was clearly visible, in clear form for the carbon ionisations. The intensity of the calcium peak from the paper substrate was low, signifying reducing X-ray production cross

sections with the increasing photon energy. Nonetheless, even with shallow penetration of the silicon ions, the two (Na and S) peaks from both spectra could be used. Fortunately, since no elements heavier than calcium are present in the ink composition, the use of silicon ions was suitable, even with low X-ray production cross sections. The silicon induced PIXE map is shown in Figure 5.18 below.
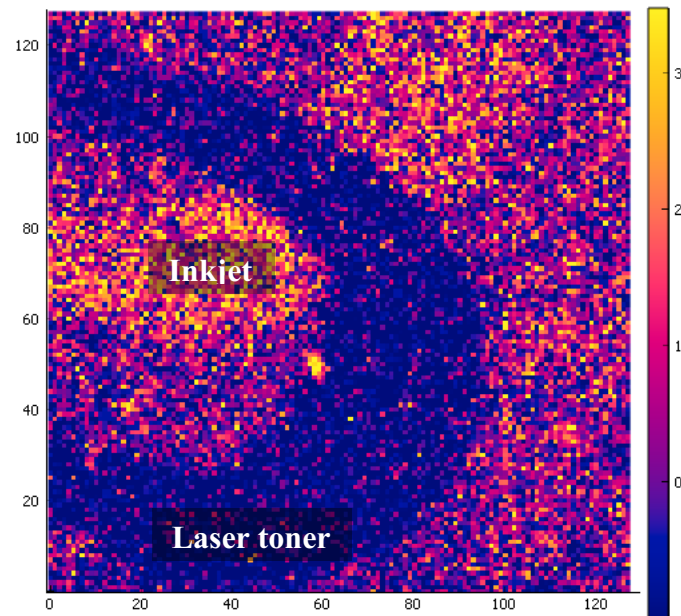
Figure 5.18. *8 MeV $^{28}Si^{4+}$ induced PIXE PCA 1 image, inkjet over laser toner*

The clear contrast between the lines/ breakage in the inkjet deposition indicated that the inkjet line was deposited after the laser toner, as no X-rays from below the laser toner surface layer were detected. This was confirmed by the carbon map, which is identical but differs only in the intensity of the events.

It was deduced then that the use of silicon for both PIXE and MeV SIMS was largely limited by the low XPCS as well as MI effects, which significantly deteriorated the X-ray spectrum. The much lighter carbon ions on the other hand, deviated only slightly from protonic ionisation, as already mentioned in Chapter 4, resulting in lower MI effects. It is for this reason that the characteristic peaks are both intense and well defined, making the evaluation of variations in the image much easier. Additionally, carbon may be suitable for samples containing heavier elements, but are limited for SIMS due to low stopping cross sections. This, along with the generally low statistics in the mass spectra, indicates that while carbon may work well for PIXE, low stopping cross sections are a limiting factor for MeV SIMS. Although reducing the

ion energy would in principle slightly increase the stopping power, the statistics in the mass spectra moreover for heavy molecules of interest would not sufficiently increase. As a potential intermediary ion between carbon and silicon, the use of oxygen ion beams was also investigated, however for a different (composition) set of inks. The mass spectra for 12 MeV $^{16}O^{4+}$ is shown in Figure 5.19.
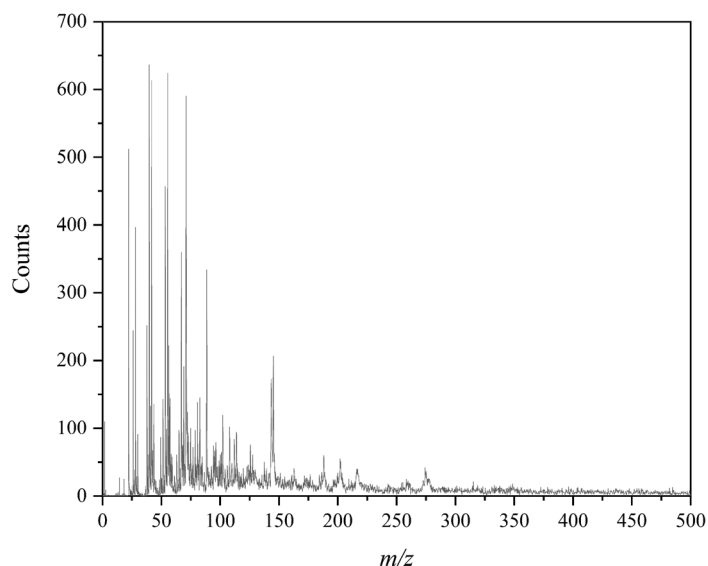
Figure 5.19. *Inkjet + laser toner MeV SIMS spectra due to 12 MeV $^{16}O^{4+}$ impact*

Although there are more counts compared to the spectra due to carbon, it can be seen that no heavy molecules were detected, albeit the difference in the composition of the inkjet ink analysed compared to that used in the carbon – silicon demonstration. Nonetheless, the comparison of the spectra as far as other lighter mass peaks (*e.g.,* PDMS at 147 *m/z*) are concerned is sufficient in showing the higher sputtering yield compared to carbon. The comparison of oxygen, carbon and silicon ions is shown later for a different set of samples. In the main, the sulphur peak can be seen from the PIXE spectra (see Fig. 5.20).
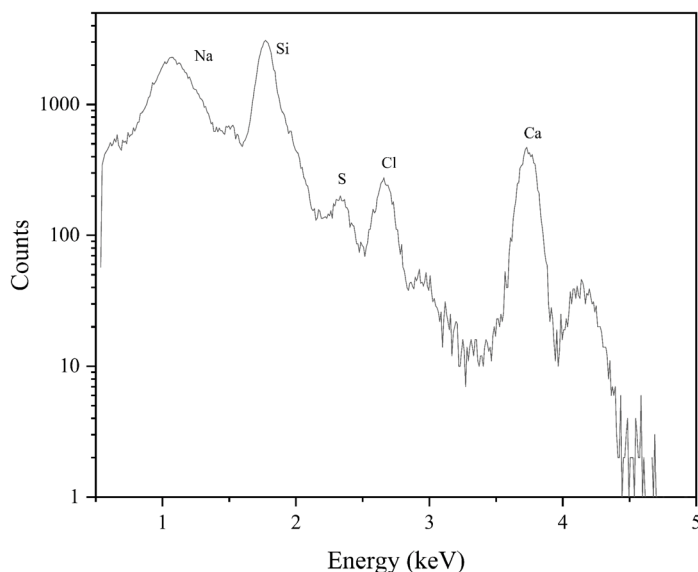
Figure 5.20. *Inkjet + laser toner HI PIXE spectra due to 12 MeV $^{16}O^{4+}$ impact*

The definition of the peaks can be seen to be less than that due to carbon, but more than that due to silicon. Similarly, a higher X-ray yield than that due to silicon was recorded. While oxygen clearly balances between carbon and silicon as far as the molecular mass and X-ray yields are concerned, it is seen to provide no additional information in the MeV SIMS spectrum. Nevertheless, MVA analyses of the MeV SIMS and PIXE images showed the largest variation (PCA 1) being mainly between the paper substrate and the inkjet ink. Both inks are shown in Figure 5.21.
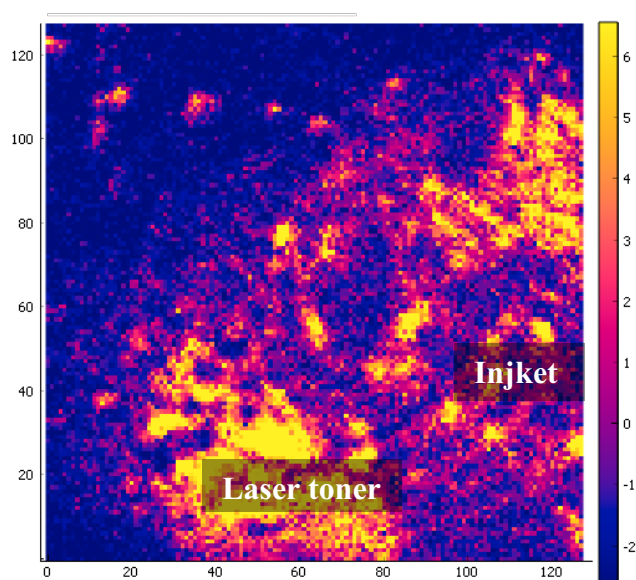
Figure 5.21. *MeV SIMS PCA 1 for laser toner over inkjet, evaluated using 12 MeV $^{16}O^{4+}$ ions*

Surprisingly, traces of the inkjet line could be seen in the MeV SIMS spectra, however yielding very low events with clear ambiguity in the overlap region. On the other hand, the laser toner could only be seen by the conture diagonal to the inkjet deposition, differing only slightly from the paper substrate. Indeed, the presence of the inkjet line cannot be asserted, as the variations may also be a result of layer erosion due to ion beam induced damage. Even so, small ink traces can be seen sparsely populating the grain like structures in the PIXE map (PCA 2). The continuity of the inkjet line nevertheless indicated that the inkjet layer was deposited first, even with no visible line from the laser toner. While the use of oxygen beams may find success, moreover invoking the use of MVA methods, it seems indifferent to the use of carbon in as far as the synergy of both IBA techniques is concerned.
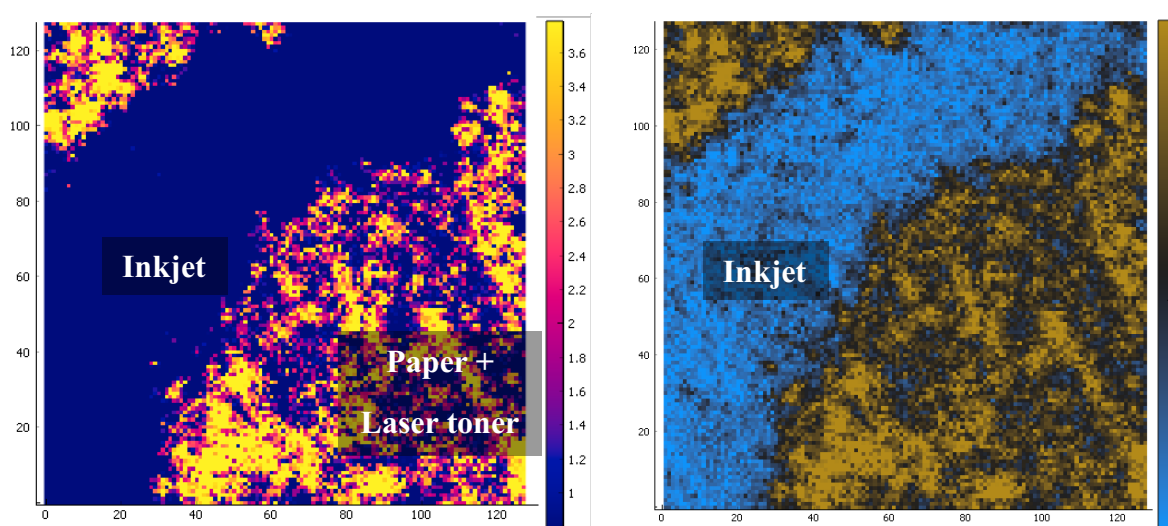
Figure 5.22. *PIXE PCA 1 (left) and PCA 2 (right) maps for laser toner over inkjet, evaluated using 12 MeV $^{16}O^{4+}$ ions. Image axis represents a 125x125 pixel array*

5.2.2. Paint pigments for cultural heritage

Similar to the evaluation of ink pigments, the use of carbon, oxygen and silicon ions for the sequential application of HI PIXE and MeV SIMS was investigated for the identification of pigments in paints. The identification of pigments from paint samples is of significant importance for cultural heritage, particularly for the restoration of ancient art pieces as well as to verify the authenticity of works of art for curators. The implementation of Ion Beam Analysis for cultural heritage is well documented in literature, underpinning the use of more than one technique to improve the efficacy of analyses [159]. One such is the use of MeV SIMS for the desorption of synthetic and organic surface molecules in order to identify the molecular

compositions of paint pigments. The intuitive implementation of proton PIXE with MeV SIMS may describe both molecular and elemental compositions, thus providing information on the chemistry of the analysed target. Of course, the use of MeV SIMS and proton PIXE sequentially means that the same analytical region is not evaluated, which limits the correlation between the two techniques (as mentioned before). The use of the same heavy ions on the same analytical region for both MeV SIMS and HI PIXE is of particular interest, moreover as the technique could potentially be expanded to in-air applications [160].

5.2.2.1. Schmincke paints

The first paint sample(s) used were commercially purchased paints, comprised of resin oil binded pigments from Schmincke. Three resin oil colours where casted on glass and left to dry, and thereafter peeled off and mounted on a silicon wafer using carbon tape. The colours where namely Turquoise – azo pigment (Cr_2O_3, Fe_2O_3), green Paul Veronese (phthalo green) - azopigments and Royal blue deep (ultramarine) (TiO_2, ZnO, $Na_7Al_6Si_6O_{24}S_3$). Ideally, paint samples are mounted on silicon wafers using indium, in order to attain a strong extraction field (as with the second set of samples reported later in the text). The non-use of indium in this case was however simply due to the glutinous nature of the resin, which unfortunately required the use of carbon tape in order to firmly fix the samples onto the silicon wafer without changing the surface mophorlogy. Changing the surface mophorlogy would result in high and low extraction points, significantly affecting the MeV SIMS map. Since indium was not used, high extraction fields were instead obtained through the use of wider silicon wafers. It should however be mentioned that even with the use of carbon tape, pressing the paints on the tape introduced some degree of surface morphology, where high emission rates were recorded from the high points in the surface structure for some samples. Nonetheless, since the objective of the study was mainly to evaluate analytical conditions for identifying different pigments using PIXE and MeV SIMS by the same heavy ions, surface roughness measurements were not undertaken.

Likewise, ToF MeV SIMS was carried out in positive ion mode, and investigated using 12 MeV $^{12}C^{q+}$, 12 MeV $^{16}O^{q+}$ and 8 MeV $^{28}Si^{q+}$. The molecular mass spectra comparing the effects of the different projectiles is shown in Figure 5.23 below.
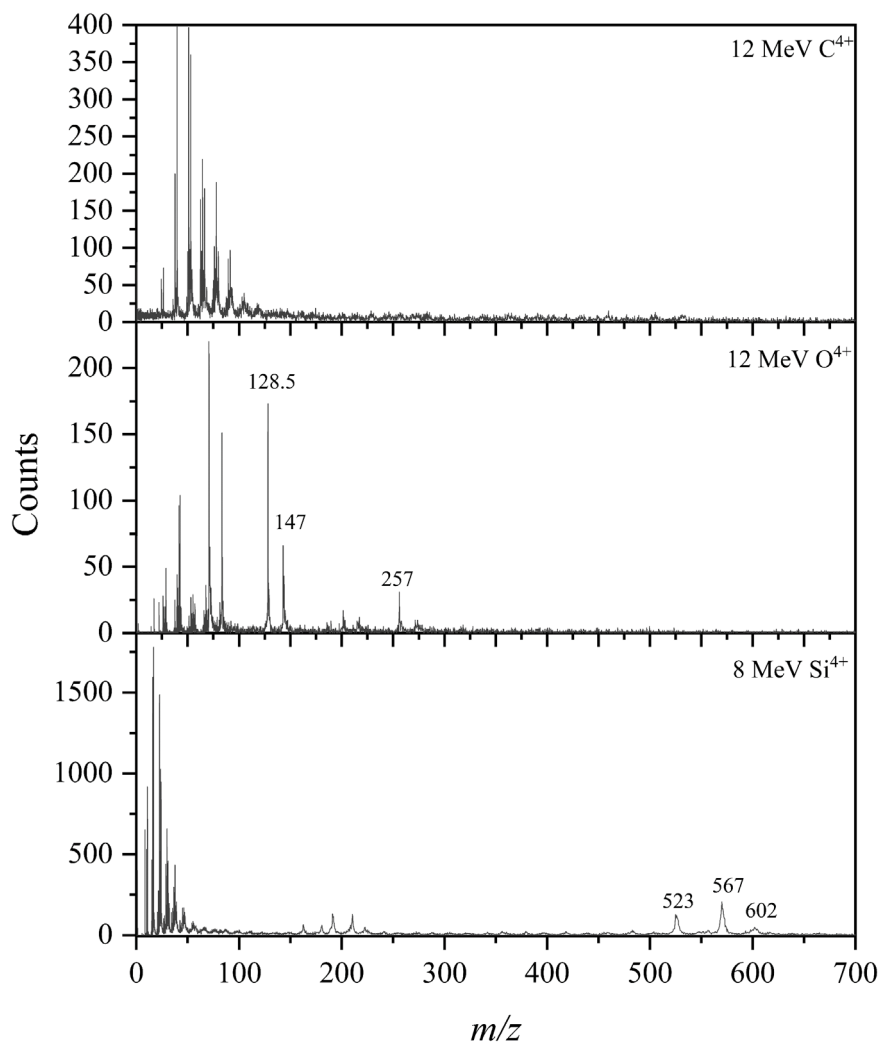
Figure 5.23. *Schmincke paints' mass spectra due to 12 MeV $^{12}C^{4+}$, 12 MeV $^{16}O^{4+}$ and 8 MeV $^{28}Si^{4+}$*

The main peak characteristic to the royal deep blue pigment was seen at 257 m/z, from the palmitic acid $[M+H]^+$ ion. The peak can be seen in the mass spectra due to oxygen, where the remaining detected peaks are due to the oil binder and additives in the material. Amongst these are also stearic acid $[M-OH]^+$ at 267, seen from turquoise. Heavier molecules were also detected from turquoise, with peaks at 523 m/z and 551 m/z (a diglyceride of palmitic acid), as seen in the silicon induced mass spectra. These heavy peaks were not visible in both the oxygen and carbon spectra.

The limitation of the low stopping powers for the lighter ions is seen even more clearly for carbon, despite the comparitively higher rate compared to oxygen, where even the royal blue deep main peak at 257 *m/z* is not visible. Even so, the identification of the pigments could be carried out using low mass fragment peaks from the pigments, such as the 128.5 *m/z* palmitic

135

acid fragment seen in the oxygen spectrum. The significant limitation where the extraction of heavy molecules using either carbon or oxygen may be only partly overcome using MVA, for the extraction of small fragment peaks for specific regions in the map. However, such data would need to be correlated with the X-ray data from PIXE, provided that the X-ray production cross section is high enough for heavy element excitation. Even so, it is clear that this limitation may provide misleading outputs, especially for sensitive materials such as paint samples where the authenticity of a paint is in question. The use of HI PIXE for identifying elements corresponding to the pigments, excited using carbon and oxygen ions is shown in the spectra below. The use of silicon ions for PIXE was not considered, as it has already been shown (*i.e.,* inks spectra) that the detection of elements above ~4 keV would be limited by low XPCS for the incident ion energies obtainable in the experimental setup used. For reference, the carbon and oxygen spectra were thus compared to 2 MeV proton induced PIXE data.
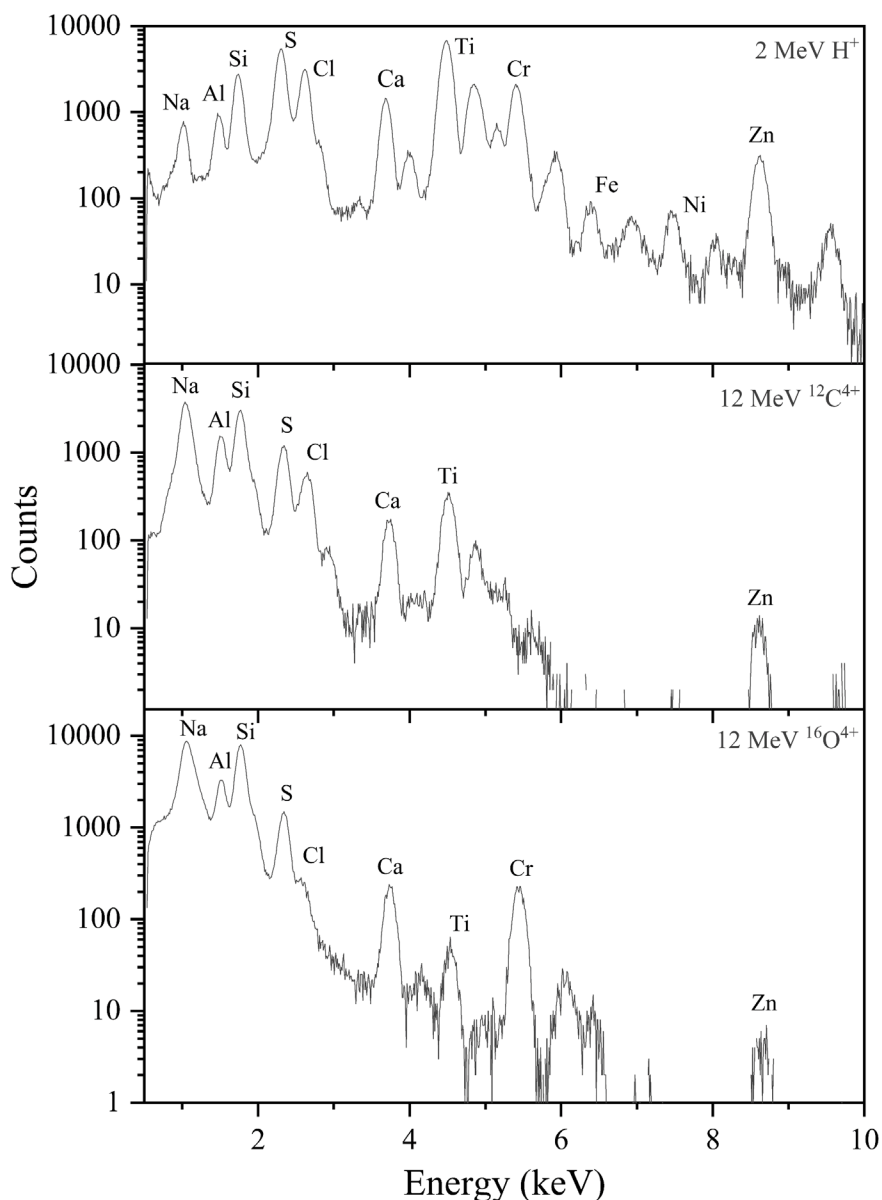
Figure 5.24. *PIXE spectra of Schmincke paints obtained with three different ions*

Although there are significant changes to the intenstiy ratios for carbon ions, which resulted in some low K_β lines, elements up to Fe could be identified. Multiple ionisation effects which resulted in significant changes in intensity ratios for oxygen, limited the detection of some elements in the multi-elemental spectra. The difference in peak intensities for Ti and Cr comparing the C and O spectra was due to differences in the contributing areas of the pigments in the scanned region. This was due to the fact that an exact analytical region could not be matched for all beam types, which indeed further illustrates the motivation for Total IBA.

The composition of the phthalo green paint was very similar to that of turquoise. For this reason, the evaluated differences in the MeV SIMS and PIXE spectra were only limited to the royal blue deep and turquoise pigments alone, as shown in the PIXE scan.
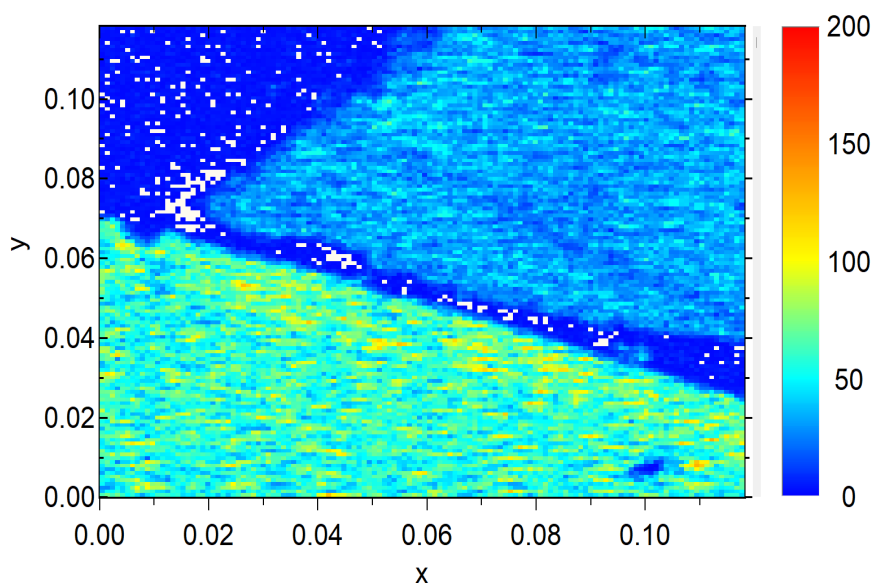
Figure 5.25. *12 MeV carbon induced PIXE 2D map of Schmincke paints. Top layer due to royal blue deep (Ti, Zn), bottom layer due to Turquoise (Cr, Fe). 10x10μm² focussed beam, 2D map axis scale in cm units*

The diamond-like structures in the map are not from the sample, but rather artifacts from experiment. These 'structures' were caused by the coinciding beam scanner and Van de Graaff accelerator charging belt frequency, where the high and low current (or beam flash points) matched with the time at which the beam dwelled on a pixel (*i.e.,* dwell time). The 'diamond' shapes therefore represented the peak and trough high intensity points. The intensity of these structures was slightly reduced by changing the dwell time in the data acquisition system, and could have been optimised further if needed. Nonetheless, the scan provided sufficient information for purposes of this study, as the main objective was to evaluate the effects of projectile mass on the PIXE and SIMS spectra.

The different intensities seen in the scan were due to different chemical environments which resulted in varying surface binding energies. This facilitated higher intensity from the turquoise in the MeV SIMS spectra (Fig.5.23). Conversely, higher intensity in the PIXE map for the turquoise was due to its atomic matrix, as it was mainly comprised of Cr and Fe oxides; fundamentally less complex than the royal blue deep matrix.

5.2.2.2. 'Cobaye_one' painting

The use of carbon ions was also investigated for a different set of pigments, sampled from a painting evaluated in an IAEA Coordinated Research Project [161]. The objective of this investigation was to identify lead compounds using the same incident ion on the same analytical region to verify the validity of the 23 cm x23 cm easel oil painting crafted on a linen canvas. The presence of lead compounds and elements was used to authenticate the artwork. An image of the painting and the sampled region are shown in Figure 5.26.

Figure 5.26. *'Cobaye_one' painting (left), and 2 cm^2 sample coupon (right)*

ToF MeV SIMS was carried out in positive ion mode, using a 15 MeV $^{12}C^{5+}$ ion beam. Although MeV SIMS is generally good for detecting organic compounds, the mass spectra was used to detect the inorganic lead white pigment $PbCO_3$ $Pb(OH)_2$, which was produced using a fine lead carbonate with vegetable drying oil. The detection of both lead oxide compounds from the lead white pigment, as well as compounds from the binder was important for validating the painting. Lead white is an important pigment which was widely used from the classical era as the most produced white pigment, including for the drawing of European easel paintings [162], [163]. The pigment was replaced by zinc and titanium white pigments, finally halting its production around the 19th century [163]. The presence of lead white compounds in a material can therefore be used to indicate whether a painting was crafted before the 20th century. This can be seen in the MeV SIMS spectra through the detection of the binder and lead oxide compounds.

The molecular spectra is shown in the Figure 5.27.
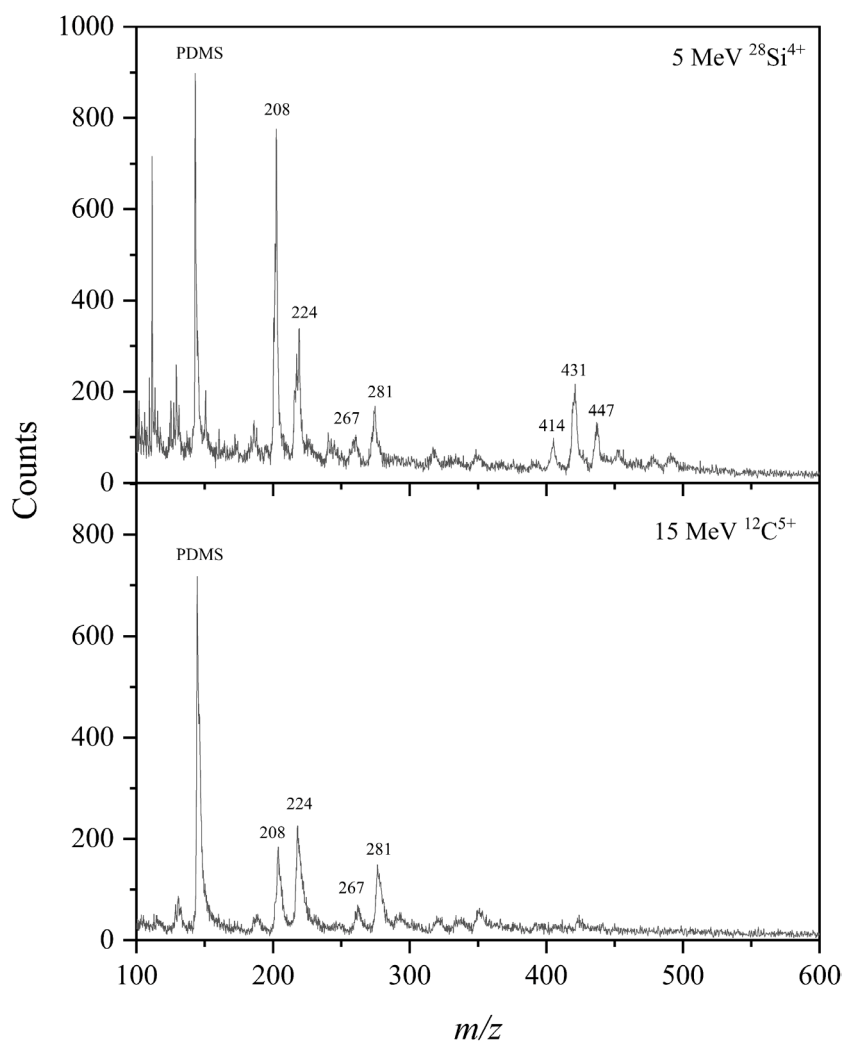
Figure 5.27. *Cobaye_one MeV SIMS spectra due to 15 MeV $^{12}C^{5+}$ and 5 MeV $^{28}Si^{4+}$. Silicon data obtained from* [161]

Three lead white compounds, namely Pb^+ at 208 *m/z*, PbO^+ at 224 *m/z* as well as the shallow Pb_2O^+ at 431 *m/z* were identified in the mass spectra. The binders where identified using the stearic and linoleic acids at 267 *m/z* and 281 *m/z* respectively. However, the limitation with the use of carbon ions is again seen with its inability to desorb heavy molecules, thus limiting the detection of the lead white molecules. Heavier molecules can be seen in the silicon induced mass spectra, shown below.
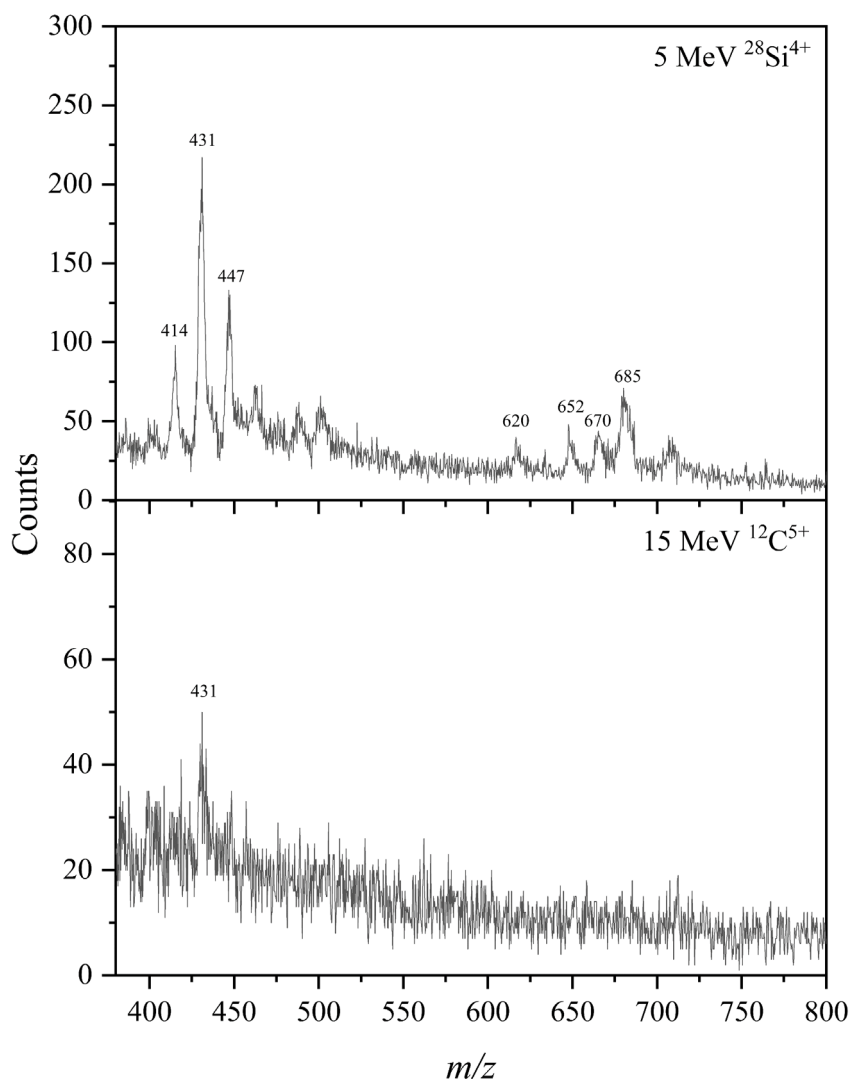
Figure 5.28. *Heavy molecules in the Cobaye_one MeV SIMS spectra obtained using C and Si ions. Silicon induced data was obtained from* [161]

Heavier lead compounds, namely Pb_3^+ at 620 *m/z*, $Pb_3O_2^+$ at 652 *m/z*, $Pb_3O_3^+$ at 670 *m/z* and $Pb_3O_4^+$ at 685 *m/z*, seen with silicon could not be extracted with carbon ions. With this limitation, the presence of the lead white pigment was further corroborated using Heavy Ion PIXE. Although not sensitive to either the lead carbonate nor oxides, the presence of lead white could be deduced from the detection of the lead L- and M- lines in the spectra. The X-ray spectra is shown in Figure 5.29.
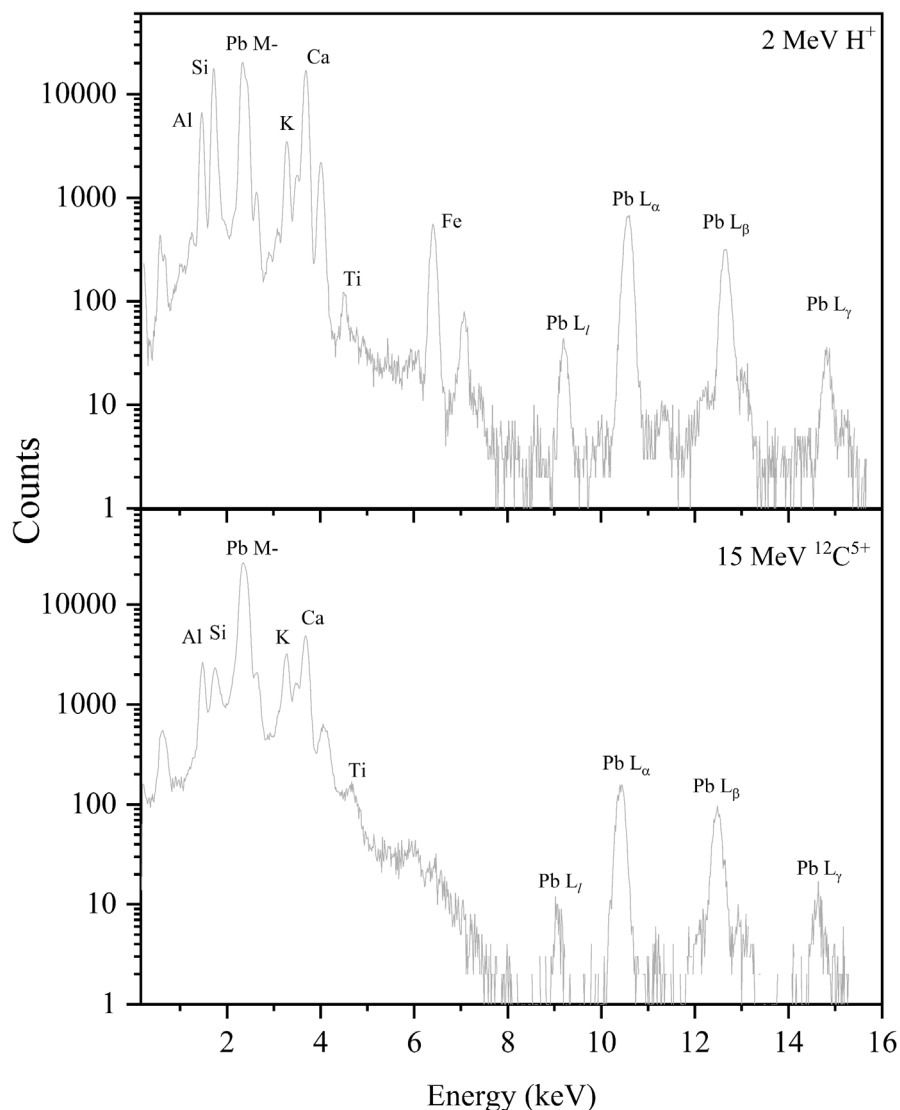
Figure 5.29. *Cobaye_one 15 MeV $^{12}C^{5+}$ PIXE spectra. Proton data was obtained from* [161]

The PIXE spectra due to carbon is comparable to the proton spectra, with the differences lying in changes in the intensity ratios. The high carbon energy enabled L-shell ionisation of even heavy elements such as lead up to the Lγ transition. The faint Fe intensity in the carbon spectra could be due to a difference in the analytical region, notwithstanding reducing X-ray production cross sections. Even within its limitations, the detection of the Pb X-rays along with Pb^+ and PbO^+ ions using carbon beams proved the existence of lead in the paint.

The correlation of the Pb^+ and PbO^+ MeV SIMS map and the Pb M- and L-lines from the PIXE scan are shown in Figure 5.31 below. The regions in the PIXE scan where no X-rays were detected were possited as being due to the presence of some organic material, for which PIXE

is not sensitive. Furthermore, sample morphology may have affected the extraction field, thus resulting in poor counts on one side of the SIMS spectra.

The isolation of the Pb molecules and peaks in both the PIXE and MeV SIMS spectra due to carbon ions was carried out and correlated as shown in the maps below (Figure 5.30).
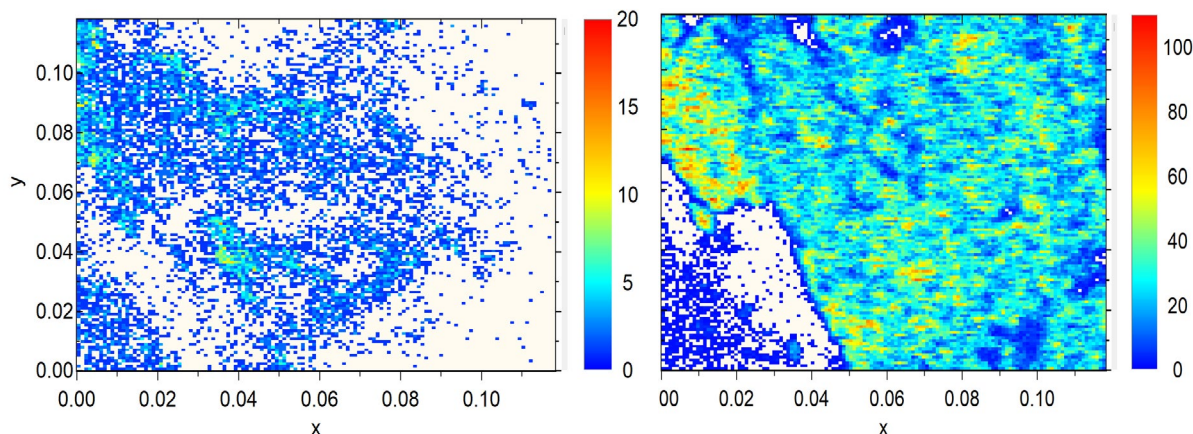
Figure 5.30. *Pb molecular (left), Pb elemental (right) distribution. 2D scan axis scale in cm units*

The molecular map only shows small traces of lead white, with the bulk of the total distribution coming from fragments and the high PDMS intensity distributed across the entire scanned region. Surface contamination by Polydimethylsiloxane (PDMS), an omnipresent organic polymer used in a wide range of applications, may have been the cause of the low Pb molecular ions' signals in the 2D MeV SIMS map seen in Figure 5.30.

The comparatively low X-ray production cross sections can be seen in the PIXE spectra already shown (Fig.5.29) for the Pb L-shell compared to the M-shell. While the use of the high Pb M-along with the L- X-ray intensity provided a very clear image of the Pb distributions in the region, it may however not always be favourable. This is because M- X-rays may coincide with soft K-shell X-rays from lower mass elements such as sulphur, which is especially important for unknown target compositions.

Nonetheless, the use of both PIXE and MeV SIMS using carbon ions, even with the underlying limitations, enabled the identification of the lead white pigment in the scanned area. This shows that the use of lighter ions such as carbon is only partially successful as it limits the efficacy in the co-implementation of the two techniques. The approach may require the use of more energetic heavier ions, such as silicon where electronic stopping powers are comparable to

those due to lower ion energies. This would ideally require the implementation of MeV SIMS with HI PIXE on a chamber mounted on a zero degree beamline selection angle, to obtain higher energies of silicon ions. Nevertheless, within the current experimental setup, where heavier projectile masses are limited by the rigidity of the switching magnet, the selection of the probing beam becomes subjective, depending on the pre-empted molecular and elemental composition/masses investigated.

Chapter 6

X-ray production cross sections

It is true that while the implementation of Heavy Ion PIXE has the potential to remedy some current limitations of IBA techniques such as ERDA and MeV SIMS, it remains restrictive in its application. This is largely due to the complex nature within which the de-excitation of a multiply ionised atom occurs, lacking the required theoretical frameworks. On the one hand, the lack of fundamental data makes the extension of conventional X-ray production models based on protonic ionisation, which generally make proton-based PIXE a favourable mainstay, infeasible. In contrast to protons, as it has been shown in this thesis, the change in collision symmetries based on both the ion and target masses implies non-universality, limiting the empirical fit of currently available datasets. This exhausts efforts at continuously measuring unavailable cross section data, due to the large number of possible ion-atom pairs. The persistence of the still small database therefore requires a re-assessment of the framework in which the generation of new heavy ion induced X-ray production cross section data is approached.

This work has shown that the non-systematic and largely random manner in which cross section data is measured is fundamentally flawed. The random selection of projectile ion-atom combinations from different laboratories has resulted in a scattered database available in the literature, which is also largely unvalidated and difficult to fully exploit.

To address these challenges, the thesis has generated heavy ion induced X-ray production cross section data for more than 20 heavy ion-atom combinations, yielding more than 100 experimental cross sections. The measurements were carried out systematically, using projectile ion beams generally used for heavy ion IBA techniques such as ToF-ERDA and MeV SIMS (*i.e.,* Si, Cl, Cu, Ag and I) covering a wide target range (*i.e.,* Cr, Ni, Ge, Zr, Mo, Sn, W, Au and Bi). The selected ion energy range (0.1 MeV/u – 1.0 MeV/u) was within the slow ion range where ion stopping is largest. The experimental cross section measurements were validated by published data where available, and compared to ECPSSR predictions. While discrepancies between the measured heavy ion induced cross section data and ECPSSR predictions were as expected, gradual agreement with increasing ion energy showed that the

continued enrichment of experimental data especially in the low energy range may improve theory.

Along with the measurement of experimental cross section data, this study has successfully developed a new semi-empirical model for predicting X-ray production cross section data, by scaling available or measured experimental XPCS with calculated theoretical proton cross sections. The use of theoretical proton cross section data was validated by measured experimental low velocity (0.2 MeV – 2.0 MeV) proton induced X-ray production cross sections using Cr, Ni, Ge, Zr, Mo, Sn, W, Au and Bi targets. This novel semi-empirical approach was tested and successfully validated by experiment, demonstrating the feasibility of using limited cross section data to interpolate and therefore extract new datasets for collision symmetries not previously measured. Indeed, while successful, the model still requires additional experimental cross section data for a given ion/target in order to evaluate a given mass range of interest. This is because changing collision symmetries result in changing cross section function gradients, as shown in chapter 4. Nonetheless, the use of semi-empirical cross sections has demonstrated that only a limited range of systematically selected projectile-target combinations can enable parameterisations for the interpolation of a wide range of currently unavailable XPCS.

In the outlook, the study proposes that the continuation of experimental XPCS measurements, in addition to the large contribution from this work, ought to focus only on incident ions and energies useful for the application of ToF-ERDA and MeV SIMS. The proposed incident ions, drawing from the reported work, are namely Si, Cu, Ag and I, for ion energies up to 1 MeV/u. Although $^{197}\text{Au}^{q+}$ ion beams are also often used for ToF – ERDA, X-ray production cross section values especially for the L-shell are expected to be very low, drawing from the XPCS data induced by $^{127}\text{I}^{q+}$, to the effect that the use of Au ions would not be practical.

The focussed enrichment of the cross-section database is expected to enable even more systematic semi-empirical parameterisations, bridging the currently wide data gap. In addition to the semi-empirical model, the study used generated experimental and semi-empirical datasets as training input data into a supervised Machine Learning (ML) ensemble, a method not yet explored at the time of this reporting. The use of ML as a powerful tool for approximating cross section data, which may enable predictions for any given ion-atom pair, was successfully shown to agree with calculated cross section data from the semi-empirical model. Similarities and discrepancies between the different ML classifications and semi-

empirical as well as theoretical cross section data indicated that a blending ensemble approach where classifications are combined/stacked may improve ML predictions. This approach is expected to result in even stronger scores when tested against experimental data, moreover where large training datasets are concerned. Although the full exploration of the use of ML for predicting cross sections was beyond the scope of the current study, the study has successfully shown that ML, with a larger coverage of experimental data, has a strong basis for further and more elaborate pursuit.

Future use of Machine Learning may also be extended to other applications for Heavy Ion PIXE, such as predictions of peak energy shifts and intensity ratios for specific collision symmetries. This data is important for quantitative applications, as demonstrated with the measurement of relative concentrations using Heavy Ion PIXE for Ag and Cd in soil as an example. From a fundamental study's perspective, the use of ML algorithms such as Neural Networks may also become beneficial in the study of Multiple Ionisation effects, moreover for high resolution PIXE spectrometry using heavy ions. As it has been well demonstrated, high resolution spectrometry is a powerful tool for the evaluation of the number of vacancies observed through satellite distributions for a given transition series, and may well be extended for other symmetries as this is yet to be explored. The successful simultaneous use of high resolution PIXE spectrometry with conventional PIXE also underpinned the extension of the PIXE technique for potential use with other applications. Even so, it was seen that the prevalence of Multiple Ionisation may in some cases not be overcome even with the use of high resolution spectrometers, more over for projectile ions heavier than carbon. Similar limitation was seen with the combination of PIXE with other correlated IBA techniques, such as ToF – ERDA and MeV SIMS.

Heavy Ion PIXE – ToF ERDA

The use of Heavy Ion PIXE simultaneously to deconvolute overlapping time of flight – energy spectra has the potential of being a powerful nuclear analytical technique. The approach was demonstrated by the use of Heavy Ion PIXE and ToF – ERDA to obtain relative atomic fractions for Cr, Fe and Ni in a stainless steel sample. The measured relative concentrations were compared to proton PIXE data, with only minimal discrepancies. It was however noted that these current limitations could potentially be remedied through further experimental work. These include optimising the X-ray and recoil rate by adjusting the X-ray detector solid angle, using an appropriate X-ray filter as well as maintaining a reasonably low beam current. Notably

amongst these limitations however, is X-ray peak broadening due to Multiple Ionisation effects which cause the subsequent overlapping of closely lying X-ray peaks. This current limitation indicated the applicability of the technique requiring a mass separation of at least two atomic mass units. As a framework for an ideal system, the study concludes that use of PIXE simultaneously with ERDA would greatly benefit from a Transition Edge Sensor (TES) based high resolution spectrometer. Since TES based spectrometers are broad band and have a high collection efficiency, they could be beneficial in separating closely lying X-ray lines. Of course, as shown before, MI satellite formation may limit the ability to separate some X-ray lines, depending on the collision symmetry.

For the simultaneous implementation of PIXE and ERDA, experimental work beyond the scope of this work is still needed to establish its feasibility for different target types. Although atomic ratios could be obtained using the PIXE spectra, low X-ray yields in the case of thin targets may limit accurate quantitation. The use of X-ray yields scaled using X-ray production cross sections can only be assumed for either homogeneous targets where no depth profile is present.

Future work should aim towards comparing experimental X-ray production cross section ratios for neighbouring elements to those of the ECPSSR for a wide range of ion-target combinations. The premise is that if the ratios are established to be equal, despite discrepancies in the absolute cross section values, then the ECPSSR cross section ratios may be used to infer the relative atomic concentrations even from Heavy Ion PIXE spectra. Nonetheless, a more accurate approach requires a wider use of the semi-empirical and ML models. The continued measurement of XPCS data is therefore paramount for this simultaneous approach.

Heavy Ion PIXE – ToF MeV SIMS

The sequential implementation of MeV SIMS and Heavy Ion PIXE on the same analytical region has proven to improve the efficacy of analyses, consolidating data using the same ion. The success of this approach was shown using paint samples as well as ink pigments deposited on paper for forensic studies. The qualitative use of PIXE with MeV SIMS meant that unlike with ToF – ERDA where peak broadening and lack of cross section data limited analyses, heavy ions could be used to identify elements, even for close lying lines. The drawbacks where unfortunately from the low X-ray production cross sections for the silicon ion beams at the energies used, which led to low X-ray yields for characteristic X-rays above ~4 keV. This meant that while slow silicon ions could be used for the extraction of heavy molecules due to high electronic stopping, heavy elements unfortunately could not be evaluated in the X-ray

spectra. Conversely, lower mass projectiles such as carbon yielded a higher X-ray yield, even partly enabling the detection of heavy element masses like lead. However, the extraction of heavier molecular masses for carbon ion impact was significantly limited. This meant that fragments of intact secondary molecular ions would instead have to be used, where applicable. Oxygen ions were seen to be an intermediary between carbon and silicon in the comparison of the X-ray and molecular mass spectra. In general, Si ions produced better yields of high mass molecular ions. However, the desorption of such molecules may be suppressed for different reasons, such as surface roughness or variations in the extraction field. It is concluded from the results obtained that the use of a single heavy ion for both MeV SIMS and HI PIXE is possible, however depending on the target under investigation. In the case where low mass elements and heavy molecular masses are investigated, a silicon beam is preferable. The use of silicon would however be limited by changes in X-ray intensity ratios and low XPCS for increasing element masses. This may however be overcome by using Multi-Variate Analyses, using unsupervised Machine Learning algorithms such as PCA. If both the molecules and elements detected are of low mass, then carbon or oxygen is an ideal heavy ion. Although the selection of carbon would compromise the yield of the mass spectra, it would however provide the best spectral profile for PIXE, almost comparable to protons. In both cases, changing intensity ratios are likely to slightly deteriorate the profile of the PIXE spectra compared to that of protons.

In the further development of this approach, the use of higher energetic silicon beams ought to enable both the detection of heavy element masses using PIXE as well as heavy molecules using MeV SIMS. Although such an exploration could not be undertaken due to experimental limitations at the time of this reporting, it was nonetheless conclusively shown that the approach is feasible for different target types. The outlook of this approach should therefore extend to other material target types, and also using higher silicon beam energies where permissible. The selection of the energy should of course trade between obtaining a high stopping power along with a reasonably moderate X-ray production cross section for the heaviest element examined.

Further work also ought to investigate damage effects from the use of heavy ions of varying masses, energies and fluences. It would therefore be important particularly for cultural heritage samples such as paintings, where non-destructive analyses are required. While the current experimental setup caters for the evaluation of small samples, it is important to reflect upon the potential realization of an 'in-air' Total IBA system, such as that presented by Matjačić and co-workers [160]. Their approach in developing an ambient pressure MeV SIMS spectrometer

carried out simultaneously with PIXE shows potential for wider scale analyses of paint samples, where the achievement of non-destructive analyses becomes even more significant.

Closing

It is thus concluded upon the reflections made, that the continued implementation of either Heavy Ion PIXE based synergy requires additional X-ray production cross section data. Even so, the study has successfully presented several new experimental heavy ion induced X-ray production cross sections for near-symmetric collisions, the novel semi-empirical model, and the use of a machine learning model for the prediction of cross section data. For the implementation of Total IBA, the self-consistent study of the use of PIXE and ToF – ERDA needs to be further studied. Similarly, the application of Heavy Ion PIXE together with MeV SIMS as an approach that is yet to be fully realised provided insightful results. Both these applications, and the wide scope of topics covered in the thesis demonstrated the potential use for heavy ion PIXE, even while research in the field has to date been lacking. The contribution of this work in extending current Ion Beam Analysis capabilities (with heavy ion PIXE now as a tangible base), has therefore opened more than one area of potential research, each of which worthy of further research. Therefore, in the study's current and significant contribution, this area of research bares the weight required for further investigation.

Bibliography

[1]   R. Ndimba, K. Cloete, L. Mehlo, J. Kossmann, C. Mtshali, and C. Pineda-Vargas, 'Using ICP and micro-PIXE to investigate possible differences in the mineral composition of genetically modified versus wild-type sorghum grain', *Nucl Instrum Methods Phys Res B*, vol. 404, pp. 121–124, 2017.

[2]   I. B. Mihalić *et al.*, 'Multivariate analysis of pixe+ xrf and pixe spectral images', *J Anal At Spectrom*, vol. 36, no. 3, pp. 654–667, 2021.

[3]   M. Uda *et al.*, 'Quantitative analysis of ancient Egyptian pigments by external PIXE', *Nucl Instrum Methods Phys Res B*, vol. 75, no. 1–4, pp. 476–479, 1993.

[4]   J. L. Campbell, G. K. Czamanske, L. MacDonald, and W. J. Teesdale, 'Quantitative analysis of major elements in silicate minerals and glasses by micro-PIXE', *Nucl Instrum Methods Phys Res B*, vol. 130, no. 1–4, pp. 608–616, 1997.

[5]   C. Jeynes *et al.*, '"Total IBA"–Where are we?', *Nucl Instrum Methods Phys Res B*, vol. 271, pp. 107–118, 2012.

[6]   C. Jeynes, V. V Palitsin, M. Kokkoris, A. Hamilton, and G. W. Grime, 'On the accuracy of Total-IBA', *Nucl Instrum Methods Phys Res B*, vol. 465, pp. 85–100, 2020.

[7]   L. G. Svendsen, N. Hertel, and G. Sørensen, 'Detection of trace elements in ash samples performed by combining RBS and PIXE', *Nuclear Instruments and Methods in Physics Research*, vol. 191, no. 1–3, pp. 414–418, 1981.

[8]   M. Tomita, N. Ikuchi, S. Miyagi, and M. Sakisaka, 'A PIXE-RBS method for measuring partial sputtering yields of stainless steel', *Nuclear Instruments and Methods in Physics Research*, vol. 213, no. 2–3, pp. 469–475, 1983.

[9]   B. N. Jones, V. Palitsin, and R. Webb, 'Surface analysis with high energy time-of-flight secondary ion mass spectrometry measured in parallel with PIXE and RBS', *Nucl Instrum Methods Phys Res B*, vol. 268, no. 11–12, pp. 1714–1717, 2010.

[10]   C. Boni, E. Caruso, E. Cereda, G. M. B. Marcazzan, and P. Redaelli, 'A PIXE-PIGE system for the quantitative elemental analysis of thin samples', *Nucl Instrum Methods Phys Res B*, vol. 40, pp. 620–623, 1989.

[11] R. Bugoi, I. Poll, G. Mănucu-Adameşteanu, C. Neelmeijer, and F. Eder, 'Investigations of Byzantine glass bracelets from Nufăru, Romania using external PIXE–PIGE methods', *J Archaeol Sci*, vol. 40, no. 7, pp. 2881–2891, 2013.

[12] B. J. Kirby and G. J. F. Legge, 'Ion beam induced damage and element loss during a microanalysis of biological tissue', *Nucl Instrum Methods Phys Res B*, vol. 54, no. 1–3, pp. 98–100, 1991.

[13] F. Fernandes *et al.*, 'Considerations about projectile and target X-rays induced during heavy ion bombardment', *Nucl Instrum Methods Phys Res B*, vol. 417, pp. 19–25, 2018.

[14] M. Pajek *et al.*, 'L X-ray emission induced by heavy ions', *Nucl Instrum Methods Phys Res B*, vol. 363, pp. 19–23, 2015.

[15] J. Miranda, O. G. De Lucio, and M. F. Lugo-Licona, 'X-ray production induced by heavy ion impact: challenges and possible uses', *Revista mexicana de física*, vol. 53, pp. 29–32, 2007.

[16] H. E. Udeogu, *Quantitative micro-PIXE analysis using the GEOPIXE software*. University of Louisiana at Lafayette, 2018.

[17] J. L. Campbell, T. L. Hopman, J. A. Maxwell, and Z. Nejedly, 'The Guelph PIXE software package III: alternative proton database', *Nucl Instrum Methods Phys Res B*, vol. 170, no. 1–2, pp. 193–204, 2000.

[18] H. R. Verma, 'Atomic and Nuclear Analytical Methods XRF, Mössbauer, XPS, NAA and Ion-Beam Spectroscopic Techniques'.

[19] A. Bendjedi *et al.*, 'L shell fluorescence yields and total ionization and x-ray production cross sections for elements with $40 \leq Z \leq 92$', *Radiation Physics and Chemistry*, vol. 117, pp. 128–134, 2015.

[20] J. E. Prieto, A. Zucchiatti, P. Galán, and P. Prieto, 'Cross sections of X-ray production induced by C and Si ions with energies up to 1 MeV/u on Ti, Fe, Zn, Nb, Ru and Ta', *Nucl Instrum Methods Phys Res B*, vol. 406, pp. 167–172, Sep. 2017.

[21] C. Ciortea *et al.*, 'K-shell ionization in (0.2–1.75) MeV/u Fe, Co+ Cr and Fe+ Cu collisions', *Nucl Instrum Methods Phys Res B*, vol. 235, no. 1–4, pp. 342–346, 2005.

[22] G. Lapicki and J. Miranda, 'Universal empirical fit to L-shell X-ray production cross sections in ionization by protons', *Nucl Instrum Methods Phys Res B*, vol. 414, pp. 184–189, 2018.

[23] J. Miranda *et al.*, 'Measurement of L X-ray production cross sections by impact of proton beams on Hf, Ir, and Tl', *Nucl Instrum Methods Phys Res B*, vol. 316, pp. 113–122, 2013.

[24] R. Mehta, H. L. Sun, D. K. Marble, J. L. Duggan, F. D. McDaniel, and G. Lapicki, 'L-shell X-ray production by 2-12 MeV carbon ions in fifteen selected elements from copper to lead', *Journal of Physics B: Atomic, Molecular and Optical Physics*, vol. 28, no. 7, p. 1187, 1995.

[25] M. Msimanga, C. A. Pineda-Vargas, and M. Madhuku, 'K-shell X-ray production cross sections in Ti by 0.3–1.0 MeV/u 12C and 28Si ions for heavy ion PIXE', *Nucl Instrum Methods Phys Res B*, vol. 380, pp. 90–93, 2016.

[26] A. Haidra, S. Fazinic, S. Ouziane, I. Zamboni, and D. Banas, 'New measurements of Mαβ, Mγ and total M-shell X-ray production cross sections induced by carbon ions on Bi and Pt targets', *Nucl Instrum Methods Phys Res B*, vol. 440, pp. 180–185, Feb. 2019.

[27] I. Gorlachev *et al.*, 'X-ray production cross sections induced by carbon ions', *Nucl Instrum Methods Phys Res B*, vol. 499, pp. 100–106, Jul. 2021.

[28] C. Jeynes, '"Total" Ion Beam Analysis—3 D Imaging of Complex Samples Using M e V Ion Beams', *Characterization of Materials*, pp. 1–12, 2002.

[29] N. P. Barradas and C. Jeynes, 'Advanced physics and algorithms in the IBA DataFurnace', *Nucl Instrum Methods Phys Res B*, vol. 266, no. 8, pp. 1875–1879, 2008.

[30] C. Jeynes *et al.*, 'External beam total-IBA using DataFurnace', *Nucl Instrum Methods Phys Res B*, vol. 481, pp. 47–61, 2020.

[31] E. Cengiz, V. Aylıkcı, N. Kaya, G. Apaydın, and E. Tıraşoğlu, 'Chemical effects on K and L shell production cross sections and transfer probabilities in Nb compounds', *J Radioanal Nucl Chem*, vol. 278, no. 1, pp. 89–96, 2008.

[32] K. L. Moore, M. Barac, M. Brajković, M. J. Bailey, Z. Siketić, and I. Bogdanović Radović, 'Determination of deposition order of toners, inkjet inks, and blue ballpoint pen combining MeV-secondary ion mass spectrometry and particle induced X-ray emission', *Anal Chem*, vol. 91, no. 20, pp. 12997–13005, 2019.

[33] L. Jeromel *et al.*, 'Development of mass spectrometry by high energy focused heavy ion beam: MeV SIMS with 8 MeV Cl7+ beam', *Nucl Instrum Methods Phys Res B*, vol. 332, pp. 22–27, 2014.

[34] S. A. E. Johansson and T. B. Johansson, 'Analytical application of particle induced X-ray emission', *Nuclear Instruments and Methods*, vol. 137, no. 3, pp. 473–516, 1976.

[35] W. R. Leo, *Techniques for nuclear and particle physics experiments: a how-to approach*. Springer Science & Business Media, 2012.

[36] M. Nastasi, J. W. Mayer, and Y. Wang, *Ion beam analysis: fundamentals and applications*. CRC Press, 2014.

[37] M. Mayer, 'Rutherford backscattering spectrometry (RBS)', in *Workshop on Nuclear Data for Science and Technology: Materials Analysis*, 2003.

[38] M. Mayer, 'SIMNRA user's guide', 1997.

[39] P. Sigmund, *Stopping of heavy ions: a theoretical approach*, vol. 204. Springer Science & Business Media, 2004.

[40] P. Sigmund and A. Schinner, 'Progress in understanding heavy-ion stopping', *Nucl Instrum Methods Phys Res B*, vol. 382, pp. 15–25, Sep. 2016, doi: 10.1016/j.nimb.2015.12.041.

[41] J. F. Ziegler, 'Stopping of energetic light ions in elemental matter', *J Appl Phys*, vol. 85, no. 3, pp. 1249–1272, 1999.

[42] Y. J. Lindhard, M. Scharff and H. E. Schiøt, '*Range concepts and heavy ion ranges',* Vol. 33, 1963.

[43] P. L. Grande and G. Schiwietz, 'Impact-parameter dependence of the electronic energy loss of fast ions', *Phys Rev A (Coll Park)*, vol. 58, no. 5, p. 3796, 1998.

[44] P. Sigmund, 'Stopping power in perspective', *Nucl Instrum Methods Phys Res B*, vol. 135, no. 1–4, pp. 1–15, 1998.

[45]   A. Schinner and P. Sigmund, 'Expanded PASS stopping code', *Nucl Instrum Methods Phys Res B*, vol. 460, pp. 19–26, 2019.

[46]   P Sigmund, P. and Schinner, A., 2002. Binary theory of electronic stopping. *Nuclear Instruments and Methods in Physics Research Section B: Beam Interactions with Materials and Atoms*, *195*(1-2), pp.64-90.

[47]   M. V Moro, P. Bauer, and D. Primetzhofer, 'Experimental electronic stopping cross section of transition metals for light ions: Systematics around the stopping maximum', *Phys Rev A (Coll Park)*, vol. 102, no. 2, p. 022808, 2020.

[48]   J. F. Ziegler and J. P. Biersack, 'The stopping and range of ions in matter', in *Treatise on Heavy-Ion Science: Volume 6: Astrophysics, Chemistry, and Condensed Matter*, Springer, 1985, pp. 93–129.

[49]   A. P. Horsfield, A. Lim, W. M. C. Foulkes, and A. A. Correa, 'Adiabatic perturbation theory of electronic stopping in insulators', *Phys Rev B*, vol. 93, no. 24, p. 245106, 2016.

[50]   C. C. Montanari and P. Dimitriou, 'The IAEA stopping power database, following the trends in stopping power of ions in matter', *Nucl Instrum Methods Phys Res B*, vol. 408, pp. 50–55, 2017.

[51]   M. Msimanga, C. B. Mtshali, and C. A. Pineda-Vargas, 'Stopping force of Ti for $6 \leqslant Z \leqslant 29$ ions measured by time of flight spectrometry', *Nucl Instrum Methods Phys Res B*, vol. 349, pp. 1–5, 2015.

[52]   P. Sigmund, 'Theory of sputtering. I. Sputtering yield of amorphous and polycrystalline targets', *Physical review*, vol. 184, no. 2, p. 383, 1969.

[53]   H. M. Urbassek, 'Status of cascade theory', *ToF-SIMS: Materials Analysis by Mass Spectrometry*, vol. 2, 2013.

[54]   C. Lehmann and P. Sigmund, 'On the mechanism of sputtering', *physica status solidi (b)*, vol. 16, no. 2, pp. 507–511, 1966.

[55]   H. Oechsner, 'Sputtering—a review of some recent experimental and theoretical aspects', *Applied physics*, vol. 8, pp. 185–198, 1975.

[56] P. Sigmund, *Sputtering processes: collision cascades and spikes*, vol. 121. Academic Press, New York, 1977.

[57] P. Sigmund, 'Sputtering by ion bombardment theoretical concepts', *Sputtering by Particle Bombardment I: Physical Sputtering of Single-Element Solids*, pp. 9–71, 2005.

[58] J. F. Ziegler and J. P. Biersack, 'SRIM-2008, stopping power and range of ions in matter', 2008.

[59] R. Kelly, 'Thermal effects in sputtering', *Surf Sci*, vol. 90, no. 2, pp. 280–318, 1979.

[60] R. Kelly, 'Theory of thermal sputtering', *Radiat Eff*, vol. 32, no. 1–2, pp. 91–100, 1977.

[61] H. M. Urbassek, 'Molecular-dynamics simulation of sputtering', *Nucl Instrum Methods Phys Res B*, vol. 122, no. 3, pp. 427–441, 1997.

[62] M. Bozoian, K. M. Hubbard, and M. Nastasi, 'Deviations from Rutherford-scattering cross sections', *Nucl Instrum Methods Phys Res B*, vol. 51, no. 4, pp. 311–319, 1990.

[63] H. H. Andersen, F. Besenbacher, P. Loftager, and W. Möller, 'Large-angle scattering of light ions in the weakly screened Rutherford region', *Phys Rev A (Coll Park)*, vol. 21, no. 6, p. 1891, 1980.

[64] D. Abriola *et al.*, 'Development of a reference database for Ion Beam Analysis and future perspectives', *Nucl Instrum Methods Phys Res B*, vol. 269, no. 24, pp. 2972–2978, 2011.

[65] W. M. A. Bik and F. Habraken, 'Elastic recoil detection', *Reports on Progress in Physics*, vol. 56, no. 7, p. 859, 1993.

[66] P. Trocellier and T. Sajavaara, 'Elastic recoil detection analysis', *Encyclopedia of Analytical Chemistry: Applications, Theory and Instrumentation*, 2006.

[67] K. Ishii, 'PIXE and its applications to elemental analysis', *Quantum Beam Science*, vol. 3, no. 2. MDPI, Jun. 01, 2019.

[68] M. Gryziński, 'Classical theory of electronic and ionic inelastic collisions', *Physical Review*, vol. 115, no. 2, p. 374, 1959.

[69] B. K. Thomas and J. D. Garcia, 'Ionization of positive ions', *Physical Review*, vol. 179, no. 1, p. 94, 1969.

[70] J. S. Hansen, 'Formulation of the binary-encounter approximation in configuration space and its application to ionization by light ions', *Phys Rev A (Coll Park)*, vol. 8, no. 2, p. 822, 1973.

[71] M. Gryzinski and J. A. Kunc, 'Collisional ionisation and the atomic model', *Journal of Physics B: Atomic and Molecular Physics*, vol. 19, no. 16, p. 2479, 1986.

[72] W. Brandt and G. Lapicki, 'Binding and Coulomb-deflection effects in L-shell Coulomb ionization by heavy charged particles. Low particle velocities', *Phys Rev A (Coll Park)*, vol. 10, no. 2, p. 474, 1974.

[73] G. S. Khandelwal and E. Merzbacher, 'Characteristic X-Ray Production in Atomic L and M Subshells', *Physical Review*, vol. 151, no. 1, p. 12, 1966.

[74] W. Brandt and G. Lapicki, 'L-shell Coulomb ionization by heavy charged particles', *Phys Rev A (Coll Park)*, vol. 20, no. 2, p. 465, 1979.

[75] G. Lapicki, R. Laubert, and W. Brandt, 'Coulomb-deflection effect in inner-shell ionization by heavy charged particles', *Phys Rev A (Coll Park)*, vol. 22, no. 5, p. 1889, 1980.

[76] W. Brandt and G. Lapicki, 'Energy-loss effect in inner-shell Coulomb ionization by heavy charged particles', *Phys Rev A (Coll Park)*, vol. 23, no. 4, p. 1717, 1981.

[77] Ž. Šmit and G. Lapicki, 'Energy loss in the ECPSSR theory and its calculation with exact integration limits', *Journal of Physics B: Atomic, Molecular and Optical Physics*, vol. 47, no. 5, p. 055203, 2014.

[78] S. J. Cipolla, 'The united atom approximation option in the ISICS program to calculate K-, L-and M-shell cross sections from PWBA and ECPSSR theory', *Nucl. Instrum. Methods Phys Res B*, vol. 261, no. 1–2, pp. 142–144, 2007.

[79] M. Vigilante, P. Cuzzocrea, N. De Cesare, F. Murolo, E. Perillo, and G. Spadaccini, 'Light-ion-induced Li ionization of $46 \leq Z \leq 60$ elements: First-and second-order corrections to PWBA', *Nucl Instrum Methods Phys Res B*, vol. 51, no. 3, pp. 232–236, 1990.

[80] L. Kocbach, 'Inner shell coulomb ionization by light ions: applications of the semiclassical approximation', 1976.

[81] D. Trautmann and F. Rösel, 'On the semiclassical description of coulomb ionization of inner shells', *Nuclear Instruments and Methods*, vol. 169, no. 2, pp. 259–272, 1980.

[82] L. Sarkadi and T. Mukoyama, 'Coupled-states model calculations of L-subshell ionisation probabilities for Ne on Yb, Pt collisions', *Journal of Physics B: Atomic and Molecular Physics*, vol. 20, no. 17, p. L559, 1987.

[83] M. Pajek *et al.*, 'Multiple ionization and coupling effects in L-subshell ionization of heavy atoms by oxygen ions', *Phys Rev A (Coll Park)*, vol. 68, no. 2, p. 022705, 2003.

[84] I. Fijał-Kirejczyk *et al.*, 'Coupling and binding-saturation effects in L-subshell ionization of heavy atoms by 0.3–1.3-MeV/amu Si ions', *Phys Rev A (Coll Park)*, vol. 77, no. 3, p. 032706, 2008.

[85] G. Lapicki, 'The status of theoretical L-subshell ionization cross sections for protons', *Nucl Instrum Methods Phys Res B*, vol. 189, no. 1–4, pp. 8–20, 2002.

[86] V. Horvat, 'ERCS08: A FORTRAN program equipped with a Windows graphics user interface that calculates ECPSSR cross sections for the removal of atomic electrons', *Comput Phys Commun*, vol. 180, no. 6, pp. 995–1003, 2009.

[87] J. Als-Nielsen and D. McMorrow, *Elements of modern X-ray physics*. John Wiley & Sons, 2011.

[88] N. A. Dyson, *X-rays in Atomic and Nuclear Physics*. Cambridge university press, 1990.

[89] C. A. Pineda-Vargas, 'Thick target PIXE analysis', 1993.

[90] J. L. Campbell and J. A. Cookson, 'PIXE analysis of thick targets', *Nucl Instrum Methods Phys Res B*, vol. 3, no. 1–3, pp. 185–197, 1984.

[91] W. Bambynek *et al.*, 'X-ray fluorescence yields, Auger, and Coster-Kronig transition probabilities', *Rev Mod Phys*, vol. 44, no. 4, p. 716, 1972.

[92] J. Crawford, D. D. Cohen, G. Doherty, and A. J. Atanacio, *Calculated K, L, and M shell X-ray line intensities for light ion impact on selected targets from Z= 6 to 100*. Australian Nuclear Science and Technology Organisation, 2011.

[93] M. H. Chen, B. Crasemann, and H. Mark, 'Relativistic K-shell Auger rates, level widths, and fluorescence yields', *Phys Rev A (Coll Park)*, vol. 21, no. 2, p. 436, 1980.

[94] J. A. Tanis, S. M. Shafroth, W. W. Jacobs, T. McAbee, and G. Lapicki, 'K-shell x-ray production in K19, Ti22, Mn25, and Br35 by 2080-MeV Cl17 ions', *Phys Rev A (Coll Park)*, vol. 31, no. 2, pp. 750–758, 1985.

[95] L. H. Toburen and F. P. Larkins, 'Effects of Multiple Ionization on the Fluorescence Yield of Carbon', *Phys Rev A (Coll Park)*, vol. 6, no. 6, p. 2035, 1972.

[96] C. M. Heirwegh *et al.*, 'Multiple ionization X-ray satellites of magnesium, aluminum and silicon in alpha particle PIXE', *Nucl Instrum Methods Phys Res B*, vol. 428, pp. 9–16, Aug. 2018.

[97] I. Božičević Mihalić, S. Fazinić, and D. Cosic, 'High resolution K X-ray spectra of selected silicates induced by MeV proton and carbon micro-beams', *Nucl Instrum Methods Phys Res B*, vol. 417, pp. 70–74, Feb. 2018.

[98] I. B. Mihalić, S. Fazinić, T. Tadić, D. Cosic, and M. Jakšić, 'Study of ion beam induced chemical effects in silicon with a downsized high resolution X-ray spectrometer for use with focused ion beams', *J Anal At Spectrom*, vol. 31, no. 11, pp. 2293–2304, Nov. 2016.

[99] F. P. Larkins, 'Dependence of fluorescence yield on atomic configuration', *Journal of Physics B: Atomic and Molecular Physics*, vol. 4, no. 5, p. L29, 1971.

[100] M. Msimanga, 'Development of a Time of Flight-Energy spectrometer for applications in Heavy Ion-Elastic Recoil Detection thin film analysis', 2010.

[101] M. Msimanga, D. Wamwangi, C.M. Comrie, C.A. Pineda-Vargas, M. Nkosi, and T. Hlatshwayo, 'The new Heavy Ion ERDA set up at iThemba LABS Gauteng: Multilayer thin film depth profiling using direct calculation and Monte Carlo simulation codes', *Nucl Instrum. and Methods in Physics Research Section B, vol. 296*, pp.54-60, 2013.

[102] T. Tadić *et al.*, 'Development of a TOF SIMS setup at the Zagreb heavy ion microbeam facility', *Nucl Instrum Methods Phys Res B*, vol. 332, pp. 234–237, Aug. 2014.

[103] G. W. Grime, 'The " Q factor" method: quantitative microPIXE analysis using RBS normalisation', *Nucl Instrum Methods Phys Res B*, vol. 109–110, pp. 170–174, 1996.

[104] A. Bergmaier, G. Dollinger, C. M. Frey, and T. Faestermann, 'Quantitative elastic recoil detection (ERD)', *Fresenius J Anal Chem*, vol. 353, pp. 582–584, 1995.

[105] S. Ritt, P. Amaudruz, and K. Olchanski, 'Maximum Integrated Data Acquisition System (MIDAS)', *Paul Scherrer Institute (PSI), Switzerland, TRIUMF, Canada*, 1993.

[106] I. Antcheva *et al.*, 'ROOT—A C++ framework for petabyte data storage, statistical analysis and visualization', *Comput Phys Commun*, vol. 180, no. 12, pp. 2499–2512, 2009.

[107] T. F. Silva *et al.*, 'MultiSIMNRA: A computational tool for self-consistent ion beam analysis using SIMNRA', *Nucl Instrum Methods Phys Res B*, vol. 371, pp. 86–89, Mar. 2016.

[108] A. F. Gurbich, 'SigmaCalc recent development and present status of the evaluated cross-sections for IBA', *Nucl Instrum Methods Phys Res B*, vol. 371, pp. 27–32, 2016.

[109] M. Bogovac, A. Gajski, and M. Jaksic, 'Accelerator Laboratory of the Ruder Boskovic Institute', 2005.

[110] I. Bogdanović Radović, 'Ruđer Bošković institute accelerator facility', *Nuclear Physics News*, vol. 30, no. 2, pp. 4–9, 2020.

[111] D. Cosic, M. Bogovac, and M. Jakšić, 'Data acquisition and control system for an evolving nuclear microprobe', *Nucl Instrum Methods Phys Res B*, vol. 451, pp. 122–126, 2019.

[112] J. L. Campbell, N. I. Boyd, N. Grassi, P. Bonnick, and J. A. Maxwell, 'The Guelph PIXE software package IV', *Nucl Instrum Methods Phys Res B*, vol. 268, no. 20, pp. 3356–3363, 2010.

[113] E. Seifert, 'OriginPro 9.1: scientific data analysis and graphing software-software review', *J Chem Inf Model*, vol. 54, no. 5, p. 1552, 2014.

[114] J. Miranda and G. Lapicki, 'Experimental cross sections for L-shell x-ray production and ionization by protons', *At Data Nucl Data Tables*, vol. 100, no. 3, pp. 651–780, 2014.

[115] M. Oswal *et al.*, 'Experimental and theoretical L-shell ionization cross sections of heavy atoms by impact of Si ions', *Radiation Physics and Chemistry*, vol. 176, p. 108809, 2020.

[116] R. Siegele, D. D. Cohen, and Z. Pastuović, 'Heavy ion PIXE cross sections in Ti, Zn, Nb, Ru and Ta for 4.8–30.0 MeV oxygen and 3.0–12.0 MeV lithium beams', *Nucl Instrum Methods Phys Res B*, vol. 450, pp. 19–23, 2019.

[117] I. Bogdanovic, S. Fazinic, M. Jakšic, and Z. Šmit, 'L-shell ionization of selected medium-Z elements by 0.22-0.83-MeV u 1 carbon ions', 1997.

[118] H. Silhadi, S. Ouziane, S. Fazinic, and G. Provatas, 'L-shell x ray production cross sections of Sm and Yb induced by carbon ions between 2 MeV and 5 MeV', *Nucl Instrum Methods Phys Res B*, vol. 478, pp. 252–259, 2020.

[119] A. Zucchiatti, P. Galán, and J. E. Prieto, 'A procedure to correct for target thickness effects in heavy-ion PIXE at MeV energies', *Nucl Instrum Methods Phys Res B*, vol. 407, pp. 1–4, 2017.

[120] J. H. Hubbell and S. M. Seltzer, 'Tables of X-ray mass attenuation coefficients and mass energy-absorption coefficients 1 keV to 20 MeV for elements Z= 1 to 92 and 48 additional substances of dosimetric interest', National Inst. of Standards and Technology-PL, Gaithersburg, 1995.

[121] J. H. Hubbell and S. M. Seltzer, 'Tables of X-Ray Mass Attenuation Coefficients and Mass Energy-Absorption Substances of Dosimetric Interest'.

[122] S. J. Cipolla, 'ISICS2011, an updated version of ISICS: A program for calculation K-, L-, and M-shell cross sections from PWBA and ECPSSR theories using a personal computer', *Comput Phys Commun*, vol. 182, no. 11, pp. 2439–2440, 2011.

[123] J. L. Campbell, 'Fluorescence yields and Coster–Kronig probabilities for the atomic L subshells', *At Data Nucl Data Tables*, vol. 85, no. 2, pp. 291–315, 2003.

[124] D. L. Walters and C. P. Bhalla, 'Nonrelativistic Auger Rates, X-Ray Rates, and Fluorescence Yields for the 2 p Shell', *Phys Rev A (Coll Park)*, vol. 4, no. 6, p. 2164, 1971.

[125] M. O. Krause, 'Atomic radiative and radiationless yields for K and L shells', *J Phys Chem Ref Data*, vol. 8, no. 2, pp. 307–327, 1979.

[126] J. H. Scofield, 'Relativistic Hartree-Slater values for K and L X-ray emission rates', *At Data Nucl Data Tables*, vol. 14, p. 121, 1974.

[127] T.J. Gray, R. Lear, R.J. Dexter, F.N. Schwettmann, and K.C. Weimer, 'Proton-induced X-ray cross sections for selected elements Fe to As and applications of X-ray analysis to semiconductor systems', *Thin Solid Films*, vol. *19, no.* 1, pp.103-119, 1973.

[128] D. S. Urch, 'The origin and intensities of low energy satellite lines in X-ray emission spectra: a molecular orbital interpretation The origin and intensities of low energy satellite lines in x-ray emission spectra : a molecular orbital interpretation'. [Online]. Available: http://iopscience.iop.org/0022-3719/3/6/009

[129] P. H. Mokler and F. Folkmann, 'X-ray production in heavy ion-atom collisions. In *Structure and Collisions of Ions and Atoms',* pp. 201-271, Berlin, Heidelberg: Springer Berlin Heidelberg, 1978.

[130] A. K. Saha *et al.*, 'Periodic variation in the I-and Ag-projectile L 1-to-L x-ray intensity ratio with the target atomic number', 1998.

[131] J. Ren *et al.*, 'Projectile energy dependence of L X-ray emission in collisions of Xe23+with in target: Role of Coulomb ionization and quasi-molecular effects', *Laser and Particle Beams*, vol. 38, no. 2, pp. 148–151, Jun. 2020.

[132] M. Goudarzi, F. Shokouhi, M. Lamehi-Rachti, and P. Oliaiy, 'L-subshell and total M-shell X-ray production cross sections of Ta, W, Pt, Au, Pb and Bi by 0.7–2.4 MeV protons', *Nucl Instrum Methods Phys Res B*, vol. 247, no. 2, pp. 217–222, 2006.

[133] D. Bhattacharya *et al.*, 'L-subshell ionization cross sections in gold and bismuth by 3.6–9.5-MeV carbon and 4.0–7.2-MeV oxygen ions', *Phys Rev A (Coll Park)*, vol. 49, no. 6, p. 4616, 1994.

[134] E. O. Ejeh, T. T. Hlatshwayo, M. Madhuku, M. Legodi, and M. Msimanga, 'Measurement of L-shell X-ray production cross sections in 89Y, 158Gd and 209Bi

due to 0.3 MeV/u–1.0 MeV/u 12C ions', *Applied Radiation and Isotopes*, vol. 177, p. 109930, 2021.

[135] I. Gorlachev *et al.*, 'K-, L-and M-shell X-ray productions induced by oxygen ions in the 0.8–1.6 MeV/amu range', *Nucl Instrum Methods Phys Res B*, vol. 381, pp. 34–38, 2016.

[136] B. Mahesh, 'Machine learning algorithms-a review', *International Journal of Science and Research (IJSR).[Internet]*, vol. 9, no. 1, pp. 381–386, 2020.

[137] G. Bonaccorso, *Machine learning algorithms*. Packt Publishing Ltd, 2017.

[138] J. Demšar *et al.*, 'Orange: data mining toolbox in Python', *the Journal of machine Learning research*, vol. 14, no. 1, pp. 2349–2353, 2013.

[139] B. Mihalić, 'Visokorazlučiva spektroskopija rendgenskoga zračenja na ionskoj mikroprobi'. [Online]. Available: https://urn.nsk.hr/urn:nbn:hr:217:033388

[140] E. R. Fossum, 'Digital camera system on a chip', *IEEE micro*, vol. 18, no. 03, pp. 8–15, 1998.

[141] M. Czarnota *et al.*, 'Satellite and hypersatellite structures of Lα1,2 and Lβ1 x-ray transitions in mid-Z atoms multiply ionized by fast oxygen ions', *Phys Rev A*, vol. 88, no. 5, 2013.

[142] M. Czarnota *et al.*, 'Multiple Ionization Effects in X-Ray Emission Induced by Heavy Ions', 2006.

[143] T. Murata, M. Kanao-Koshikawa, and T. Takamatsu, 'Effects of Pb, Cu, Sb, In and Ag contamination on the proliferation of soil bacterial colonies, soil dehydrogenase activity, and phospholipid fatty acid profiles of soil microbial communities', *Water Air Soil Pollut*, vol. 164, pp. 103–118, 2005.

[144] W. Liu *et al.*, 'The effectiveness of nanobiochar for reducing phytotoxicity and improving soil remediation in cadmium-contaminated soil', *Sci Rep*, vol. 10, no. 1, 2020.

[145] F. U. Haider *et al.*, 'Cadmium toxicity in plants: Impacts and remediation strategies', *Ecotoxicology and Environmental Safety*, vol. 211. Academic Press, 2021.

[146] P. Wang, H. Chen, P. M. Kopittke, and F.-J. Zhao, 'Cadmium contamination in agricultural soils of China and the impact on food safety', *Environmental pollution*, vol. 249, pp. 1038–1048, 2019.

[147] K. Hämäläinen, 'Coincidence measurements with X-ray synchrotron sources', *Nuclear Instruments and Methods in Physics Research Section A: Accelerators, Spectrometers, Detectors and Associated Equipment*, vol. *297, no.* 3, pp.521-525, 1990.

[148] K. Arstila *et al.*, 'Potku–New analysis software for heavy ion elastic recoil detection analysis', *Nucl Instrum Methods Phys Res B*, vol. 331, pp. 34–41, 2014.

[149] J. M. de Jesus *et al.*, 'Correlative imaging of trace elements and intact molecular species in a single-tissue sample at the 50 μm scale', *Anal Chem*, vol. 93, no. 40, pp. 13450–13458, 2021.

[150] V. Mathayan, M. Sortica, and D. Primetzhofer, 'Determining the chronological sequence of inks deposited with different writing and printing tools using ion beam analysis', *J Forensic Sci*, vol. 66, no. 4, pp. 1401–1409, 2021.

[151] R. E. Goacher, L. G. DiFonzo, and K. C. Lesko, 'Challenges determining the correct deposition order of different intersecting black inks by Time-of-Flight secondary ion mass spectrometry', *Anal Chem*, vol. 89, no. 1, pp. 759–766, 2017.

[152] R. L. Brunelle and R. W. Reed, *Forensic examination of ink and paper*. CC Thomas Springfield, IL, 1984.

[153] S. Banerjee and D. I. Wimpenny, 'Laser printing of polymeric materials', in *2006 International Solid Freeform Fabrication Symposium*, 2006.

[154] P. Calvert, 'Inkjet printing for materials and devices', *Chemistry of materials*, vol. 13, no. 10, pp. 3299–3305, 2001.

[155] V. A. Solé and E. Papillon, 'PyMCA–X-Ray Spectrum Analysis in Python'. NoBUGS, 2004.

[156] T. H. J. Niedermeyer and M. Strohalm, 'mMass as a software tool for the annotation of cyclic peptide tandem mass spectra', 2012.

[157] S. Wold, K. Esbensen, and P. Geladi, 'Principal component analysis', *Chemometrics and intelligent laboratory systems*, vol. 2, no. 1–3, pp. 37–52, 1987.

[158] C. Ding and X. He, 'K-means clustering via principal component analysis', in *Proceedings of the twenty-first international conference on Machine learning*, 2004, p. 29.

[159] J. Salomon *et al.*, 'Present and future role of ion beam analysis in the study of cultural heritage materials: The example of the AGLAE facility', *Nucl Instrum Methods Phys Res B*, vol. 266, no. 10, pp. 2273–2278, 2008.

[160] L. Matjačić, V. Palitsin, G. W. Grime, N. Abdul-Karim, and R. P. Webb, 'Simultaneous molecular and elemental mapping under ambient conditions by coupling AP MeV SIMS and HIPIXE', *Nucl Instrum Methods Phys Res B*, vol. 450, pp. 353–356, 2019.

[161] T. Calligaro *et al.*, 'Emerging nuclear methods for historical painting authentication: AMS-14C dating, MeV-SIMS and O-PTIR imaging, global IBA, differential-PIXE and full-field PIXE mapping', *Forensic Sci Int*, vol. 336, p. 111327, 2022.

[162] R. J. Gettens, H. Kühn, and W. T. Chase, '3. Lead white', *Studies in conservation*, vol. 12, no. 4, pp. 125–139, 1967.

[163] V. Gonzalez, D. Gourier, T. Calligaro, K. Toussaint, G. Wallez, and M. Menu, 'Revealing the origin and history of lead-white pigments by their photoluminescence properties', *Anal Chem*, vol. 89, no. 5, pp. 2909–2918, 2017.

Appendix A: X-ray production cross sections

Table 1. *Proton induced K-shell XPCS (units in barns) in mid-Z elements*

Z_1; Z_1/Z_2	v (MeV/u)	K_α	K_β	K_{Total}
^{52}Cr; **0.042**	2.0	73.96	10.22	84 (12)
	1.0	17.99	2.403	20 (3)
	0.8	9.607	1.300	11 (2)
	0.6	4.181	0.562	4.74 (66)
	0.4	1.143	0.141	1.28 (18)
	0.3	0.404	0.052	0.46 (6)
^{59}Ni; **0.036**	2.0	34.94	4.717	40 (6)
	1.0	6.662	0.898	8 (1)
	0.8	3.458	0.457	3.91 (55)
	0.6	1.302	0.177	1.48 (21)
	0.4	0.306	0.040	0.35 (5)
	0.3	0.127	0.014	0.14 (2)
^{73}Ge; **0.031**	2.0	14.16	2.022	16 (2)
	1.0	2.411	0.336	2.75 (38)
	0.8	1.071	0.149	1.22 (17)
	0.6	0.393	0.058	0.45 (6)
	0.4	0.084	0.011	0.095 (13)
	0.3	0.025	0.003	0.029 (4)
^{96}Mo; **0.024**	2.0	1.389	0.240	1.63 (23)
	1.0	0.173	0.027	0.20 (3)
	0.8	0.073	0.009	0.082 (12)
	0.6	0.019	0.006	0.025 (3)

Table 2. *Proton induced L-shell XPCS (units in barns) in ^{119}Sn, ^{184}W and ^{209}Bi*

Z_1; Z_1/Z_2	v (MeV/u)	L_α	L_β	L_γ	L_{Total}
^{119}Sn; **0.020**	2.0	175.6	85.36	23.90	285 (40)
	1.0	72.20	37.07	6.583	116 (2)
	0.8	44.48	22.03	2.502	69 (10)

	0.6	24.94	11.18	0.579	37 (5)
	0.4	2.124	0.989	0.134	3.25 (45)
	0.3	0.384	0.052	0.251	0.575 (80)
^{184}W; 0.014	2.0	36.81	14.71	1.171	53 (7)
	1.0	8.125	2.951	0.121	11 (2)
	0.8	4.482	1.492	0.115	6.09 (85)
	0.6	1.765	0.575	0.109	2.45 (34)
	0.4	0.405	0.131	0.038	0.57 (8)
	0.3	0.092	0.029	0.011	0.13 (2)
^{209}Bi; 0.012	2.0	16.01	5.177	0.222	21 (3)
	1.0	2.701	0.716	0.055	3.47 (49)
	0.8	1.558	0.377	0.039	1.97 (28)
	0.6	0.530	0.126	0.017	0.67 (9)
	0.4	0.098	0.017	0.006	0.12 (17)
	0.3	0.016	0.003	0.0002	0.020 (3)

Table 3. *C, F, Cl and Ti induced XPCS (units in barns) in Bi*

Z_1; Z_1/Z_2	v (MeV/u)	L_{Total}	ECPSSR (DI)
C; 0.057	0.50	2.8 (3)	6.3
	0.67	7.3 (7)	18.7
	0.83	15 (2)	40.1
	1.00	25 (3)	71.5
F; 0.091	0.32	0.47 (7)	1.04
	0,42	2.3 (2)	3.8
	0.58	7.7 (8)	14.6
	0.68	15 (2)	26.6
	0.74	18 (2)	36.1
	0.84	29 (3)	55.9
	1.00	43 (4)	99.3
Cl; 0.17	0.20	0.045 (4)	0.027
	0.60	3.3 (3)	14
	0.80	38 (4)	43.9
	1.00	84 (8)	99

Ti; 0.23	0.31	1.3 (1)	0.376		
	0.42	5.3 (5)	2.01		
	0.50	14 (1)	4.67		
	0.58	30 (3)	9.09		
	0.67	51 (5)	16.7		

Table 4. $^{28}Si^{q+}$ *induced L-shell XPCS (units in barns) in* $^{119}Sn,$ $^{184}W,$ ^{197}Au *and* ^{209}Bi

Z_1; Z_1/Z_2	v (MeV/u)	q	L_l	L_α	L_β	L_γ	L_{Total}
^{119}**Sn; 0.28**	0.75	6	32.74	674.9	420.7	81.14	1209 (156)
	0.61	5	17.87	428.5	235.9	40.54	723 (43)
	0.54	4	13.86	327.3	196.5	29.99	568 (76)
	0.43	4	12.49	243.6	92.54	22.84	372 (75)
	0.32	3	6.785	138.6	43.12	19.82	208 (31)
	0.21	3	2.903	49.09	11.74	4.667	68 (14)
^{184}**W; 0.19**	0.75	6	3.006	66.13	24.92	5.071	99 (13)
	0.61	5	1.210	24.86	11.22	1.056	38 (5)
	0.54	4	0.664	15.04	6.895	0.715	23 (5)
	0.43	4	0.221	5.373	2.495	0.371	8 (2)
	0.32	3	0.056	1.326	0.806	0.083	2.27 (62)
	0.21	3	7.5E-5	0.160	0.082	0.004	0.245 (67)
^{197}**Au; 0.18**	0.75	6	1.220	23.66	11.22	0.897	37 (2)
	0.61	5	0.346	6.653	3.785	0.336	11 (1)
	0.54	4	0.195	4.488	2.851	0.230	8 (2)
	0.43	4	0.073	1.395	0.981	0.086	2.54 (41)
	0.32	3	0.009	0.304	0.226	0.042	0.58 (13)
	0.21	3	8.5E-6	0.021	0.013	0.002	0.038 (9)
^{209}**Bi; 0.17**	0.75	6	0.793	17.66	7.694	0.749	26.9 (5.9)
	0.61	5	0.338	6.822	3.479	0.339	11 (1)
	0.54	4	0.165	3.081	1.773	0.188	5.21 (73)
	0.43	4	0.082	1.253	0.803	0.069	2.21 (52)
	0.32	3	0.017	0.210	0.134	0.015	0.375 (96)
	0.21	3	3.35E-4	3.39E-4	3.36E-4	3.35E-4	0.00135 (18)

Table 5. $^{63}Cu^{q+}$ *induced Total L-shell XPCS (units in mb) in* ^{92}Zr

Z_1/Z_2	v (MeV/u)	L_{Total}
0.7	0.33	71 (8)
	0.28	119 (14)
	0.25	68 (8)
	0.22	83 (10)

Table 6. $^{63}Cu^{q+}$ *induced L-shell XPCS (units in mb) in* ^{119}Sn

Z_1/Z_2	v (MeV/u)	L_l	$L_{\alpha1,2}$	$L_{\beta3,4,15}$	$L_{\beta9,10}$	L_γ	L_{Total}
0.54	0.33	1.1	29.3	48.3	6.7	4.5	90 (10)
	0.28	1.4	31.1	53.1	5.4	8.8	100 (11)
	0.25	0.8	18.4	29.9	3.0	4.3	56 (6)
	0.22	0.6	14.8	23.3	2.2	2.1	43 (5)
	0.19	0.4	9.43	14.2	1.4	2.6	28 (3)

Table 7. $^{63}Cu^{q+}$ *induced L-shell XPCS (units in mb) in* ^{197}Au

Z_1/Z_2	v (MeV/u)	$L_{\alpha1,2}$	$L_{\beta4,15}$
0.32	0.33	6.4 (7)	0.73 (8)
	0.28	6.3 (7)	0.82 (9)
	0.25	4.3 (5)	0.53 (6)
	0.22	5.7 (7)	0.65 (8)
	0.19	2.0 (2)	0.26 (3)

Table 8. $^{63}Cu^{q+}$ *induced M-shell XPCS (units in mb) in* ^{197}Au

Z_1/Z_2	v (MeV/u)	$M_{\xi1}$	$M\alpha_{1,2}$; M_β	M_β, M_η	$M_{\gamma1,2}$	M_{Total}
0.32	0.33	13.5	495	96	85	960 (79)
	0.28	27.2	660	42	252	981 (112)
	0.25	18.4	540	127	65	750 (86)
	0.22	33.2	803	75	249	1160 (133)
	0.19	5.51	325	61	32	424 (48)

Table 9. $^{63}Cu^{q+}$ *induced L-shell XPCS (units in mb) in* ^{209}Bi

Z_1/Z_2	v (MeV/u)	$L_{\alpha1,2}$	$L_{\beta4,15}$
0.31	0.33	4.46 (50)	0.54 (6)
	0.28	2.41 (3)	0.37 (4)
	0.25	1.41 (20)	0.16 (2)
	0.22	2.23 (30)	0.23 (3)
	0.19	0.47 (5)	0.06 (1)

Table 10. $^{63}Cu^{q+}$ *induced M-shell XPCS (units in mb) in* ^{209}Bi

Z_1/Z_2	v (MeV/u)	$M_{\xi 1}$	$M_{\alpha 1,2}$; M_β; M_η	$M_{\gamma 1,2}$	M_2N_4	M_{Total}
0.31	0.33	21.2	1020	148	212	1410 (161)
	0.28	14.2	706	104	143	968 (111)
	0.25	17.9	514	61.8	125	718 (82)
	0.22	19.5	977	122	189	1310 (150)
	0.19	4.83	269	29.8	49	353 (40)

Table 11. $^{108}Ag^{q+}$ *induced Total L-shell XPCS (in mb units) in* ^{184}W

Z_1/Z_2	v (MeV/u)	L_{Total}
0.55	0.26	2883 (346)
	0.24	2323 (279)
	0.22	3012 (361)
	0.20	1470 (176)
	0.19	1293 (155)

Table 12. $^{108}Ag^{q+}$ *induced Total L-shell XPCS (in mb units) in* ^{197}Au

Z_1/Z_2	v (MeV/u)	L_{Total}
	0.24	14769 (1772)
	0.22	10641 (1277)
	0.20	7507 (901)
	0.19	6903 (828)

Table 13. $^{127}I^{q+}$ *induced Total L-shell XPCS (in mb units) in* ^{92}Zr

Z_1/Z_2	v (MeV/u)	L_{Total}
0.7	0.18	314 (36)
	0.16	267 (31)
	0.14	773 (88)
	0.13	272 (31)
	0.11	186 (21)
	0.09	189 (22)
	0.08	179 (20)

Table 14. $^{127}I^{q+}$ *induced* $L_{\alpha 1,2}$ *XPCS (in mb units) in* ^{119}Sn

Z_1/Z_2	v (MeV/u)	$L_{\alpha 1,2}$
0.54	0.18	143 (16)
	0.16	159 (18)
	0.14	760 (87)
	0.13	166 (19)
	0.11	119 (14)
	0.09	127 (15)
	0.08	181 (21)

Table 15. $^{127}I^{q+}$ *induced M-shell XPCS (in mb units) in* ^{197}Au

Z_1/Z_2	v (MeV/u)	$M_{\xi 1}$	$M_{\alpha 1,2}$; M_β	M_β, M_η	$M_{\gamma 1,2}$	M_{Total}
0.32	0.18	24.9	845	211	258	1340 (153)
	0.16	30.6	858	221	248	1360 (155)
	0.14	42.9	1900	473	502	2910 (334)
	0.13	120	3630	1100	786	5630 (645)
	0.11	20.1	646	163	167	996 (114)
	0.09	19.1	584	132	139	874 (100)
	0.08	16	464	92.3	113	686 (78)

Table 16. $^{127}I^{q+}$ *induced M-shell XPCS (in mb units) in* ^{209}Bi

Z_1/Z_2	v (MeV/u)	$M_{\xi 1}$	$M_{\alpha 1,2}$; M_β, M_η	$M_{\gamma 1,2}$	M_2N_4	M_{Total}
0.31	0.18	36.3	1270	202	105	2460 (281)
	0.16	29.8	1500	154	121	2080 (239)
	0.14	4110	2720	499	272	4110 (471)
	0.13	6990	4270	832	413	6990 (800)
	0.11	1900	1280	216	124	1900 (218)
	0.09	2010	1370	224	199	2010 (230)
	0.08	1380	950	148	168	1380 (158)

Table 17. *Semi-empirical Total L-shell XPCS due to N and O in Bi (in barns)*

Ion	v (MeV/u)	Calculated (HI/p)	ECPSSR (DI)
O	0.32	1.2 (1)	0.97
	0.4	4.1 (5)	2.9
	0.5	11 (1)	7.53
	0.7	35 (4)	27.5
	0.9	73 (9)	65.1
	1.0	98 (12)	91.4
N	0.32	1.1 (1)	0.93
	0.4	3.6 (4)	2.7
	0.5	10 (1)	7.03
	0.7	30 (4)	25.2
	0.9	61 (7)	59
	1.0	83 (10)	82.3

Table 18. *Semi-empirical Total L-shell X-ray production cross sections in Bi (in barns) due to Na and Si*

Ion	v (MeV/u)	HI/p (calculated)	ECPSSR (DI)	ECPSSR (DI + EC)
Si	0.4	2.6 (4)	2.6	3.6
	0.6	12 (2)	15.8	24.2
	0.8	30 (5)	48.1	80.2
	1.0	49 (7)	106	192
Na	0.4	2.3 (4)	3.0	3.4
	0.6	11 (2)	17.1	20.6
	0.8	26 (4)	50.1	62.2
	1.0	42 (6)	107	138

Table 19. *Characteristic X-ray energy shifts (eV) due to $^{127}I^{q+}$*

Element	v (MeV/u)	$L_{\alpha1.2}$	$M_{\alpha1,2}$	$M_{\beta, \eta}$
Sn	0.18	109	-	-
	0.16	106	-	-
	0.14	102	-	-
	0.13	101	-	-
	0.11	98	-	-
	0.09	95	-	-
	0.08	93	-	-
Au	0.18	-	143	153
	0.16	-	142	146
	0.14	-	135	135
	0.13	-	134	135
	0.11	-	132	134
	0.09	-	131	131
	0.08	-	125	119

Bi	0.18	-	145	164
	0.16	-	138	152
	0.14	-	135	152
	0.13	-	133	150
	0.11	-	128	139
	0.09	-	126	139
	0.08	-	126	137

Table 20. *Characteristic X-ray energy shifts (eV) due to $^{63}Cu^{q+}$*

Element	v (MeV/u)	$L_{\alpha1.2}$	L_β	$M_{\alpha1,2}$	$M_{\beta,\eta}$
Sn	0.33	95	145	-	-
	0.28	89	141	-	-
	0.25	87	138	-	-
	0.22	82	133	-	-
	0.19	81	132	-	-
Au	0.33	61	317	188	137
	0.28	54	296	112	129
	0.25	51	283	109	116
	0.22	47	272	105	116
	0.19	36	252	90	112
Bi	0.33	56	204	122	150
	0.28	46	178	116	135
	0.25	45	166	111	132
	0.22	41	160	106	129
	0.19	26	148	101	112

Biography

Masedi Carington Masekane was born on the 14th December 1994 in the town of Phalaborwa, South Africa. He was raised in the capital city, Pretoria, where he began his journey in science at the Tshwane University of Technology, becoming one of the first graduates of the then inaugural Diploma programme in Industrial Physics (Nuclear Technology) (2016). It was during this time that he was introduced to Ion Beam Analysis, at the iThemba Laboratory for Accelerator Based Sciences (LABS), through a Work Integrated Learning programme. Masedi proceeded to obtain a coveted Postgraduate diploma in Nuclear Science and Technology from the Nuclear Engineering department of the North-West University in Potchefstroom (South Africa), leading him to a Master of Science degree (*cum laude,* 2020) in Physics from the University of South Africa. His notable achievements include his participation in the one-month 2016 student practice at the Joint Institute for Nuclear Research in Dubna, Russia. He was also awarded best MSc talk given in the division for Radiation and Particle Physics at the 2018 South African Institute of Physics (SAIP) conference in Bloemfontein (South Africa), and the Michel Cantarel Prize for young emerging researchers at the 2019 international Ion Beam Analysis (IBA) conference in Antibes, France. Masedi completes his doctorate as an International Atomic Energy Agency (IAEA) fellow, through which he has spent two years at the Laboratory for Ion Beam Interactions (LIBI) of the Ruđer Bošković Institute in Croatia. During his fellowship, he was bestowed the young scientist award at the Abdus Salam International Centre for Theoretical Physics (ICTP) (Trieste, Italy) during the 2022 Joint IAEA/ICTP "advanced workshop on future trends in Multidisciplinary Ion Beam Analysis" and has presented his doctoral results at the 2023 international IBA/PIXE conference in Toyama, Japan. His current research focuses on the development of Total Ion Beam Analysis using Heavy Ion PIXE, which is the basis of his joint PhD (*Cotutelle*) between the University of South Africa and the University of Zagreb.

Publications:

- M.C. Masekane, I. Bogdanović-Radović, I. Božičević-Mihalić, A. Mioković, S.J. Moloi, M. Msimanga, and S. Fazinić, 'Experimental subshell vacancies in a multiply ionised Sn atom by heavy ion impact', *Radiation Physics and Chemistry*, p.112211, 2024.

- M.C. Masekane, M. Msimanga, I. Bogdanović-Radović, M. Madhuku and S.J. Moloi, 'Semi-empirical parameterization of HI/p L-shell X-ray production cross section ratios in Bi for Heavy Ion PIXE', *Scientific Reports*, vol. *13, no.* 1, p.20942, 2023.
- M.C. Masekane, I. Bogdanović-Radović, M. Msimanga and S.J. Moloi, 'Experimental low velocity proton and 28Siq+ induced X-ray production cross sections for select elements within 24≤ Z≤ 83', *Radiation Physics and Chemistry*, vol. *213*, p.111208, 2023.
- M.C. Masekane, S.J. Moloi, M. Madhuku and M. Msimanga, 'Measurement of 12Cq+ and 35Clq+ ion induced X-ray production cross sections in V, Zr and Sn metal oxide films at 0.1 MeV/u-1.0 MeV/u energies', *Radiation Physics and Chemistry*, vo. *176*, p.109083, 2020.